Doctoral Dissertation

Doctoral Program in Mechanical Engineering (30thcycle)

Numerical Modeling and Experimental Testing of a Pendulum Wave Energy Converter (PeWEC)

By

Nicola Pozzi
******

Supervisor(s):
Prof. Giuliana Mattiazzo

Doctoral Examination Committee:
Prof. Angelo Iollo, Referee, Université de Bordeaux (France)
Prof. Benedetto Allotta, Referee, Università degli Studi di Firenze (Italy)
Prof. Marco Belloli, Politecnico di Milano (Italy)
Prof. Massimo Sorli, Politecnico di Torino (Italy)
Prof. Stefano Mauro, Politecnico di Torino (Italy)

Politecnico di Torino

2018

Declaration

I hereby declare that, the contents and organization of this dissertation constitute my own original work and does not compromise in any way the rights of third parties, including those relating to the security of personal data.

<div align="right">

Nicola Pozzi
2018

</div>

Ai miei genitori,
a Cinzia e Alberto,
a Ersilia, Massimo e Maria Angela,
alla mia famiglia,
a Olivia,
a tutte le persone che mi sono state accanto in questi splendidi anni.

Acknowledgements

Abstract

The research activities described in the present work aims to develop a pendulum converter (PeWEC: Pendulum Wave Energy Converter) for the Mediterranean Sea, where waves are shorter, thus with a higher frequency. In particular, the Pantelleria Island site wave climate is assumed as reference. The research activities started from the preliminary investigation of the working principle validity in the case of the Mediterranean Sea wave characteristics, taking into account a 1:45 scale prototype. The numerical model reliability and the success of experimental tests motivated the design and development of a 1:12 scaled device, useful for a deeper investigation of the technology capabilities and performances. Globally, the technology readiness level (TRL) was increased from 1 to 4. Important effort were focused in the development of a reliable model-based design and optimization methodology for the investigation of a full scale configuration. The latter was widely used to identify a preliminary full scale configuration and to assess the economic viability of the PeWEC technology in the Mediterranean Sea context. Results were benchmarked against the ISWEC pilot plant, deployed in 2015, in Pantelleria Island. One of the major outcomes of this analysis is a detailed overview of the advantages and drawbacks of an active (ISWEC) and a passive (PeWEC) technology, together with some guidelines for the improvement of this technology.

Contents

8   Conclusions   **239**

List of Figures

List of Tables

Chapter 1

Introduction

1.1 Renewable energy: motivation and current status

Every historical period has some important challenge to deals with. Nowadays, the most important problems of the society are climate changing, pollution, limited energy resources (fossil fuels) and a continuous increasing of energy demand. These issues are the results of the industrialization and automation process that started in Europe in the past century and spread almost all over the World, even if with different velocity in each Country. This process is still ongoing and it is mainly driven by coal, oil, gas and their derivatives.

Regarding the World primary energy demand, it rose by about one-third from 2000 to 2014 with an annual average of around 1.8% since 2011, although the rate of growth has slowed in the past few years, with wide variations by country. More in detail, a larger growth in primary energy demand has occurred largely in developing countries, whereas in developed countries it has slowed or even declined. By looking to next 20 years, the energy demand will 25% higher than in 2014 [42][98].

The most important problems directly related to the energy demand are pollution and CO_2 emissions, the key driver of greenhouse effects and climate changing. The atmospheric CO_2 levels fluctuations before pre-industrial activity were primarily caused by the release of carbon to the atmosphere from deforestation and other activities related to the use of the land. Emissions from fossil fuel combustion

became the dominant source of CO_2 to the atmosphere from around 1920, with a constant increase up to the present [93].

Looking at the last decades, the carbon emission average rate of growth was 2.2%, while from 2013 to 2016 the rate was almost flat at 0.2%, breaking away from the dangerous rate of the previous decades. The CO_2 emission reduction was largely due to declining coal use worldwide but also to improvements in energy efficiency and to increasing power generation from renewable energy sources (RES) [98]. The emission rate reduction is also the results of a positive signal of awareness by the International Community, that in 1992 shared the first treaty in which signatory States commit themselves in reducing carbon emission (*United Nations Framework Convention on Climate Change*) [121]. Few years later, in 1997, the Kyoto Protocol quantified the objectives about emission reduction and nowadays are the reference for the 2020 time horizon [122]. In 2015, International Community drafted the Paris Climate Agreement, which will regulate carbon emission objectives in the post 2020 time frame.

For instance, in the recent years, more than 170 countries have established renewable energy targets and around 150 of them have subscribed policies to promote investments in renewable energy technologies, with the aim to mitigate climate change and enhance access to modern sources of energy. An interesting datum is represented by the exceed of renewables installed power capacity over non-renewables in 2012. Nowadays, renewables represent the 61% of all new power generating capacity added worldwide [57]. In particular, in 2015, the worldwide installed renewable sources capacity grew by 154 *GW*, corresponding to an increase of 9.3% over 2014, as reported in Fig. 1.1.

In the same year, the global electricity demand was 24,100 *TWh* and the 23.5% of total amount was covered by renewable energy sources. As shown in Fig. 1.2, the most important contribution of this portion is represented by the more mature hydropower and wind power which, together with photovoltaic panels, in the recent years entered in the energy mix with competitive costs. For instance, in 2015, wind and solar power commanded about 90% of the investments in RES, leading to a sharp reduction of wind turbines and photovoltaic (PV) modules capital costs and thus to grid parity of the corresponding Levelized Cost Of Energy (LCOE) (see Fig. 1.3).
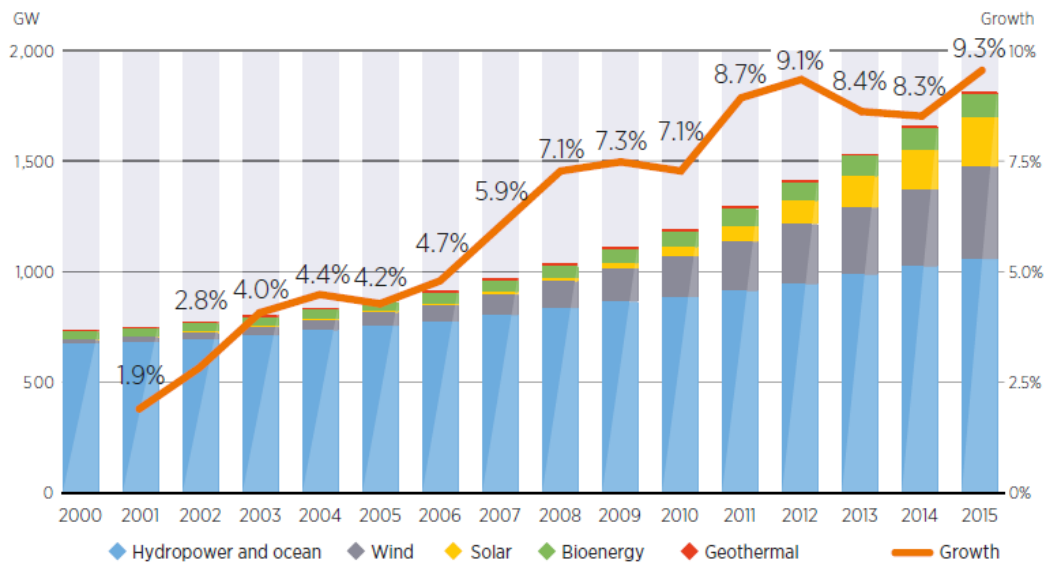
Fig. 1.1 Renewable power capacity and annual grow rate between 2000 and 2015 [57].

Beside wind power, in the Seventies, many efforts were concentrated to attempt the harvesting of the untapped energy potential of waves. This was the first time that research activities where systematically performed in this field. The different and unexplored basis of wave power, did not lead to a unique layout for energy harvesting like in the case of wind power. In fact, nowadays Wave Energy is not yet part of the renewable energy mix, but a slow and constant developments are confirming its potentialities.
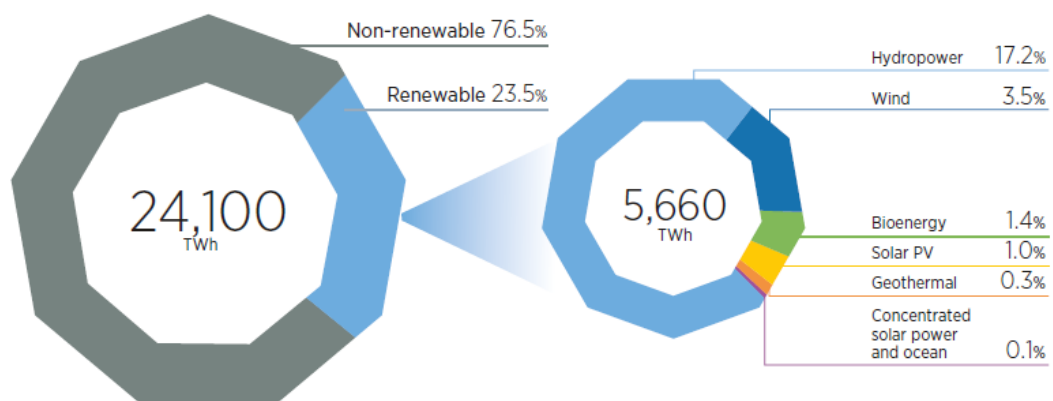
Fig. 1.2 Global electricity generation by source, 2015 [57].
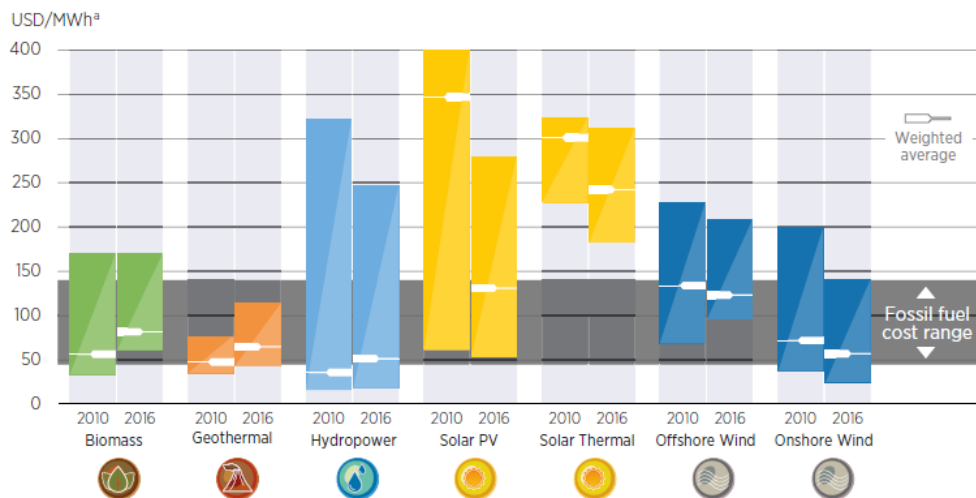
Fig. 1.3 Levelized cost of energy for utility-scale power (ranges and averages), 2010 and 2016 [57].

Focusing on investments, in Fig. 1.4 the vertical bar chart shows the comparison between developed and developing countries new investments (in billion of dollars) in RES, between 2004 and 2016. It is interesting to note the constant increasing of investments carried out by developing economies, which reached the leadership of developed economies in 2015.

However, as reported by the horizontal bar graph of Fig. 1.4, investments in renewables (excluding large hydro) fell by 23% from 2015 to 2016, even if the new worldwide installed capacity was installed and more than 50% of the new capacity was represented by renewables (wind, solar, biomass and waste, geothermal, small hydro and marine). The most important reasons of this contrast are due to the decline of the capital costs for wind and solar, a different timing between investments and commissioning of new plants and the less positive note of a slowing activity in two key markets, China and Japan [120].

Despite that, the global potential for renewable energy is very wide and in the perspective of an appropriate and sustained policy supporting the increment of renewable power plant in the energy mix and the replacement of inefficient non-renewable production system, the actual technologies could be the right solution to address climate concerns within a critical time frame.
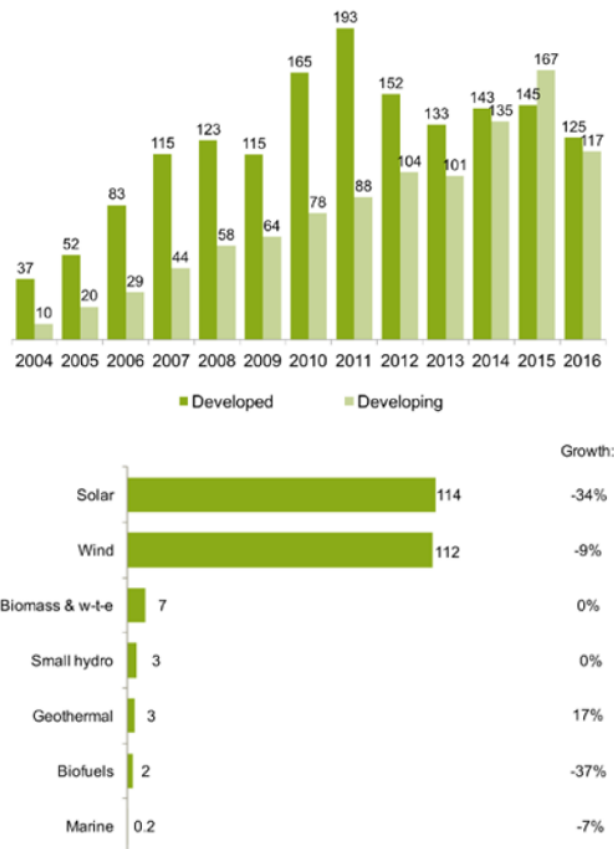
Fig. 1.4 Developed and developing countries new investments in RES (billion of dollars) between 2004 and 2016 (top) and new investments by sector in 2016 and growth on 2015 (bottom) [120].

1.2 Wave Energy

In the renewables context, Ocean Energy offers a remarkable potential around the World, distributed on different sources, such as waves, tidal and ocean currents, ocean thermal energy and osmotic power (salinity gradient). The attractiveness of Ocean Energy is represented by the fact that 70% of the Earth is covered by water and around 44% of the population is concentrated nearby coasts [118].

1.2.1 Energy distribution

Focusing on Wave Energy, its potential has been estimated to be (on average) 2 *TW*, corresponding to a theoretical available energy resource of 17,520 *TWh* [52]. Other

important aspects that make wave power attractive are the higher energy density ($2 - 3 \frac{kW}{m^2}$) with respect to solar and wind power ($0.1 - 0.2 \frac{kW}{m^2}$ and $0.4 - 0.6 \frac{kW}{m^2}$, respectively), the higher predictability of waves with respect to wind [35][68] and the almost zero land consumption. The higher waves predictability is favoured by the fact that the sea surface acts to constrain energy flows and enhance blockage, unlike the atmosphere [22][97].

As most forms of renewable sources, wave energy is distributed not uniformly over the Earth. In Fig. 1.5, the theoretical fluxes per meter width of incoming wave around the World are indicated. The wave atlas proposed is the result obtained combining the best quality wave model data with the historical measured data. In particular, it was originated from ECMWF (European Centre for Medium-Range Weather Forecast) WAM model archive, based on 10 years period / 6 hourly time series on a 0.5° latitude/longitude grid and calibrated using TOPEX and JASON satellites altimeter and buoy data from many measurement campaigns [10][77].
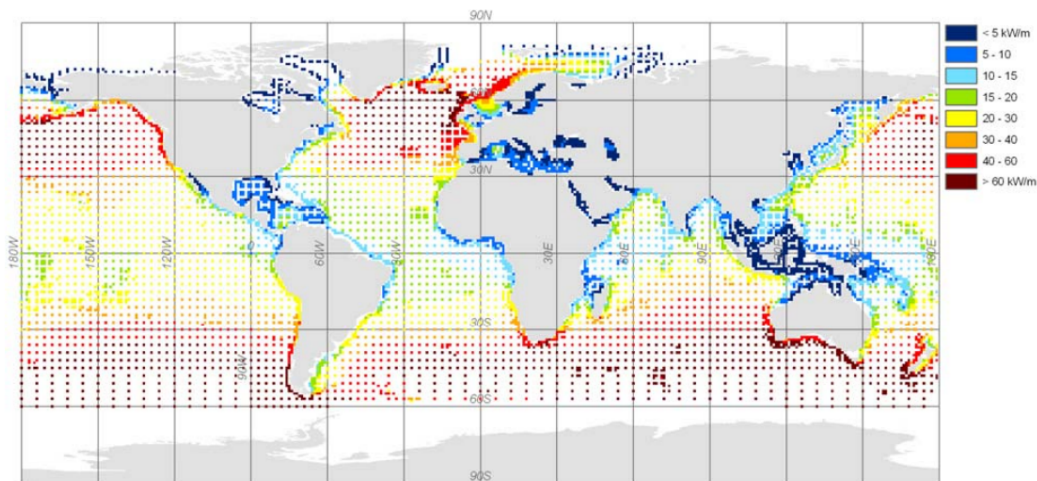
Fig. 1.5 Global wave power density distribution $\left(\frac{kW}{m}\right)$ [77].

Observing Fig. 1.5, it is possible to see that an increased wave activity is found between the latitudes of 30° and 60° on both hemispheres, induced by the prevailing western winds (Westerlies) blowing in this regions. The latter are also responsible for a higher wave power density in front of the coasts facing west than the ones facing east. This fact can be easily seen comparing, for example, the wave power density along western and eastern North America coastlines or the one along south-western and north-eastern Australia coastlines.

Considering the western coast of Europe, the long-term annual wave power level increases from about 33 $\frac{kW}{m}$ along the southern part of Europe's Atlantic coastline (southern Portuguese coastline) up to 76 $\frac{kW}{m}$ near Ireland and Scotland. In the North Sea, the resource changes significantly, varying from 38 $\frac{kW}{m}$ in the most exposed area (northern area) to about 15 $\frac{kW}{m}$ in the more sheltered area (southern area), as reported in Fig. 1.6.
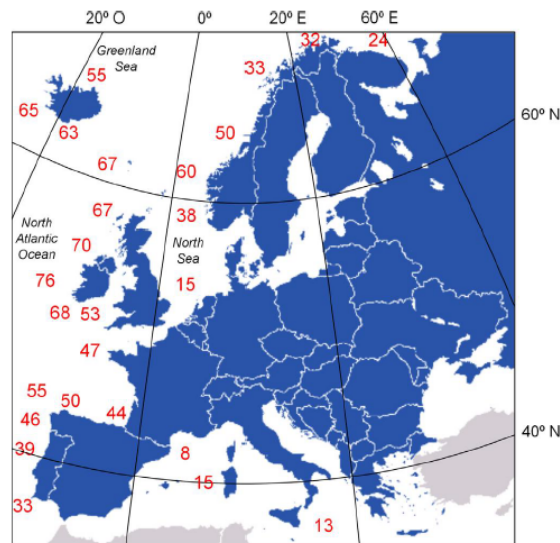
Fig. 1.6 European wave power density distribution $\left(\frac{kW}{m}\right)$.
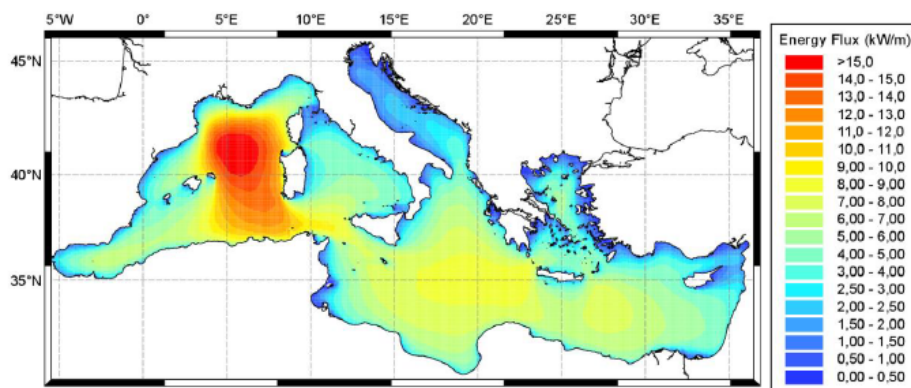
Fig. 1.7 Mediterranean Sea wave power density distribution $\left(\frac{kW}{m}\right)$.

Looking at the Mediterranean Sea, several studies have been performed by different authors in order to assess its potential in the perspective of wave energy exploitation [9][17][66]. Observing Fig. 1.7, the wave energy density levels decrease

significantly if compared with respect to the global map, varying from 1.5 $\frac{kW}{m}$ around the coasts of the Adriatic Sea and of the Aegean Sea up to 15 $\frac{kW}{m}$ in the area included between Sardinia, French coastline and Balearic Islands. Other interesting zones are the Sicily channel and the Ionian Sea, with power fluxes around 10 $\frac{kW}{m}$.

1.2.2   Wave Energy history

The father of the modern Wave Energy is Yoshio Masuda, who in 1940s developed a floating oscillating water column converter, used to supply navigation buoys [43] [71]. In the 1970s, the oil crisis encouraged the development of renewables and in the context of the Wave Energy, McCormick in the United States, Stephen Salter and Kjell Budar, researchers at the Universities in Scotland and Norway respectively, started a systematic research, laying the wave power theoretical basis and introducing the concept of Wave Energy Converter (WEC) [30][103].

Starting from these results, several Wave Energy Converter concepts based on different operating principles were developed in Europe and in other countries (see section 1.2.3). Looking at the European scenario, the European Commission financed more than thirty projects since 1991, when wave power was introduced in the R&D program on renewables. The economic help of European Commission boosted the technology development and different concepts grew from small scale prototypes to devices ready to be commercialized [68][116].
In 2015, the United States Department Of Energy (DOE) financed the *Wave Energy Prize* (WEP) competition based on a multiple-gate structure, aiming to select the best technology to be funded. Each concept was analyzed according to a specific metric and evaluating different aspects such as materials, device complexity, failure rate, levelized cost of energy [38]. A similar approach was adopted by the Wave Energy Scotland (WES) grant program, focused on the R&D activities about innovative solutions to the technical challenges facing the wave energy sector, aiming to produce reliable and cost effective technologies wave energy generation [128]. The multiple-gate structure methodology proved to be particularly efficient for the identification of the best technologies and teams, avoiding the waste of public money.

Although the considerable R&D efforts pursued in more than 40 years, wave power has not reached a convergence of the final conversion concept, like in the case of hydropower and wind power. This is a crucial point for the cost reduction

and entering in the renewable energy production mix. The reasons why wave power did not converged to a final solution are various. First of all the irregularity in wave amplitude, phase and direction makes difficult to obtain maximum efficiency of a device over the entire range of excitation frequencies. Secondly, the harsh and hostile marine conditions environment cause problems in durability and corrosion. For instance, during extreme weather condition, structural loads can be one hundred times the rated ones. Moreover, the hostility of the marine environment makes the maintenance of a WEC particularly difficult, resulting in quite significant operational and maintenance costs. Lastly, the largest amount of wave power is usually located in remote areas away from the shore, increasing the installation costs.

On the other hand, as mentioned before, wave power combines crucial economic, environmental and social factors that affects positively the R&D investments toward the identification of a final conversion concept. Moreover, Wave Energy is generally considered to provide a clean source of renewable energy, with limited negative environmental impacts.

1.2.3   Wave Energy Converters classification

As described in previous section, several WEC concepts have been developed throughout wave power history. In this section, a brief overview of the WECs classification is given. A more detailed introduction to the possible solutions and classification can be found in [23][35][40][43][68][94].
Starting from the scheme reported in Fig. 1.8, WECs can be classified in five categories, according to their working principle: *Oscillating Water Column* (OWC), *Pressure differential*, *Floating structure*, *Overtopping* and *Oscillating Wave Surge*.

Oscillating Water Column devices are constituted by a partially submerged hollow structure, open to the sea below the water line and enclosing a column of air on top of the column of water. The air column is compressed and decompressed as consequence of the vertical oscillations of the water column, caused by waves. The trapped air flows to and from the atmosphere via a Wells turbine connected to the electrical generator. Wells turbine is able to rotate regardless of the direction of the airflow. Examples of installations are LIMPET, Oceanlinx and OE buoy.
Pressure differential WECs are typically located near shore or offshore and fixed to the seabed. The motion of the waves causes the sea level to rise and fall above
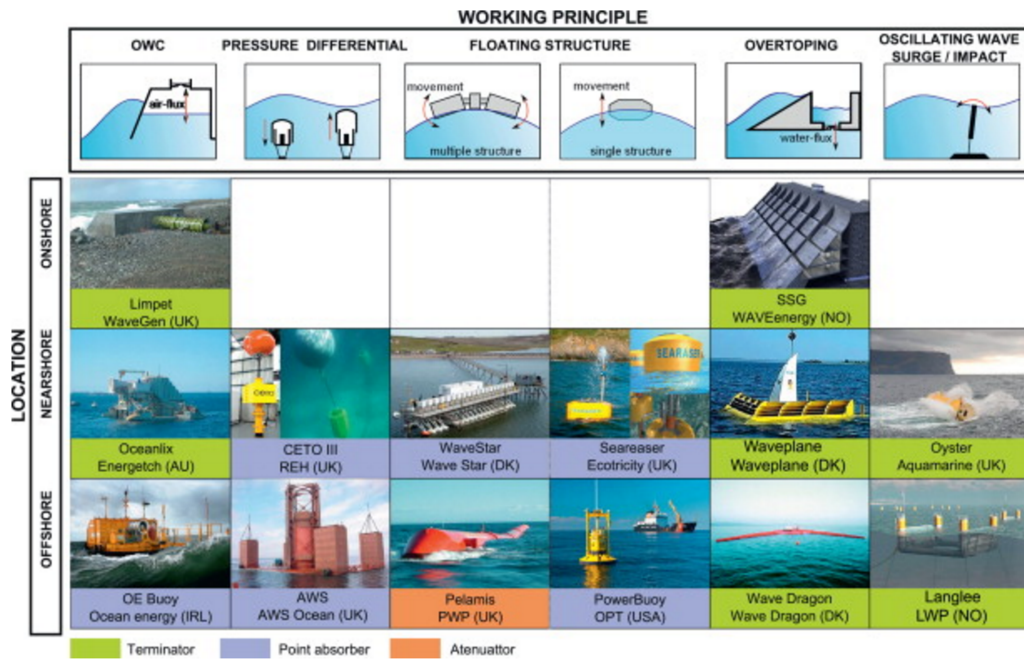
Fig. 1.8 Wave Energy Converters classification [68].

the device, inducing a pressure differential on the device. The alternating pressure pumps fluid through a system to generate electricity. CETO project and AWS project are an example of pressure differential WECs.

Floating structures, instead, can be subdivided in multi-body or single body devices. The pressure and kinetic energy of the waves is converted in mechanical energy by the floating body/bodies. The relative motion occurring between the different bodies or between the body and the seabed or a fixed structure, is used to produce electricity. WaveStar and Pelamis devices are relevant examples of multiple body WECs, while Seareaser and PowerBuoy are typical examples of single body devices.

Overtopping devices are equipped with a ramp over which waves break into a storage reservoir. Here, a head of water above the free water surface is generated. The water is then returned to the sea passing through a conventional low-head turbine, generating power. SSG, Waveplane and Wave Dragon project are representative examples of this category.

Lastly, *Oscillating Wave Surge* WECs extract energy from wave surges and the movement of water particles. This movements allow to drive an arm which oscillates as a pendulum mounted on a pivoted joint, typically fixed to the seabed. Examples of installations are Oyster project and Langlee.

According to Fig. 1.8, WECs can be also categorized according their size and direction of elongation. *Attenuators* are elongated structures with dimensions larger than the wavelength of the waves and are oriented parallel to the wave propagation direction, while *point absorbers* have dimensions much smaller than the wavelength of waves. Instead, *terminators* are similar to the attenuators, but they are oriented perpendicularly with respect to the wave propagation direction.

Another widespread classification is represented by the installation location, following which it is possible to identify three possibilities: *Onshore*, *Nearshore* and *Offshore* devices.

Onshore devices are situated on the shoreline above the sea surface. The advantages of these WECs are the easy installation and maintenance. Furthermore, moorings or long lengths of underwater electrical cable are not required. On the other hand some schemes could be limited by technical requirements (shoreline geology, tidal range) or by problems associated to the environmental impact (preservation of coastal scenery).

Nearshore WECs are generally placed few hundred meters from the shore, in moderate water depths (10 - 25 m) and fixed on the seabed. In other cases, they are floating structures moored on the seabed.

Lastly, *Offshore* devices are placed far from the shore, where the water depth is more than 40 m. Here, it is possible to exploit more powerful waves. Offshore WECs can be floating or submerged, but in both case are moored to the seabed. The most significant disadvantages of this category are the lower reliability and survivability, due to the higher stresses induced by the powerful waves of open sea. Moreover, the long underwater cable required together with mooring lines are particularly expensive, as well as the maintenance operations.

1.3   Motivation

As presented in the previous section, more than forty years of R&D in the wave energy field produced a great development of wave power technologies around the Europe and more in general around the World, even if large scale commercial installations are not yet in operation. Research on wave power is particularly advanced in the Europe countries bordering on the Atlantic Ocean (Ireland, Portugal, Spain,

Norway and UK), where a greater wave energy potential is available (see section 1.2.1).

It is undeniable that a higher energy availability is the factor that primarily affects the overall plant energy production and thus attractiveness of potential investors. However, it is important to underline that a higher energy potential implies, in general, stronger sea states during extreme events, that might compromise the plant survivability. Beside these issues, higher development, installation, operating and maintenance costs are generally expected. Considering instead the Mediterrean Sea scenario, the calmer and semi-enclosed sea offers lower amount of energy, but the milder extreme wave climate facilitates the technical issues related to these events. Clearly, because of the lower amount of energy available, an accurate design and engineering of the WEC is required in order to make energy production still economically viable. In this context, several studies have been performed in order to provide detailed reports about energy potential and its characteristic around Mediterranean coastlines, an aspect of crucial importance for the identification of the most suitable installation site and for an accurate device optimization [9][17][66].

Focusing on the Italian panorama, the relative long coastlines and the minor islands not connected to the mainland grid (Pantelleria, Lampedusa) make wave power particularly attractive. Since 2012, Italian Government has promoted the development of renewable energy technologies introducing new policies and the possibility to access to public funding. Encouraged by these initiatives, R&D programs advanced in both Universities and private companies, leading to different concepts specifically designed for the Mediterranean Sea wave climate. ISWEC, REWEC3, 40South Energy R115 and Poly-OWC are some of the most representative technologies developed in Italy, that will be described more in detail in Chapter 2.

The PeWEC project, objective of this work, was born in 2014 from the collaboration between ENEA (the Italian National agency for new technologies, energy and sustainable economic development) and the Politecnico di Torino research group that, few year before, developed the ISWEC device for the Pantelleria Island installation site. The development of the PeWEC technology has been financed by the Italian Govenment through the grant *Accordo di Programma ENEA-MiSE 2015*.

The wave power exploitation through a floating pendulum based device is not novel. For instance, the most famous example is represented by the SEAREV Wave Energy Converter developed at the École Centrale de Nantes for the oceanic site of

the Isle of Yeu (France) [31][32][102]. However, the novelty of this thesis regards the study of a pendulum WEC specifically designed for the Pantelleria Island wave climate, where waves are shorter and characterized by a lower wave amplitude. According to the recommendations for the development of new Wave Power technologies [41][54][84], in this thesis a 1:45 scale prototype has been designed and tested in regular waves at the INSEAN wave basin (Rome, Italy) with the aim to assess the validity of the working principle and validate numerical models. Numerical models are then used to design the 1:12 scaled device. The prototype has been widely tested at the INSEAN wave basin, in both regular and irregular waves. Regarding irregular waves, scaled irregular wave profiles recorded at the Pantelleria Island site have been used. In this testing session, the performances of the device are evaluated and experimental data are used for a further investigation of the numerical model reliability. Numerical models proved to be in good agreement with experimental data, therefore they have been used to develop a detailed design and optimization methodology.

In the last part of this work, the optimization methodology previously developed, coupled with a techno-economic analysis, is used to perform a preliminary design of the full scale PeWEC device. The optimal solution determined is compared against the full scale ISWEC device, considering performances, economic viability and highlighting also the advantages and disadvantages of the technologies considered. In fact, one of the main objective of this work is to point out the differences between an *active* and a *passive* technology. As will be described more in detail in Chapter 2, the ISWEC is an inertial *active* device, since its dynamic response can be adapted by varying the gyroscope flywheel speed. Therefore, the device needs to drain a small amount of the produced power to keep the flywheel in rotation [111]. On the other hand, the PeWEC device does not need to be powered to produce inertial effect, so here it is referred as to *passive* device [36][99].

1.4   Contents of the Thesis and main contributions

The thesis is composed of 7 additional chapters following this chapter. Each chapter is provided with a dedicated introduction and references, since the nature of the subject material of each chapter is substantially different. The following describes the content of each chapter in brief, highlighting also the main contributions.

In Chapter 2, an overview of the most representative wave power technologies developed in the Italian scenario is presented, starting from the PeWEC device. Particular attention is given to the ISWEC project features, since it constitutes the reference for the comparison of the PeWEC device performances with respect to the Pantelleria Island site wave climate. Other three WEC concepts are presented with the aim to complete the description of the Italian state of the art.

In Chapter 3, the PeWEC numerical model is developed, starting from the derivation of the internal swinging mass dynamic equations. A multi-body approach coupled with the Lagrange method is used instead of the classical Newtonian approach. Both nonlinear and linear equations formulation are presented.
Beside mechanical equations, the hydrodynamic model describing the interaction between floater and wave is presented. In the perspective of the implementation of a lumped parameters Wave-to-Wire model, the linear integro-differential Cummins equation is considered, highlighting the main advantages and drawbacks of the potential-flow theory based hydrodynamic models. The techniques used to introduce nonlinear effects are explained, highlighting the most important literature references. A particular attention is given to wave forces modeling and their influence on the mooring line. More in detail, drift forces (second order wave forces) are analyzed and introduced into the model, together with a quasi-static representation of the mooring line force-displacement characteristic.
Lastly, pendulum dynamic equations and hydrodynamic model are coupled together obtaining the complete mathematical representation of the device dynamic behavior, considering both linear and nonlinear formulation. The aspects related to the second order wave force modeling and hydrodynamic nonlinear phenomena have been widely studied and implemented by the candidate during the research activity period carried out at Massachusetts Institute of Technology (MIT) Sea Grant Department, under the supervision of Prof. Stefano Brizzolara.

In Chapter 4, the Pantelleria Island site wave climate is described together with the 1:45 scale PeWEC device features. The prototype experimental set up and WiFi data logging system (fully synchronized with tank testing wave monitoring system) is presented, together with the experimental results. The latter are used to evaluate the device frequency domain response, the technical feasibility in the Mediterranean wave climate context and to preliminary validate numerical models. The relatively small scale of the device did not allow to determine clearly the device performances and efficiency, because of a remarkable influence of the pendulum

bearings friction, especially in resonance conditions. Despite that, models proved to be in good agreement with experimental data and reliable enough for the design of an intermediate scale device.

In Chapter 5, the 1:12 PeWEC prototype model-based design methodology is widely described, highlighting the hypothesis and solutions adopted for the implementation of the different device subsystems.
More than 120 tests have been performed at the INSEAN wave basin, evaluating the PeWEC performances in both regular and irregular waves. The latter have been generated scaling down the real time histories acquired at the Pantelleria Island installation site. The experimental campaign involved the investigation of four different prototype configurations (including the design one), with the aim to determine, from the experimental point of view, the device performances sensitivity with respect to some of the system physical parameters, such as floater pitching inertia, pendulum mass, etc.). Moreover, the various tests performed on the 1:12 scale prototype allowed to outline some considerations about the device tunability with respect to the sea state and its potentialities in the context of the Mediterranean Sea scenario.

In the first part of Chapter 6, an overview of the numerical model validation against the experimental results carried out at the INSEAN tank testing on the intermediate scale prototype is presented. More in detail, the hydrodynamic nonlinear effects are identified and introduced into the numerical model, as well as the pendulum bearings friction losses, even if marginal with respect to the overall mechanical harvested power. Also in this case, numerical models proved to be in agreement with respect to experiments. Therefore, the validated models have been used to create a design and optimization methodology, suitable for the development of a full scale PeWEC device.
The methodology is described in the second part of Chapter 6. It consists in three different tools characterized by an increasing level of fidelity and complexity. The idea of subdividing the design process in different steps is based on the consideration that higher fidelity means, in general, higher computational costs and at the begin of the design process a simpler model would be preferred.
The *PeWEC Linear Optimization Tool*, based on the linear frequency domain model, allows to extrapolate a preliminary optimized device configuration (pendulum mass, moment of inertia, length, pendulum hinge position, etc.), taking into account the installation site occurrences scatter diagram and the floater geometry. This tool has very low computational costs, for instance it can compute hundred thousands of

parameters combinations, in the time horizon of one hour. The preliminary optimal configuration can be investigated through the *PeWEC Design Tool*, based on linear time-domain formulation of the system's equations. The device productivity is assessed simulating the device behavior in irregular sea state, accordingly to the installation site scatter diagram properties. Lastly, a confirmation and a more detailed simulation of the WEC performances can be carried out through the *PeWEC Parametric Tool*, including life prediction of its components, PTO saturations, hydrodynamic and mechanical nonlinearities.

In Chapter 7, a preliminary design of the PeWEC full scale configuration is proposed. It has been determined through the methodology described in Chapter 6 and considering different possible device configurations. The design and optimization procedure has been accompanied with a structural and feasibility analysis of the most important mechanical components (pendulum structure, shafts, bearings, PTO, etc.). Regarding pendulum, a concrete filled solution has been evaluated and proposed, highlighting its benefits in term of costs and manufacturing.
As widely described in Chapter 1, the economic viability assessment is crucial for a positive entering of wave power in the renewable energy mix of a country. Therefore, the Levelized Cost of Energy (LCOE) has been calculated and used as parameter for the identification of the most promising solution among the ones taken into account. Then the optimal configuration is benchmarked against the ISWEC device, from both performances and economic point of view, highlighting the advantages and drawbacks of the two different technologies.

Lastly, conclusions and possible future directions of the research activity presented in this thesis are summarized in Chapter 8.

1.5   Candidate publications

The candidate publications carried out during the Doctoral Program reflects his involvement in the different areas of the PeWEC project. It is worth noting that some of the publications regards the ISWEC project, since the latter has been a valuable reference and source of information for the development of the PeWEC device proposed in this work.

The list of publications in which the candidate has been involved is hereafter presented:

- PeWEC device research activities

    - Assessment of Loads and Performances of a Wave Energy Converter for the Mediterranean Sea [2]

    - Wave Tank Testing of a Pendulum Wave Energy Converter 1:12 Scale Model [90]

- Hydrodynamic modeling

    - Experimental evaluation of different hydrodynamic modelling techniques applied to the ISWEC [91]

    - Numerical and Experimental Analysis of Oscillating Fluid Tanks [82]

    - A performance assessment methodology for floating pitching WEC arrays [110]

- Control

    - ISWEC linear quadratic regulator oscillating control [125]

    - Application of a Passive Control Technique to the ISWEC [21]

- Renewables integration

    - Integration of renewable energy to power public transport at the Island of Pantelleria [24]

Chapter 2

The PeWEC project and the Italian state of the art

In this Chapter, the PeWEC device working principle is described, together with the history and the most important milestones of the project. Most of the activities summarized in the project history are the objective of this thesis, in particular the development of the intermediate scale device and the preliminary design of the full scale plant.

As already mentioned in section 1.3, wave power exploitation through a pendulum based WEC has been already applied and different concepts for oceanic wave climate have been studied [67]. The most famous example is the SEAREV device, widely developed by Clément at the LHEEA Laboratory, (École Centrale de Nantes) for the oceanic site of the Isle of Yeu (France) [14][31][102]. Several studies were performed about the determination of the optimal floater shape, the applicability of a hydraulic PTO and the improvement of the performances by using a different control techniques (damping, latching-declutching, etc.) [15]. A wide synthesis of the development stages the SEAREV project, including the numerical modeling and optimization techniques, the experimental testing and the techno-economic analysis of the various configuration tested can be found in [32].

On the other hand, the novelty of the PeWEC device concerns the implementation and optimization of the working principle for the Mediterranean Sea wave climate. In the context of the Mediterranean Sea and in the recent years several projects have

been studied and deployed to exploit the energy available. In the following, a brief description of the most representative projects is reported.

2.1 PeWEC: Pendulum Wave Energy Converter

2.1.1 Working principle

The PeWEC (Pendulum Wave Energy Converter) device, objective of this work, is an offshore, floating, single body, pendulum-based Wave Energy Converter. It is mainly composed of a floating hull moored on the seabed and a pendulum connected to the shaft of an electrical generator, which is integral with the hull structure. In other words, the generator shaft constitutes the pendulum hinge. Likely in the case of ISWEC device (see section 2.2), pendulum, electrical generator and all other equipment necessary for the device functioning are enclosed in the hull. Therefore, they are protected against the corrosive action of sea water and a greater level of durability is guaranteed (see Fig. 2.1).

The PeWEC working principle of PeWEC can be explained, from the qualitative point of view, using a bi-dimensional representation, as shown in Fig. 2.2. In the initial time, the hull and the pendulum are supposed to be at rest. As the waves tilt the hull, it begins its motion along surge, heave and pitch directions. Since pendulum hinge is integral with the hull structure, it moves in the space with it and as consequence, pendulum oscillations are induced. The relative rotation of the pendulum with respect to the hull is used to drive the electrical generator shaft. The extraction of energy from the system is achieved by damping the pendulum oscillations through the electrical generator (Power Take Off, PTO), which is controlled to act as a rotary damper coupled to the pendulum [89][90]. The PeWEC device is also classified as *passive* device, since it does not need to be powered to produce inertial effect [36][99].

2.1.2 Project history

The idea of the implementation of a pendulum WEC specifically designed for the Mediterranean Sea wave climate started at the Department of Mechanical and Aerospace Engineering (DIMEAS) of the Politecnico di Torino in 2013. The main
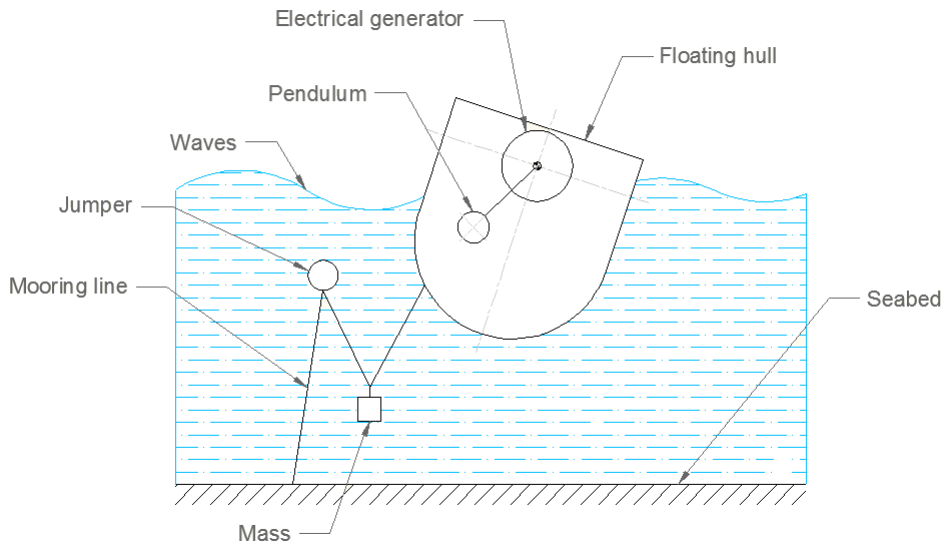
Fig. 2.1 The PeWEC scheme [90].
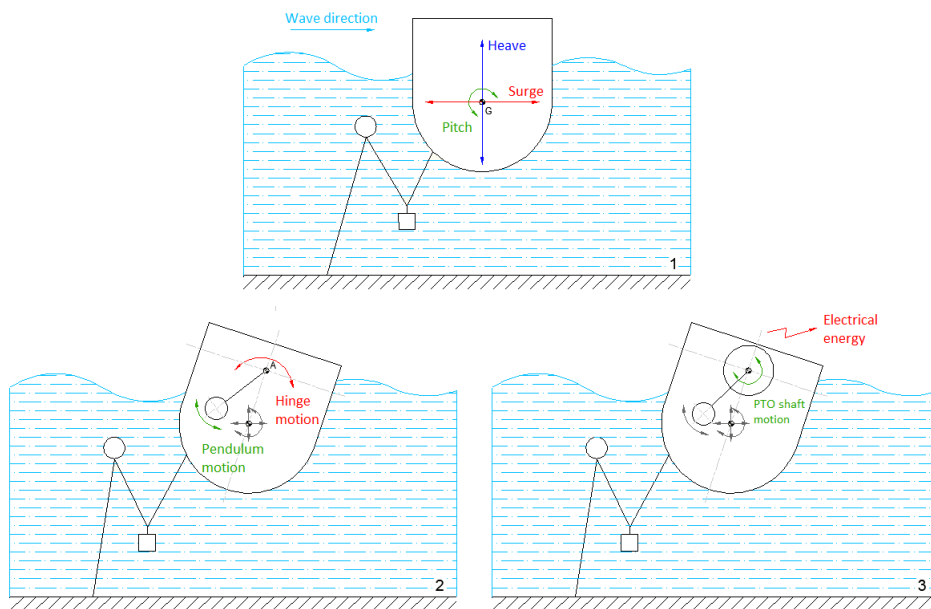
Fig. 2.2 The PeWEC working principle [90].

objective was to identify the differences between a *passive* (pendulum) and *active* (ISWEC) device. The latter was developed at the same University, as will be described later in section 2.2.

In the same year, an experimental campaign was carried out at the Department of Environment, Land and Infrastructure Engineering (DIATI) of the Politecnico di Torino on the first proof of concept, testing the effectiveness of the conversion principle and validating a simplified numerical model (frequency domain, one degree of freedom model) [36].

A collaboration between ENEA (the Italian National agency for new technologies, energy and sustainable economic development) and the Politecnico di Torino research group started in 2014, with the aim to develop the technology from small scale prototypes toward the full-scale device, according to the Technology Readiness Level (TRL) stages recommended by EquiMar, reported in Fig. 2.3 [41][54][84].
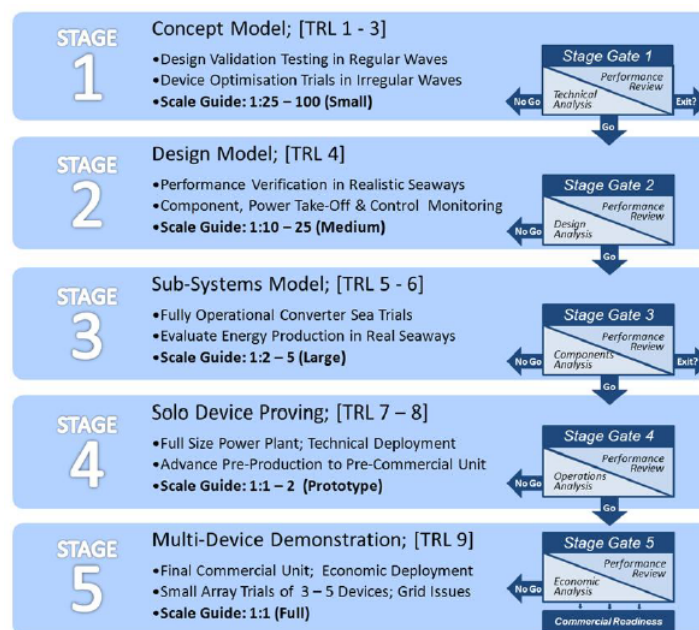
Fig. 2.3 Wave Power technologies development stages [54].

In 2014, the 1:45 scale device (TRL 1-3) was designed and built, assuming as reference the Pantelleria Island wave climate. The device was named PeWEC (Pendulum Wave Energy Converter) and between March 2014 and July 2014 a revision and an improvement of numerical models was performed, together with a new experimental campaign at the DIATI laboratory [89]. The reliability of the numerical models and the experience gained from the experimental activities were

widely used for the design and optimization of the 1:12 scale prototype (TRL 4). The preliminary design activities started in January 2015, while in June 2015 the prototype was ready to be tested. Beside these activities, further investigation on the 1:45 scale prototype were carried out at the INSEAN wave tank (Rome, Italy), during May 2015.

In July and September 2015, the intermediate scale prototype was successfully tested at INSEAN wave tank, in both regular and irregular waves. Device performances, efficiency and dynamic behavior were evaluated with a higher degree of fidelity. Experimental data were also used to benchmark the numerical models, proving again their reliability [90]. All the activities related to the 1:12 scaled device where funded by the Italian Govenment through the grant *Accordo di Programma ENEA-MiSE 2015*. Actually, a preliminary full scale device layout has been studied and compared with the ISWEC device on both technical and economic points of view.

2.2   ISWEC: Inertial Sea Wave Energy Converter

The ISWEC (Inertial Sea Wave Energy Converter) is an offshore, single body, floating device, constituted by a slack moored hull equipped with two gyroscopic units. The mooring line configuration, together with the shape of the floater allows the self orientation of the device with respect to the dominant wave direction. Gyroscopes, control units and the electrical power conditioning systems are sealed into the floater, thus they are completely protected against the corrosion phenomena due to the salinity of the water. This solution should reduce the maintenance costs and the probability of failure related to moving parts in direct contact with sea water. Moreover, another advantage of the ISWEC device regards its low environmental impact: ISWEC is moored on the seabed, therefore no foundations are required and in case of failure of the internal gyroscope, oil leakages are confined inside the floater. In Fig. 2.4, a scheme of the ISWEC device is depicted.

During normal operation, the floater is aligned with the wavefront direction: waves induces the hull pitching motion around the δ axis. The flywheel spinning velocity $\dot{\varphi}$ combined with pitching velocity generates an inertial action discharged on the precession axis ε, used to drive an electrical generator. The power absorption occurs controlling the electrical generator (also called Power Take Off) as a rotary damper. An interesting feature of this technology is the possibility to vary the
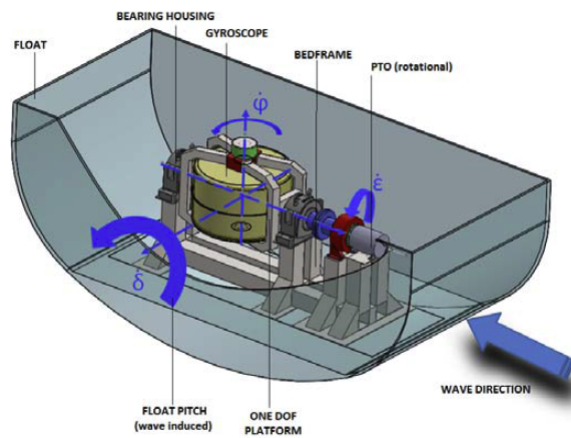
Fig. 2.4 ISWEC device scheme.

flywheel speed according to the foreseen incoming wave climate. The flywheel speed variation induces a variation of the gyroscope angular momentum and thus of the device resonance frequency. Clearly, in order to keep the flywheel rotating, a small amount of the produced power needs to be recirculated to supply the flywheel electric motor. In stationary flywheel speed conditions, the torque given by the motor balance the dissipation due to bearing friction, seals and ventilation losses [94][124]. Accordingly to these features, as already mentioned in Chapter 1, the ISWEC device is also classified as an inertial *active* device.

Regarding the ISWEC history, the project started in 2005 at the Department of Mechanical and Aerospace Engineering of Politecnico di Torino, Italy from the idea to exploit the gyroscopic effect to harvest wave energy potential of the Mediterranean Sea, characterized by low amplitude and high frequency waves. In fact, it has been demonstrated that gyroscopic effects are proportional to the square of the radian frequency of the incoming wave. The first proof of concept of the system was developed by the research group in 2007, with the aim to test the effectiveness of the conversion principle and to validate the preliminary numerical models developed [73][23][27]. According to the general practice adopted in the Wave Energy field [41][54][84], the 1:45 scale device was developed in 2009 and tested successfully both at the Politecnico di Torino and at the wave tank of the University of Edinburgh (UK) [26][26]. A picture of the 1:45 scale device is reported in Fig. 2.5.

Fig. 2.5 ISWEC 1:45 scale device (top), 1:8 scale prototype (middle) and full scale device (bottom).

In 2010, a waves and currents sensor was installed near the Pantelleria Island harbor (Italy) and between January 2010 and December 2011 data were collected in order to achieve a complete identification of the installation site wave climate [25]. Later, in 2012, a 1:8 scaled device was built and tested in Rome, at the INSEAN wave basin (see Fig. 2.5). The experience and results obtained from this campaign draw the main guidelines for the ISWEC design and the identification of the problems related to power conversion losses. In the same year, a dry hardware in the loop test rig was also developed [28] and the *Wave for Energy s.r.l.* spin-off company was founded at the same University.

From 2012 to 2014, the full scale device specifications, design and optimization were carried out [94], while in the autumn of 2014 started the construction of the different subsystems of the plant, that were concluded in summer 2015. In August 2015, the ISWEC device was deployed near shore of Pantelleria Island (see Fig. 2.5) and the first experimental testing campaign in real sea conditions began [124].

2.3 REWEC3: Resonant Wave Energy Converter 3

The REWEC3, also called U-OWC, is a wave energy converter belonging to the family of Oscillating Water Columns (OWCs), but differently from the traditional OWCs it is equipped with a U-shaped duct used for connecting the water column to the open sea field. This feature allows to increase significantly the hydrodynamic performances with respect to the traditional OWC plants and it was proposed for the first time by Professor Paolo Boccotti of Mediterranea University of Reggio Calabria (Italy), in 2003 [19]. During the past decades, small field experiments and theoretical analyses provided its potential for full scale applications and a spin-off company was founded in 2009 at the same University [8]. At present, the first full-scale prototype is under construction in the Civitavecchia's harbor in the Tyrrhenian Sea within the context of the major port enlargement, integrating REWEC3 caissons in the new breakwaters section. Since 2015, the internal pressure of a pair of chambers is monitored by a series of pressure gauges [7][114].

As previously mentioned, the REWEC3 plant has been embodied into an upright breakwater, including the U-shaped duct that connects the open sea field to the water column. In Fig. 2.6, it is possible to see the comparison between the traditional OWC design and the innovative U-OWC solution. Thanks to this additional element,
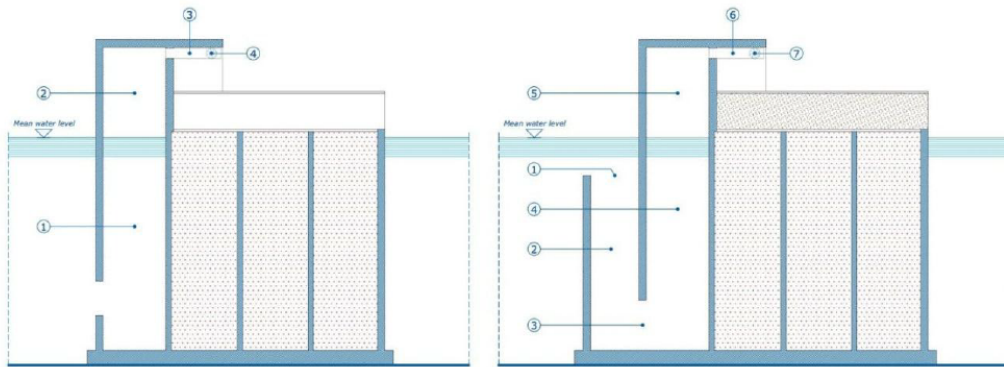
Fig. 2.6 Traditional OWC design (left) and U-OWC scheme (right) [19].

during the design process is possible to tune the device eigenperiod very close to the peak period associated to the most energetic wave of the installation site. This is not possible in the case of traditional OWC, where the resonance period is typically smaller than the period of incident waves. Furthermore, the REWEC3 design has a structural resistance greater than the traditional design.

Regarding the working principle, the wave pressure of the incident wave acting at the U-shaped duct opening induces water column oscillations. The latter compresses and decompresses the air mass above, which can flow through a turbine located in the U-duct. The rotating motion of the turbine is used to drive the electrical generator. In Fig. 2.7, the REWEC3 working principle is summarized.
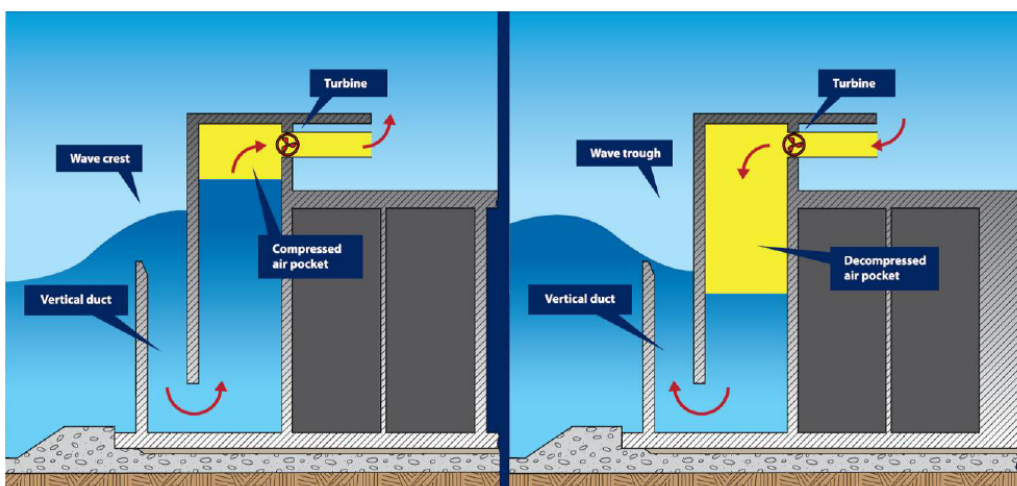
Fig. 2.7 The REWEC3 working principle [7].

2.4   Poly-OWC: Polymeric Oscillating Water Column

In recent years, Scuola Superiore Sant'Anna of Pisa (Italy) introduced the new class of Polymeric Wave Energy Converters, characterized by the employment of Dielectric Elastomer Transducers (DETs). They are constituted by a stack of multiple Dielectric Elastometers (DE) (non conductive part) separated by electrodes (conductive part) and can be used as actuators, sensors and generators. In generator mode, DETs operate via the variable capacitance electrostatic generation principle, where the voltage of the charges lying on DET is increased by the deformation of the membrane.

The use of DETs as Power Take Off in the Wave Energy context would introduce a radical change in the traditional architecture of WECs, substituting mechanical wave absorbers, mechanical transmission, turbines, etc. with a single deformable lightweight and low cost polymeric element. Other advantages are large energy densities, direct-drive and cyclic operation, good and rate-independent efficiencies, good shock and corrosion resistance, silent operation [123].

The first small scale prototype built and tested is the Poly-OWC (Polimeric Oscillating Water Column). It uses the traditional OWC configuration, where the turbine is substituted by a Circular Diaphragm Dielectric Elastomer Generator (CD-DEG). When the incident wave pressure acts on the structure, the water column starts its oscillating motion, causing compression-expansion of the entrapped air and thus the inflation-deflation of the CD-DEG. In Fig. 2.8, a schematic sequence of the Poly-OWC working principle is represented.
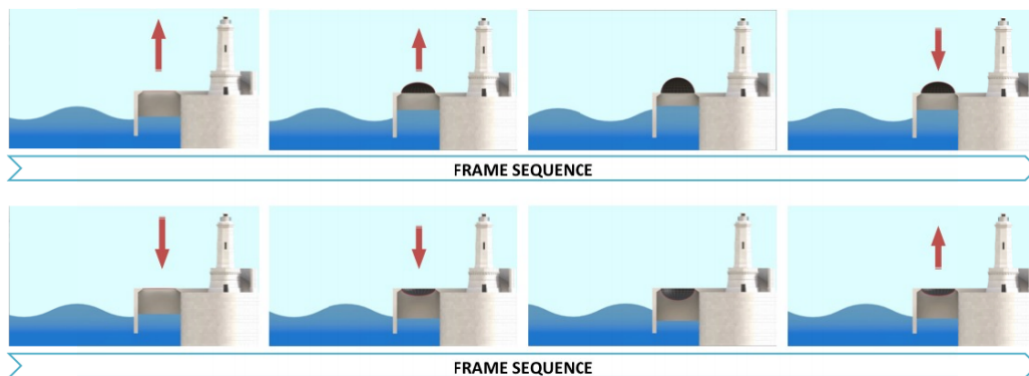
Fig. 2.8 The Poly-OWC working principle [123].

2.5   40South Energy R115

The 40South Energy R115 device is constituted by two parts, the *Lower Member* and the *Upper Member*. The first is submerged at a depth of 15-25 *m* depending on the model and of the water depth of the installation site, while the second is submerged at a lower depth comprised between 1-12 *m*, according to the sea state and operating conditions. The two components are connected by four piston arms, allowing the relative motion between Lower and Upper Member. The mechanical energy is transformed in electricity through the TEP (Transmission, Electronics and Power) modules. In Fig. 2.9, the device concept is depicted. Moreover, 40South Energy device works beneath the surface, varying dynamically and automatically its working depth, according the sea state condition. For example, when the sea state is particularly strong the device works at a higher depth, while in the case of a milder wave climate, it works at lower depth. The advantage of this controlling methodology is the possibility to obtain a approximately constant power production from low to very high waves.
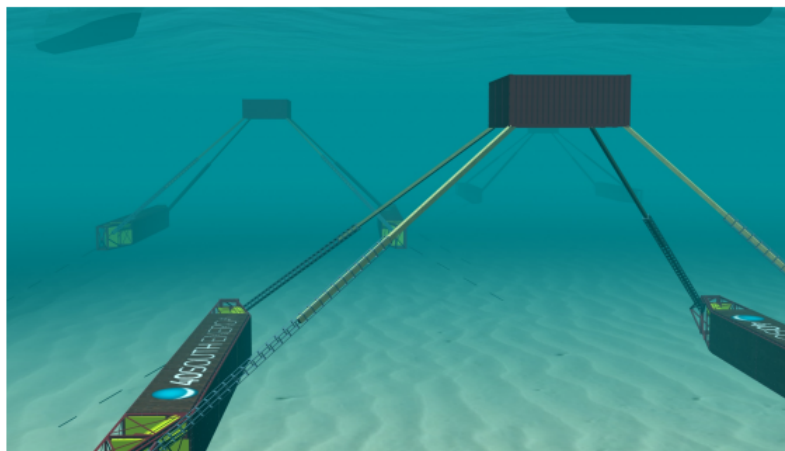
Fig. 2.9 40South Energy R115 [1].

The R115 full scale prototype has been tested from 2012 to 2014 in open sea near Punta Righini, in Tuscany (Italy) and recently the company claimed that the device became ready for commercialization [1].

Chapter 3

PeWEC Modeling

In this chapter, the mathematical model of the PeWEC device is presented. The entire system dynamics depends on different phenomena: the interaction between the waves and floater, the floater and mooring line, the pendulum and the floater. For reasons of clarity, the physical representation of each phenomenon is described separately, starting from the pendulum dynamic equations and the reference frames chosen for their derivation.

The second part deals with the hydrodynamic model of a floating body under the linear hypothesis of potential flow theory. An overview of such theory is given, as well as a description of the floater dynamic equations in frequency domain and time domain. The limitation of the theory considered in the case of WECs modeling is highlighted.

A way to overcome the inaccuracies of the linear hydrodynamic model is the introduction of nonlinear hydrodynamic viscous forces. Such forces can be directly introduced in the time domain representation, while in the case of the frequency domain model a linearization process is required. For this purpose, a methodology for the linearization of these forces has been developed.

Another important aspect, highlighted in this chapter, is the wave forces modeling for both regular and irregular sea state. A focus has been set on irregular wave forces, where second order drift forces are particularly important for a proper representation of the floater motion along surge direction and of the interaction between floater and moorings.

A specific section is dedicated to the mooring line actions discharged on the floater. In this case a quasi-static nonlinear model is taken into account, as well as a linearized version suitable for the fully linear model of the device.

Lastly, the complete dynamic model of the PeWEC device is derived coupling the equations previously developed for each subsystem. The complete dynamic equations constitutes the base of the *Wave-to-Wire* model, that is commonly used in Wave Power application for the estimation of the device performances and loads, starting from the resource characteristics up to the electrical grid. More in detail, the linear frequency domain, linear and nonlinear time domain dynamic equations formulations are presented.

3.1   Reference frames

The PeWEC dynamic equations can be derived starting from the definition of a proper set of reference frames. In Fig. 3.1, a simplified scheme of the system is reported, together with the significant reference frames.
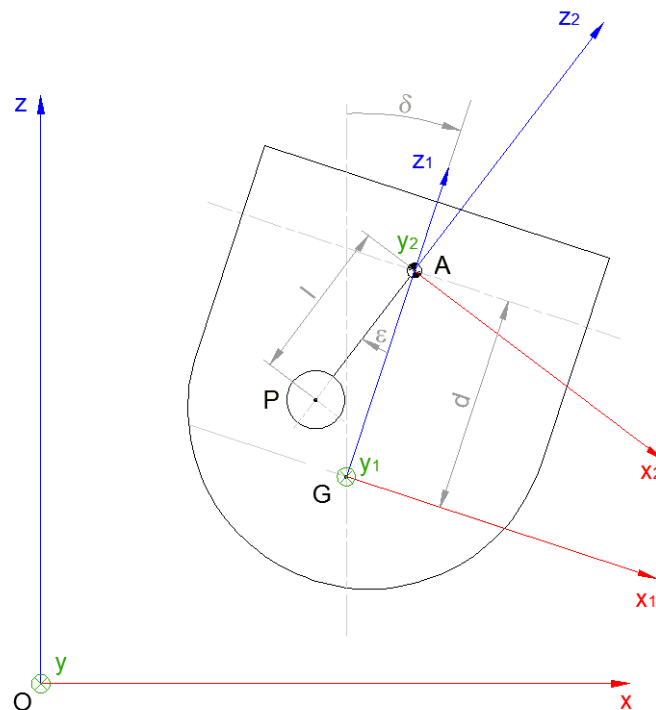
Fig. 3.1 The PeWEC reference frames [90].

G is the center of gravity (COG) of the system, *A* identifies the position of the pendulum hinge and *P* is the center of gravity of the pendulum mass. Moreover, let *l* be the pendulum length and *d* the distance between *A* and *G*. Regarding the floater, m_b corresponds to its mass, while I_b to its inertia (evaluated with respect to the hull's center of gravity, *G*). m_p is the pendulum mass and I_y its inertia evaluated with respect to the mass center of gravity, *P*.

The reference frames used to describe the kinematics and the dynamics of the system are:

- $O - xyz$: right hand fixed reference frame with origin *O*;

- $G - x_1 y_1 z_1$: right hand reference frame of the floating body with origin coincident with its center of gravity *G*;

- $A - x_2 y_2 z_2$: right hand reference frame of the moving mass with origin coincident with its center of rotation *A*.

The *x* axis is parallel to the wave direction, with positive direction concordant with the wave propagation. The *z* axis positive direction is defined from bottom upwards, while the *y* axis direction is determined according to the right hand rule. The same orientation for the x_1, y_1, z_1 and x_2, y_2, z_2 axes is assumed.

The PeWEC mathematical model, here proposed, is based on the hypothesis of a two-dimensions representation. Such hypothesis is hold by the fact that the pendulum does not exchange forces along the *y* axis. Moreover, it is supposed that the device it is able to align itself with respect to the dominant wave direction. This property can be achieved with a proper design of the hull and mooring line [68]. A consequence of this assumption is the possibility to maximize the extracted power, especially when the installation site is characterized by a variable waves direction during the year.

However, this hypothesis has some limitations from the computational point of view: it is not possible to investigate roll, sway and yaw motions occurring during the transient state of the device allignment with the main wave direction or in the case of a more realistic representation of multi-directional sea state, where waves come from different directions [37][58][74]. As consequence, it is not possible to estimate the influence of the sea state multi-directionality on the device performance [16][69].

Under this assumption, the motion of the hull takes place in $O - xz$ plane and it can be described by the surge motion x_G, the heave motion z_G and the pitch motion δ around y axis. The relative motion between the hull and the inner pendulum is individuated by the angular coordinate ε.

3.1.1 Homogeneous transformation matrices

The device described above can be assimilated to a multi-body system. In this way, its kinematics and the relations between the different reference frames can be represented through the homogeneous transformation matrices, a tool widely used in robotics. This kind of mathematical representation will be useful also during the derivation of the pendulum dynamic equations, described in the following section.

By considering the coordinate systems shown in Fig. 3.1, it is straightforward to determine the following transformation matrices:

$$
{}^{0}\hat{\mathbf{A}}_{1} = \begin{bmatrix} \cos\delta & 0 & \sin\delta & x_G \\ 0 & 1 & 0 & 0 \\ -\sin\delta & 0 & \cos\delta & z_G \\ 0 & 0 & 0 & 1 \end{bmatrix} \tag{3.1}
$$

$$
{}^{1}\hat{\mathbf{A}}_{2} = \begin{bmatrix} \cos\varepsilon & 0 & \sin\varepsilon & 0 \\ 0 & 1 & 0 & 0 \\ -\sin\varepsilon & 0 & \cos\varepsilon & d \\ 0 & 0 & 0 & 1 \end{bmatrix} \tag{3.2}
$$

${}^{0}\hat{\mathbf{A}}_{1}$ is the homogeneous transformation matrix, which denotes translation and rotation of reference frame 1 with respect to reference frame 0, while ${}^{1}\hat{\mathbf{A}}_{2}$ expresses the relation between reference frames 2 and 1. On the other hand, the link between the pendulum and absolute coordinate system is defined by the product of the homogeneous matrices written above.

$$
{}^{0}\hat{\mathbf{A}}_{2} = \begin{bmatrix} \cos(\delta+\varepsilon) & 0 & \sin(\delta+\varepsilon) & x_G + d\sin\delta \\ 0 & 1 & 0 & 0 \\ -\sin(\delta+\varepsilon) & 0 & \cos(\delta+\varepsilon) & z_G + d\cos\delta \\ 0 & 0 & 0 & 1 \end{bmatrix} \tag{3.3}
$$

3.1.2   Position and velocity vector of points *P* and *G* in the fixed reference frame

The derivation of the pendulum dynamic equations implies the knowledge of hull and pendulum COG (identified respectively by the points *G* and *P*) position and velocity with respect the fixed reference frame.

By considering the point *P*, it is possible to write its position in the reference frame $A - x_2 y_2 z_2$, as well as its position in the fixed reference frame by means of the $^1\hat{\mathbf{A}}_2$ matrix.

$$^2\hat{\boldsymbol{p}} = \begin{Bmatrix} 0 \\ 0 \\ -l \\ 1 \end{Bmatrix} \tag{3.4}$$

$$^0\hat{\boldsymbol{p}} = {}^0\hat{\mathbf{A}}_2\,{}^2\hat{\boldsymbol{p}} = \begin{Bmatrix} x_G + d\sin\delta - l\sin(\delta + \varepsilon) \\ 0 \\ z_G + d\cos\delta - l\cos(\delta + \varepsilon) \\ 1 \end{Bmatrix} \tag{3.5}$$

Taking into account the non homogeneous notation used for vectors in space:

$$\overrightarrow{OP} = \begin{Bmatrix} x_G + d\sin\delta - l\sin(\delta + \varepsilon) \\ 0 \\ z_G + d\cos\delta - l\cos(\delta + \varepsilon) \end{Bmatrix} \tag{3.6}$$

The velocity of the point *P* in the fixed reference frame is obtained through the time derivative of the vector components defined by Eq. 3.6.

$$\dot{\overrightarrow{OP}} = \begin{Bmatrix} \dot{x}_G + d\dot{\delta}\cos\delta - l(\dot{\delta} + \dot{\varepsilon})\cos(\delta + \varepsilon) \\ 0 \\ \dot{z}_G - d\dot{\delta}\sin\delta - l(\dot{\delta} + \dot{\varepsilon})\sin(\delta + \varepsilon) \end{Bmatrix} \tag{3.7}$$

The position and velocity of the floater COG in the $O - xyz$ coordinate system, instead, are represented by the following vectors in space:

$$\overrightarrow{OG} = \begin{Bmatrix} x_G \\ 0 \\ z_G \end{Bmatrix} \tag{3.8}$$

$$\dot{\overrightarrow{OG}} = \begin{Bmatrix} \dot{x}_G \\ 0 \\ \dot{z}_G \end{Bmatrix} \tag{3.9}$$

3.2   Pendulum dynamic equations

The pendulum constitutes the core of the conversion chain inside the PeWEC device: its motion actuates the rotation of the Power Take Off shaft, which is managed in order to brake the pendulum motion, allowing the conversion of mechanical energy into electricity. In this section, the pendulum dynamic equations are derived and presented. For the sake of simplicity, the steps of the equations derivation are omitted, however a better detail and a proof of the results reported can be found in [89].

The derivation of the pendulum dynamic equations has been performed according to the Lagrange approach. The Lagrangian function $\mathscr{L}$ of a dynamic system is a function that summarizes its dynamics. In classical mechanics, the natural form of the Lagrange function is defined as the difference between the kinetic energy E_k of the system and its potential energy E_p. In symbols:

$$\mathscr{L} = E_k - E_p \tag{3.10}$$

The expressions of the kinetic and potential energy require the definition of the generalized coordinates q_i of the system. In analytical mechanics, the term *generalized coordinates* refers to the parameters that describe, at each instant of time, the system configuration of the system with respect to a certain reference configuration. Of course, it is possible to define generalized velocities, which are the first time derivative of generalized coordinate.

The choice of generalized coordinates it is not unique: in general, the system parameters are usually selected so that the specification of the system configuration and the form of its equations are simpler. If the selected parameters are independent,

then the number of independent generalized coordinates is defined by the number of degrees of freedom of the system. Moreover, if the Lagrange function of a system is known, then equations of motion are obtained by a direct substitution of its expression into the Euler-Lagrange equation. The latter has the following form:

$$\frac{d}{dt}\left(\frac{\partial E_k}{\partial \dot{q}_i}\right) - \frac{\partial E_k}{\partial q_i} + \frac{\partial E_p}{\partial q_i} = 0 \tag{3.11}$$

The Euler-Lagrange equation may be completed by introducing the Rayleigh dissipation function F used to handle the effects of velocity proportional frictional forces. Then, Eq. 3.11 becomes:

$$\frac{d}{dt}\left(\frac{\partial E_k}{\partial \dot{q}_i}\right) - \frac{\partial E_k}{\partial q_i} + \frac{\partial E_p}{\partial q_i} + \frac{\partial F}{\partial \dot{q}_i} = 0 \tag{3.12}$$

Observing the PeWEC scheme shown in Fig. 3.1 and taking into account the hypothesis of planar motion, it is possible to identify three degrees of freedom (surge, heave and pitch motion) for the floater, plus the rotation of the pendulum around its hinge. The external and the internal degrees of freedom listed previously constitutes a proper set of independent variables for the description of generalized coordinates vector. In symbols:

$$\boldsymbol{q} = \begin{Bmatrix} x_G \\ z_G \\ \delta \\ \varepsilon \end{Bmatrix} \tag{3.13}$$

Once the generalized coordinates of the system under analysis are defined, it is possible to derive the kinetic and potential energy both for the floater and pendulum.

More in detail, the kinetic and potential energy of the pendulum are respectively:

$$E_{k,p} = \frac{1}{2}I_y\left(\dot{\delta} + \dot{\varepsilon}\right)^2 + \frac{1}{2}m_p|\overrightarrow{OP}|^2 \tag{3.14}$$

$$E_{p,p} = m_p g\left(\overrightarrow{OP}\right)_z = m_p g\left[z_G + d\cos\delta - l\cos\left(\delta + \varepsilon\right)\right] \tag{3.15}$$

On the other hand the kinetic and potential energy of the floater result be:

$$E_{k,b} = \frac{1}{2}I_b\dot{\delta}^2 + \frac{1}{2}m_b|\overrightarrow{OG}|^2 \tag{3.16}$$

$$E_{p,b} = m_p g\left(\overrightarrow{OG}\right)_z = m_p g z_G \tag{3.17}$$

Regarding the Rayleigh dissipation function F, it can be used to include the action of the Power Take Off. In this work, the PTO torque (T_ε) is modeled as a linear rotary damper with damping coefficient c. In symbols:

$$T_\varepsilon = c\dot{\varepsilon} \tag{3.18}$$

$$F = \frac{1}{2}c\dot{\varepsilon}^2 \tag{3.19}$$

3.2.1   Nonlinear equations

The calculation of the partial derivatives of the kinetic and potential energy of the pendulum and floater with respect to the four generalized coordinates, according to the Euler-Lagrange equation (Eq. 3.12), leads to the following differential equation.

$$\mathbf{M_s}\begin{Bmatrix}\ddot{x}_G\\\ddot{z}_G\\\ddot{\delta}\\\ddot{\varepsilon}\end{Bmatrix} + \mathbf{D_{PTO}}\begin{Bmatrix}\dot{x}_G\\\dot{z}_G\\\dot{\delta}\\\dot{\varepsilon}\end{Bmatrix} + \boldsymbol{F}_{gr} + \boldsymbol{F}_{cor} = \mathbf{0} \tag{3.20}$$

Where $\mathbf{M_s}$ is the mass matrix of the system, $\mathbf{D_{PTO}}$ is the damping matrix of the PTO. Their expression are given by Eq. 3.21 and Eq. 3.22.

$$\mathbf{M_s} =$$

$$\begin{bmatrix} m_p + m_b & 0 & m_p[d\cos\delta - l\cos(\delta+\varepsilon)] & -m_p l\cos(\delta+\varepsilon) \\ 0 & m_p + m_b & -m_p[d\sin\delta - l\sin(\delta+\varepsilon)] & m_p l\sin(\delta+\varepsilon) \\ m_p[d\cos\delta - l\cos(\delta+\varepsilon)] & -m_p[d\sin\delta - l\sin(\delta+\varepsilon)] & I_b + I_y + m_p(d^2+l^2) - 2m_p dl\cos\varepsilon & I_y + m_p l^2 - m_p dl\cos\varepsilon \\ -m_p l\cos(\delta+\varepsilon) & m_p l\sin(\delta+\varepsilon) & I_y + m_p l^2 - m_p dl\cos\varepsilon & I_y + m_p l^2 \end{bmatrix} \tag{3.21}$$

$$\mathbf{D_{PTO}} = \begin{bmatrix} 0 & 0 & 0 & 0 \\ 0 & 0 & 0 & 0 \\ 0 & 0 & 0 & 0 \\ 0 & 0 & 0 & c \end{bmatrix} \tag{3.22}$$

$\boldsymbol{F_{cor}}$ is the vector of Coriolis action due to the motion of the pendulum hinge and $\boldsymbol{F_{gr}}$ is the vector of the forces due to gravity action. The explicit expressions of these terms are:

$$\boldsymbol{F_{cor}} = \left\{ \begin{array}{c} m_p \left[l(\dot{\delta}+\dot{\varepsilon})^2 \sin(\delta+\varepsilon) - d\dot{\delta}^2 \sin\delta \right] \\ m_p \left[l(\dot{\delta}+\dot{\varepsilon})^2 \cos(\delta+\varepsilon) - d\dot{\delta}^2 \cos\delta \right] \\ -m_p dl \sin\varepsilon \left[(\dot{\delta}+\dot{\varepsilon})^2 - \dot{\delta}^2 \right] \\ -m_p dl \dot{\delta}^2 \sin\varepsilon \end{array} \right\} \tag{3.23}$$

$$\boldsymbol{F_{gr}} = \left\{ \begin{array}{c} 0 \\ 0 \\ -m_p g \left[d\sin\delta - l\sin(\delta+\varepsilon) \right] \\ m_p g l \sin(\delta+\varepsilon) \end{array} \right\} \tag{3.24}$$

It is worth noting that the mass matrix can be rewritten as the sum two independent contribution:

$$\mathbf{M_s} = \mathbf{M_{s,d}} + \mathbf{M_{s,c}} \tag{3.25}$$

Where:

- The diagonal matrix $\mathbf{M_{s,d}}$, that takes into account the mass and inertial properties of the buoyant and pendulum

$$\mathbf{M_{s,d}} =$$
$$\begin{bmatrix} m_p + m_b & 0 & 0 & 0 \\ 0 & m_p + m_b & 0 & 0 \\ 0 & 0 & I_b + I_y + m_p(d^2 + l^2) - 2m_p dl \cos\varepsilon & 0 \\ 0 & 0 & 0 & I_y + m_p l^2 \end{bmatrix} \tag{3.26}$$

- The matrix $\mathbf{M_{s,c}}$ with non-null off diagonal terms, that takes into account the coupling between the pendulum and the floater.

$$\mathbf{M_{s,c}} = \begin{bmatrix} 0 & 0 & m_p[d\cos\delta - l\cos(\delta+\varepsilon)] & -m_pl\cos(\delta+\varepsilon) \\ 0 & 0 & -m_p[d\sin\delta - l\sin(\delta+\varepsilon)] & m_pl\sin(\delta+\varepsilon) \\ m_p[d\cos\delta - l\cos(\delta+\varepsilon)] & -m_p[d\sin\delta - l\sin(\delta+\varepsilon)] & 0 & I_y + m_pl^2 - m_pdl\cos\varepsilon \\ -m_pl\cos(\delta+\varepsilon) & m_pl\sin(\delta+\varepsilon) & I_y + m_pl^2 - m_pdl\cos\varepsilon & 0 \end{bmatrix} \tag{3.27}$$

3.2.2   Linearized equations

The equations obtained in the previous paragraph with the Lagrange approach are a set of nonlinear equations. In general, in the initial design phase, it is quite interesting working with a linear system of equations.

The main hypothesis for the equation linearization is to assume sufficiently small oscillation of pitch and pendulum motions around their equilibrium position, defined by $\delta = 0$ and $\varepsilon = 0$. Then, under these assumptions, the pendulum equations of motion become:

$$\mathbf{M_s^{lin}} \begin{Bmatrix} \ddot{x}_G \\ \ddot{z}_G \\ \ddot{\delta} \\ \ddot{\varepsilon} \end{Bmatrix} + \mathbf{D_{PTO}} \begin{Bmatrix} \dot{x}_G \\ \dot{z}_G \\ \dot{\delta} \\ \dot{\varepsilon} \end{Bmatrix} + \mathbf{K_p} \begin{Bmatrix} x_G \\ z_G \\ \delta \\ \varepsilon \end{Bmatrix} = \mathbf{0} \tag{3.28}$$

$\mathbf{K_p}$ is the restoring matrix of the system and depends on the linearized terms of the gravitational vector, $\mathbf{M_s^{lin}}$ is the linearized matrix of the inertial actions of the system. The Coriolis vector is negligible, since it depends on the square of the angular pitching velocity and pendulum angular velocity.

$$\mathbf{K_p} = \begin{bmatrix} 0 & 0 & 0 & 0 \\ 0 & 0 & 0 & 0 \\ 0 & 0 & -m_pg(d-l) & m_pgl \\ 0 & 0 & m_pgl & m_pgl \end{bmatrix} \tag{3.29}$$

$$\mathbf{M_s^{lin}} = \begin{bmatrix} m_p + m_b & 0 & m_p(d-l) & -m_p l \\ 0 & m_p + m_b & 0 & 0 \\ m_p(d-l) & 0 & I_b + I_y + m_p(d-l)^2 & I_y + m_p l^2 - m_p dl \\ -m_p l & 0 & I_y + m_p l^2 - m_p dl & I_y + m_p l^2 \end{bmatrix} \quad (3.30)$$

3.3 Hydrodynamic model

The interaction between floater and waves is the first stage of the energy conversion from waves to electricity. It is well known that fluid dynamics phenomena are particularly hard to be analyzed, both from the analytical and numerical point of view. Generally, there is no analytical formulation for the description of motion and the system is described using finite elements and the Navier-Stokes equations or the potential flow theory.

The aim of the modeling activity presented in this chapter is the development of a lumped parameter numerical model of the device. This branch of models is very effective in terms of computational costs and so particularly suitable for the model-based design methodology. The linear integro-differential Cummins equation is a sufficiently accurate tool that can be used to represent the hydrodynamic loads acting on a floating structure, as well as its motions in waves [46][59].

3.3.1 Hydrodynamic loads

Hydrodynamic loads acting on marine structure are caused by different phenomena:

- Kinematics of the water particles in waves;

- Motion of the structure;

- Interaction between the waves and the structure.

Moreover, they can be subdivided in the three categories:

- *Drag load*: induced by the fluid viscosity and it is proportional to the square of the relative velocity between fluid particles and structure surface. This kind

of load is important when the structure is slender and the wave amplitude is large;

- *Wave excitation load*: this load can be subdivided in two parts:

    - *First order incident wave force (Froude-Krylov)*: wave excitation load in small wave amplitude;

    - *Diffraction force*: induced by the disturbance wave due to the existence of a body. In larger sea, also the second order forces need to be taken into account together with the first order forces. Eventually, if the severe sea state is considered, bottom and flare slamming transient forces should also be included;

- *Wave inertia load* and *radiation load*: caused by the disturbed waves induced by the body motions.

The fluid potential flow theory is widely used for the determination of the wave inertia load and wave excitation loads. Moreover, it constitutes the base for the computation of the hydrodynamic coefficients of the Cummins equation that, as will be described later, is commonly adopted for the motion prediction of a floating body.

3.3.2   Potential flow theory

Hypothesis

The linear potential flow theory is based on the following assumptions:

- The body or the bodies have zero or very small forward speed;

- The fluid is assumed inviscid and incompressible;

- The fluid flow is supposed irrotational;

- The incident wave is harmonic and regular;

- The incident wave acting on the body is characterized by small amplitude when compared to its length (small slope);

- The body motions are sinusoidal;

- The *Linear Superposition Theorem* validity is hold by linear assumptions;

- The linearized drag damping on the Morison elements or any additional viscous damping can be optionally included in the equation of motion.

The theory can be used to calculate the wave excitation on fixed bodies and the wave excitation forces and radiation forces on floating bodies.

Radiation and diffraction analysis - Zero-forward speed theory

The potential flow theory defines a fluid flow field by a velocity potential:

$$\Phi(x,y,z,t) = \phi(x,y,z)e^{-j\omega t} \tag{3.31}$$

The complex function ϕ can be decomposed into different contributions:

- Radiation waves due to the six modes of body motion;

- Incident wave field;

- Diffracted or scattered wave field.

The problem can be split in two separate problems and their effects can be superimposed, according to the linear assumptions. More in detail, the two problems are the following:

- *Problem of floating body undergoing harmonic oscillations in still water*: the body motions cause the fluid to react on the body and this effect induces the radiation wave forces. These forces are a function of the motions and in general are written in terms of added mass and wave damping coefficients;

- *Problem of a fixed body being subjected to a regular wave train*: the wave forces acting on the fixed body are considered to be the wave excitation forces. This contribution can be split in two components: Froude-Krylov and wave diffraction force components.

The total potential due to the unit amplitude incident wave, diffraction and radiation waves can be rewritten as:

$$\phi\left(x,y,z\right)e^{-j\omega t} = \left[\left(\phi_I + \phi_d\right) + \sum_{i=1}^{6}\phi_i x_i\right]e^{-j\omega t} \tag{3.32}$$

Where:

- ϕ_I: incident wave potential;

- ϕ_d: diffracted wave potential;

- ϕ_i: potential due to the *i-th* motion;

- x_i: *i-th* motion per unit of wave amplitude;

- ω: frequency of the incident wave.

The potential for the undisturbed incident wave field, at a certain point of coordinates $\left(x,y,z\right)$ in the fluid domain, is:

$$\phi_I = \frac{-jg\cosh\left[k\left(d+z\right)\right]e^{-jk\left(x\cos\theta + y\sin\theta\right)}}{\omega\cosh\left(kd\right)} \tag{3.33}$$

In which:

- d: water depth;

- k: wave number;

- θ: wave direction (zero degrees along *x* axis direction).

The potentials functions are complex, but the resultant physical quantities such as the fluid pressure and body motion are obtained taking into account the real part. The unknown potentials are determined using the Green's theorem together with the required boundary conditions on the surfaces that define the fluid domain. The potentials are solved via numerical algorithm, for a discrete number of points on the wetted body surface. When the potentials are known the first order hydrodynamic pressure distribution can be calculated thanks to the linearized Bernoulli's equation.

$$p = -\rho \frac{\partial \Phi}{\partial t} \tag{3.34}$$

Given the pressure distribution the different fluid forces contribution can be calculated by integrating the pressure over the wetted surface of the body. The fluid forces can be described in terms of reactive and active components. The active forces result be:

$$F_i = -\int_{S_0} p n_i \, dS = -\int_{S_0} j\omega\rho \left(\phi_I + \phi_d\right) n_j \, dS \tag{3.35}$$

Where:

- F_i: active force per unit of wave amplitude in the *i-th* direction;

- n_i: generalized surface normal for *i-th* direction, $(n_1, n_2, n_3) = \overrightarrow{n}$, $(n_4, n_5, n_6) = \overrightarrow{r} \times \overrightarrow{n}$

- S_0: wetted surface of the body in the equilibrium position in still water.

The forces given in Eq. 3.35 can be split in two components:

$$F_{i,FK} = -\int_{S_0} j\omega\rho \, \phi_I n_i \, dS \tag{3.36}$$

$$F_{i,d} = -\int_{S_0} j\omega\rho \, \phi_d n_i \, dS \tag{3.37}$$

$F_{i,FK}$ corresponds to the Froude-Krylov forces, while $F_{i,d}$ takes into account the diffraction forces.

On the other hand, the radiation forces acting on the body, caused by the body motions, can be written in the following way:

$$F_{ij} = -\int_{S_0} p_j n_i \, dS = -\int_{S_0} j\omega\rho \, \phi_j n_i \, dS \tag{3.38}$$

F_{ij} corresponds to the reactive force per unit of wave amplitude in the *j-th* direction due to *i-th* motion. Since the potential ϕ is a complex function, it can be

splitted in real and imaginary parts. Then, it can be substituted into Eq. 3.38, in order to obtain the added mass and the wave damping coefficients.

$$\phi_j = \text{Re}\{\phi_j\} + i\,\text{Im}\{\phi_j\} \tag{3.39}$$

The motion of the body is supposed to be harmonic, then Eq. 3.39 can be expressed in terms of coefficients which are in phase with body velocity $\dot{x}_i$ and acceleration $\ddot{x}_i$.

$$F_{ij} = -A_{ij}\ddot{x}_i - B_{ij}\dot{x}_i \tag{3.40}$$

The coefficients A_{ij} and B_{ij} of Eq. 3.40 are respectively:

- $A_{ij} = \frac{\rho}{\omega} \int_{S_0} \text{Im}\{\phi_j\} n_i \, dS$: added mass coefficient in the *j-th* direction due to the *i-th* motion;

- $B_{ij} = \rho \int_{S_0} \text{Im}\{\phi_j\} n_i \, dS$: wave damping coefficient in the *j-th* direction due to the *i-th* motion.

By means of the Green's theorem, the velocity potentials of diffraction and radiation waves can be expressed in terms of pulsating sources distributed over the mean wetted surface of floating structures.

Second order wave force coefficients

Observing a floating structure undergoing to the action of the waves, it is possible to denote a mean displacement of the structure. This is due to a constant load component, called mean drift force.

The drift force is caused by non-linear (second order) wave potential effects. Together with the mooring system, these loads determine the new equilibrium position. Generally, the new equilibrium position is a combination of a translation and a yaw angle of the structure in the earth-fixed coordinate system.
The mean wave drift forces and moments are proportional to the square of the wave amplitude and are function of the wave frequency. Despite drift forces are non-linear, it is possible to show that mean drift force coefficients can be derived from the results of the diffraction-radiation analysis described in the previous subsection [55].

Mainly, there are two distinct methods for the calculation of the mean drift force coefficients. For the sake of simplicity, here only a brief presentation is given, omitting the mathematical formulation. For instance, more details can be found in [6]

- *Far Field solution*: method used for the evaluation of the mean drift forces on a floating body in the horizontal plane. This approach is based on the evaluation of the rate of change of linear angular momentum within a prescribed fluid domain [55][92];

- *Near Field solution*: method based on the direct integration of the pressure acting on the wetted surface of the body. The mean wave drift forces on a floating body are evaluated both in the horizontal and vertical planes. In the case of the *Near Field Solution*, it is possible to calculate the also the slow-varying drift force by including the second-order velocity term in the Bernoulli's equation. The latter is very important in the case of the irregular sea state (as will be presented later), since it is responsible for mooring system resonance frequency excitation [59]. More in detail, the information of the slow-varying drift force are summarized in term of frequency-dependent force coefficients through the *Quadratic Transfer Functions* (QTFs) [6].

In general, the *Near Field Solution* is preferred with respect to the *Far Field solution*, because of its wider range of validity: multiple interacting bodies, multi-directional waves and the drift force coefficients evaluated in both the horizontal and vertical planes.

3.3.3   Cummins equation

Frequency domain equation

The 6 DOF equation of motion of a rigid floating marine structure with zero forward speed can be written, in frequency domain, according to the decomposition developed by Cummins in 1962, who studied the linear hydrodynamic problem [33].

$$\left[\mathbf{M}+\mathbf{A}\left(\omega\right)\right]\ddot{\mathbf{X}}+\mathbf{B}\left(\omega\right)\dot{\mathbf{X}}+\mathbf{K}\mathbf{X}=\mathbf{F_w}\left(j\omega\right) \qquad (3.41)$$

Since this equation is based on linear theory, then it is valid only for small amplitude motions. In the expression above $\mathbf{M}$ represents the mass matrix of the floater, $\mathbf{A}(\omega)$ the added mass matrix, $\mathbf{B}(\omega)$ the potential damping matrix, $\mathbf{K}$ the linear hydrostatic stiffness (due to the buoyancy forces), $\boldsymbol{F_w}(j\omega)$ the wave forces vector. The wave force is expressed as the product of the half of the wave height $\frac{H}{2}$, multiplied by the wave force coefficients per unit of wave amplitude $\boldsymbol{f_w}(j\omega)$, also called Froude-Krylov coefficients (see Eq. 3.42).

$$\boldsymbol{F_w}(j\omega) = \frac{H}{2}\boldsymbol{f_w}(j\omega) \tag{3.42}$$

$\boldsymbol{X}$ is the vector containing the six degrees of freedom.

$$\boldsymbol{X} = \begin{Bmatrix} surge \\ sway \\ heave \\ roll \\ pitch \\ yaw \end{Bmatrix} = \begin{Bmatrix} x \\ y \\ z \\ rot_x \\ rot_y \\ rot_z \end{Bmatrix} \tag{3.43}$$
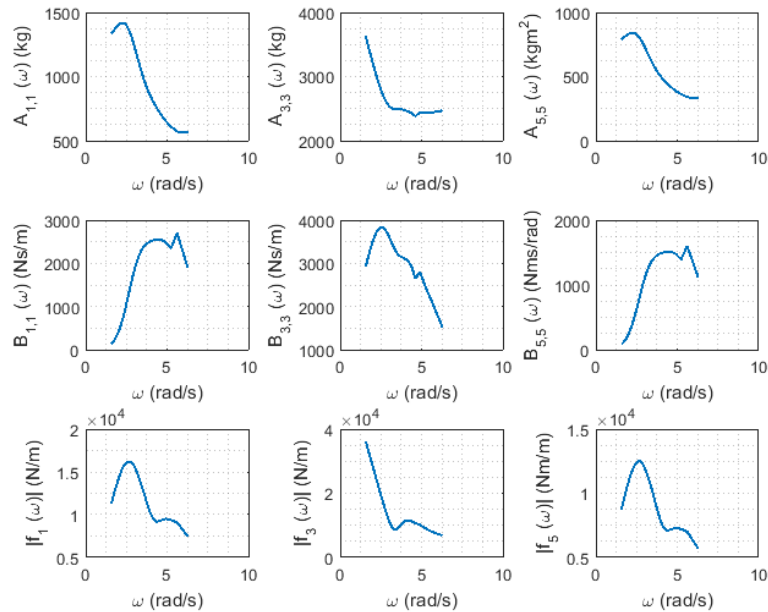
Fig. 3.2 Example of frequency domain hydrodynamic coefficients determined through Ansys AQWA.

The frequency dependent elements of Eq. 3.41 are calculated, by using Boundary Element Method codes such as ANSYS AQWA or WAMIT [6][127]. The calculation method, as stated previuosly, is based on the linear potential flow theory and the panels method. Fig. 3.2 shows an example of the added mass (up), radiation damping (middle) and wave excitation forces (bottom), the case of surge (left), heave (middle) and pitch (right) degrees of freedom for the 1:12 scale PeWEC device.

Another aspect of relevant importance is the coupling between the different DOFs. In the case of the planar representation, where surge, heave and pitch are involved, the surge-pitch coupling is particularly strong and needs to be taken into account for a proper modeling of the floater dynamics. In Fig. 3.3, the added mass and radiation damping for the surge-pitch and pitch-surge coupling are reported. It is also noticeable that the coupling terms are equal, since added mass and radiation damping matrices are symmetric.
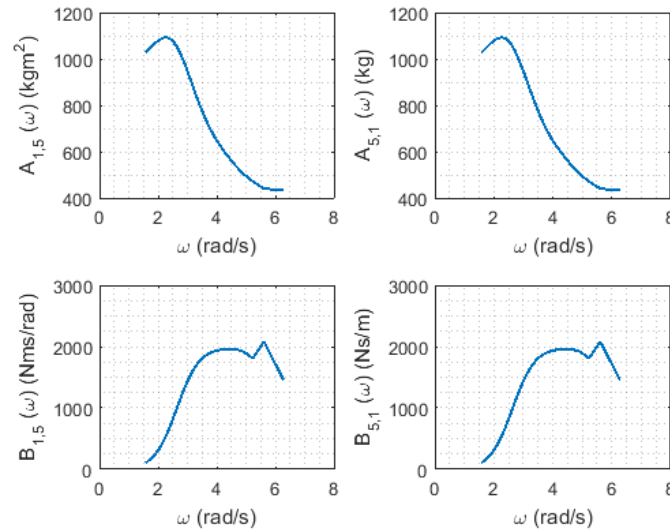
Fig. 3.3 Example of surge-pitch and pitch-surge frequency domain hydrodynamic couplings.

Starting from the Cummins equation defined by Eq. 3.41, it is possible to determine the expression of the Response Amplitude Operator (RAO), which determines the dynamic response of a floating structure with respect to the frequency of the incoming wave. It is defined, for the *i-th* degree of freedom, as the ratio between the amplitude of the *i-th* hull motion and the wave amplitude. It is important to underline that this expression is valid for a free floating structure, where the mooring action and other external forces are not taken into account.

$$RAO_i = \frac{X_i}{\left(\frac{H}{2}\right)} = \frac{f_{w,i}}{\left(-\omega^2\left(M_{ii} + A_{ii}(\omega)\right)\right) + j\omega B_{ii}(\omega) + K_{ii}} \tag{3.44}$$

In Fig. 3.4, an example of the Response Amplitude Operator for surge, heave and pitch DOFs is reported.
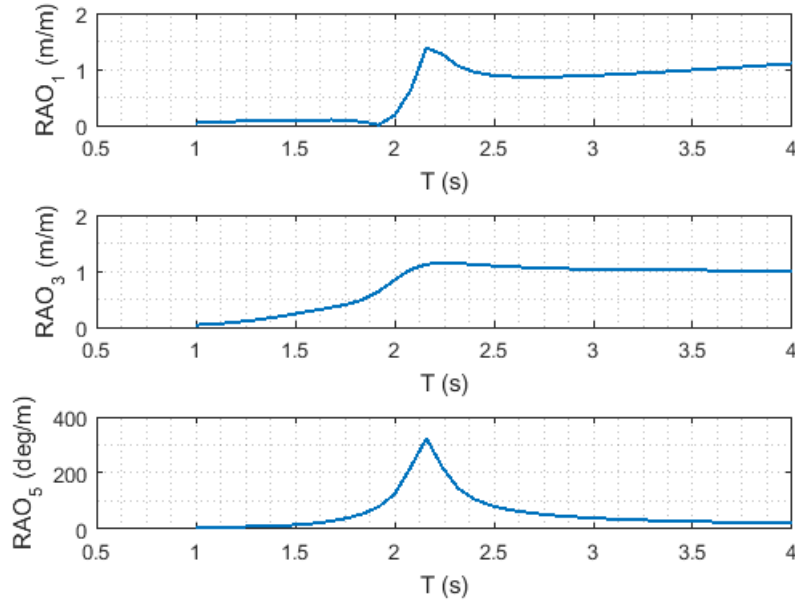
Fig. 3.4 Example of RAO for surge, heave and pitch DOFs.

Time domain equation

The 6 DOF frequency-domain equation was converted into a time-domain dynamic equation by Ogilvie in 1964. According to the Ogilvie's decomposition, Eq. 3.41 becomes [81] :

$$\left[\mathbf{M} + \mathbf{A}(\infty)\right]\ddot{\boldsymbol{X}} + \int_0^t \mathbf{h_r}(t - \tau)\dot{\boldsymbol{X}}d\tau + \mathbf{K}\boldsymbol{X} = \boldsymbol{F_w}(t) \tag{3.45}$$

In Eq. 3.45, $\mathbf{A}(\infty)$ represents the added mass matrix evaluated for infinite oscillation frequency, while $\mathbf{h_r}(t - \tau)$ is the impulse response function of the radiation forces. The convolution term of Eq. 3.45 models the radiation hydrodynamic problem in an ideal fluid, with a linear force pressure distribution. In particular, the impulse response functions of the radiation forces takes into account the fluid mem-

ory effect and incorporates the energy of the radiated waves generated by the body motion.

It is important to highlight that the time-domain equation can be evolved with the introduction of nonlinear effects and it is very useful for the computation of the floater response in irregular waves. On the other hand, the frequency domain equation (Eq. 3.41) involves linear quantities, steady state conditions and it is valid only for monochromatic wave excitation forces.

Radiation forces modeling

The numerical computation of the convolution integral can be very time consuming and for this reason not suitable for the Wave Energy Converter model-based design methodology proposed in this work. Pérez and Fossen, in 2008, suggested a methodology useful to overcome the problem described above [87].

Considering the analytical expression of the impulse response transfer function given by Eq. 3.46, it is possible to execute a parametric frequency domain identification of such transfer function. The goal is to find an appropriate order transfer function which satisfies the criteria of minimum approximation error, stability and passivity.

$$\mathbf{H}_r(j\omega) = \mathbf{B}(\omega) + j\omega(\mathbf{A}(\omega) - \mathbf{A}(\infty)) \tag{3.46}$$

Since the convolution integral is a linear dynamic operator, the radiation force F_r, calculated for each degree of freedom, can be converted in a linear ordinary differential equation, expressed through the state space representation, as reported in Eq. 3.47:

$$\boldsymbol{F_r} = \int_0^t \mathbf{h}_r(t-\tau)\dot{\boldsymbol{X}}d\tau \cong \begin{cases} \dot{\boldsymbol{\zeta}} = \mathbf{A_r}\boldsymbol{\zeta} + \mathbf{B_r}\dot{\boldsymbol{X}} \\ \boldsymbol{F_r} = \mathbf{C_r}\boldsymbol{\zeta} \end{cases} \tag{3.47}$$

Where $\boldsymbol{\zeta}$ is the state vector, while $\mathbf{A_r}$, $\mathbf{B_r}$, $\mathbf{C_r}$ corresponds to the state space representation matrices.

The identification described above can be performed by means of the toolbox developed by Pérez and Fossen, for each one of the degrees of freedom taken into account the floater dynamic modeling [88].

In Fig. 3.5, an example of the identification results for the pitch DOF of the 1:12 scale PeWEC floater is reported. In this case a fifth-order transfer function (blue) is able to approximate the radiation force for the hull under investigation.
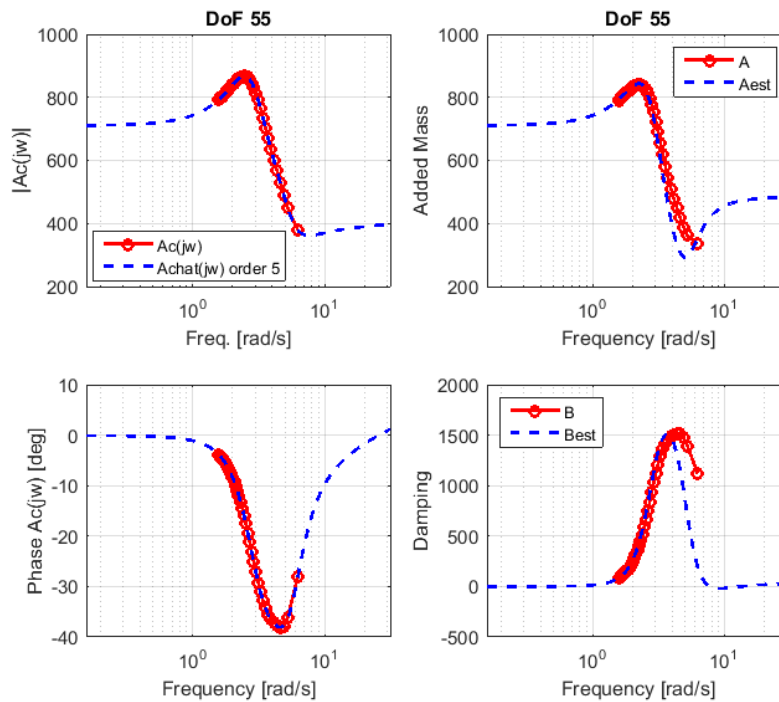
Fig. 3.5 Example of radiation forces identification for pitch degree of freedom.

3.3.4   Sea state and wave forces modeling

In the previous section, the mathematical modeling of a floating body dynamics has been introduced, as well as the methodology for the identification of the hydrodynamic coefficients required for its solution. In the case of the time domain equation, as previously stated, it is possible to solve the floater dynamics both in regular and irregular sea state. For this reason, it is necessary to introduce the sea state representation, which is fundamental for description of the wave forces. The sea state modeling is a relatively wide topic and for the sake of brevity, in this section a brief overview is given. In particular, the main results here reported are based on

the *linear wave theory*, first published by Airy in the 19th century [3] and used up to nowadays for the wave-body interaction modeling.

Regular sea state

The simplest kind of wave motion is the *linear regular wave*, that corresponds to a sinusoidal long-crested, progressive wave, as reported in Fig. 3.6.
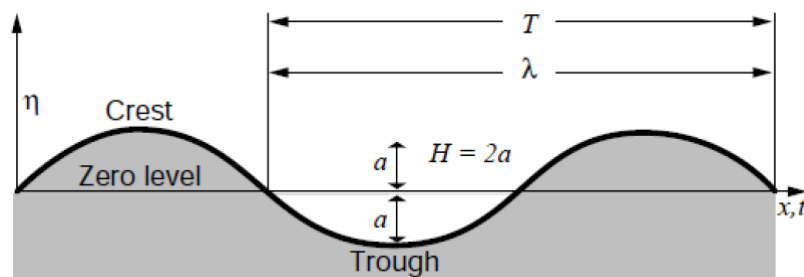
Fig. 3.6 Linear regular wave.

The sinusoidal descriptor means that the wave repeats itself and has the smooth form of the sine curve, while the long-crested descriptor says that the wave is a series of long and parallel wave crests which are all equal in height and equidistant from each other. The progressive nature is seen in their moving at a constant speed in a direction perpendicular to the crests and without change of form. The basic definitions that describe a linear regular wave are the following:

- *Amplitude, a*: magnitude of the maximum displacement from mean sea-level;

- *Wave height, H*: difference in surface elevation between the wave crest and the previous wave trough. For a simple sinusoidal wave $H = 2a$;

- *Wavelength, λ*: horizontal distance between two successive crests;

- *Period, T*: time interval between the passage of successive crests passed a fixed point;

- *Rate of propagation, c_p*: speed at which the wave profile travels or, in other words, the speed at which the crest and trough of the wave advance. It is commonly referred to as *wave speed or phase speed*;

- *Wave steepness, $\frac{H}{\lambda}$*: ratio of the height to the length.

The regular wave profile is described in space and in time by the following equation:

$$\eta(x,t) = \frac{H}{2}\sin(\omega t - Kx) \qquad (3.48)$$

Where:

- $K = \frac{2\pi}{\lambda}$: *wave number*, which defines the periodicity in space;

- $\omega = \frac{2\pi}{T}$: *radian frequency*, that defines the periodicity in time.

Once the wave profile is defined, it is interesting to evaluate the energy transported by the wave. The *Wave Power Density* (WPD) is the physical quantity that expresses the power per unit of wave front and it depends on the propagation conditions of the wave: *deep water* or *shallow water*. In *deep water* conditions, the particles describe vertical circles that become progressively smaller with increasing depth. The radius decreasing is exponential. When waves propagate into *shallow water*, for example when approaching a coast, the characteristics of the waves change as they begin to *feel* the bottom. Because of that, the motion becomes elliptical, wave speed decreases with the decreasing of depth and only the wave period remains constant. In Fig. 3.7, the difference between deep and shallow water is reported.
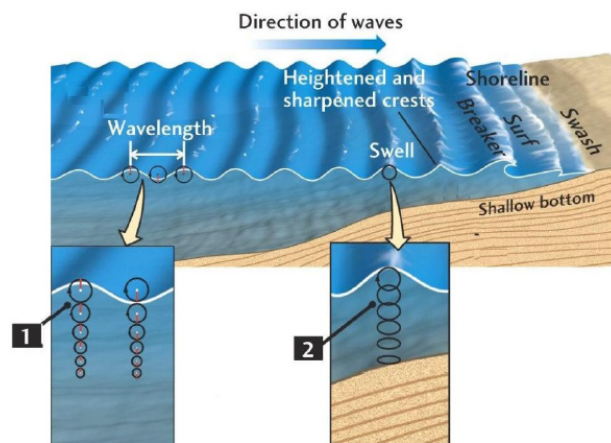
Fig. 3.7 Wave water particles trajectories in deep water (1) and shallow water (2).
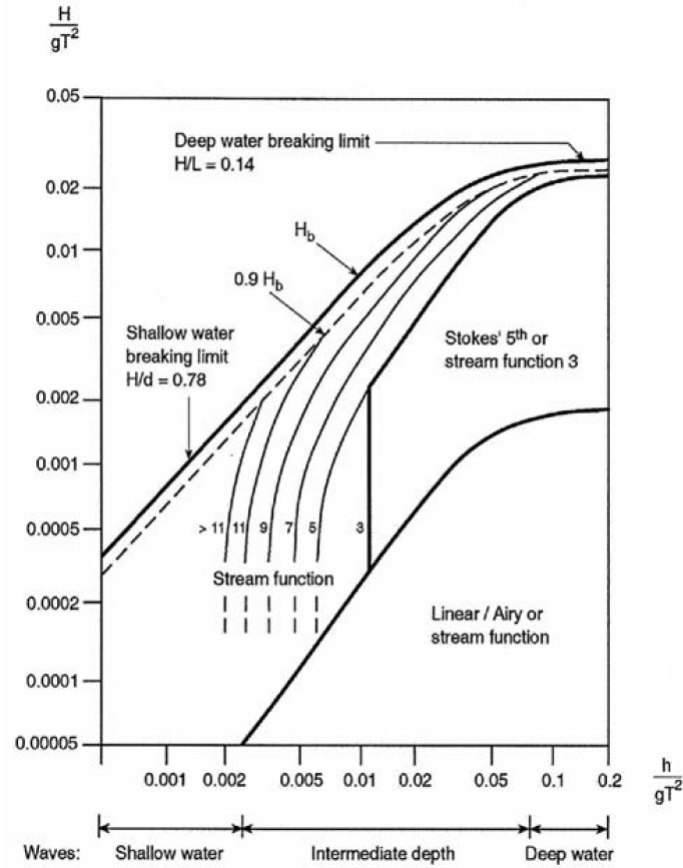
Fig. 3.8 Ranges of validity of various wave theories and breaking zone as a function of the shallowness $\frac{h}{gT^2}$ and steepness $\frac{H}{gT^2}$.

It is important to underline that, when the water depth is greater than $\frac{\lambda}{2}$, the influence of the bottom on the movement of water particles can be considered negligible. A more complete description of the wave propagation conditions can be observed in Fig. 3.8, which represents the wave theory suggested for wave modeling, as a function of the shallowness $\frac{h}{gT^2}$ (where h is the water depth) and steepness $\frac{H}{gT^2}$ [34]. Another important phenomena highlighted by the graph is the breaking zone, where the waves form the foamy, bubbly surface called surf.

The *Wave Power Density* in deep water, which is the condition of interest for the Wave Energy application proposed in this work, is defined as follows:

$$WPD = H^2 T \tag{3.49}$$

Wave Power Density is measured in $\frac{kW}{m}$.

The regular first-order wave forces that excite the floating body can be described combining the regular wave profile definition and the Froude-Krylov force coefficients determined for the structure under analysis. Given the wave height H and period T of the regular wave, the wave force acting on the *i-th* degree of freedom, results be:

$$F_{w,i}(t) = \frac{H}{2}|f_{w,i}(j\omega)|\cos\left(\omega t + \angle(f_{w,i}(j\omega))\right) \tag{3.50}$$

Where $\omega = \frac{2\pi}{T}$.

In the case of the surge motion, it is important to underline that the floater is also subjected to the drift force. The latter, in regular sea state conditions, can be modeled as a constant force, by using the frequency dependent mean drift force coefficients. From the mathematical point of view, the drift force acting on the *i-th* degree of freedom results be:

$$F_{d,i}(t) = \left(\frac{H}{2}\right)^2 f_{d,i}(\omega) = const. \tag{3.51}$$

Irregular sea state

Real sea waves are completely different from the regular wave profile shown in Fig. 3.6. In fact, they appear as a confused and constantly changing water surface, since waves are continually being overtaken and crossed by others. The idea at the basis of the real sea state description is the superposition of infinite simple waves, moving in different direction and with different height, frequency, wavelength and phase, as shown in Fig. 3.9.

The sea surface due to wind waves and swells can be described using random waves and random linear wave theory. It is important to underline that a measured wave record never repeats itself exactly: this is due to the random appearance of the sea surface. However, if the sea state is stationary, the statistical properties of the distribution of periods and heights will be similar from one record to another. This means that the sea state may be considered as a stochastic process and its probability distribution does not change when shifted in time. It is also noticeable that in a given
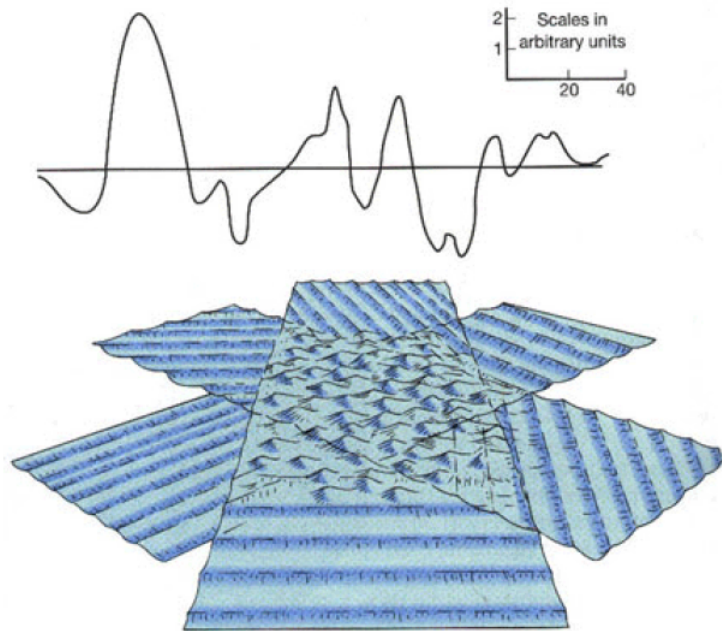
Fig. 3.9 Irregular waves as a superimposition of a set of regular waves with different height, frequency, wave length and phase.

sea state the range of wavelengths it isn't very large, so the wave elevation η can be assimilated to a Gaussian process [59].

An irregular wave is completely characterized when also the parameters related to the energy or to the power transported are determined. As discussed above, an irregular wave can be described as the superposition of infinite simple waves with different values height, frequency, wavelength and phase. Following this idea, it is possible to define the wave energy spectrum $S_\eta(f)$, which indicates the level of energy transported by the different frequency components f, in which the real sea has been decomposed.

In the past, several experimental campaigns were performed with the aim to determine standard wave spectra able to describe the sea state frequency components distribution. For instance, *JONSWAP* and *Bretschneider* wave spectra are commonly used for the representation of the sea state in ocean engineering applications [46][59][115][129]. In Fig. 3.10 an example of wave spectrum is reported.

The decomposition of the wave record may be performed by means of Fourier analysis. This analysis says that each signals can be expressed as the sum of an infinite number of sinusoidal waves of different frequencies, amplitudes and phases.
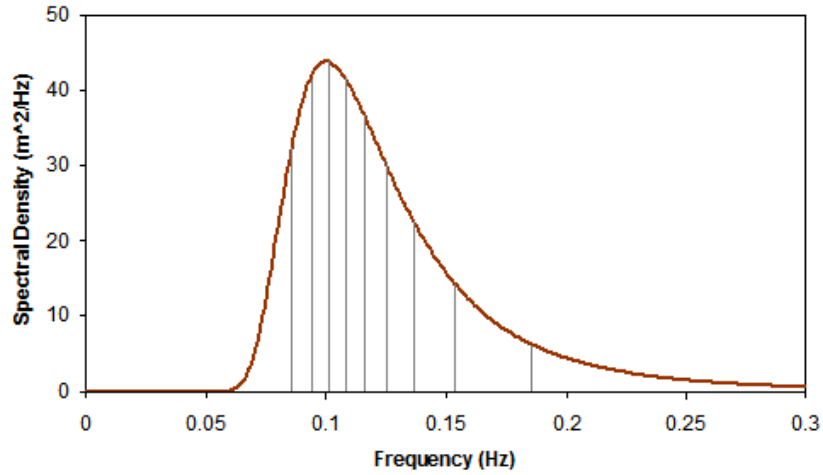
Fig. 3.10 Example of wave energy spectrum.

However, in the common practice, the Fourier series is made up by a finite sum of sinusoidal terms and the result is an approximation of the original signal. By considering the case of irregular waves, for a surface elevation varying in time in a single direction, the Fourier series can be written as:

$$\eta(x,t) = \eta_0 + \sum_{n=1}^{N} \eta_{a,n} \sin(\omega_n t - K_n x + \phi_n) \qquad (3.52)$$

Where:

- $\eta(x,t)$: recorded wave elevation of the water surface at time t;

- η_0: mean elevation and this is related to the depth of the seabed;

- $\eta_{a,n}$: wave amplitude of the *n-th* component;

- ω_n: wave radian frequency of the *n-th* component;

- K_n: wave number of the *n-th* component;

- ϕ_n: phase angle of the *n-th* component;

- N: Fourier analysis total number of components.

The phase angle takes into account the fact that the components are not all in phase, i.e. their maxima generally occur at different times. Starting from the wave

energy spectrum, it is possible to identify the statistical wave parameters, by means of the spectral moments. In general, the *n-th* order spectral moment is defined as follows:

$$m_n = \int_0^\infty f^n S_\eta(f) df \qquad (3.53)$$

As example, here below the most important statistical wave parameters used in the Wave Energy field are reported. More details can be found in [115].

- *Significant wave height*, H_s: defined as the average of the highest one-third of the individual through-to-crest heights in a wave record. H_s is proportional to the square root of the zero-order spectral moment. The latter corresponds to the area under the wave energy spectrum $S_\eta(f)$.

$$H_s = 4\sqrt{m_0} \qquad (3.54)$$

- *Maximum wave height*, H_{max}: maximum wave height occurring in a record;

- *Energy period*, T_e: it is strictly related to the lower frequency band of the spectrum, where most of the power is contained. This parameter is important for the evaluation of the energy transported by the wave and it is defined as the ratio between the minus one and zero-order spectral moments.

$$T_e = \frac{m_{-1}}{m_0} \qquad (3.55)$$

- *Peak period*, T_p: period corresponding to the frequency at which the wave spectrum has its maximum value;

- *Average zero-crossing wave period*, $\bar{T}_z$: time interval between two consecutive instants, where the wave elevation crosses the zero level in the upward or downward direction.

- *Significant wave period*, T_s: calculated as the mean of the zero up-crossing periods associated with the highest one third of the waves (the ones determining H_s).

By imposing the spectrum shape function, it is possible to convert among the periods T_p, T_z, T_e [34]. A particular attention must be given to the significant wave period T_s, which cannot be linked analytically to the other statistical wave period definitions. Assuming the JONSWAP spectrum, the relation between the energy period and the significant period, has been estimated empirically by Goda [50]:

$$T_e \simeq 0.9 \cdot T_s \tag{3.56}$$

Significant wave height and energy period allows to define the Wave Power Density of the irregular wave, measured in $\frac{kW}{m}$:

$$WPD = 0.49 H_s^2 T_e \tag{3.57}$$

Once the wave profile and the corresponding wave energy spectrum are known, it is possible to define the wave loads acting on the floating structure. However, the irregular wave profile is not enough, indeed for the evaluation of such forces the results of the hydrodynamic analysis performed for a given floating structure are required.

The time history of the irregular first-order wave force acting on the *i-th* degree of freedom results be a sum of finite regular harmonics.

$$F_{w,i}(t) = \sum_{n=1}^{N} F_{w0,i,n} \cos\left(\omega_n t + \phi_{i,n} + \theta_n\right) \tag{3.58}$$

Where $F_{w0,i,n}$ is the amplitude of the *n-th* force component, function of the Froude-Krylov force coefficients and wave amplitude evaluated at the *n-th* spectrum frequency component.

$$F_{w0,i,n} = |f_{w,i}(\omega_n)| \sqrt{2 S_\eta(\omega_n) \Delta\omega} \tag{3.59}$$

The angle $\phi_{i,n}$ corresponds to the phase of the Froude-Krylov coefficients, while θ_n is the angle between the harmonics components of the spectrum can either be chosen as random phase or can be guided by a groupiness factor [101] or, in case of real sea state data acquisitions, may be the phase angle given by the Fast Fourier Transform (FFT) analysis of the wave time series.

$$\phi_{i,n} = \angle\big(f_{w,i}(\omega_n)\big) \tag{3.60}$$

The modeling of the second-order wave forces is fundamental for a proper evaluation of the moored system dynamics along surge direction. The wave amplitudes provide information about the slowly-varying wave force of an irregular wave train. The wave envelope is an imaginary curve joining successive wave crests (or troughs), as shown in Fig. 3.11.
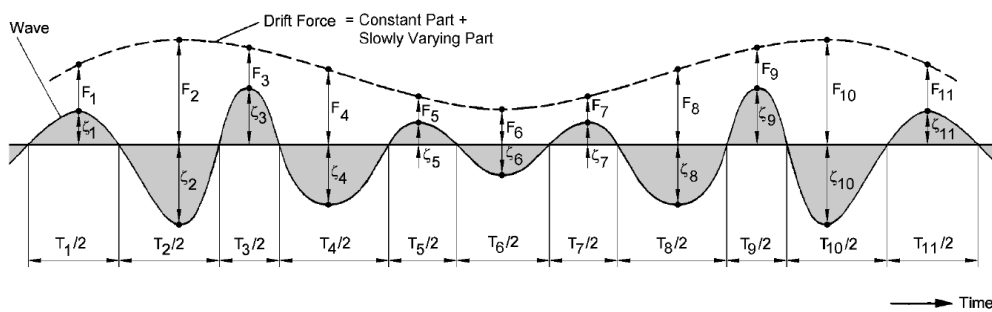
Fig. 3.11 Irregular wave record and slowly-varying envelope.

It seems logical, considering the results related to the mean wave drift force, that the square of the envelope amplitude provides information about the drift forces in irregular waves. To do this, one would (in principle) make a spectral analysis of the square of the wave envelope. In other words, the spectral density of the square of the wave amplitude provides information about the mean period and the magnitude of the slowly-varying wave drift force. In practice, it is very difficult to obtain an accurate wave envelope spectrum due to the long wave record required. Assuming that about 200-250 oscillations are required for an accurate spectral analysis and that the mean period of the wave envelope record is about 100 seconds, the total time that the wave elevation has to be recorded can be up to 7 hours [59].

From the practical point of view, the low-frequency wave drift forces are derived using the Quadratic Transfer Functions (QTFs), as described in section 3.3.2. The general expression for the second-order wave drift force in irregular sea state is:

$$
\begin{aligned}
F_{d,i}(t) = \sum_{m=1}^{N} \sum_{n=1}^{N} \eta_{a,m}\eta_{a,m} & \left[P_{i,m,n}^{+}\cos\Big((\omega_m + \omega_n)t + (\varepsilon_m + \varepsilon_n) \Big) + \right. \\
& \left. Q_{i,m,n}^{+}\sin\Big((\omega_m + \omega_n)t + (\varepsilon_m + \varepsilon_n) \Big) \right] + \\
\sum_{m=1}^{N} \sum_{n=1}^{N} \eta_{a,m}\eta_{a,m} & \left[P_{i,m,n}^{-}\cos\Big((\omega_m - \omega_n)t + (\varepsilon_m - \varepsilon_n) \Big) + \right. \\
& \left. Q_{i,m,n}^{-}\sin\Big((\omega_m - \omega_n)t + (\varepsilon_m - \varepsilon_n) \Big) \right] +
\end{aligned}
\tag{3.61}
$$

Where:

- $\eta_{a,m}$: wave amplitude of the *m-th* frequency component;

- $\eta_{a,n}$: wave amplitude of the *n-th* frequency component;

- $P_{i,m,n}^{+}$: real part of the QTF for the sum frequency of two wave components, evaluated for the *i-th* degree of freedom;

- $Q_{i,m,n}^{+}$: imaginary part of the QTF for the sum frequency of two wave components, evaluated for the *i-th* degree of freedom;

- $P_{i,m,n}^{-}$: real part of the QTF for the difference frequency of two wave components, evaluated for the *i-th* degree of freedom;

- $Q_{i,m,n}^{-}$: imaginary part of the QTF for the difference frequency of two wave components, evaluated for the *i-th* degree of freedom;

Considering Eq. 3.61, it is possible to see that the wave drift force in irregular sea is made up both from low-frequency and high frequency components. Furthermore, the force is mainly constituted by the summation of two incident wave at radian frequency ω_m and ω_n. The high frequency components can be neglected, since they do not contribute to the excitation of the mooring system. This simplification can be justified considering that the resonance frequency of the mooring system coupled to the floating structure is very low. Thus, high frequency components are filtered by the mooring system.

The direct summation of Eq. 3.61 is relatively time consuming even if the high-frequency components are neglected. Newman, in 1974, proposed an approximation for equation Eq. 3.61 [80].

The terms out of diagonal $P_{i,m,n}^-$ and $Q_{i,m,n}^-$ can be obtained starting from the diagonal coefficients $P_{j,n,n}^-$ and $Q_{j,n,n}^-$. This means that the second-order velocity potential is not required, since the QTF diagonal terms coincides with the mean-drift force coefficients calculated from the results of the first-order problem.

$$P_{i,m,n}^- = P_{i,n,m}^- = \frac{1}{2}\left(P_{i,m,m}^- + P_{i,n,n}^-\right) \tag{3.62}$$

$$Q_{i,m,n}^- = Q_{i,n,m}^- = 0 \tag{3.63}$$

Newman proposed to further approximate Eq. 3.61, elaborating the double sum by the square of a single series. This implies that only N terms should be added together at each time step compared to N^2 terms of Eq. 3.61. The formula can be written as follows:

$$
\begin{aligned}
F_{d,i}(t) = 2\left(\sum_{n=1}^{N} \eta_{a,n}\sqrt{P_{i,n,n}}\cos\left(\omega_n t + \phi_n\right)\right)^2 = \\
2\left(\sum_{n=1}^{N} \eta_{a,n}\sqrt{f_{d,i}(\omega_n)}\cos\left(\omega_n t + \phi_n\right)\right)^2
\end{aligned}
\tag{3.64}
$$

3.3.5 Hydrodynamic nonlinearities

The Cummins equation is quite reliable when small amplitude motions occur. This working condition is valid for most of the marine applications but not for Wave Energy Converters, which are designed to work in resonance conditions with respect to the incoming wave (maximization of the extracted power) [44].

In resonance conditions, linear hypothesis are not valid anymore: from one side higher motions induce a variation of the wetted surface in time, while on the other different nonlinear phenomena, such as vortexes, arise into the fluid [53]. Thus, the linear hydrodynamic model reveals its weakness for WECs modeling. However,

as widely suggested in literature, it is common to add viscous contributions that summarizes the nonlinearities and allow to improve the model accuracy [53][85][86].

The estimation of the viscous contributions can be performed in different ways, starting from experimental free-decay tests, up to fully-viscous Computational Fluid Dynamics (CFD) simulations of the structure under investigation [11][18][60].

In the next paragraphs, the analytical formulation of the viscous term for surge and pitch degrees of freedom is given. It is important to highlight that surge and pitch motions, taking into account the planar representation of the system, are the DOFs mainly affected by viscous effects.

Surge nonlinear viscous force

The surge viscous force can be evaluated according to the drag force contribution of the Morison equation, assuming the hypothesis of low forward speed.

$$F_{v,x} = -\frac{1}{2}\rho C_d A \dot{x}|\dot{x}| \tag{3.65}$$

Where:

- ρ: water density;

- C_d: drag coefficient. It is a dimensionless coefficient that can be found in literature for simple geometries. For more complicate geometries an experimental or numerical identification is required;

- A: wetted area of floater;

- $\dot{x}$: floater instantaneous surge speed

Pitch nonlinear viscous torque

For what concern the pitch motion, the viscous torque acting on the floater can be expressed as follows:

$$T_{v,\delta} = -\beta_\delta \dot{\delta}|\dot{\delta}| \tag{3.66}$$

Where β_δ is the nonlinear hydrodynamic viscous damping that can be identified, as stated above, through experimental tests or fully viscous CFD simulations. In Chapter 6, the results of the experimental identification of the hydrodynamic viscous damping coefficient for the 1:12 PeWEC device are reported.

Viscous forces linearization

The hydrodynamic viscous forces, as described in the previous paragraphs, have a nonlinear nature. The nonlinear formulation is suitable for the time domain Cummins equation, while in the case of the frequency domain model is required a linearization of the viscous force. The methodology developed for the hydrodynamic viscous forces linearization is here explained considering, as example, the pitch viscous torque.

The linearization takes into account two different boundaries:

- T_{res}: resonance period of the floater determined, for instance, through the RAO;

- δ_0: motion amplitude with respect to the linearization is performed.

The pitch oscillation velocity, in regular waves and under linear assumptions, can be expresses as follows:

$$\dot{\delta}_0 = \frac{2\pi}{T_{res}} \delta_0 \qquad (3.67)$$

Substituting Eq. 3.67 into the nonlinear hydrodynamic viscous torque equation (Eq. 3.66), it is possible to represent such torque as a function of the pitch angle. Then, the nonlinear torque can be linearized through the secant for the selected amplitude δ_0, as reported in Fig. 3.12. The slope of the secant corresponds to the linearized viscous damping coefficient β_δ^{lin} and the force can be expressed as a linear function of the velocity.

$$T_{v,\delta}^{lin} = -\beta_\delta^{lin} \dot{\delta} \qquad (3.68)$$

In Fig. 3.12, the hydrodynamic viscous damping torque linearization is proposed for different pitch amplitudes.
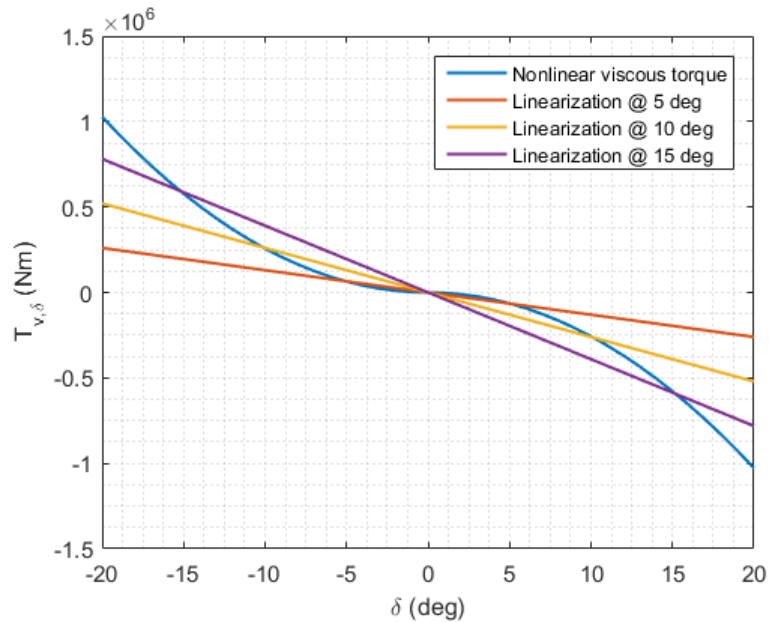
Fig. 3.12 Linearization of the nonlinear hydrodynamic viscous torque on pitch DOF, for different motion amplitudes.

3.4 Mooring model

The last subsystem of the PeWEC device that needs to be modeled is the mooring system. The latter allows to keep the device in place when subjected to the actions of the waves.

The mooring line, as shown in Fig. 3.13, is mainly composed by three different lines (chains) assumed as rigid bodies with COG respectively in points G_1, G_2, G_3. It is important to underline that the last assumption is particularly strong, since in general a chain tends to behave like a catenary, instead of a rigid body. A buoy (jumper) with a net buoyancy force F_b is connected to point A, while a clump weight with net gravity force F_a is connected to point B. The connection point of the mooring line with the device is defined by point C.

The behavior of this kind of mooring is comparable to a hardening spring behavior, with reduced stiffness for small displacement and high restoring force at big displacements. Such behavior is desired because it allows small forces on the PeWEC for normal operations and high forces before end stroke, thus reducing snatches in extreme wave conditions. The mooring stiffness is particularly influ-
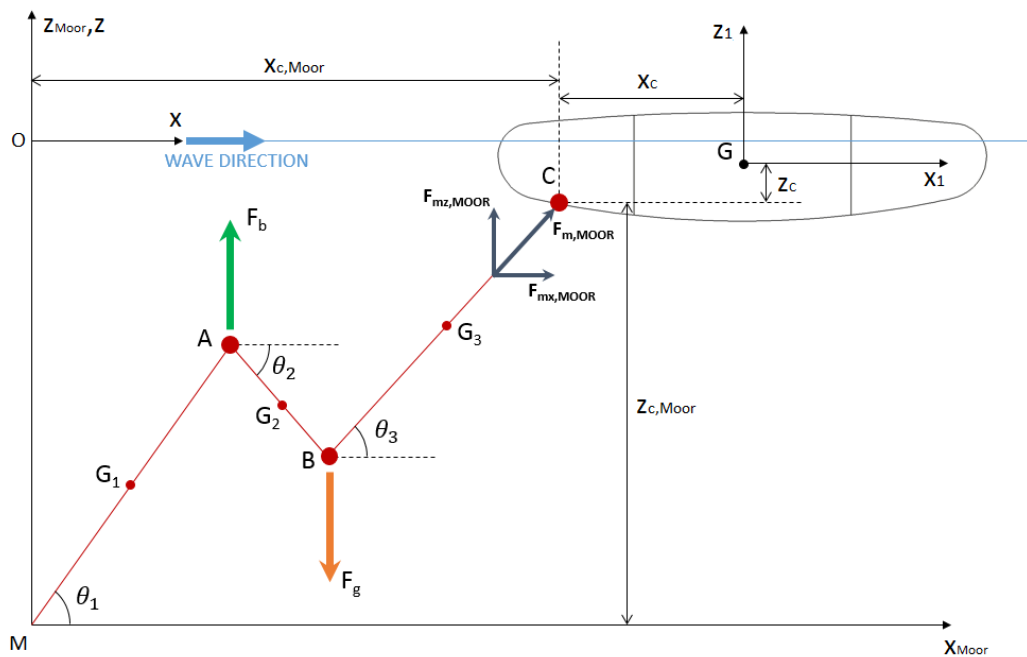
Fig. 3.13 Mooring system layout.

enced by the weight per unit of length of chains, the mass of the clump weight and the length of chain sections.

3.4.1 Quasi-static modeling

The compliant mooring proposed can be modeled according to a quasi-static approach: the static equilibrium of the system is studied varying x and z coordinates of the connection point C, within a work space defined with respect to the mooring reference frame and compatible with the maximum extension of the mooring line.

For all the different values of $x_{C,Moor}$ and $z_{C,Moor}$, the potential energy is calculated as a function of the angle θ_1. The equilibrium condition is determined when the potential energy reaches its minimum value. The mooring line tension $F_{m,Moor}$ at the connection point C can be calculated respect to the mooring reference frame and it can be decomposed along the x_{Moor} and z_{Moor} coordinates. In Fig. 3.14, the displacement-force mooring characteristics along the horizontal and vertical directions are reported.
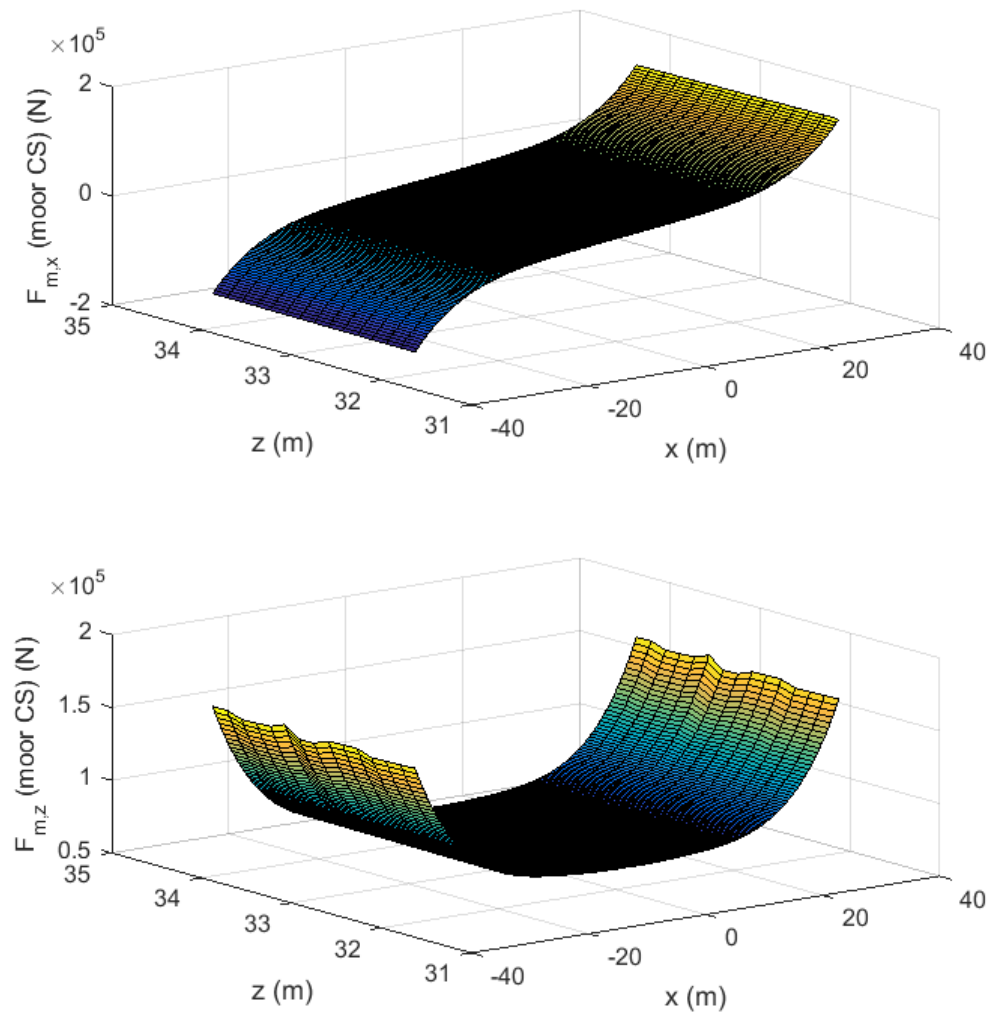
Fig. 3.14 Mooring forces maps evaluated in the mooring coordinate system.

In order to obtain the mooring tensions (which are expressed in the mooring reference frame), it is necessary to evaluate the motion of point C with respect mooring reference frame $M - x_{Moor}y_{Moor}z_{Moor}$. The motion of point C with respect to the mooring coordinate system can be computed starting from hull motions expressed in the $O - xyz$ coordinate system, thanks to a transformation matrix between the two coordinate systems considered.

The position of point C with respect to $G - x_1y_1z_1$ coordinate system is:

$$^1\boldsymbol{p_C} = \begin{Bmatrix} x_C \\ 0 \\ z_C \end{Bmatrix} \tag{3.69}$$

It is noticeable that the value of x_C is negative, while z_C can be both positive or negative, according to its position with respect to the hull COG. The position of hull COG with respect to mooring coordinate system is:

$$^M\boldsymbol{p_G} = \begin{Bmatrix} x_G \\ 0 \\ H_{0,G} + zG \end{Bmatrix} = \begin{Bmatrix} x_C \\ 0 \\ (z_{C,Moor} + |z_c|) + zG \end{Bmatrix} \tag{3.70}$$

Where $H_{0,G}$ corresponds to the distance of the COG with respect to the seabed in static conditions. The homogeneous transformation matrix that allows to express, in the mooring reference frame, the orientation and the position of a vector described in the $O - xyz$ coordinate system results be:

$$^M\mathbf{A_1} = \begin{bmatrix} \cos\delta & 0 & \sin\delta & x_G \\ 0 & 1 & 0 & 0 \\ -\sin\delta & 0 & \cos\delta & H_{0G} + z_G \\ 0 & 0 & 0 & 1 \end{bmatrix} \tag{3.71}$$

The position of point C in mooring coordinate system can be defined in the following way:

$$^M\boldsymbol{p_C} = {}^M\mathbf{A_1}\,{}^1\boldsymbol{p_C} = \begin{Bmatrix} xG + x_C\cos\delta + z_C\sin\delta \\ 0 \\ (H_{0G} + z_G) - x_C\sin\delta + z_C\cos\delta \end{Bmatrix} \tag{3.72}$$

Using the hull motions computed in the $O - xyz$ reference frame, it is possible to evaluate the position of point C in $M - x_{Moor}y_{Moor}z_{Moor}$ reference frame and then the forces due to the mooring lines, computed in the same coordinate system. At this point, the moor tension evaluated through two look-up tables (LUT) (see Fig. 3.14) can be transported in the $O - xyz$ reference frame thanks to a transformation matrix. Three different contribution can be distinguished:

- $^1F_{m,x}$: mooring forxe along the x-axis;

- $^1F_{m,z}$: mooring forxe along the z-axis;

- $^1F_{m,\delta}$: mooring forxe along the y-axis;

The mooring line forces discharged on the hull, along x and z axis, have the same modulus of the ones computed by means of look-up tables, but with opposite direction:

$$^1F_{m,x} = -\left(^{Moor}F_{m,x}\right) \tag{3.73}$$

$$^1F_{m,z} = -\left(^{Moor}F_{m,z}\right) \tag{3.74}$$

In the end, the torque discharged on the hull can be determined in the following way:

$$^1F_{m,\delta} = -\sqrt{x_C^2 + z_C^2}\left[-\left(^{Moor}F_{m,x}\sin\left(\text{atan}\left(\frac{|z_C|}{|x_C|}\right) - \delta\right)\right) + \left(^{Moor}F_{m,z}\cos\left(\text{atan}\left(\frac{|z_C|}{|x_C|}\right) - \delta\right)\right)\right] \tag{3.75}$$

3.4.2   Mooring forces linearization

As showed in the previous paragraph, the mooring action of the floater is highly nonlinear and in the perspective of the integration of such forces in the linear model, a simplification of the problem is required.

The idea is to define the equivalent horizontal and vertical linear stiffness, starting from the nonlinear mooring forces characteristics. In particular, the stiffness values can be obtained from the slope of the linear portion of the displacement-force characteristics along surge and heave directions, as shown in Fig. 3.15.

Then, mooring line can be approximated as a couple of linear springs connected in correspondence of point C, with stiffness k_x and k_z respectively. Lastly, it is possible to collect the k_x and k_z in the mooring matrix $\mathbf{K_m}$.
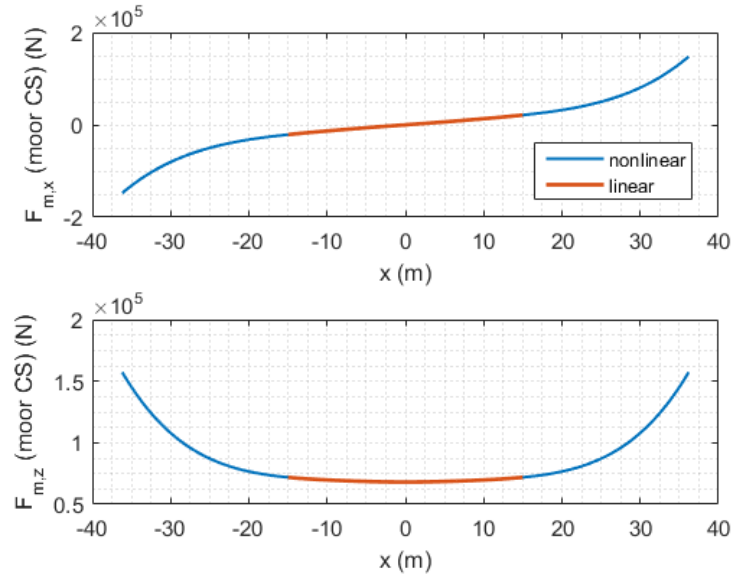
Fig. 3.15 Linearized mooring displacement-force characteristic along surge and heave directions.

3.5 PeWEC full model

Starting from the results presented in the previous sections about floater, pendulum and mooring line modeling, it is possible to derive the dynamic equations that describe the complete device behavior.

The complete dynamic equations constitutes the base of the *Wave-to-Wire* model, that is commonly used in Wave Power application for the estimation of the device performances and loads, starting from the resource characteristics.

More in detail, in this section the linear frequency domain, linear time domain and nonlinear time domain formulation of the dynamic equations are given.

3.5.1 Frequency domain equation

The frequency domain representation is the simplest model that can be used for the evaluation of the dynamic behavior of the system in regular sea state. It particularly useful during the initial design stage of the device or when a sensitivity analysis is required for the comprehension of the influence of each system parameter on the overall device performances.

Such representation can be achieved coupling the linearized pendulum dynamic equation, hydrodynamic model and linearized mooring forces. Regarding the hydrodynamic model, it is important to highlight that the linearized viscous forces must be taken into account and only surge, heave and pitch equations needs to be considered.

On the base of the last comment, let be now X_{sys} the vector containing the floater degrees of freedom and the pendulum angular coordinate

$$X_{sys} = \begin{Bmatrix} x \\ z \\ \delta \\ \varepsilon \end{Bmatrix} \tag{3.76}$$

Then, the frequency domain equation results be:

$$\left[\mathbf{M_s^{lin}} + \mathbf{A}(\omega)\right]\ddot{X}_{sys} + \left[\mathbf{B}(\omega) + \mathbf{B_v^{lin}} + \mathbf{D_{PTO}}\right]\dot{X}_{sys} +$$
$$\left[\mathbf{K} + \mathbf{K_p} + \mathbf{K_m}\right]X_{sys} = F_w(j\omega) \tag{3.77}$$

Where $\mathbf{B_v^{lin}}$ is the linearized hydrodynamic viscous damping matrix.

3.5.2 Linear time domain equation

The frequency domain model can be converted in time domain taking into account the time domain representation of the hydrodynamic problem. This formulation, even if linear, is suitable for the system performances assessment in the case of irregular waves.

$$\left[\mathbf{M_s^{lin}} + \mathbf{A}(\infty)\right]\ddot{X}_{sys} + \int_0^t \mathbf{h_r}(t-\tau)\dot{X}_{sys}d\tau + \left[\mathbf{B_v^{lin}} + \mathbf{D_{PTO}}\right]\dot{X}_{sys} +$$
$$\left[\mathbf{K} + \mathbf{K_p} + \mathbf{K_m}\right]X_{sys} = F_d(t) + F_w(t) \tag{3.78}$$

3.5.3   Nonlinear time domain equation

Lastly, the nonlinear time domain equation constitutes the most complete representation developed in this work. The nonlinear dynamic equation can be used for both regular and irregular sea state and it can be considered a sufficiently reliable tool for the estimation of the WEC performances and of the loads acting on mechanical components and on PTO.

$$
\begin{aligned}
\left[\mathbf{M_s} + \mathbf{A}\left(\infty\right)\right]\ddot{\boldsymbol{X}}_{sys} + \int_0^t \mathbf{h_r}\left(t - \tau\right)\dot{\boldsymbol{X}}_{sys}d\tau + \mathbf{B_v}|\dot{\boldsymbol{X}}_{sys}|\dot{\boldsymbol{X}}_{sys} + \mathbf{K}\boldsymbol{X}_{sys} = \\
\boldsymbol{F_d}\left(t\right) + \boldsymbol{F_w}\left(t\right) + \boldsymbol{F_m}\left(t\right) + \boldsymbol{F_{gr}}\left(t\right) + \boldsymbol{F_{cor}}\left(t\right) + \boldsymbol{F_{PTO}}\left(t\right)
\end{aligned}
\tag{3.79}
$$

It is important to underline that nonlinear dynamic equations can be coupled with a complete model of the PTO that, for instance, takes into account electrical generator torque and velocity constraints or specific control strategies that may intervene in extreme working conditions, in order to preserve the device. For this reason, the PTO matrix $\mathbf{D_{PTO}}$ has been substituted with a more generic vector $\boldsymbol{F_{PTO}}\left(t\right)$.

As example, the nonlinear equations system can be implemented in the MAT-LAB/Simulink $^{\circledR}$ environment, particularly suitable for the multi-physics system modeling.

Chapter 4

1:45 PeWEC prototype experimental testing

This chapter deals with the description of the experimental campaign performed in May 2015, on the 1:45 PeWEC device. This campaign has been designed with the aim to test an innovative WiFi data logging layout to be implemented on the 1:12 PeWEC device that will be described in the next chapter. In fact, at the time of the testing campaign here described, the 1:45 scale prototype was already tested and the results achieved during the tests in the wave flume of the Politecnico di Torino allowed to validate the technology and part of the numerical models in frequency domain. More details can be found in [89]. Conversely, the 1:12 scale device was in its design phase and a verification of the WiFi data logging layout and of the infrastructures offered by the INSEAN wave basin was fundamental.

The first part of this chapter is concerned about the reference installation site definition and its sea state characteristics summarized through the s scatter diagram. In particular, the Pantelleria Island site has been chosen as reference since, as previously described, the project described in this works has the aim to define a pendulum based passive device for Mediterranean Sea. Moreover, the full scale ISWEC plant was deployed in Pantelleria Island in July 2015, thus it constitutes a robust reference for the development of the PeWEC technology.

Another important aspect parallel to the site scatter diagram is the definition of the design sea state, with respect to it is possible to start the design of the device and to refer the scale of the prototypes. As will be described more in detail in the next

sections, the most energetic sea state condition of Pantelleria Island scatter diagram has been chosen, since it constitutes a good compromise between the prototype scale (1:45) and the performances of the INSEAN wave basin, where the prototype has been tested.

The second part of this chapter is dedicated to the description of the prototype, its mechanical components and the equipment used for prototype monitoring and control, as well as the characteristics of the INSEAN wave basin and the experimental layout adopted for the device testing.

The campaign has been focused on the identification of the device performances in monochromatic sea state: for this reason the floater pitch RAO has been determined, together with the frequency response of the device with constant PTO damping coefficient and unlocked pendulum. In the last part of the chapter, the methodology used for data elaboration and the results are widely described, proving an adequate functioning of the WiFi layout and of experimental testing methodology.

Lastly, a comparison between experimental and numerical data is provided, with the aim to show the reliability of the numerical model and the pendulum technology feasibility. These results are very important in order to justify the prosecution of the development activity toward the 1:12 scale prototype.

4.1 Reference scatter diagram

The 1:45 prototype has been designed considering the sea state properties of the Pantelleria Island site, where the ISWEC full scale prototype was installed in July 2015. In Fig. 4.1, a satellite view of the Island is reported, as well as a indication of the ISWEC position.

Scatter diagrams are a tool widely used in ocean engineering application for a synthetic representation of the sea state characteristics of a certain site. The characterization of a site is in general performed through specific monitoring campaigns: a wave climate sensor acquires in real time, at a fixed sampling frequency and for a suitable time interval, wave elevation, wave direction and currents. The data logging campaign can lasts for different years in order to achieve a sufficiently robust statistical description of the site.

Fig. 4.1 Satellite view of the Pantelleria Island and ISWEC position.

Then, according to the methodologies briefly described in section 3.3.4, the real wave elevation records are analyzed and the statistical parameters describing the sea state are determined. Data are clustered into two entries tables called *scatter diagrams*: for instance the first entry (row) can represent the energy period T_e, while columns can be associated to the significant wave height H_s. Furthermore, column and rows have, respectively, fixed intervals. In this way, it is possible to define a grid that allows to identify the position of each wave.

By considering the entire data logging records, it is possible to build the site occurrences matrix: each element of the matrix indicates the amount of hours that a certain sea state (individuated by a couple (H_s, T_e), as example) happened during the entire year.

The Pantelleria Island site ($36°50'0''$N, $11°57'0''$E) wave climate was determined after a data logging campaign conducted from January 2010 to December 2011, using a NORTEK AWAC submerged wave climate sensor, placed at the depth of 16 m offshore the Island harbor (see Fig. 4.1) [25]. Data were recorded every 3 hours for a 30 minutes duration at 2 Hz. In Fig. 4.2, the occurrences and energy scatter diagrams of the Pantelleria Island site are reported, highlighting the significant wave height H_s and energy period T_e of the most recurrent and most energetic waves.
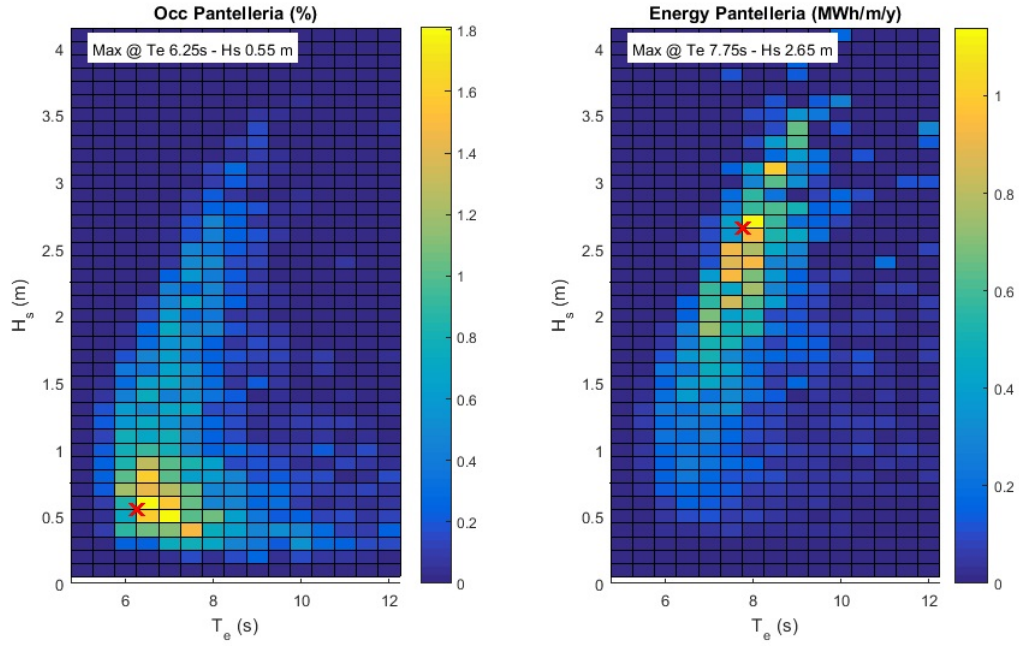
Fig. 4.2 Pantelleria installation site occurrences scatter diagram and wave energy density scatter diagram.

It is important to underline that the wave energy density scatter diagram (*WED*) is determined by the product of occurrences and wave power density (*WPD*) matrices:

$$\mathbf{WED} = \mathbf{WPD} \cdot \mathbf{Occ} \qquad (4.1)$$

Where each element of the **WPD** matrix is calculated according to Eq. 3.57.

4.2   Design wave condition

The design condition has been defined comparing and scaling the most recurrent and most energetic wave properties, according to the Froude scaling law and the 1:45 scaling factor chosen [39][83]. Observing Table 4.1, it is possible to see that the most recurrent wave is characterized by a very low power density and wave height. This fact may lead to different problems from the experimental point of view: the wave maker is not able to generate accurately the wave and/or the power generated by the PTO cannot be measured with a satisfying degree of accuracy. For this reason, the most energetic sea state has been considered as reference.

Table 4.1 Most recurrent and most energetic wave: full scale and 1:45 scale properties.

	Irregular sea state					
	Full scale			1:45 scale		
	$H_s(m)$	$T_e(s)$	$WPD\left(\frac{kW}{m}\right)$	$H_s(m)$	$T_e(s)$	$WPD\left(\frac{kW}{m}\right)$
Max. occurrence	0.55	6.25	0.94	0.012	0.93	$6.7 \cdot 10^{-4}$
Max. energy	2.65	7.75	26.7	0.06	1.15	$2 \cdot 10^{-3}$
	Iso-energetic regular sea state					
	Full scale			1:45 scale		
	$H(m)$	$T(s)$	$WPD\left(\frac{kW}{m}\right)$	$H(m)$	$T(s)$	$WPD\left(\frac{kW}{m}\right)$
Max. occurrence	0.39	6.25	0.94	$8.6 \cdot 10^{-3}$	0.93	$6.7 \cdot 10^{-4}$
Max. energy	1.86	7.75	26.7	0.04	1.15	$2 \cdot 10^{-3}$

It is important to underline that the reference wave here selected might not be the most convenient in the perspective of the design of a full scale plant. In fact, according to the studies carried out by Falnes and Budar, the design wave should be identified taking into account the boundaries defined by the amount of energy available in the site and the maximum energy that can be harvested by the converter[30][44][45][117].

Despite that, the methodology used to design and test the 1:45 and 1:12 scale PeWEC devices, reported in the current Chapterand in Chapter 5, can be considered of general validity and thus applicable with any desired reference wave.

Once the reference irregular sea state is chosen, the equivalent regular wave parameters can be derived according to the iso-energetic approach. The latter is based on the following hypothesis:

$$\begin{cases} WPD_{reg} = WPD_{irr} \\ Te \cong T \end{cases} \tag{4.2}$$

From Eq. 4.2 results that, in order to maintain constant the *WPD*, it is necessary to determine the proper value of regular wave height. Remembering the expressions of regular and irregular wave power densities (Eq. 3.49 and Eq. 3.57 respectively), the desired regular wave height is:

$$
\begin{cases}
H = \sqrt{0.49}H_s \\
T = T_e \\
WPD_{reg} = WPD_{irr}
\end{cases}
\tag{4.3}
$$

In Table 4.1, the properties of most energetic and recurrent wave are summarized, as well as the corresponding regular waves.

4.3 The prototype

The PeWEC 1:45 scale prototype is composed by a floating hull, a frame that supports the electrical generator and the pendulum. The latter is directly connected to the electrical generator shaft. The device has been designed considering the same floater geometry used for the 1:45 ISWEC prototype, with the aim to have common element for the comparison of the two technologies. Fig. 4.3 shows the prototype deployed in the wave basin.
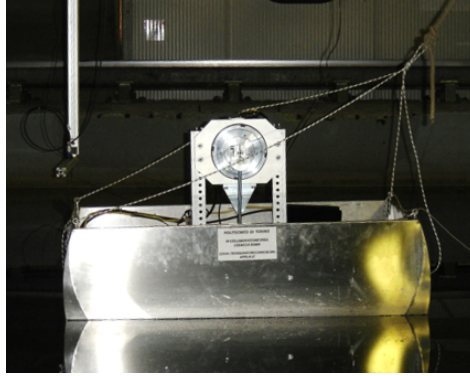
Fig. 4.3 1:45 PeWEC scale device.

Inside the floater, other equipment fundamental for device operation and monitoring are located. In particular, the prototype is equipped with different sensors for the estimation of the hull movements, PTO torque, pendulum position and angular velocity and the electric generator control unit.

The signals coming out from sensors are logged through a data acquisition system and transferred via WiFi connection to the monitoring station. The monitoring station is basically constituted by a laptop equipped with a graphical user interface that

allows to manage the data storage and more in general the entire device electronic equipment. For instance, from the graphical user interface it is possible to modify the PTO control damping or to disable the generator in case of emergency.
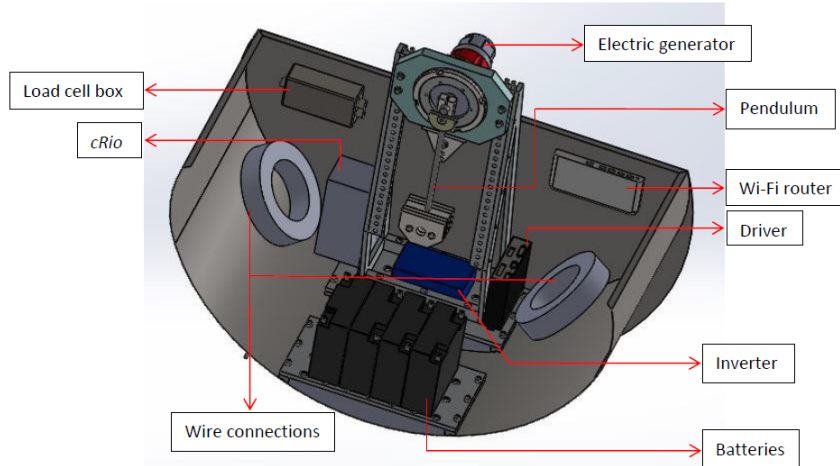
Fig. 4.4 3D CAD model of the 1:45 PeWEC device.
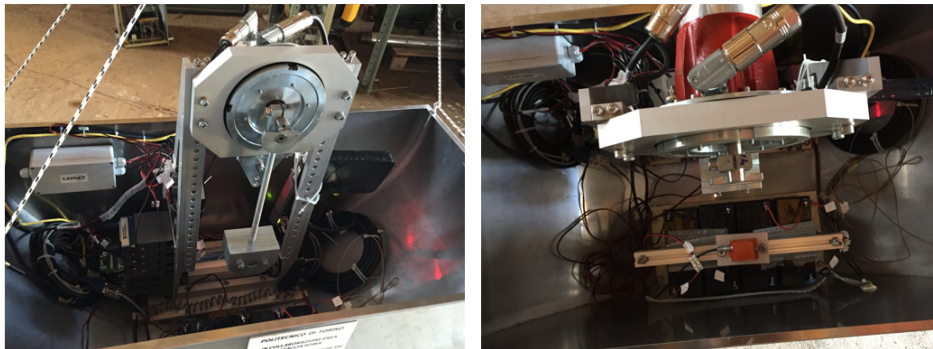
Fig. 4.5 1:45 PeWEC scale device, internal view.

The prototype is battery supplied and this feature, together with the WiFi data transmission, allows to eliminate cables that may affect the prototype dynamics. On the other hand, the total integration of the control systems inside the device required a rigorous study of the components location, in order to reach a proper balancing of the structure, as well as a correct moment of inertia and center of gravity position. The latter are fundamental for the definition of the floater resonance period, that needs to be close to the design wave period. The design of the system layout has been performed through a 3D CAD model of the prototype and equipment installed inside. Fig. 4.4 shows the rendering of the 3D CAD model, while in Fig. 4.5 the

internal view of the real 1:45 scale device is reported. In the next paragraphs, a detailed description of the 1:45 scale prototype components is given.

4.3.1 Floater

The hull is made of stainless steel sheets (1 mm thick) welded together, in order to take the shape designed. The floater is constituted by a central cylindrical section with radius of 0.52 m and 0.505 m wide. It is also provided with two vertical wings that help the stabilization and the alignment of the device with respect to the incoming wave. The total mass of the floater structure is of 48 kg.

As described in Chapter 3, the system needs to be kept in place through a mooring system. To accomplish this task, four holes have been made on each wing of the hull, equidistant in angular direction. Through the holes a threaded rod has been set, put in pretension by a bracket in order to avoid any elastic response. Changing the position of the threaded rod, it is possible to study the mooring influence on the system dynamics. In Fig. 4.6, the layout of the mooring connection point is depicted.

Fig. 4.6 1:45 PeWEC scale device mooring connection system.

4.3.2 Frame

The frame is bolted on the hull and supports a plate where the PTO is settled. The frame is made of ionized aluminum components joined by screws. In Fig. 4.7, the frame installed on the hull is represented.

Fig. 4.7 1:45 PeWEC scale floater with frame installed inside.

Moreover, it offers a 22 different settings for the PTO vertical position, however only 16 of these are available when the longest configuration of the pendulum is considered. Changing the position of the electrical generator, it is possible to modify the distance between the pendulum hinge and the hull COG.

4.3.3   Floater movement sensor

The floater has been equipped with a inertial platform for the monitoring of its motions, in particular the pitching motion. More in detail, the *MTi* device has been used. It offers the possibility to measure the accelerations along the three Cartesian coordinates, as well as the rotations along such coordinates. The accelerations measured are referred to the floater coordinate system, thus they are not suitable to identify the motions with respect to a global reference frame. For this purpose it is required a motion tracking system.

The *MTi* has been fixed inside the floater, orientating the device reference frame according to the definitions given in Chapter 3. In Fig. 4.8, a detail of the *MTi* inside the PeWEC prototype is proposed.
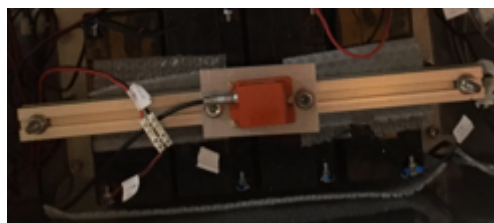
Fig. 4.8 *MTi* inertial platform installed inside the device.

4.3.4   Pendulum

Pendulum is the component that develops the mechanical energy, which is converted in electrical by the PTO. It is made by a mass composed by 5 blocks hold together by a couple of screws. The central block of the mass is provided with a threaded hole, which engages on the threaded pendulum rod. On the opposite end of the rod, a plate for the pendulum clamping on PTO shaft is fixed. More in detail, the rotation is guaranteed not only by the clamping force but also by a key. On the locking plate, it is also possible to fix a disk provided with a groove, that allows to adjust its position with respect to the pendulum hinge and therefore the overall inertia of the pendulum. Fig. 4.9 shows the pendulum completed with the inertial disk.
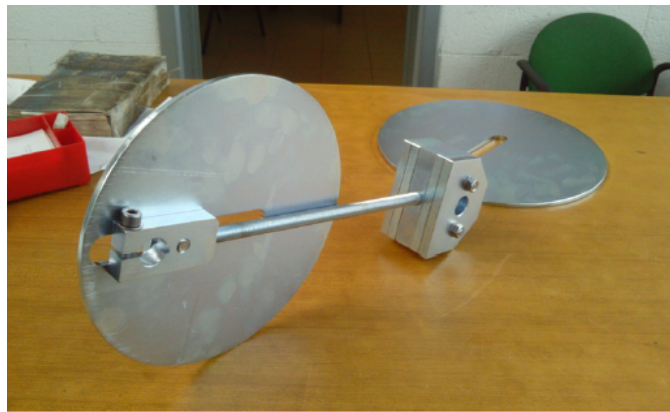
Fig. 4.9 Pendulum with two inertial disks of different dimensions.

The settings available to set the pendulum properties are the following:

- *Pendulum mass*: it can be selected between 1, 2 or 3 *kg*;

- *Rod length*: if the inertial disk is not installed, it is possible to set the pendulum length between 94 and 334 *mm*. Obviously, if the inertial disk is mounted, the shortest length cannot be reached. In this case the shortest length depends on the position selected for the inertial disk;

- *Inertial disk position*: the disk position with respect to the pendulum hinge can be adjusted according to the groove length equal to 125 *mm* and the pendulum length.

In Table 4.2, the mass and inertial properties of the pendulum components are summarized.

Table 4.2 Mass and inertial properties of the pendulum components.

Description	Value	U.M.
Masses block		
Mass	1, 2 or 3	*kg*
Inertia	$1.2 \cdot 10^{-3}, 2.5 \cdot 10^{-3}$ or $3.7 \cdot 10^{-3}$	kgm^2
Rod		
Mass	0.309	*kg*
Inertia	$5.6 \cdot 10^{-6}$	kgm^2
Distance for inertia transfer	0.21	*m*
Locking plate		
Mass	0.273	*kg*
Inertia	$1.52 \cdot 10^{-4}$	kgm^2
Distance for inertia transfer	0.015	*m*
Inertial disk		
Mass	1.81	*kg*
Inertia	0.0124	kgm^2
Distance for inertia transfer	$0 - 0.125$	*m*

Considering the parameters reported in Table 4.2, it is possible to write the expression that allows to calculate the total pendulum inertia, with respect to its rotation center. The analytical equation is the following:

$$I_A = I_{G,mass} + m_{mass}d_{mass}^2 + I_{G,rod} + m_{rod}^2 +$$
$$I_{G,lock} + m_{lock}d_{lock}^2 + I_{G,disk} + m_{disk}d_{disk}^2 \tag{4.4}$$

The natural period of the compound pendulum under the hypothesis of small oscillations is:

$$T_n = 2\pi \sqrt{\frac{I_A}{m_p g l}} \tag{4.5}$$

Where I_A is the total inertia of the pendulum calculated with respect to the pendulum hinge, m_p its mass and l its length. The latter is calculated as the distance between the hinge and the COG position of the complete pendulum.

During experimental tests, the inertial disk has not been installed. Thus, taking into account this simplification, it has been possible to represent the overall inertia and natural period as a function of the pendulum mass and length, according to Eq. 4.4 and Eq. 4.5 (see Fig. 4.10).
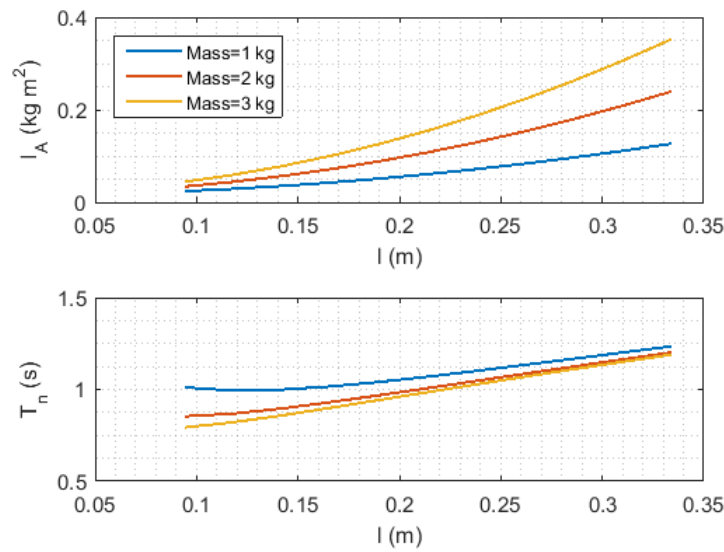
Fig. 4.10 Pendulum inertia and natural period as a function of the pendulum mass and length.

4.3.5 Power Take Off (PTO)

The conversion of mechanical energy into electrical is achieved by means of a electrical generator. The stator of the generator is fixed on the frame, while its shaft is directly connected to pendulum.

The generator used for this application is a synchronous brushless motor with permanent magnets, developed by the *Motor Power Group*.

The *SKA DDR* motor is designed to drive directly the mechanic load connected to the shaft. In this way, it is possible to avoid the use of gearboxes and to eliminate the problems due to backlash of a gearbox. Furthermore, this kind of electrical motor is equipped with an encoder that allows to control it in position and in velocity [78].

In Fig. 4.11, the rear view of the PTO mounted on the frame is shown, while in Table 4.3 the main features of the *SKA DDR 090.60.3,5* are summarized [78].
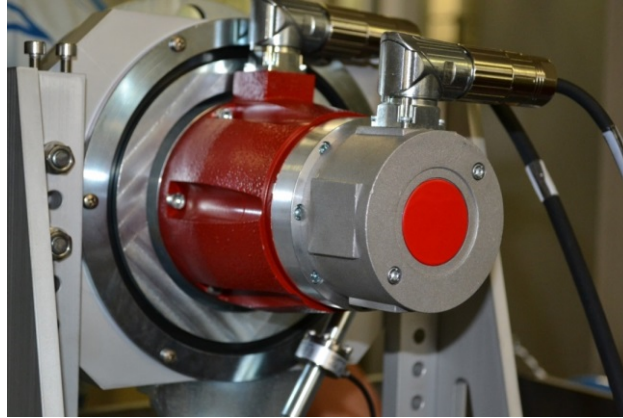
Fig. 4.11 PTO installed on the frame.

Table 4.3 SKA DDR 090.60.3,5 main features.

Description	Symbol	Value	U.M.
Rated torque	T_{rated}	3.5	*Nm*
Maximum torque	T_{max}	28	*Nm*
Rated speed	n_{rated}	90	*rpm*
Maximum speed	n_{max}	1200	*rpm*

4.3.6 Load cell

The PTO torque is measured through a load cell installed between the flange that support the PTO stator and the plate fixed on the frame. The flange is decoupled from the frame through a bearings. Therefore the load cell locks the bearing movement and acts as constraint. Fig. 4.12 shows a detail of the torque measuring system.

The *Leane UMM* load cell has a rated capacity of 10 *kg* [63] and has been is equipped with two spherical joints, in order to guarantee only the axial force transmission. The spherical joints were adjusted so that the load cell axis is tangent to the PTO flange. In this way, the arm used for the evaluation of the torque corresponds to the distance between the PTO axis and the axis of threaded pin on the PTO's flange, where one of the spherical joints of the load cell is locked. This
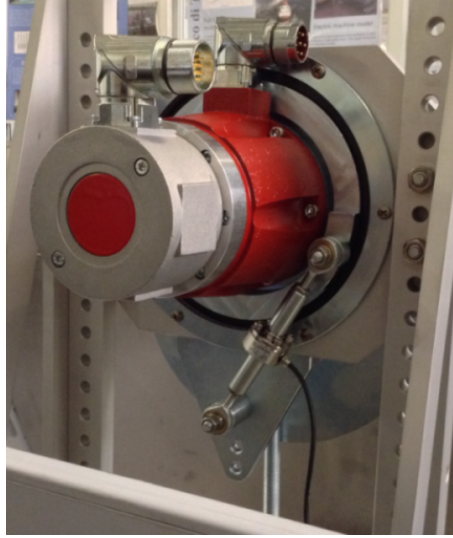
Fig. 4.12 Load cell installed on the PTO support frame.

distance is equal to 70 *mm*. It is important to underline that the measured torque include also the torque due to the friction losses on the PTO shaft.

The load cell is connected to its conditioner, which amplify and transform the Wheatstone bridge signal into standard signal, in the $\pm$ 10 *V* range. The conditioner requires a 24 *V DC* power supply.

4.3.7   Digital servo drive, PTO control and data logging system

The PTO is controlled in order to obtain a braking torque proportional to the pendulum speed. The proportionality is managed through the PTO damping coefficient c, as expressed by Eq. 4.6.

$$T_\varepsilon = c\dot{\varepsilon} \tag{4.6}$$

The control law has been implemented through the *National Instrument CompactRio* system (*NI cRIO*). The *NI cRIO* is a real-time embedded industrial controller, that can be used as headless system (without a user interface) or it can be connected to a host PC for supervisory purposes and displaying logged data. It is mainly composed by four parts:

- *Real-time controller*: a powerful processor with a wide range of clock frequencies for implementing the control algorithm;

- *Re-configurable I/O modules*: the *NI cRIO* can be equipped with a wide variety of input/output modules, that can be personalized according to the input/output signals that need to be managed. In the case of this work, the *NI cRIO* has been equipped with the following modules:

  - *Analog input module*: acquisition of the PTO load cell signal in the ± 10 *V* range;

  - *Digital I/O module*: the input pins have been used to acquire the digital signal coming from the PTO encoder, while the output pins have been used to generate a digital signal for the trigger activation. The trigger allows to synchronize the data logging between the *NI cRio* and the wave basin probes, by generating a TTL digital signal; this aspect will be described more in detail in section 4.4.2;

  - *Serial port module*: allows to manage the serial protocol communication between the drive and the *NI cRio* for the management of the reference torque. Moreover, this module has been programmed in order to acquire the *MTi* signals.

- *FPGA module*: used for implementing low level logic on the data acquired using the I/O modules. The *FPGA* is connected to the real-time controller by a *High-Speed PCI Bus*;

- *Ethernet Expansion chassis*: the Ethernet port can be used for connecting the *NI cRio* to a host PC, on which it is possible to implement a personalized user interface for the system monitoring.

In Fig. 4.13, the *NI cRio* during the installation phase is depicted.

The PTO is connected to the digital servo drive that receives a command from the *NI cRio* serial port module; the reference signal is proportional to the torque that needs to be generated. As described by Eq. 4.6, it is a function of the pendulum angular velocity, which is measured by the encoder and transmitted to the *NI cRio* through the serial communication protocol. Moreover, the digital servo drive is equipped with an external braking resistor, that allows to dissipate the power produced. The

Fig. 4.13 NI CompactRio and its modules during the installation into the prototype.

resistor is required since the digital servo drive is not a reversible converter, therefore it cannot manage the reverse power flow that arise when the servomotor works as a generator.

Fig. 4.14 shows the digital servo drive *MOTOR POWER FLEXI PRO 1D5* used for the management of the servo motor *SKA DDR* and the external breaking resistor.

Fig. 4.14 Digital servo drive and braking resistor.

The latter is required to dissipate the extra-voltage induced on the digital servo drive DC bus, when the motor is acting as a brake.

The digital servo drive is a AC/DC–DC/AC converter: it is composed by a rectifier (AC/DC) and an inverter (DC/AC), connected through to a DC bus. The latter is constituted by a series capacitors. The AC stage of the rectifier is connected to the power supply (e.g. 230 V ac), while the AC stage of the inverter is connected

to the motor. Moreover, the DC/AC converter is a reversible device, therefore the power flow can travel from the DC bus to the motor and vice-versa. On the other hand, the AC/DC converter is a non-revesible device, thus it cannot accept a power flow travelling from the DC bus to the AC power supply.

For this reason, when the motor is acting as a brake, an extra voltage is generated on the DC bus connecting the AC/DC and DC/AC converters. Since the DC bus voltage is limited by the capacitors breakdown voltage, the extra-voltage needs to be dissipated through a resistor.

Lastly, the *NI cRio* is connected to a router WiFi, that transmits data to a laptop. The latter allows to manage and visualize the signals thanks to a customized front panel (user interface) programmed in the *National Instruments LabView* environment. The frequency sampling of the data logging has been set at 50 *Hz*.

4.3.8   Power supply system

The prototype has been designed to be completely autonomous from the energetic point of view, thus no external connections are required. As described previously, this feature allows to avoid the undesired interaction of cables, that may interfere with the prototype dynamics. Therefore, it has been equipped with four 12 *V DC* batteries, with a capacity of 18 *Ah* each. More in detail, batteries have been organized in two different packs: the first battery pack is composed by two elements connected in series, generating the 24 *V* voltage. It supplies the *NI cRio*, *MTi* and load cell conditioner. The second battery pack is used to generate the 12 *V DC* voltage. The batteries are connected in parallel and the total capacity of the pack is of 36 *Ah*. The battery pack *DC* voltage is converted into the 230 *V ac* 50 *Hz* voltage, required for the PTO drive and router WiFi supply. The voltage conversion is performed thanks to a *DC/AC* converter.

4.3.9   Mooring system

The mooring line has been built according to the scheme described in section 3.4: it is composed by three segments of a metal chain, a submerged buoy and a steel block. In Table 4.4, the mooring components properties are summarized.

Table 4.4 Mooring components features.

Description	Symbol	Value	U.M.
Chains			
Chain mass per unit of length	m_l	0.037	$\frac{kg}{m}$
First chain section length	l_1	2	m
Second chain section length	l_2	0.4	m
Third chain section length	l_3	2	m
Jumper			
Net buoyancy force	F_b	15.4	N
Mass			
Net weight	F_g	8.4	N

4.4   Experimental campaign

4.4.1   Testing facility

The test campaign has been carried out in May 2015 at the INSEAN towing tank, in Rome. The towing tank used for the experimental campaign on PeWEC is 220 *m* long, 9.0 *m* wide and 3.5 *m* deep, as shown in Fig. 4.15 [56].
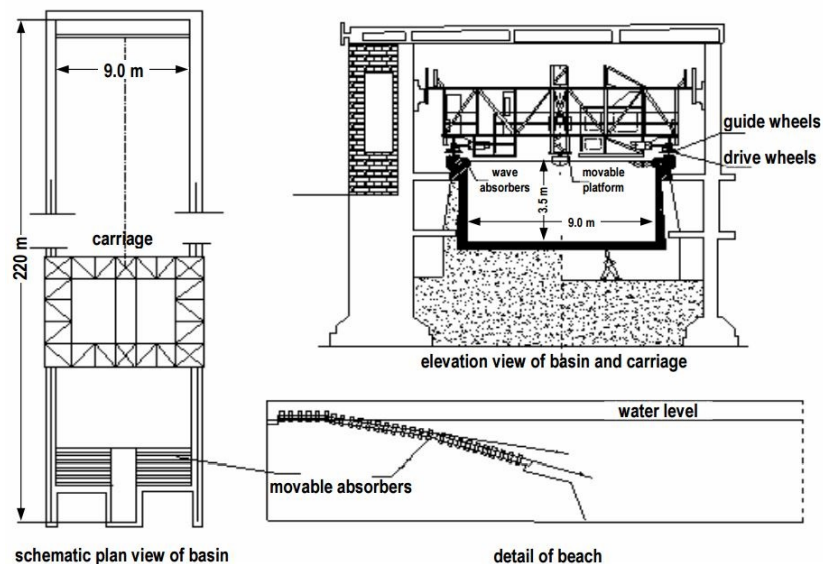
Fig. 4.15 INSEAN wave basin detail.

The generation of the waves is guaranteed by a one-side flap-type, 9 *m* wide, electro-hydraulically powered wave maker. The flap is moved via 3 pumps of 38.5 *kW* total power and controlled by a 100 harmonic components electronic programming device, in which is possible to modulate each harmonic both in amplitude and frequency. The wave maker is able to generate regular waves from 1 to 10 *m* in length, with corresponding height from 100 up to 450 *mm* and irregular waves according to any desired sea spectrum condition in appropriate scale. The absorber, placed on the opposite side of the wave tank with respect to the wave maker, is constituted by two crossed layers of square tubular equally spaced. The towing tank is also equipped with two movable carriages.

4.4.2   Experimental set-up

Wave basin

The 1:45 scale PeWEC device has been deployed in the wave basin and moored through its mooring system on the seabed of the towing tank. The attachment point is constituted by a reinforced concrete dead body. The latter has been positioned at 60 *m* from the wave maker, assumed as reference (0 *m*) (see Fig. 4.16).
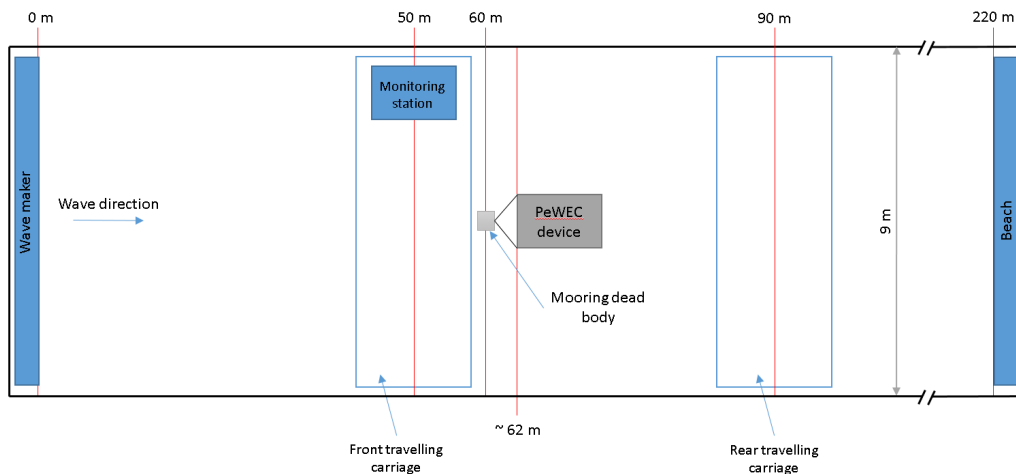
Fig. 4.16 Experimental set-up scheme.

During the operating conditions, the bow of the hull was, on average, between 60 and 62 *m* from the wave maker.

The distance of the prototype from the wave maker has been chosen in order to guarantee a sufficiently long time span exempt from wave reflections phenomena. The latter is very important for the identification of the WEC performances.

More in detail, the relation between the WEC position in the wave basin and the useful time interval can be determined calculating the wave phase velocity, that in deep water conditions results be:

$$c_g = \frac{gT}{2\pi} \tag{4.7}$$

Once the phase velocity is known, it is possible to determine the instant of time when the wave reaches the device (t_1) and the beginning of the wave reflection phenomena (t_2) (instant of time where wave reaches the absorber). The difference corresponds to the test time interval (t_u). Table 4.5 summarizes the results related to the set-up proposed in this work.

Table 4.5 Useful time span exempt from wave reflection phenomena, as a function of the wave period.

T (s)	$c_g\left(\frac{m}{s}\right)$	$t_1(s)$	$t_2(s)$	$t_u(s)$
1	1.56	38.4	243.4	205.0
1.1	1.72	34.9	221.3	186.3
1.2	1.87	32.0	202.8	170.8
1.3	2.03	29.6	187.2	157.7
1.4	2.19	27.4	173.8	146.4

One of the two carriages available has been placed in front of the device under investigation and used as monitoring station: here all the equipment required for the system controlling and data logging have been housed. Furthermore, the probes for wave monitoring have been fasten on this carriage, according to the layout shown in Fig. 4.17.

In particular, two typologies of probes have been used: capacitive probes (*c*) and ultrasonic probes (*u*). A capacitive probe (*2c*) has been placed around 6 *m* in front of the device around the center line of the wave basin, with the aim to measure the profile of the undisturbed wave field, while the other capacitive probes available have been distributed in the area in front of the device as depicted in Fig. 4.17. Alongside probes *7c*, *1c*, *8c* and *6c*, the ultrasonic probes *1u*, *2u*, *3u* and *4u* have
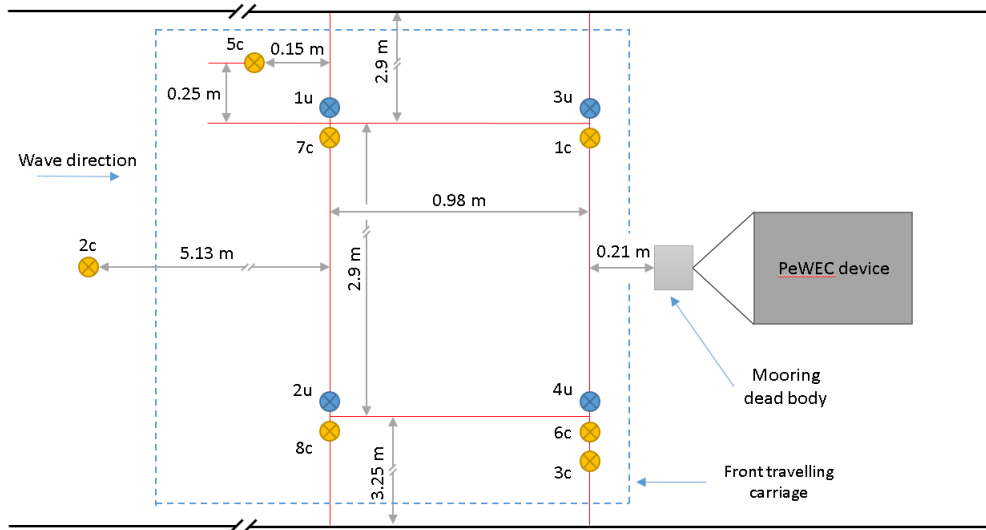
Fig. 4.17 Experimental set-up scheme detail.

been positioned. The two typologies of probes used are managed by two different data logging systems, synchronized via a TTL trigger signal given, at the begin of each test, by the on board PeWEC control system.

Prototype configuration

As previously described, the prototype offers a wide variety of settings. The set-up chosen for the prototype is summarized in this section.

The floater mass, including all the electronic apparatus and pendulum, amount to 78 kg, that corresponds to a draft of 245 mm. The PTO has been placed in the highest position available and the overall pitch moment of inertia with respect to the floater COG is equal to 7.22 kgm^2. The COG is 50 mm below the water plane and taking into account the PTO positioning, the distance between the COG and the pendulum hinge amount to 0.476 m.

The pendulum mass has been chosen equal to 3 kg, the inertial disk has not been installed, while the pendulum length has been tuned at 0.334 m, that leads to a 1.18 s resonance period (see Fig. 4.10).

Lastly, the mooring line has been connected to the point closest to the bow, that guarantees the maximum floater alignment action.

4.4.3   Regular wave tests

Regular waves or monochromatic tests constitute an important part during the development program of a Wave Energy Converter. This kind of tests provide an indication of the device behavior and the main results that can be obtained are the validation/calibration of the mathematical models, the representation of the frequency domain response operator and the evaluation of the higher order effects in finite waves [39].

For this reason a set of regular waves has been designed taking into account, from one side, the characteristics of the design wave and to the other, the capabilities of the testing facility wave maker and of the device dynamic response. Regarding the wave maker capabilities, as described in section 4.4.1, it is able to generate wave with a minimum height of 100 *mm*, value not suitable for the sea state conditions required (40 *mm*). Because of that, the wave maker controller has been tuned in order to obtain the desired wave height, even if the calibration procedure did not allowed to generate wave height lower than 50 *mm*. The wave height difference between the theoretical value and the obtained one has been considered acceptable. In fact, it is important to remark that the test campaign on the 1:45 scale device has the main goal to validate the WiFi data logging system, that needs to be implemented on the 1:12 scale device.

Table 4.6 summarizes the regular wave conditions used for the 1:45 scale PeWEC tank testing.

Table 4.6 Regular wave set used for the 1:45 scale device experimental testing.

Code	$H\ (m)$	$T\ (s)$	$WPD\ \left(\frac{W}{m}\right)$
A	0.05	1	2.5
B	0.05	1.1	2.7
C	0.05	1.2	3
D	0.05	1.3	3.2
E	0.05	1.4	3.5

Moored system Response Amplitude Operator

The first part of regular tests concerns the estimation of the moored system Response Amplitude Operator, that as defined in section 3.3.3, describes the dynamic response

of a floating structure with respect to the frequency of the incoming wave (see Eq. 3.44).

As stated before, the resonance of the hull must be close to the period of the design wave, in order to achieve the maximum power extraction. The optimal ballast positioning inside the floating structure has been determined through a 3D CAD software, during the design phase. Such positioning has been properly replicated during the experimental activity.

The pitch degree of freedom RAO has been experimentally determined tilting the floater with the regular waves from A to E given in Table 4.6, while the internal pendulum has been kept locked. Since the floater has not been equipped with a motion tracking system, surge and heave RAOs have not been determined. The wave duration of each test has been fixed at 300 s

The wave and pitch records have been elaborated in the following way:

- Signal filtering with a zero-phase digital filter. This operation is required in order to remove noise that eventually can occur during data logging;

- Considering the wave elevation time record, a useful interval is chosen. The latter is selected excluding the initial transient and the beginning of the reflection, according to the indications reported in Table 4.5. The time interval determined previously is used to truncate the pitch time record;

- Both wave and pitch truncated time series are elaborated with the aim to obtain an entire number of cycle (at least 10);

- Wave period and wave height are identified by analyzing the wave profile through the FFT algorithm. The same methodology is uses to identify the pitch motion amplitude. Moreover, in the case of the pitch motion also minimum, maximum, average and root mean square values are calculated.

As example, in Fig. 4.18, the complete wave and pitch records at s are depicted, while Fig. 4.19 shows wave elevation and pitch motion filtered and truncated over 10 cycles.

Lastly, in Fig. 4.20, the experimental pitch RAO is reported, proving that the floater is very reactive around 1.2 s, wave period assumed as approximation of the
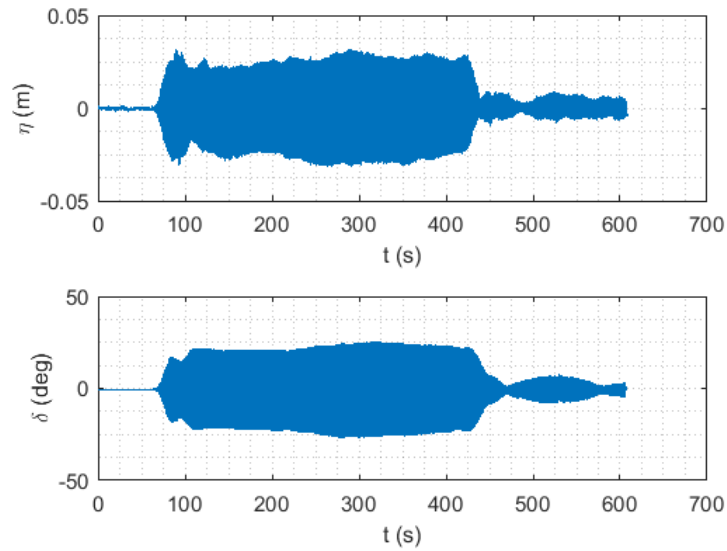
Fig. 4.18 Wave elevation (top) and pitch motion (bottom) records for the 1.2 *s* wave period test.
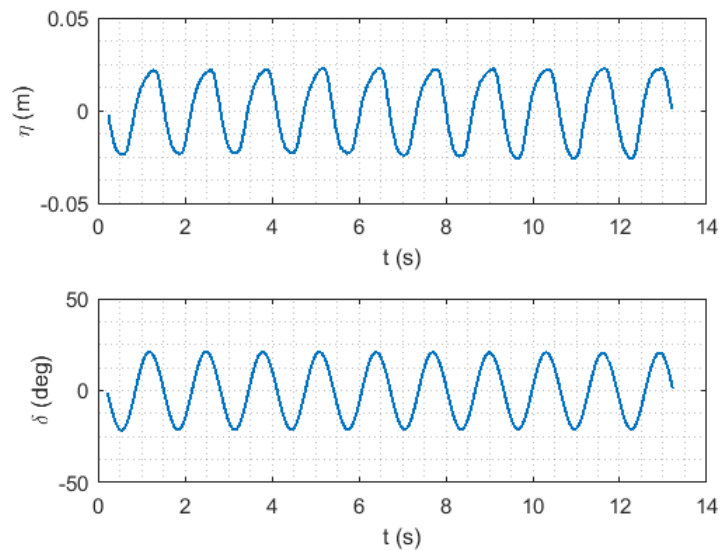
Fig. 4.19 Filtered and truncated wave elevation (top) and pitch motion (bottom) records, for the 1.2 *s* wave period test.
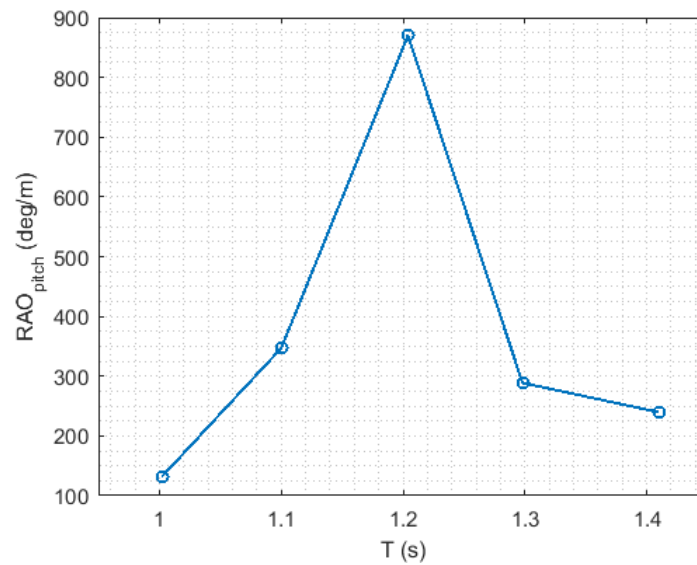
Fig. 4.20 1:45 scale PeWEC device pitch RAO.

design wave period of 1.15 s, determined according to the calculations reported in section 4.2.

Frequency sweep

The second part of the regular wave tests has been developed with the aim to both investigate the device frequency domain performances and data logging system functionality, when the pendulum is able to swing inside the floater and the PTO control is activated.

Similarly to the RAO tests, the PeWEC frequency domain response has been determined tilting the floater with waves from A to E given in Table 4.6 and imposing a PTO damping coefficient equal to 0.5 $\frac{Nms}{rad}$. In this case, the following physical quantities have been monitored:

- Pendulum angular position and velocity;

- PTO reference torque, given by the digital servo drive;

- Load cell voltage, for the estimation of the overall PTO torque, including the bearings friction.

Data have been elaborated according to the methodology described previously in section 4.4.3 and extending the procedure to all the measured quantities.

Starting from the analysis of the pitch motion, the floater presents a peak of the frequency response between 1.2 and 1.3 s wave period, as shown in Fig. 4.21.
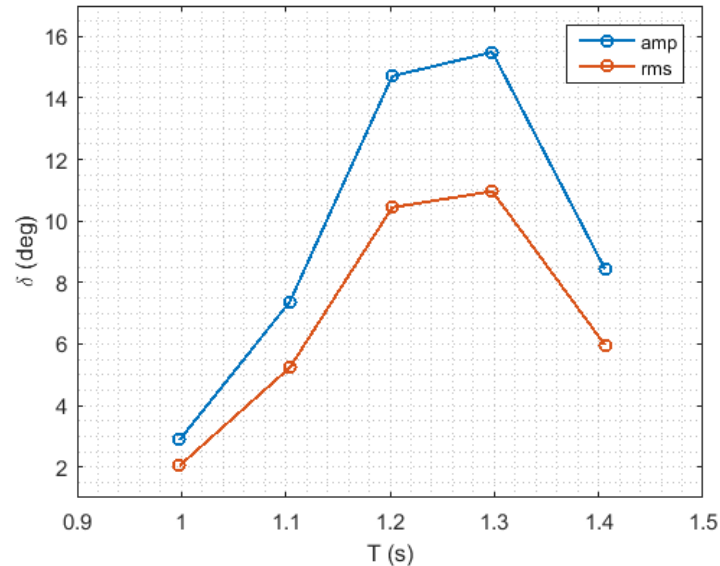
Fig. 4.21 1:45 PeWEC device pitch frequency response with unlocked pendulum.

Furthermore, Fig. 4.21 shows both pitch motion root mean square and amplitude, as a function of the wave period.

The peak is not well defined since the wave period discretization is sparse, however it is possible to assume that the peak should be at around 1.25 s wave period. The variation of the floater resonance period with respect to the locked pendulum case, is due to the action of pendulum, that reduces the floater pitch hydrostatic stiffness. This consideration can be clearly seen taking into account the linear model equations (Eq. 3.77 and Eq. 3.78) and the definition of the pendulum restoring matrix (Eq. 3.29).

Fig. 4.22 summarizes the pendulum angular position and velocity and the PTO torque imposed through the digital servo drive on the base of the proportional control law. The pendulum angular displacement coordinate shows a maximum in correspondence of the 1.2 s wave period, proving that the tuning of floater and pendulum has been correctly carried out, achieving a resonance in correspondence

of the design period. The same consideration is valid for pendulum angular velocity and PTO torque.
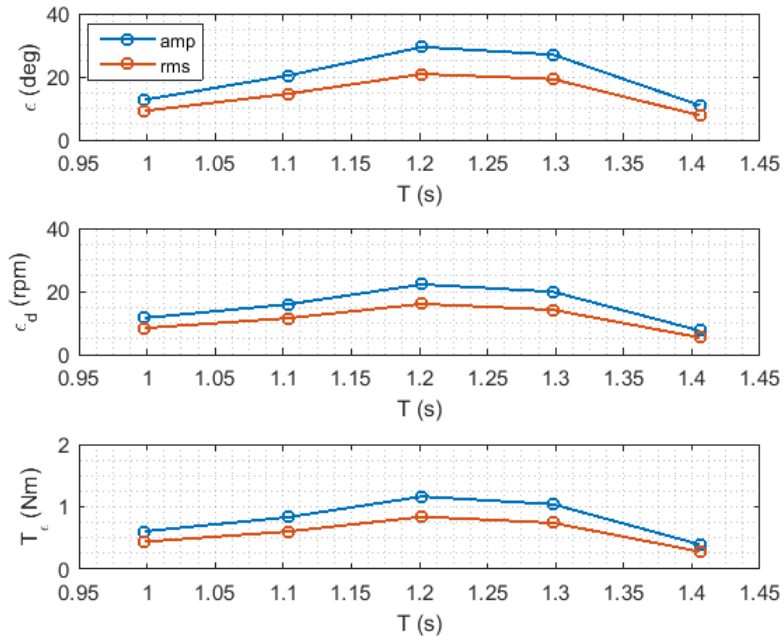
Fig. 4.22 1:45 PeWEC device pendulum motion and PTO torque as a function of the wave period.

The PTO torque has been compared with the torque estimated through the load cell, aiming to determine the entity of the generator bearings friction. In Fig. 4.23, the comparison between the amplitude values of the torques considered is represented. More in detail, it is possible to see that friction torque becomes relevant near resonance condition, representing the 13% of the reference torque. On the other hand, in correspondence of 1, 1.1 and 1.4 s wave periods, friction torque is not significant (less than 5% of the reference torque). In the case of small scale prototypes, friction forces can be relevant and may influence the device dynamics. For this reason, a greater device scaling factor is generally preferred for a more reliable assessment of the technology performances.

In Fig. 4.24, a detail of the reference and load cell torque records evaluated at 1 and 1.3 s wave period tests are reported, highlighting the effect of the friction torque due to PTO bearings, varying the motion frequency, discussed above.

Lastly, the average extracted power has been computed and represented as a function of the wave period (see Fig. 4.25). Note that the power extracted from
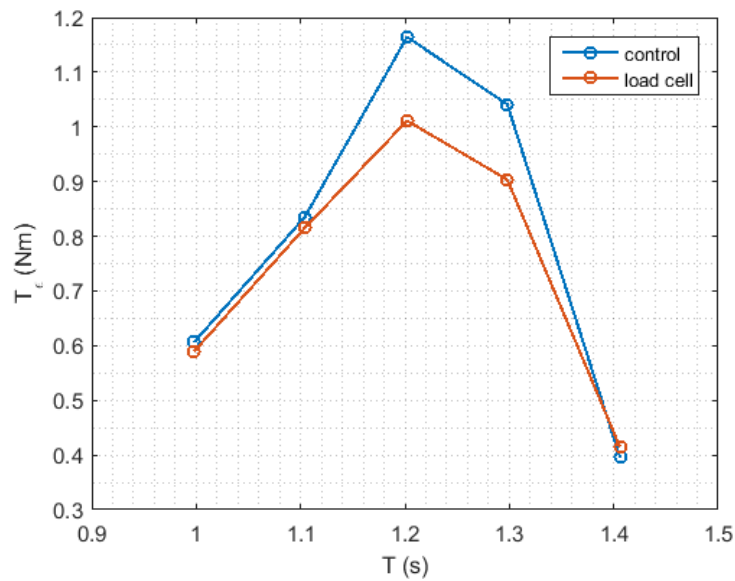
Fig. 4.23 Comparison between reference torque (control) and estimated torque (load cell) as a function of the wave period.
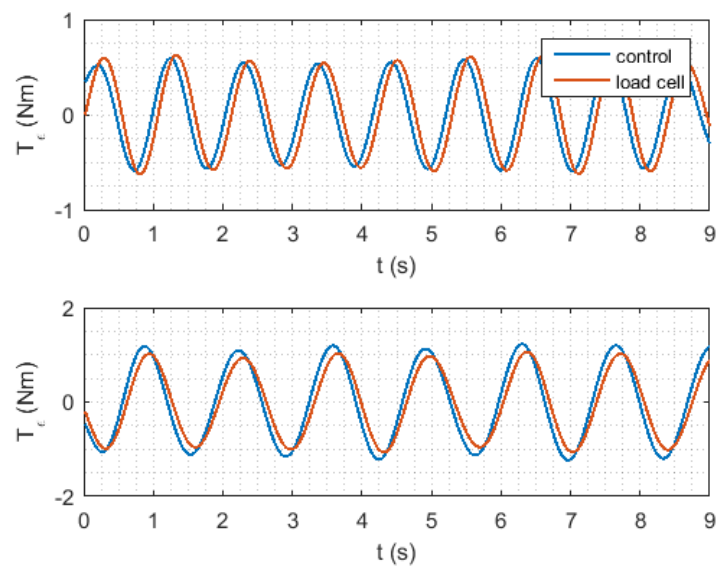
Fig. 4.24 Comparison between reference torque (control) and estimated torque (load cell) at 1 *s* wave period (top) and 1.3 *s* wave period (bottom).
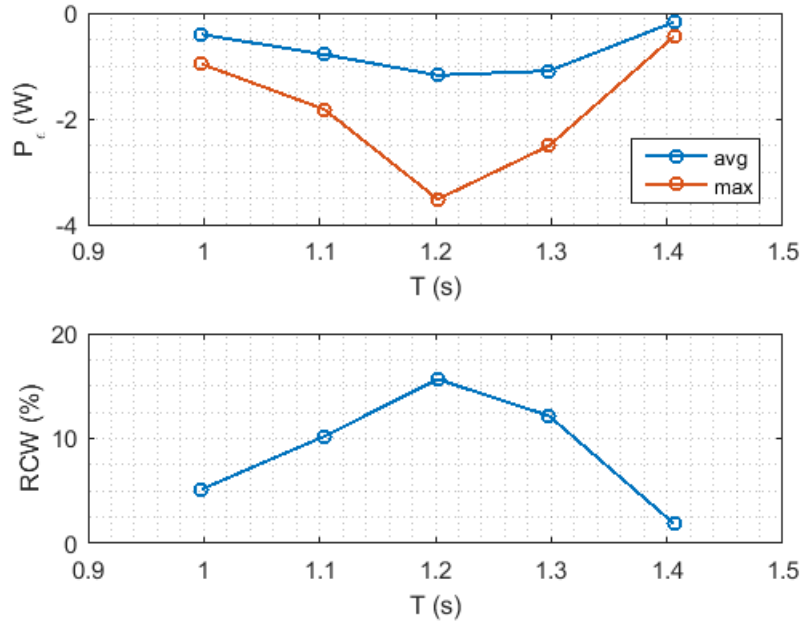
Fig. 4.25 Average and peak PTO power as a function of the wave period.

the PTO is assumed negative, while the power eventually supplied to the PTO is positive. Moreover, together with the average extracted power, the Relative Capture Width (RCW) of the device has been calculated. The latter corresponds to the ratio between the average generated power and the wave power density multiplied by the floater width *W*. The latter results be the power intercepted by the WEC. Thus, the Relative Capture Width defines somehow the overall efficiency of the Wave Energy Converter.

$$RCW = \frac{\overline{P_\varepsilon}}{WPD \cdot W} \tag{4.8}$$

In the case of the 1:45 scale device tests, the maximum average power of 1.2 *W* has been achieved during the test at 1.2 *s* wave period, that leaded to a *RCW* of 15.6%. Moreover, observing Fig. 4.25, it is also possible to see the difference between mean and maximum power: the latter corresponds to the maximum power reached during each pendulum oscillation. This fact can be seen more clearly in Fig. 4.26, where a portion of the power recorded at 1.2 *s* wave period is depicted. These consideration allows to demonstrate that the power flow is not constant in time, thus PTO needs to be designed properly in order to catch power peaks that occur in resonance condition. For instance, in the case of the tests presented in this section,
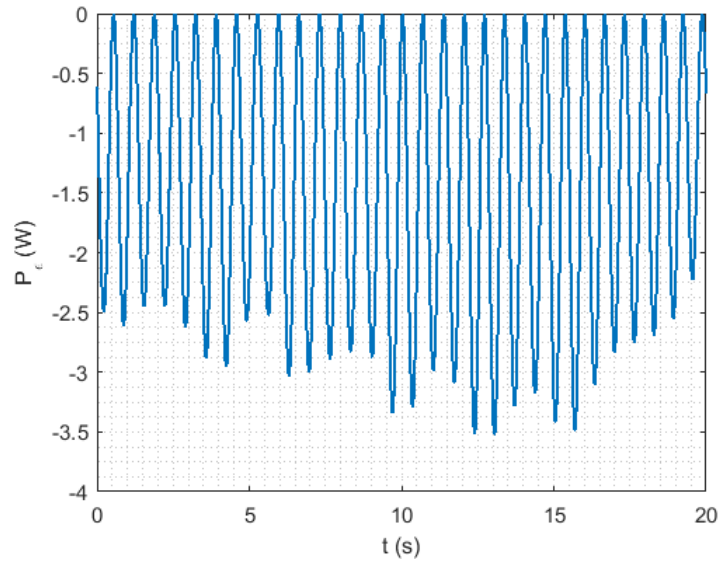
Fig. 4.26 Detail of the PTO power measured during the test at 1.2 *s* wave period.

the peak power reached was equal to 3.5 *W* compared to an average produced power of 1 *W*.

4.4.4 Numerical model validation

The experimental results, obtained from the 1:45 scale prototype testing campaign, have been used to validate the linear numerical model presented in Chapter 3. The reliability verification of the numerical model against experimental data is of primary importance, since it will be widely used for the design of the intermediate scale prototype, reported in Chapter 5. The validation of nonlinear model is proposed in Chapter 6, where a wide set of data coming from the 1:12 scale prototype testing is available, in order to avoid making the discussion cumbersome.

Fig. 4.27, Fig. 4.28 and Fig. 4.29 summarize, respectively, the comparison between numerical and experimental pitch motion, pendulum swinging angle and angular velocity, PTO torque and average extracted power. In the case of the kinematic variables, both root mean square values and amplitude are taken into account.

The numerical model proved to be in good agreement with respect to experimental data, however it is important to highlight that numerical model has been tuned
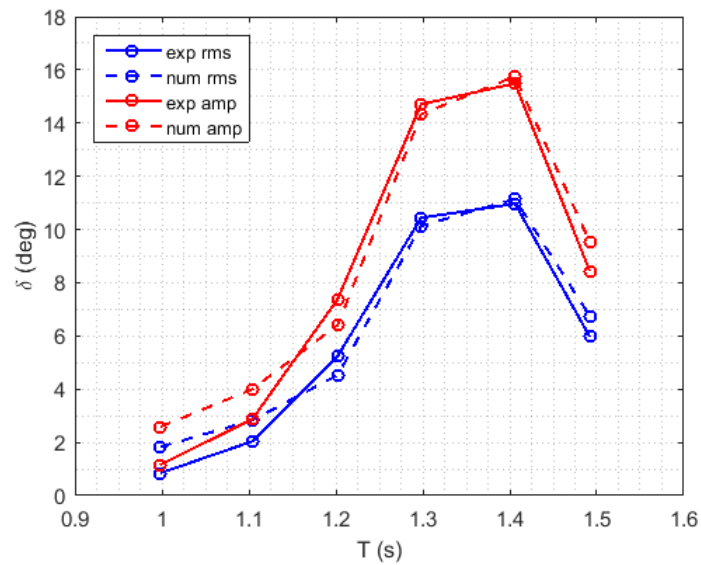
Fig. 4.27 Experimental pitch root mean square value and amplitude comparison against numerical model.
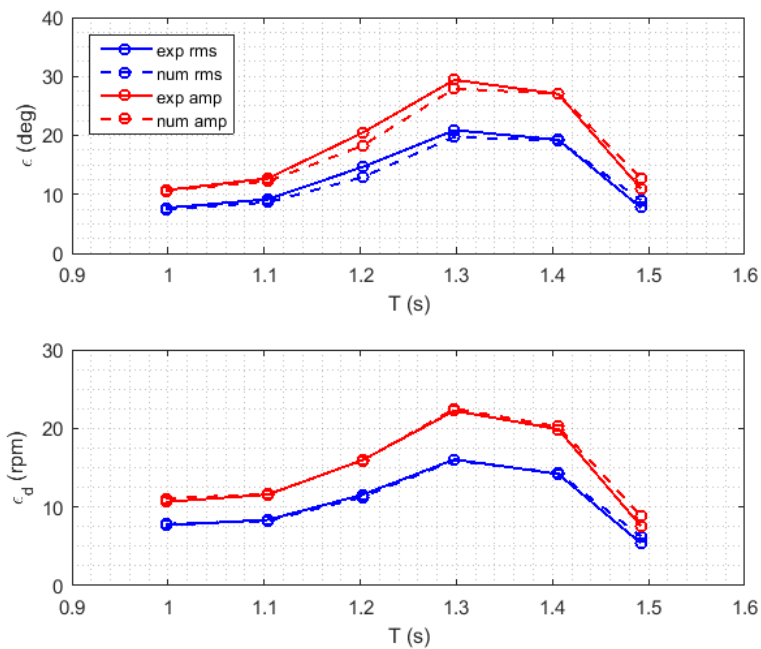
Fig. 4.28 Experimental and numerical pendulum swinging angle (top) and angular velocity (bottom) comparison.
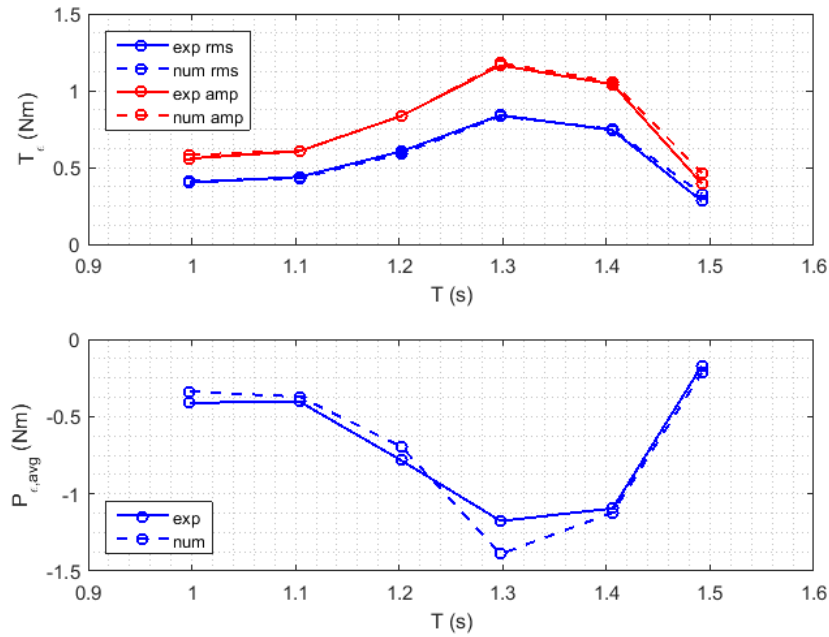
Fig. 4.29 Experimental and numerical PTO torque (top) and average extracted power (bottom) comparison.

introducing the effect of the linearized hydrodynamic viscous damping and the effect of the friction forces acting on the PTO shaft.

More in detail, Fig. 4.30 shows the comparison between experimental and computed pitch motion when the hydrodynamic dissipation are neglected, proving the model overestimation around the system resonance frequency.
Also friction forces have a relevant role, especially in the case of small scale prototypes. In fact, observing Fig. 4.31, it is possible to underline that neglecting PTO bearing friction, even if the hydrodynamic viscous damping is taken into account, an overestimation of the computed pendulum motion and PTO torque is obtained.

4.4.5   Final remarks

The experimental activity performed on the 1:45 scale PeWEC device aimed at a preliminary validation of the numerical models developed in Chapter 3. This step is of fundamental importance before the design of the intermediate scale prototype. Moreover, the 1:45 scale prototype has been equipped with a of WiFi data logging system, used to eliminate cable that may interfere with the prototype dynamics and
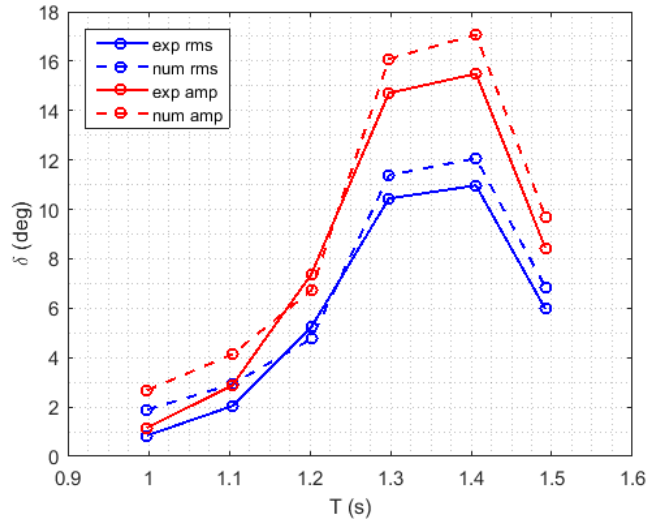
Fig. 4.30 Experimental pitch root mean square value and amplitude comparison against numerical model, without nonlinear viscous damping.
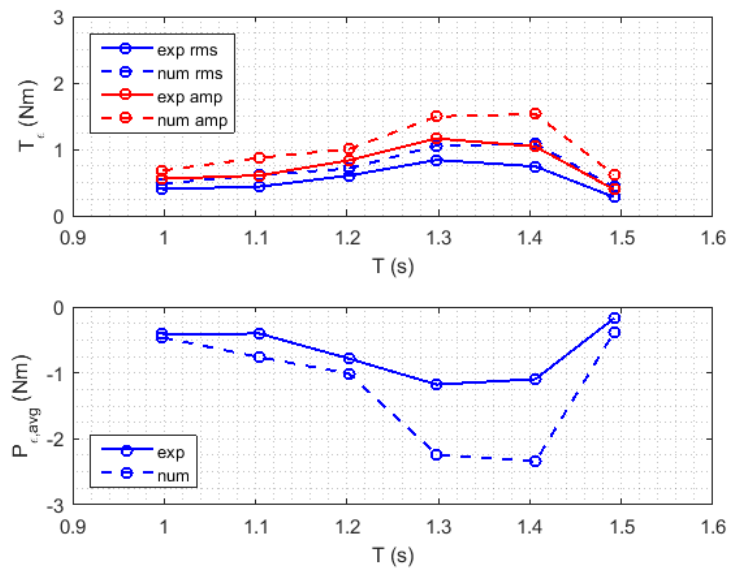
Fig. 4.31 Experimental and numerical PTO torque (top) and average extracted power (bottom) comparison, without friction forces modeling.

able to communicate with the wave basin data logging system (probes and wave maker). The layout here developed constitutes the basics for the development of the intermediate scale device controlling system.

A satisfying agreement between numerical and experimental data has been proved, once the nonlinear hydrodynamic viscous damping is identified, together with the PTO bearings friction. The latter constitutes the 20% of the measured PTO torque, thus they influence considerably the estimation the device performances. In the light of these considerations and according to the guidelines given by EquiMar protocols [54], an intermediate scale device development is required, aiming a better characterization of the technology performances.

Chapter 5

1:12 PeWEC prototype: design and experimental testing

This chapter deals with the design and the experimental testing of the 1:12 PeWEC prototype that, according to the EquiMar protocols [54], it can be classified as the *design prototype* or the *intermediate scale device*. The goal of this development stage should be the device performances verification in realistic seaways, together with a test of the conversion components such as PTO and of structural components like moorings.

Starting from the results presented in Chapter 4, in the first part of this chapter the design methodology adopted for the 1:12 scale prototype development is presented. It is important to highlight that the device design has been based on the numerical models described in Chapter 3 and preliminarily validated against the experimental results carried out during the 1:45 scale prototype tank testing.

Then, simulations results have been transposed into specification that have been used for the identification of the technical solutions required for the prototype mechanical design and for the selection of the electrical and mechanical components required. Moreover, a wide description of the prototype control and monitoring systems is given.

Conversely, the second part of this chapter is concerned with the presentation of the experimental set-up and of the testing campaign performed at the INSEAN wave basin. Four different prototype configurations have been tested starting from the design one, with the aim to determine, from the experimental point of view,

the device performances sensitivity with respect to some of the most significant physical parameters of the device, such as floater pitching inertia, pendulum mass, vertical COG position and pendulum hinge distance. Such configurations have been tested considering both regular and irregular sea states. In particular, irregular waves have been generated scaling down the real time histories acquired during the characterization of the Pantelleria installation site (section 4.1).

Lastly, the various tests performed on the 1:12 scale prototype allowed to outline some consideration about the device tunability with respect to the sea state and to highlight a good agreement (even if from the qualitative point of view) between the behavior predicted trough numerical models and experimental results. A quantitative comparison between experiments and numerical model is reported in Chapter 6.

5.1 Prototype design

5.1.1 Design wave condition and scaling factor

The reference scatter diagram chosen, as described in section 4.1, represents the Pantelleria Island wave climate. According to the observations developed in Chapter 4 for the 1:45 scale device, the most energetic wave properties have been taken into account for the design of the prototype. It is important to remember that the most energetic wave condition was chosen instead of the most recurrent wave, since it leads to a sufficiently high power density, thus to a suitable energy flux for the prototype performances evaluation (see section 4.2).

The first step of the design process, once the design sea state is defined, regards the choice of the scaling factor. The latter is in general defined as the best compromise between the full scale reference sea state condition and wave basin capabilities. The wave basin chosen for the intermediate scale tests is the INSEAN wave basin (Rome, Italy), described in section 4.4.1.
Table 5.1 summarizes the most energetic irregular wave properties and the corresponding iso-energetic regular wave, as a function of the scale factor. The wave properties scaling has been performed according to the Froude scaling law.

The selection of the most appropriate scaling factor, starting from the comparison between wave properties and the INSEAN wave basin capabilities. More in detail,

Table 5.1 Most energetic irregular wave properties and the corresponding iso-energetic regular wave, as a function of the scale factor.

Scaling factor	Irregular wave			Iso-en. regular wave		
	$H_s(m)$	$T_e(s)$	$WPD\left(\frac{kW}{m}\right)$	$H(m)$	$T(s)$	$WPD\left(\frac{kW}{m}\right)$
1:1	2.65	7.75	26.7	1.86	7.75	26.7
1:8	0.33	2.74	0.15	0.23	2.74	0.15
1:10	0.27	84.3	0.084	0.19	2.45	0.084
1:12	0.23	2.24	0.053	0.15	2.24	0.053
1:15	0.18	2.00	0.031	0.12	2.00	0.031

considering the limitation of the wave length of 10 *m*, that corresponds to a 2.5 *s* regular wave period, the 1:8 and 1:10 scaling factors have been excluded.

The 1:12 scale reference wave offers a higher WPD than the 1:15 scale wave, thus it should be preferable. However, its is closer to the upper limits of 10 *m* wave length. Despite that, the wave amplitude is less than the half of the highest wave amplitude that can be generated in the tank, then it is possible to reach wave period higher than 2.5 *s*. In particular, in these conditions a maximum wave period of 2.8 *s* can be reproduced.

Both 1:12 and 1:15 scale waves are across deep and intermediate water condition, discussed in Chapter 3. However, since the transition between deep and intermediate water is mild (see Fig. 3.8), it is possible to assume that waves are approximately in deep water condition.

In conclusion, the 1:12 scaling factor has been chosen for the design of the prototype: in Table 5.2 the corresponding design wave condition are reported.

Table 5.2 1:12 scale design irregular and iso-energetic wave condition.

Scaling factor	Irregular wave			Iso-en. regular wave		
	$H_s(m)$	$T_e(s)$	$WPD\left(\frac{kW}{m}\right)$	$H(m)$	$T(s)$	$WPD\left(\frac{kW}{m}\right)$
1:12	0.23	2.2	0.05	0.15	2.2	0.05

5.1.2   Floater

Design and optimization

The design procedure of the 1:12 scale prototype floater started from the indications given by the direct scaling up of the 1:45 scale hull geometry, according to the Froude scaling law. Under this assumption, the hull should be 1.89 *m* wide, 3.9 *m* long and 1.95 *m* high. Regarding the mass, a direct scaling might not be properly correct, since most of the 1:45 scale device mass is due to the electronic equipment installed inside, which are not clearly in scale. For this reason, instead of scaling the overall mass, the draft similitude has been maintained. Then mass is calculated starting from the submerged volume. More in detail, the draft has been maintained around 50% of the floater height. The mass calculated in this way corresponds, clearly to the overall mass of the device, including the internal systems.

The overall dimensions previously determined have been used as the first input for the hull geometry optimization in term of dimensions. The optimization process is based on the following criteria:

- The natural frequency of the hull as close as possible to the frequency of the design wave;

- Length of the floating body between one third of and half of the wavelength;

- Minimal added mass and dissipation;

- Floater roll and pitch hydrostatic stability.

The first criterion is based on the principle that, in regular waves, energy is exploited most efficiently when the un-damped natural frequency of the device is close to the dominant frequency of the incoming wave [44]. In the case of the 1:12 scale prototype, it has been assumed to tune the floater resonance close to the design wave period (2.2 *s*).

The second criterion is a compromise between using the maximum wave slope and reducing the floater size and costs. The hull length limits defined by this criterion and the design wave length are 1.89 and 3.78 *m*. It is important to observe that the floater length calculated through the direct scaling up methodology is not suitable.

The third criterion has been adopted with the aim to minimize energy dissipation and ineffective interactions between waves and hull. Furthermore, in order to avoid hydrodynamic interactions between floater and tank walls, it has been imposed a minimum distance between floater and tank sides of more than one time the floater length.

The last criterion aims to guarantee a proper stability of the floater with respect to roll and pitch degrees of freedom. According to the small angle stability theory, the floater can be considered stable when the transverse and longitudinal metacentric heights are respectively greater than zero, as summarized by Eq. 5.1 [6][46][59].

$$
\begin{cases}
\overline{GM}_t = \frac{K_{44}}{\rho g V_0} > 0 \\
\overline{GM}_l = \frac{K_{55}}{\rho g V_0} > 0
\end{cases}
\tag{5.1}
$$

Where K_{44} and K_{55} are roll and pitch hydrostatic stiffness matrix elements respectively, while V_0 is the displaced volume. K_{44} and K_{55} can be seen also as the restoring moments per unit of roll and pitch angle.

On the base of the assumptions discussed above, a parametric simulation of the floater varying radius and width of the cylindrical shape has been performed, according to the ranges reported in Table 5.3.

Table 5.3 Radius and width span used for floater parametric optimization.

Description	Symbol	Value	U.M.
Radius	*R*	1 - 1.25 - 1.5 - 1.75	*m*
Width	*W*	1.5 - 2 - 2.5 - 3	*m*

Minimum an maximum radius values have been designed considering the limitations given by the second criterion, while the width span has been chosen starting from the direct scaling calculation.

The floater mass has been calculated once the draft has been imposed around the 50% of the floater height. Then, mass has been rounded to next integer, aiming to defined different floater families identified by the same mass.

The inertial tensor and COG position of each configuration has been calculated starting from a complete CAD representation of the floater layout reported in Fig. 5.1. Observing Fig. 5.1, it is possible to see that the ballast can be allocated in
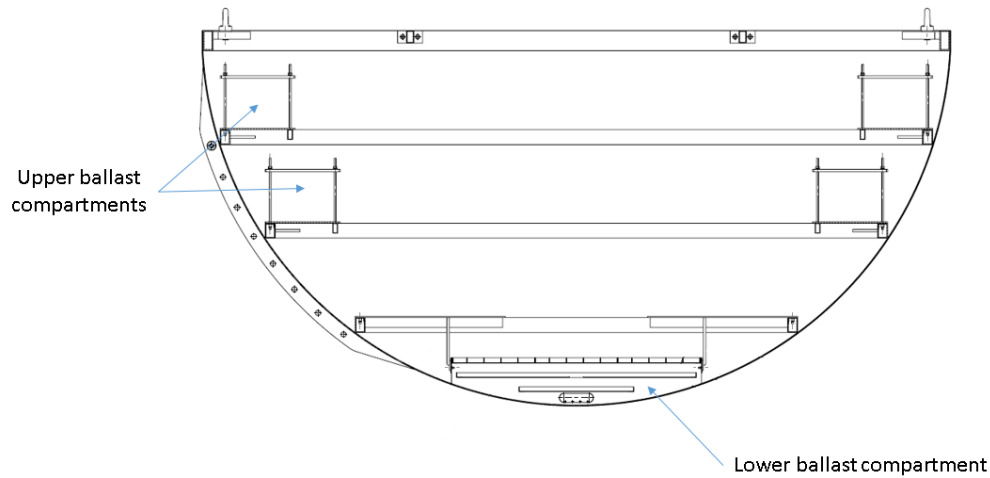
Fig. 5.1 Floater section view and ballast compartments.

different zones of the floater, allowing to achieve the desired pitch moment of inertia, COG position and overall mass.

It is noteworthy that the number of configurations to be simulated is considerable, thus a mathematical representation of the mass distribution of the layout presented in Fig. 5.1 has been implemented: varying floater radius an mass it was possible to calculate the corresponding inertial tensor and COG position.

Table 5.4 Extract of parametric simulation results.

Description	Parameter	Values					U.M.
Radius	R	1	1.25	1.25	1.5	1.5	*m*
Width	W	3	2	2.5	1.5	2	*m*
Draft	D	0.52	0.63	0.63	0.72	0.78	*m*
Mass	m	2000	2000	2500	2000	3000	*kg*
Pitch res. period	$T_{n,\delta}$	2.45	2.3	2.03	2.14	2.15	*s*
Roll hydr. stiff	K_{44}	642	187	209	38	192	$\frac{Nm}{deg}$
Pitch hyd.stiff	K_{55}	186	233	291	279	419	$\frac{Nm}{deg}$

Each configuration has been simulated in Ansys AQWA environment determining the corresponding hydrodynamic database, RAOs and metacentric height. In Table 5.4, an extract of the complete numerical campaign is given, in which some of the most interesting results are highlighted. It is important to underline that in Table 5.4, the variable *m* refers to the overall mass of the device, including both the buoyant

and pendulum mass. In the initial stage of the design, it appears clear that it is not possible to distinguish the contribution of each mass.

The database containing the set simulated configurations needs to be filtered in order to converge to a optimal solution. For this reasons, some new constraints have been introduced. First of all, the cases where the restoring moment (metacentric height) is too close to the stability limit have been discarded. For instance, observing Table 5.4, it is possible to see that the configuration 1.5x1.5x2000 (*RxWxm*) has a roll restoring moment per unit of angle of only 38 *Nm*, that might not be sufficient for a safe stability of the device.
Moreover, a length to width ratio between 1 and 2 has been assumed, since the space distribution needs to be maximized in the fore-aft direction. The ratio has been limited to 2 because the higher values may lead to roll instability. According to this constraint, configurations similar to the 1x3x2000 reported in Table 5.4 have been discarded.
At the end of the selection process, only the solutions reported in Table 5.5 remained among the optimal configurations.

Table 5.5 Optimal configurations for the 1:12 PeWEC floater.

Description	Symbol	Values			U.M.
Radius	R	1.25	1.25	1.5	*m*
Width	W	2	2.5	2	*m*
Draft	D	0.63	0.63	0.78	*m*
Mass	m	2000	2500	3000	*kg*
Pitch res. period	$T_{res,\delta}$	2.3	2.03	2.15	*s*
Roll hydr. stiff	K_{44}	187	209	192	$\frac{Nm}{deg}$
Pitch hyd.stiff	K_{55}	233	291	419	$\frac{Nm}{deg}$

The final identification of the most suitable floater has been achieved introducing a further constraint related to the pendulum dimensions. In first approximation, it is possible to consider the formulation of simple gravity pendulum, where its resonance period is described by the following equation:

$$T_n = 2\pi\sqrt{\frac{l}{g}} \tag{5.2}$$

If the resonance period is set in correspondence of the design wave period of 2.2 *s*, then the pendulum length results be of 1.2 *m*. Taking into account an appropriate safety margin, it follows that the 1.5x2x3000 configurations is the most suitable. Table 5.6 summarizes the specifications in term of device mass, COG vertical position and inertial properties.

Table 5.6 Floater specifications.

Description	Symbol	Values	U.M.
Radius	R	1.5	*m*
Width	W	2	*m*
Draft	D	0.78	*m*
Mass	m	3000	*kg*
Center of gravity	COG	[0 0 -0.098]	*m*
Roll moment of inertia	I_{xx}	1063	kgm^2
Pitch moment of inertia	I_{yy}	2200	kgm^2
Yaw moment of inertia	I_{zz}	1918	kgm^2

It is important to underline that the COG vertical position is given with respect to the waterline. In Fig. 5.2, the RAOs for surge, heave and pitch DOFs are reported.
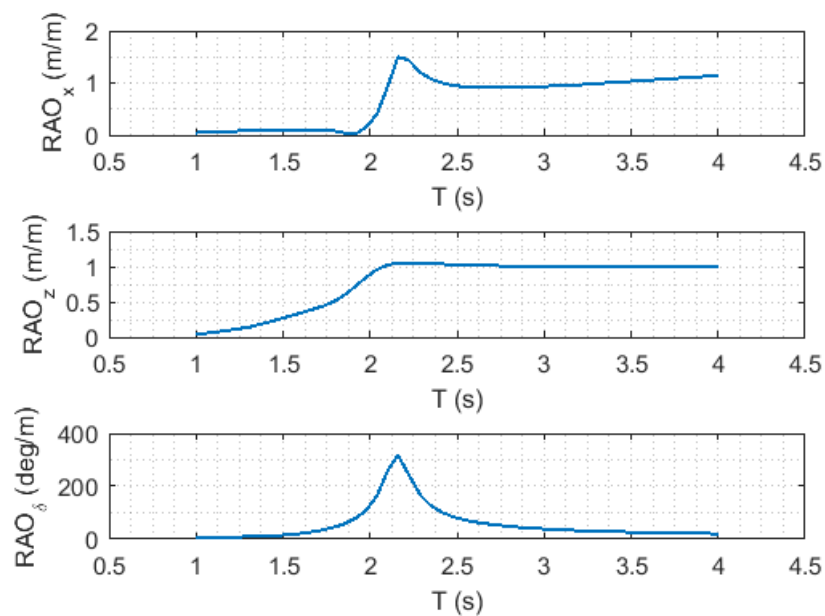
Fig. 5.2 Surge, heave and pitch RAOs for the optimal configuration.

3D CAD model and structural design

A detailed CAD model of the configuration determined has been developed (see Fig. 5.3), introducing structural elements such as stiffeners, ballast compartments, ballast locking systems and the basement for the installation of the PTO frame, that will be described in section 5.1.3.
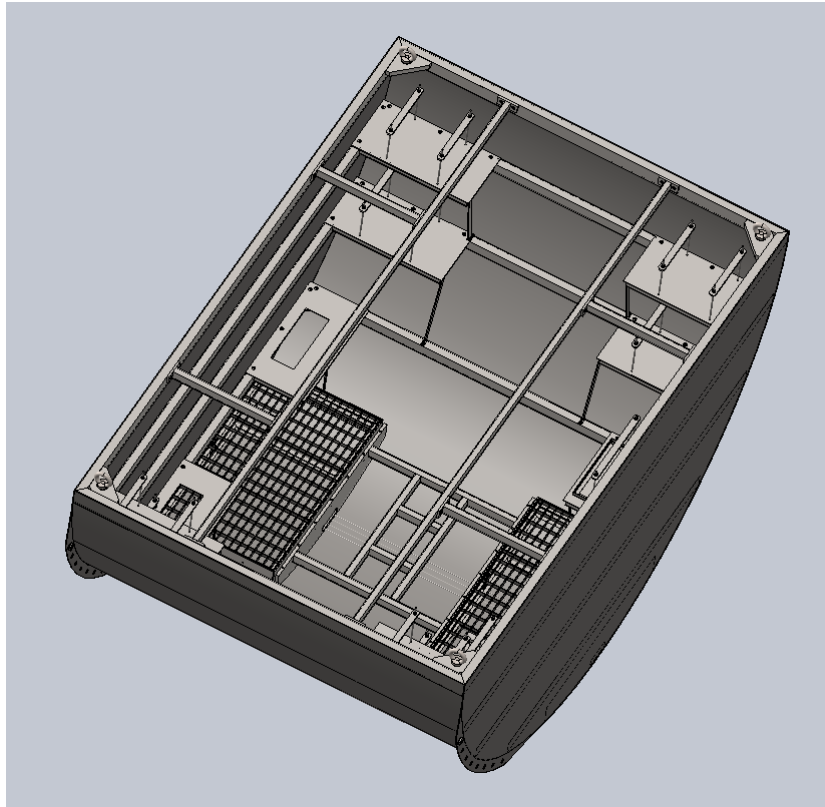
Fig. 5.3 3D CAD model of the 1:12 PeWEC floater.

More in detail, the external part of the floater has been realized with 4 *mm* thickness stainless steel AISI 304 L sheets. Sides have been cut via laser process, while the cylindrical central part has been formed through calendering. The different parts have been welded together with a continuous weld joint, guaranteeing the floater water tightness. Moreover, on each side, a small fin with a series of holes has been provided, allowing the mooring line anchoring.

The internal stiffeners and the plates required for electrical devices and ballasts location are constituted by S355J2G3 structural steel. The disposition of the stiffeners has been studied in order to guarantee a sufficient rigidity of the device with respect

to the external and loads. The overall floater mass achieved, excluding ballasts, is of 988 *kg*.

Another important aspect is the lifting points design and the verification of the structure strength during lifting operations. In order to guarantee the maximum safety, a *Finite Element Method* (FEM) model of the entire structure has been developed with the *SolidWorks* FEM analysis toolbox [4]. In particular, as worst case, it has been considered the full load condition, that includes the weight of ballast, electrical systems, pendulum and its frame and PTO. In Fig. 5.4, the results of the analysis are reported: the maximum static stress calculated via Von Mises criterion is of 115 *MPa*, while the steel yield strength is equal to 315 *MPa*, that leads to a 2.7 static safety factor.
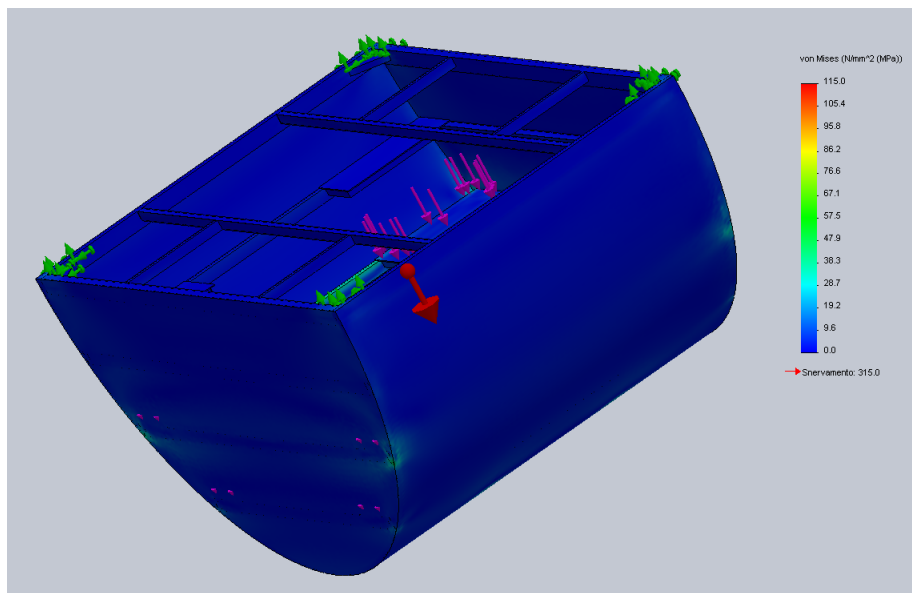
Fig. 5.4 Floater FEM analysis results: stress distribution (Von Mises criterion) .

Ballasts have been obtained through a series of steel bars that can be distributed in the upper and lower compartments shown in Fig. 5.1.
The upper ballast compartments are subdivided in two different levels and each level is constituted by two different compartments, situated on the floater sides, as shown in Fig. 5.3. The lower level position has been optimized in order to achieve the pitch moment of inertia previously determined, while the upper level can be used to increase the pitch moment of inertia. Each compartment can be filled with 16 steel bars 50x50 *mm* section and 550 *mm* long. The overall mass hosted by each compartment is of 171.2 *kg*, while the overall mass hosted on a level is of 685 *kg*.

Fig. 5.5 shows the RAO variation as a function of the level chosen for the upper ballast compartments. Thanks to this adjustment, it is possible to shift the floater pitch resonance period from 2.2 *s* (design wave period) to 2.45 *s*.
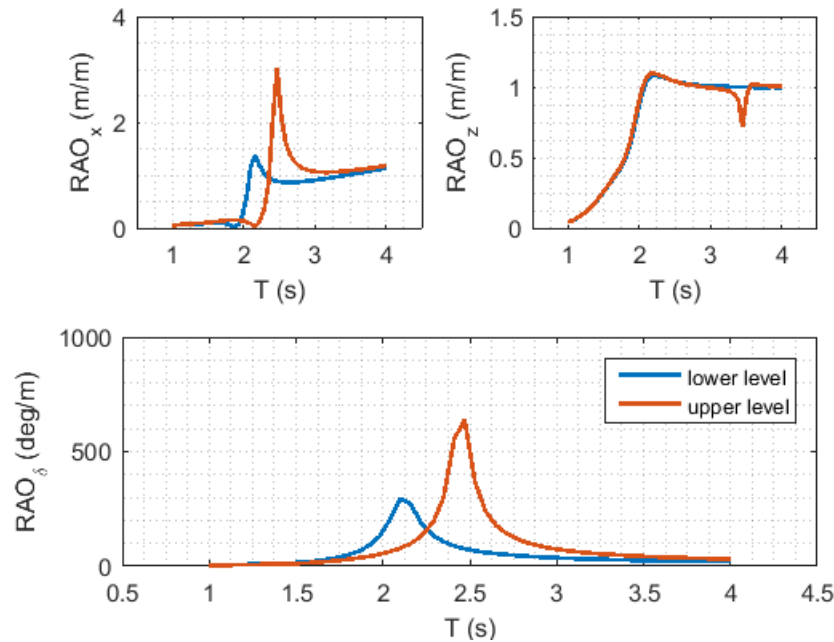
Fig. 5.5 RAO variation as a function of the level chosen for the upper ballast compartments.

The lower ballast compartments are situated on the bottom, one per each floater side. They have been designed to host ballast bars required to achieve the desired mass without changing the pitch moment of inertia and to balance the device with respect to roll axis. In this case, bars are 50x50 *mm* section and 580 *mm* long. Each compartment can be filled with up to 28 bars that leads to a mass of 634 *kg*.

5.1.3   Frame

The second element of the 1:12 PeWEC prototype that has been designed is the frame required for the support of PTO and pendulum. Similarly to the 1:45 prototype, it is desired to have the possibility to variate the vertical PTO axis position with respect to the system COG, that as will be shown later, influences significantly the WEC dynamic performances.

More in detail, the possibility to variate the PTO axis position can be also combined with the ballast positioning, in order to exploit configurations with dif-

ferent floater dynamic response or to adjust the PTO axis position according to the
pendulum length chosen.

In Fig. 5.6 a 3D CAD model of the steel frame is reported: it is constituted by a
fixed part that can be bolted on the floater and a movable part on which the PTO can
be positioned. The vertical motion is actuated via a motorized irreversible screw-nut
system (*UNIMEC TPR 407 MBS 1/30 650 TC80 B14*), that allows a platform stroke
of 500 *mm*. The platform height has been designed in order to achieve the COG
vertical position requirement, given in Table 5.6, when the movable part is placed at
half of the available stroke (250 *mm*). Moreover, in these conditions it is possible to
install the pendulum configuration characterized by the maximum length available.
The upper extreme position of the platform has been limited in order to guarantee
the roll and pitch hydrostatic stability requirements.
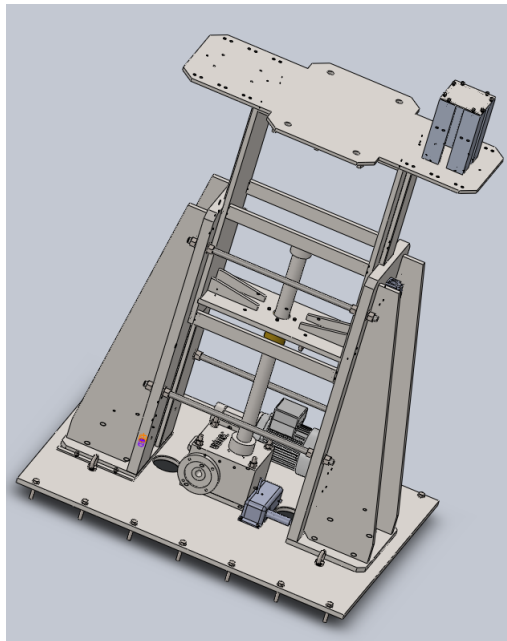
Fig. 5.6 PTO frame 3D CAD model.

The vertical position can be set via the control system and it is monitored through
a cable position transducer *Celesco DV301*, while the a couple of *Honeywell BS20-GLAC-20B* limit switches allows to interrupt the electrical motor supply, when the
platform reaches the upper or lower limit.

On the platform, a small column (depicted in Fig. 5.6) has been also fixed. It is constituted by reference surface, used for the installation of the *MTi* inertial platform, described in section 4.3.3.

5.1.4   Pendulum

The pendulum is, together with the Power Take Off, the core of the energy conversion from waves to electricity. In this section, the methodology used for the pendulum design is described.

Geometry

The design process starts from the identification of different geometries that could be used for the implementation of the pendulum. In this case, oval and circular shapes have been considered, as represented in Fig. 5.7. The choice of geometry typology started from the consideration that the circular geometry is quite easy to be realized and that it can be easily evolved into an ellipse, a geometry that may help the reduction of the pendulum workspace dimensions.
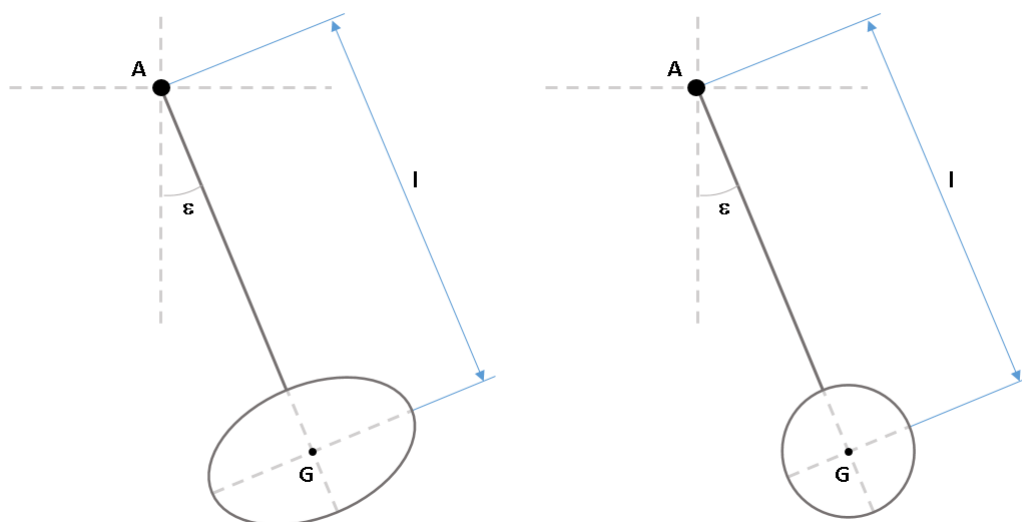
Fig. 5.7 Pendulum geometries investigated: elliptical (on the left) and circular (on the right).

Resonance period and workspace maps

The idea is to model the pendulum on the base of the compound pendulum theory, under the hypothesis of small oscillations and to determine the resonance period and workspace maps, as a function of the pendulum dimensions and geometry. The geometrical information given by the pendulum workspace can be related to the space available inside the hull and to the design of the frame described in section 5.1.3.

The un-damped dynamic equation of the compound pendulum, describing its oscillation under linear assumption is:

$$I_A \ddot{\varepsilon} + m_p g l \varepsilon = 0 \qquad (5.3)$$

Where I_A is the pendulum moment of inertia with respect to its hinge, m_p and l the pendulum mass and length respectively. The natural period of the un-damped pendulum results be:

$$T_n = 2\pi \sqrt{\frac{I_A}{m_p g l}} \qquad (5.4)$$

The pendulum moment of inertia I_A can be written, according to the Huygens-Steiner theorem as the composition of the oval or circular disk moment of inertia about its COG and the moment of inertia due to the eccentricity of the mass with respect to pendulum hinge. Here, it is assumed that the pendulum rod mass is negligible.

$$I_A = I_y + m_p l^2 \qquad (5.5)$$

Since the circular shape of the disk can be considered as a particular case of the elliptical geometry, the latter is assumed as reference for the determination of the pendulum moment of inertia.

Let be a and b the semi-major and semi-minor axis of the ellipse respectively. Moreover, let also be λ the ratio between a and b. The ellipse moment of inertia with respect to its COG is:

$$I_A = \frac{1}{4}m_p\left(a^2+b^2\right)+m_pl^2 \tag{5.6}$$

Substituting Eq. 5.6 in Eq. 5.5 and taking into account the ratio λ, the resonance period of the pendulum expressed as a function of the ellipse semi-major axis and pendulum length results be:

$$T_n = \frac{2\pi}{\sqrt{g}}\sqrt{\frac{a^2\left(1+\frac{1}{\lambda^2}\right)}{4l}+l} \tag{5.7}$$

Lastly, the pendulum workspace can be expressed as follows:

$$w = l+b = l+\frac{a}{\lambda} \tag{5.8}$$

The circular disk, as previously described , is a particular case of the elliptical formulation. Thus, assuming that λ is unitary and that $a = b = r$, the resonance period and the workspace formulations become:

$$T_n = \frac{2\pi}{\sqrt{g}}\sqrt{\frac{r^2}{2l}+l} \tag{5.9}$$

$$w = l+r \tag{5.10}$$

Fig. 5.8 shows the resonance period and workspace maps, as a function of the disk dimension and pendulum length, for different values of λ.

It is important to observe that increasing the ratio between semi-major and semi-minor axis and maintaining the same value of a, it is possible to obtain the same resonance period with a smaller pendulum workspace. Furthermore, it is also worth noting that the same resonance period can be obtained with different combinations of a and l, moving from a longer pendulum with a small disk at the extremity, toward to a more squat pendulum, characterized by a bigger disk and a shorter length.

The choice of the best configuration, fixed a certain resonance period, is determined by the space available and by the pendulum required pendulum mass. More in detail, the leaner configuration is particularly suitable for small values of mass
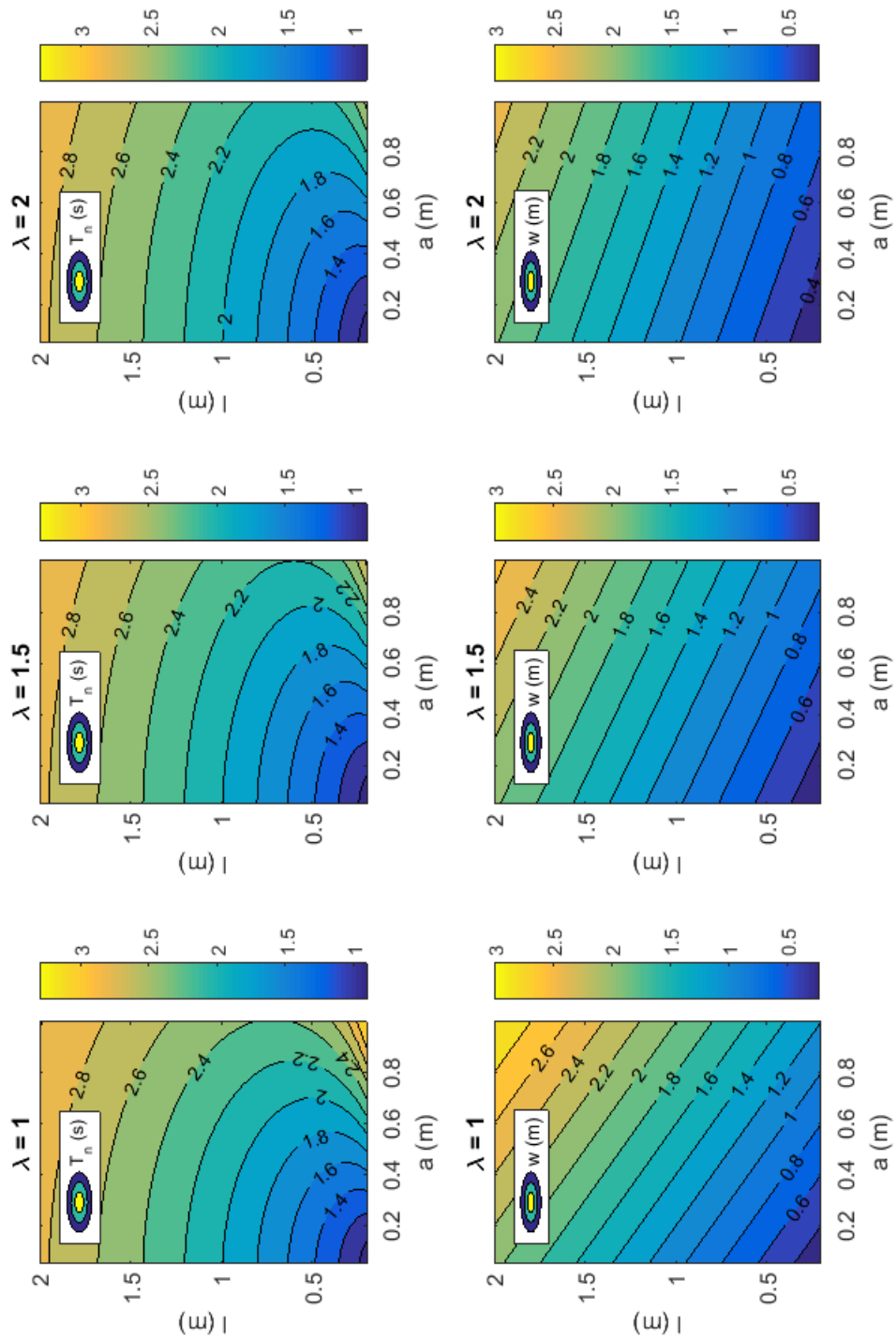
Fig. 5.8 Pendulum resonance period and workspace maps, as a function of the disk dimension and pendulum length, for different values of λ.

while, in the case of higher mass values, a more squat pendulum is recommended, since it is possible to allocate the desired mass limiting the disk thickness.

Mass identification

The pendulum mass has been designed on the base simulations results performed with the linear frequency domain model. Simulations have been carried out imposing the design wave period and wave height and varying the pendulum geometry (circular or elliptical) and the pendulum dimensions (a and r). In correspondence of each pendulum configuration, the device performances have been computed, obtaining a map describing the PeWEC behavior, as a function of the pendulum configuration. Moreover, maps have been completed with the constant resonance period curve (2.2 s) and the constant workspace curve (1.5 m).

Fig. 5.9 and Fig. 5.10 shows, respectively, the average extracted power maps in the case of device equipped with circular or elliptical pendulum, varying the pendulum mass. The semi-axis ratio chosen for the elliptical pendulum is 1.85 and it corresponds to the best compromise between the desired resonance period, pendulum workspace and space available inside the floater.

Observing Fig. 5.9, it is possible to note that only masses between 100 and 400 kg allow to determine pendulum configurations within the optimal average extracted power area, that guarantee a 2.2 s resonance period and a workspace smaller than 1.5 m. Most of the configurations fall in the region of the slender pendulums, however they are not suitable with the selected masses, because of a excessive pendulum thickness.

On the other hand, the elliptical pendulum allows to identify suitable configurations over the entire mass span investigated, that falls in the area of more squat pendulums, allowing the reduction of the pendulum thickness.

On the base of such consideration the pendulum has been realized considering the elliptical configuration and assuming the 400 kg mass as the nominal value. The final design of the pendulum has been developed taking into account the possibility to variate the mass between 200 and 500 kg. Regarding the pendulum dimensions, they have been determined according to the 3D CAD representation of the device: the maximum pendulum workspace allowable is of 1.45 m. Therefore, on the base of the pendulum map reported in Fig. 5.11, the 2.2 s resonance period can be achieved
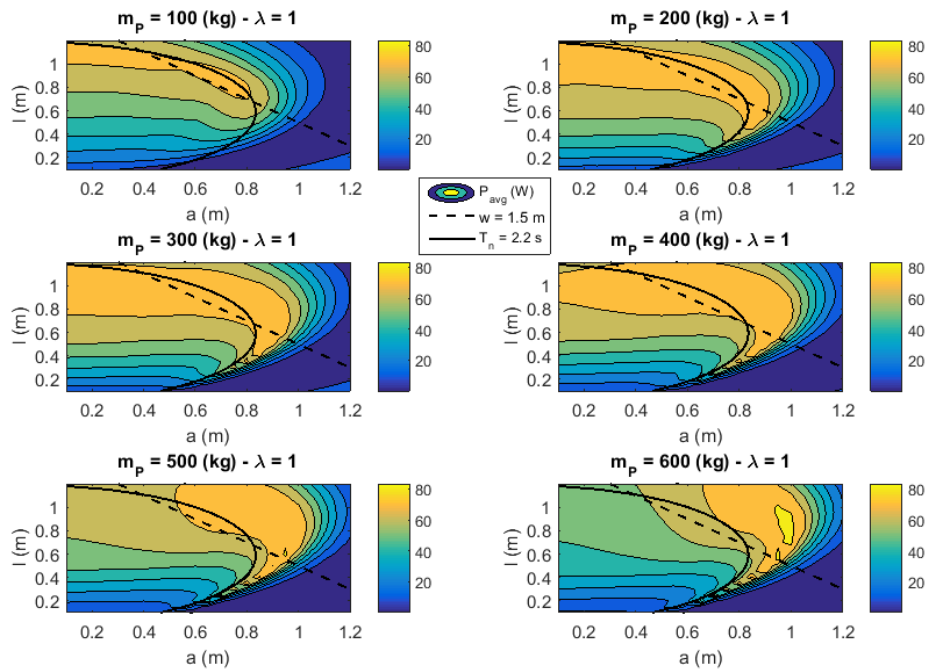
Fig. 5.9 Average extracted power maps at the design wave condition, as a function of the pendulum mass, circular disk dimensions and pendulum length.
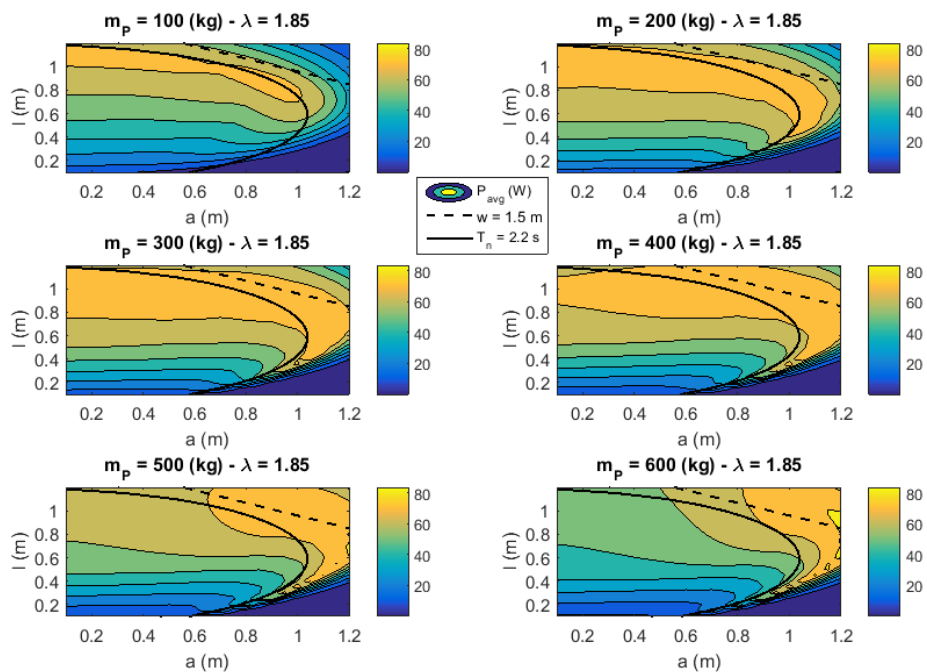
Fig. 5.10 Average extracted power maps at the design wave condition, as a function of the pendulum mass, elliptical disk dimensions and pendulum length.
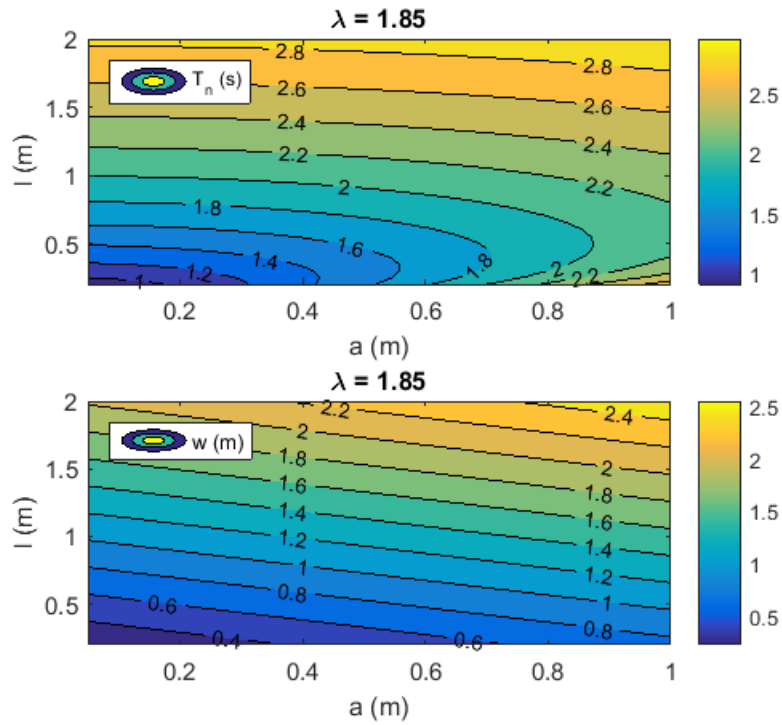
Fig. 5.11 Elliptical pendulum resonance period and workspace maps, $\lambda = 1.85$.

with a pendulum characterized by a major semi-axis a equal to 0.8 m and a length l of 1 m.

Starting from the target mass of 400 kg and to the elliptical disk dimensions, it is possible to determine the ellipse moment of inertia about its COG, according to the following equation:

$$I_y = \frac{1}{4} m_p \left(a^2 + b^2 \right) = \frac{1}{4} m_p a^2 \left(1 + \frac{1}{\lambda^2} \right)$$ (5.11)

The pendulum target values that need to be respected are summarized in Table 5.7.

Lastly, in order to check the validity of the results achieved at the end of the pendulum design process, a frequency domain simulation of the system has been performed, aiming the evaluation of the overall behavior varying wave period and PTO control damping. The wave amplitude has been fixed at 0.15 m.

Table 5.7 Pendulum specifications.

Description	Symbol	Values	U.M.
Semi major axis	a	0.8	*m*
Ellipse semi-axis ratio	λ	1.85	-
Mass	m_p	400	*kg*
Inertia	I_y	84	*kgm^2*
Length	l	1	*m*

Starting from the average extracted power reported in Fig. 5.12, it is possible to see that a maximum is reached at 2.2 *s* wave period, when the PTO damping is set at 900 $\frac{Nms}{rad}$ (the maximum value considered), proving that the pendulum design methodology adopted is correct. Moreover, the coupling between the floater and swinging mass induces two resonance periods, that in the specific case arise at 2 and 2.5 *s* wave period. In correspondence of such resonances, the device is able to extract an average power level comparable to the maximum shown at 2.2 *s* wave period. It is important to underline that the the maxims at 2 and 2.5 *s* wave period are achieved with different values of the PTO control damping. Thus, it is clear that optimizing the PTO control damping, it is possible to determine the envelope of the average extracted power maximum over the entire wave period span chosen.
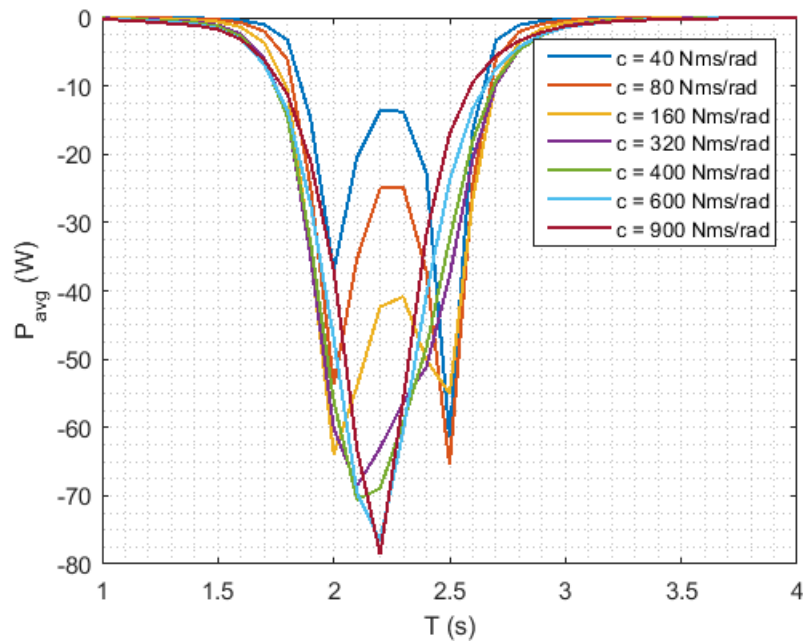
Fig. 5.12 Average extracted power varying wave period and PTO control damping.
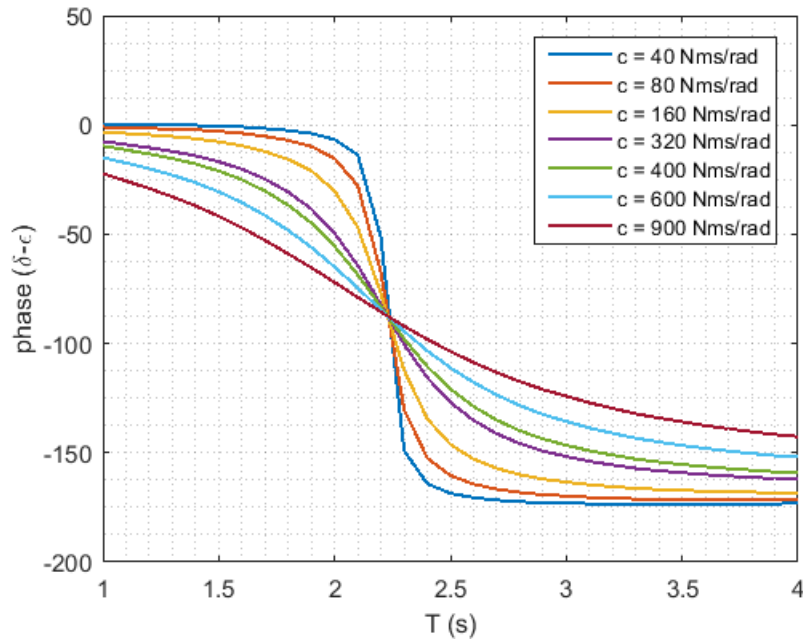
Fig. 5.13 Pitch and pendulum angle relative phase, as a function of wave period and PTO control damping.

The behavior depicted in Fig. 5.12 is quite interesting in the perspective of the development of a full scale device, where it is necessary to maximize the device performances over a wide range of working conditions, in term of wave period.

More in detail, such behavior can be related to the pitch and pendulum motion amplitude, according to the following considerations:

- At 2.2 *s* wave period, pitch and swinging angle are in quadrature (Fig. 5.13). The performances are maximized increasing the PTO damping coefficient, which leads to a reduction of the pendulum motion (Fig. 5.14) and an intensification of the floater pitch amplitude (Fig. 5.15). In fact, reducing the pendulum motion, the floater is less influenced by the pendulum inertial forces and its dynamics tends to the one determined by the RAO, which is computed with locked pendulum.

- In the case of wave periods lower than 2.2 *s*, the pendulum tends to be in phase with the floater motion, while power is maximized increasing the PTO damping coefficient up to a optimal value. For instance, at 2 *s* wave period, the average power is optimal for a PTO damping coefficient equal to 180 $\frac{Nms}{rad}$.
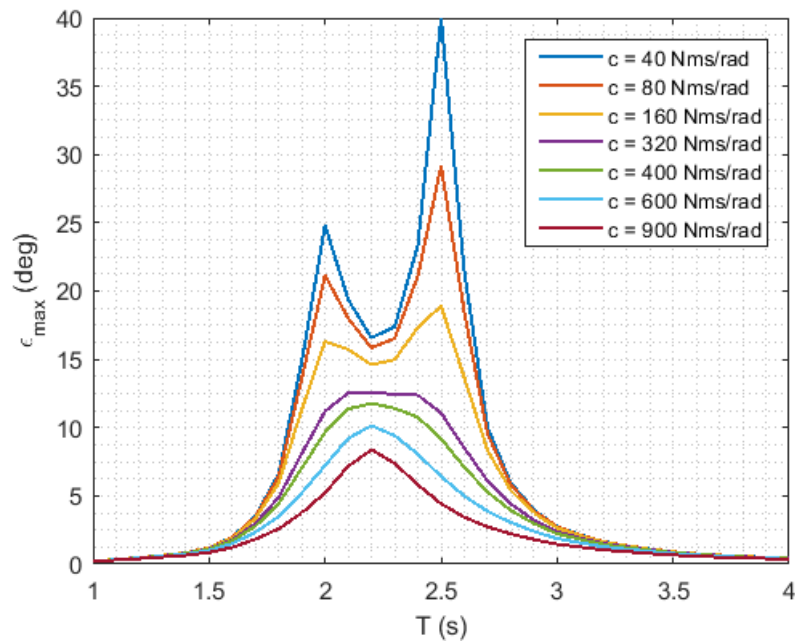
Fig. 5.14 Maximum pendulum oscillation angle, as a function of wave period and PTO control damping.
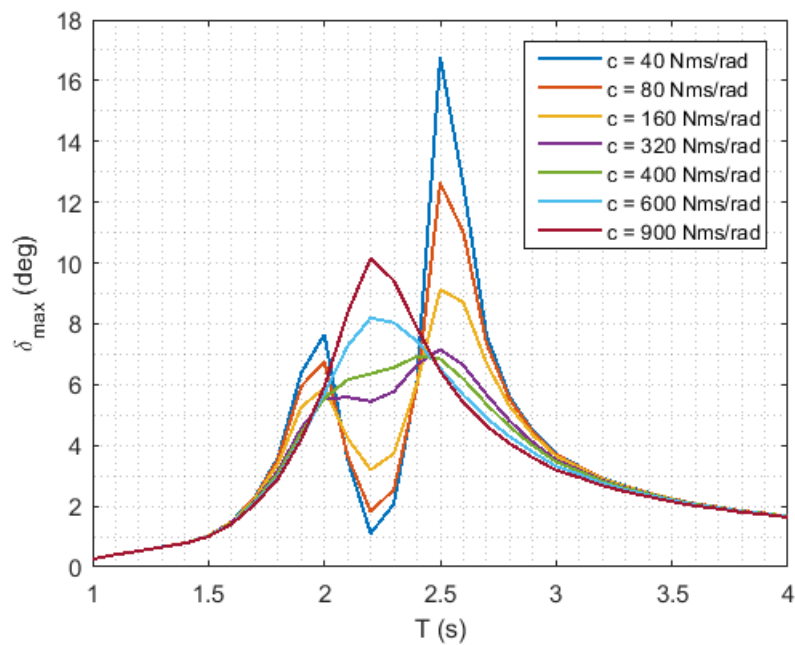
Fig. 5.15 Maximum pitch angle, as a function of wave period and PTO control damping.
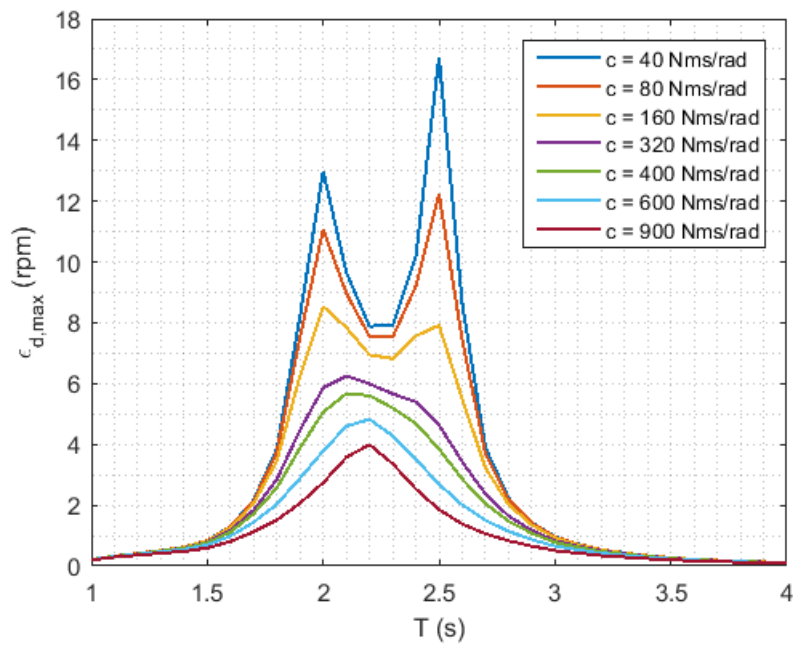
Fig. 5.16 Maximum pendulum angular velocity, as a function of wave period and PTO control damping.
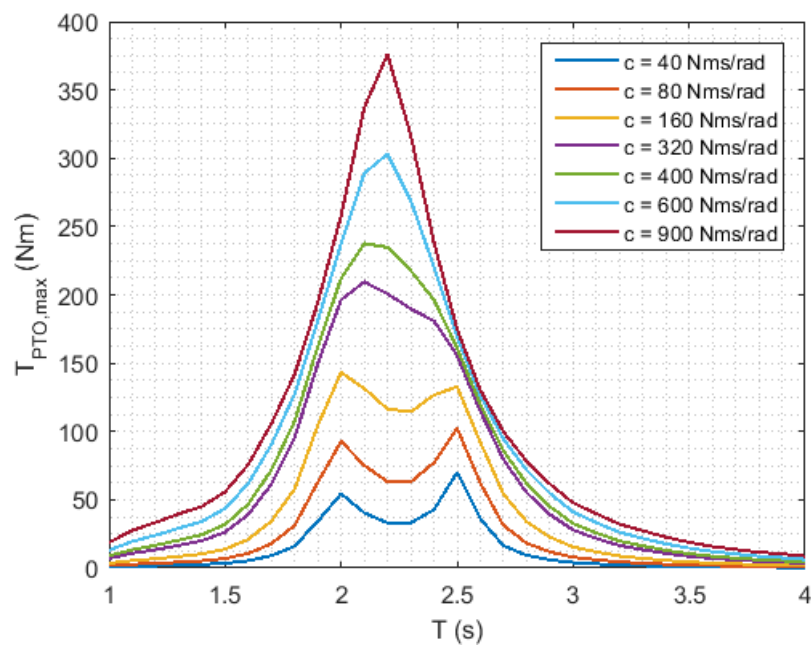
Fig. 5.17 Maximum PTO torque, in function of wave period and PTO control damping.

- Wave periods higher than 2.2 *s* induces a phase lag between δ and ε greater than 90 *deg*. In these conditions, the optimal extracted power is achieved lowering the PTO damping coefficient. The pendulum motion is higher and it influences significantly the floater dynamics increasing its motion amplitude.

It is important to observe that the device has not been designed for a complete revolution of the pendulum, thus the swinging mass motion amplitude needs to be limited. According to the 3D CAD model of the prototype, a maximum angle of 70 *deg* is allowed.

Lastly, in Fig. 5.16 and Fig. 5.17, the maximum torque and pendulum angular velocity are reported. These physical quantities are the input for the PTO design, as will be described later in section 5.1.5.

3D CAD model and structural design

The pendulum has been modeled through a 3D CAD software, in order to design a structure able to meet the requirements previously determined , but also able to allow the variation of pendulum mass and geometry. In order to keep the system symmetry, the idea is to place one pendulum per each side of the frame. Obviously, they are both connected to the same PTO shaft. In Fig. 5.18, the pendulum configuration developed is depicted.
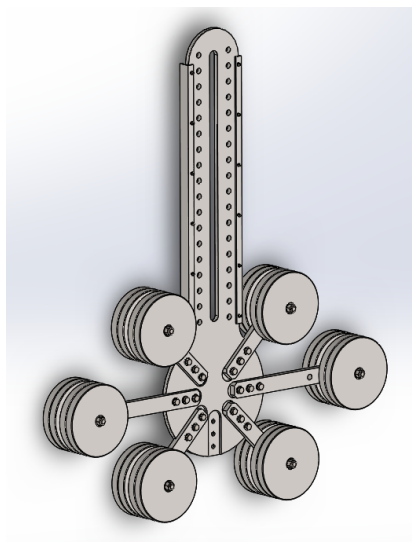
Fig. 5.18 1:12 PeWEC device elliptical pendulum.

The pendulum is composed by a 15 *mm* thickness central plate, on which a series of steel arms can be fixed. The latter support the disks that allow to achieve the desired mass. Each disk has a diameter of 230 *mm* and a mass of 10 *kg*. This configuration allows to approximate the elliptic geometry described previously, where the mass has been supposed uniformly distributed over the ellipse. Distributing the mass around the ellipse periphery, it has been possible to reduce the semi-major axis, leading to a reduction of the overall ellipse dimensions, even if the moment of inertia around its COG respect the specification. Lastly, also in the case of this approximation, the ratio between ellipse semi-axis has been maintained equal to 1.85. The central plate is equipped with a series of evenly spaced holes, that can be used to adjust the pendulum length and thus the resonance period for a certain mass. More in detail, 17 positions are available, with a relative distance of 50 *mm*.

Fig. 5.19 reports the resonance period characteristics as a function of pendulum length and mass of the equivalent pendulum, seen as the composition of two identical pendulums. It is also possible to note that mass can be adjusted within the range of 200 and 500 *kg*, according to the specifications mentioned in section 5.1.4.
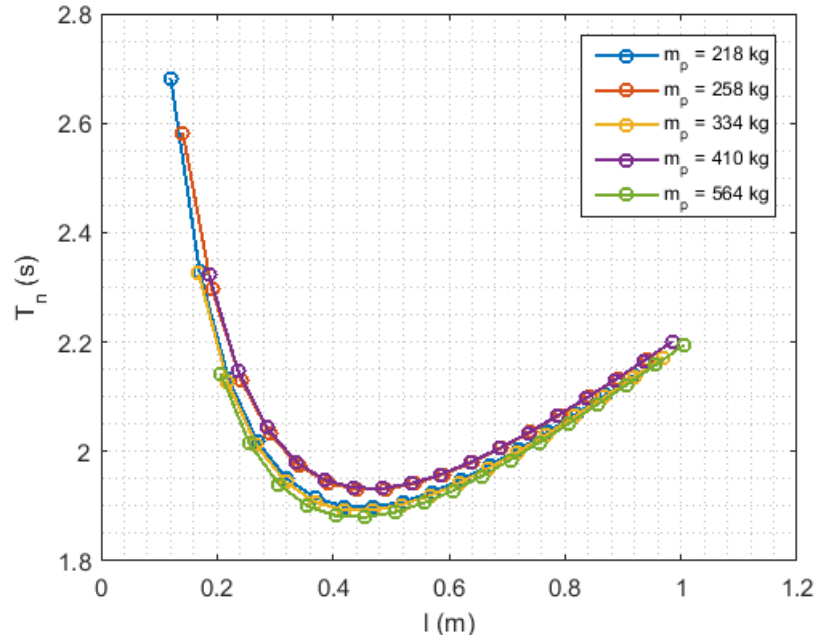
Fig. 5.19 Elliptical pendulum resonance period characteristics, as a function of the pendulum length and mass.

The components constituting the pendulum system have been verified, from the structural point of view, through a static FEM analysis. The latter has been performed on the overall structure, including gravity force and centrifugal force due to the rotation of the pendulum. The worst case condition has been considered, assuming the maximum pendulum length and mass allowable, as well as the maximum pendulum angular velocity. Such velocity has been estimated from the simulations presented in section 5.1.4.
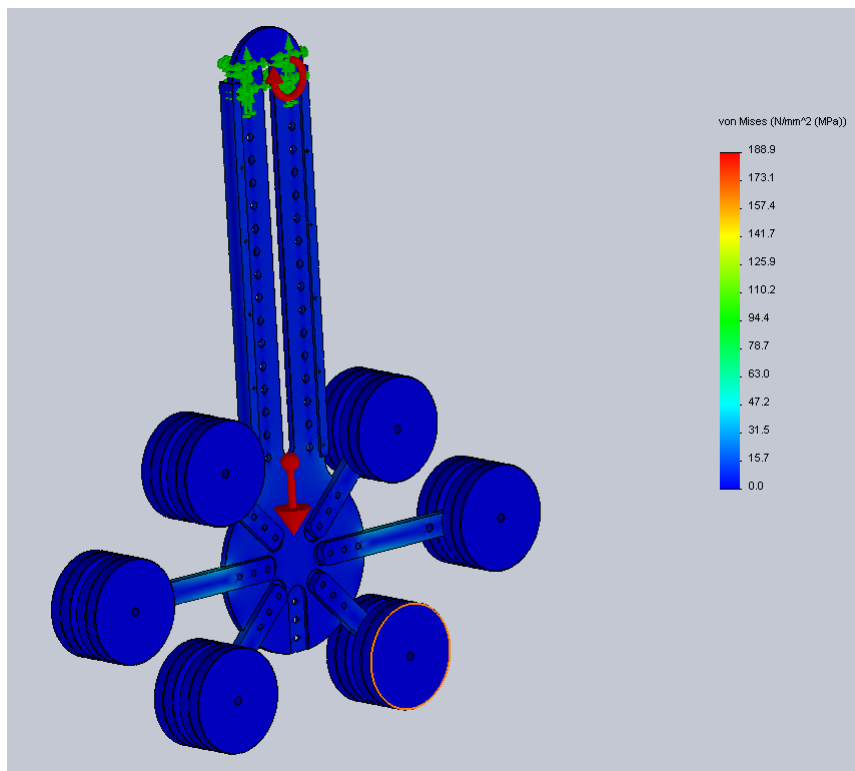
Fig. 5.20 Pendulum FEM analysis results: stress distribution.

Results reported in Fig. 5.20 shows that most of the structure is characterized by very low values of stress. The highest stress values are denoted for the longest disks suspension arms, that reaches 60 *MPa*. However, considering that pendulum is constituted by S355J2G3 structural steel with a 315 *MPa* yield strength, the static safety factor is approximately 5, that can be assumed enough for the application.

The highest stress values of 188 *MPa* are basically due to localized phenomena, that arise from the contact between the longer arms and the relative groove created on the central plate, as reported in Fig. 5.21.
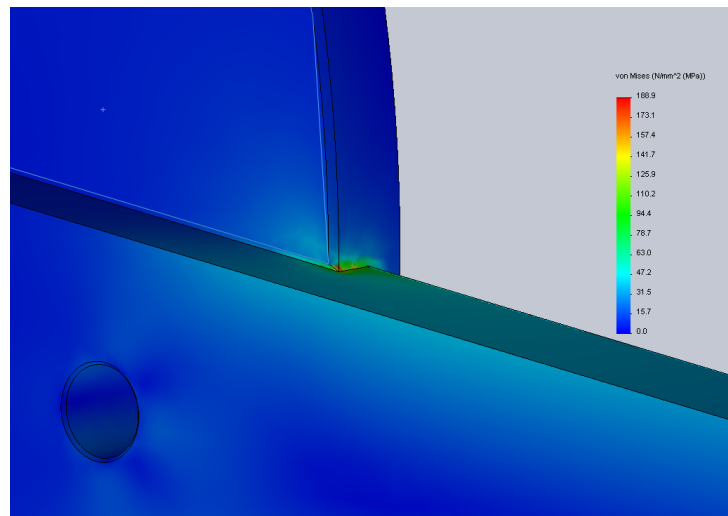
Fig. 5.21 Detail of the localized stress in correspondence of the contact area between the longer arm and the corresponding groove.

Other geometries available

The swinging mass configuration presented above has been designed also to give the possibility to investigate other geometries. For instance, in Fig. 5.22, two other possible geometries have been reported: semi-elliptical and circular approximations.
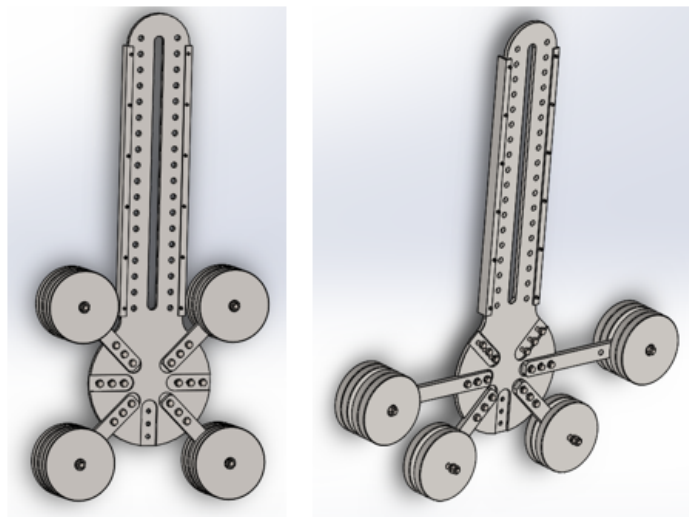
Fig. 5.22 Circular (on the left) and semi-elliptical (on the right) geometries approximations.

5.1.5   PTO

Electrical generator identification

In this section the methodology used for the Power Take Off selection is described. The first stage of this activity is the identification of the possible working conditions expected during the device functioning in wave basin. More in detail, in the case of the PTO the working conditions corresponds to the couples torque-angular velocity that may occur during the tests. The linear frequency domain numerical results presented in section 5.1.4 have been used as input for the identification of the PTO typology. Observing Fig. 5.16 and Fig. 5.17, it is possible to see that the PTO is subjected to high torque and low speed conditions. For this reason, the PTO choice needs to be oriented toward electrical direct drive permanent magnet synchronous torque motors.

The *Motor Power Company* offers a wide range of synchronous direct drive torque motors. The *SKA RT* series is designed specifically for high torque and low speed applications. Moreover, they are equipped with hollow shaft, allowing the installation of one pendulum per side of the PTO [79]. The *SKA RT 335.90* is the model supposed to be suitable for this application (Fig. 5.23).

The selection among the models available has been carried out superimposing torque-angular velocity couples determined with numerical model over the PTO torque-velocity map, as reported in Fig. 5.24: rated torque-velocity curve (black) and maximum torque-velocity (red). Observing the PTO limit torque-velocity characteristic, it is possible to individuate two distinct regions: the first corresponds to the constant torque region that is valid up to 70 *rpm*, while the second is the constant power region, where the PTO torque decreases with the angular velocity increasing, up to the maximum velocity of 120 *rpm*.

The numerical results presented in Fig. 5.24 have been calculated considering the design regular wave height (0.15 *m*) and wave period span evenly spaced between 1 and 4 *s* of 0.1 *s*, while the pendulum mass and length have been set according to the specifications reported in Table 5.7.

The computed root mean square and peak working condition are both within the respective limits defined by the PTO map, even if the generator is underused in terms of velocity, because of the intrinsic slowness of the wave phenomena and so of
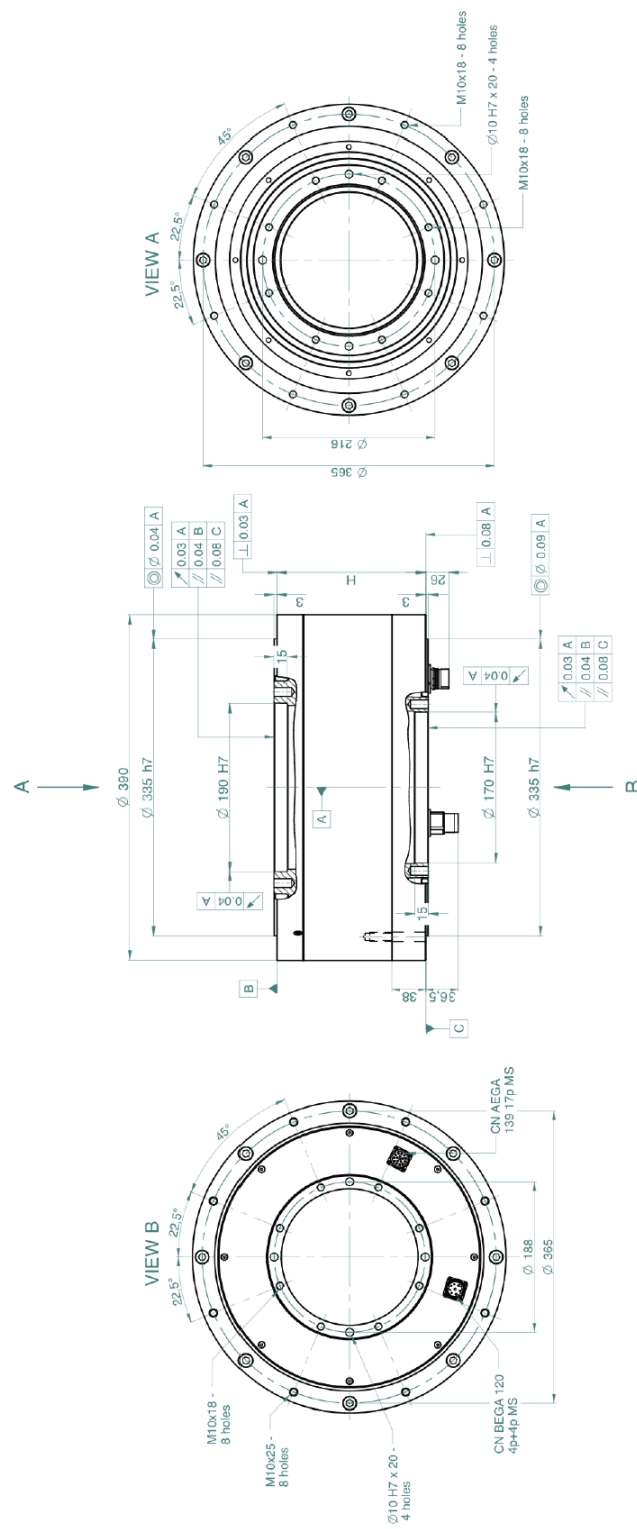
Fig. 5.23 *Motor Power Company SKA RT 335.90* technical drawing.
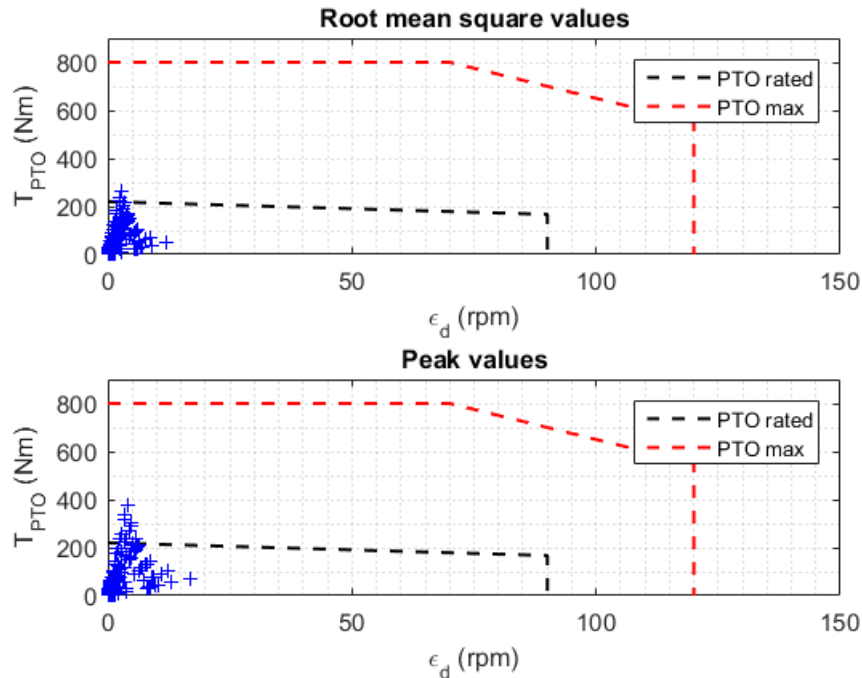
Fig. 5.24 Superimposition of the simulated PTO working conditions over the *SKA RT 335.90* torque - angular velocity map ($H = 0.15\ m$, $T = 1$ - $4\ s$, $m_p = 400\ kg$).

the swinging mass. In order to better understand the map of the computed working conditions, a zoom of Fig. 5.24 is reported in Fig. 5.25.

In these conditions, a gearbox between pendulum and PTO shafts would be the right solution to increase the electrical generator velocity, together with a reduction of the torque and thus of the electrical machine size. However, in this case, the space available is not enough for the installation of a transmission.

The unique drawback of the direct drive solution is that in low speed - high torque conditions the generator efficiency is very low and could compromise the overall efficiency of the conversion chain. However, the prototype will not be connected to the electrical grid, then the efficiency of the generator is not relevant. In fact, the aim of the tests is to validate the mechanical power available on the generator shaft.

For the sake of completeness, the results related to other prototype configurations have been reported. In particular, Fig. 5.26 shows the computed PTO working conditions, when the wave height is increased of the 60% with respect to the design value, maintaining a pendulum mass of 400 *kg*. On the other hand, in Fig. 5.27 a case where the pendulum mass is set at 200 *kg* and the wave height at 0.15 *m* is
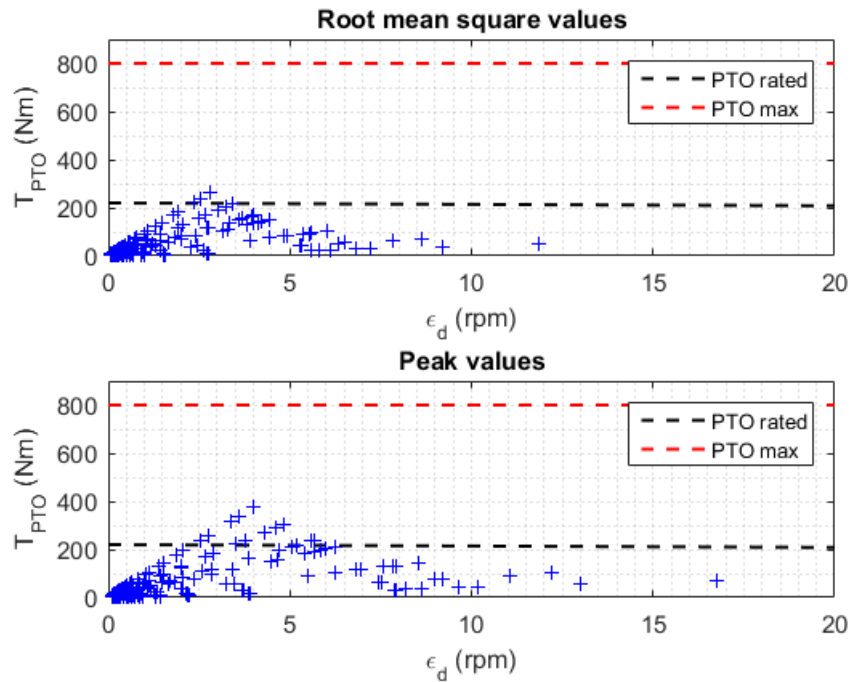
Fig. 5.25 Detail of the simulated PTO working conditions over the *SKA RT 335.90* torque - angular velocity map superimposition ($H = 0.15\ m$, $T = 1 - 4\ s$, $m_p = 400\ kg$).
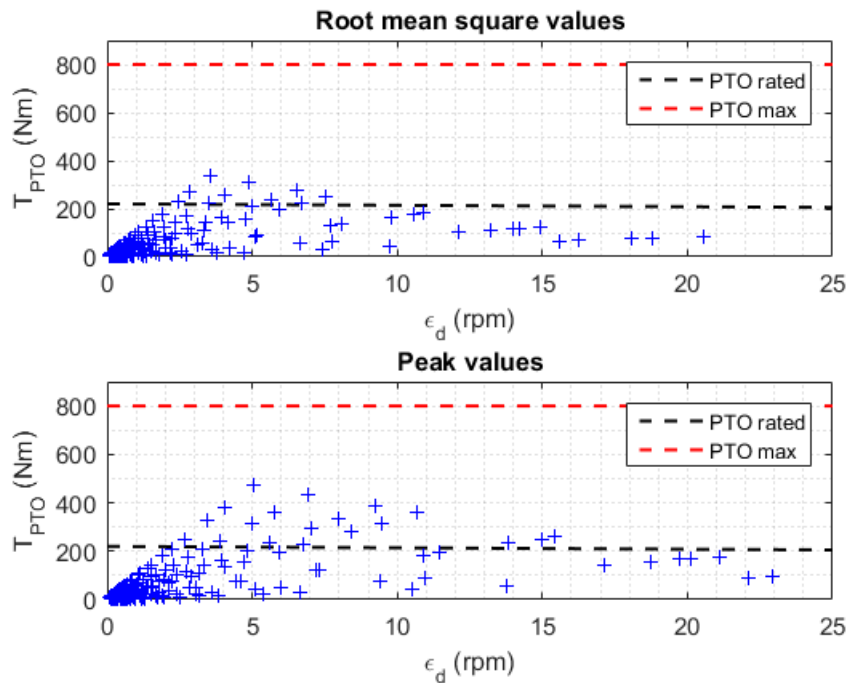
Fig. 5.26 Detail of the simulated PTO working conditions over the *SKA RT 335.90* torque - angular velocity map superimposition ($H = 0.25\ m$, $T = 1 - 4\ s$, $m_p = 400\ kg$).
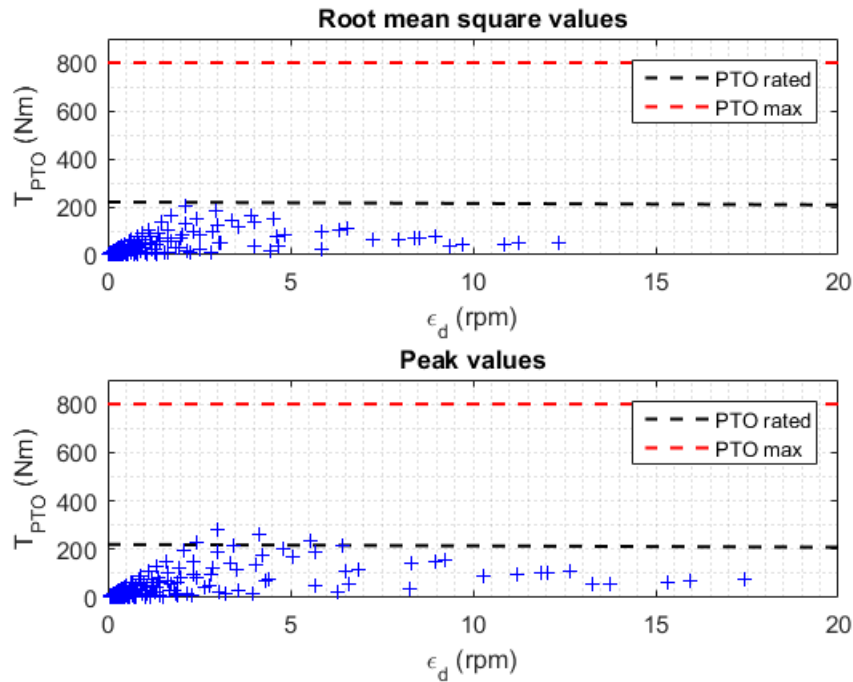
Fig. 5.27 Detail of the simulated PTO working conditions over the *SKA RT 335.90* torque - angular velocity map superimposition ($H = 0.15\ m$, $T = 1$ - $4\ s$, $m_p = 200\ kg$).

depicted, proving that decreasing the pendulum mass the torque required is lower, while the pendulum angular velocity is higher.

Digital servo drive

The PTO is managed through its digital servo drive that, as described in section 4.3.7, provides voltage and currents proportional to the command given in input. In the case of the PeWEC device, the command is constituted by the desired torque calculated through the control law equation (see Eq. 4.6).

More in detail, the electrical generator has been matched with the digital servo drive provided by the *Motor Power Company*, corresponding to the *FlexiPro FPRO 013* [79].

3D CAD model and structural design

The PTO subsystem layout has been developed integrating the electrical generator with a shaft needed to support pendulums, the coupling system of the shaft with respect to the generator shaft and the shaft supporting bearings. In Fig. 5.28 and Fig. 5.29, the PTO unit 3D CAD model and its section are respectively reported.
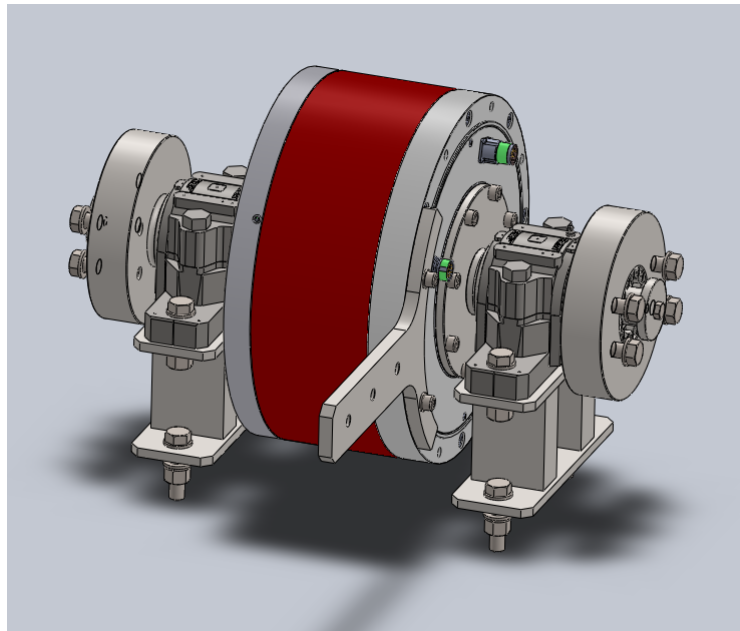
Fig. 5.28 PTO unit 3D CAD model.

The pendulum shaft is supported by a couple of SKF spherical roller bearings (*SKF 22211 E*), seated in the respective *SKF SNL 211* housings [113]. At each shaft extremity, a flange is mounted and the latter is connected to shaft through a locking device (*SIT-LOCK 1 55x85*) [112]. On the flanges, four bolts are available for the pendulum connection to the PTO. In a similar way, the pendulum shaft is connected to the generator flange through another locking device (*SIT-LOCK 5B 65x95*) [112]. Locking devices have been chosen because of the possibility to avoid the typical backlashes due keys or spline shafts in the keyways or spline hubs, respectively. In fact, in this case the motion is oscillatory and backlashes can influence the PTO control. Moreover, locking devices do not require any special mechanical process, such as the manufacturing of keyway or key seat on the shaft. Lastly, the shaft results more robust, since it is devoid of notches that can locally increase internal stresses. The pendulum shaft has been built with 30CrNiMo8 hardened steel and it has been
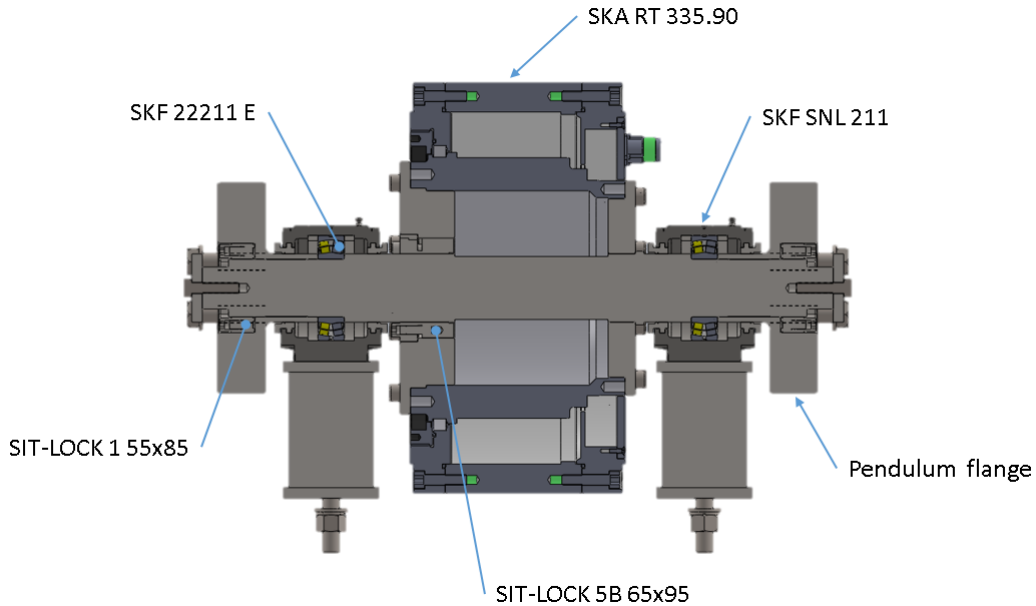
Fig. 5.29 PTO unit 3D CAD model, section view.

designed to support the cyclic loads and torque acting on it, whilst flanges have been made with C40 hardened carbon steel.

Bearings have been designed to support both static and dynamic load due to the pendulum oscillations, paying attention to an accurate selection of the components in order to minimize friction forces.

Load cell

Observing Fig. 5.28, it also possible to note the lever fixed to the PTO stator. It is used to connect a load cell to the PTO frame, in order to measure the instantaneous torque (Fig. 5.30). The system here used is very similar to the one adopted for the 1:45 PeWEC prototype and described in section 4.3.6.

The load cell chosen corresponds to a *Leane DBBE 200* able to measure a rated force of 200 *kg*, in both directions (compression and tension) [64]. The load cell rated capacity has been chosen as the best compromise between the possibility to measure the PTO maximum torque of 800 *Nm* and a suitable length of the arm. In this case, a distance of 408 *mm* between PTO axis and load cell is required. However, considering that the external PTO diameter is equal to 390 *mm*, a 213 *mm* long lever is needed. Such, dimension is suitable with the space available. Furthermore, the
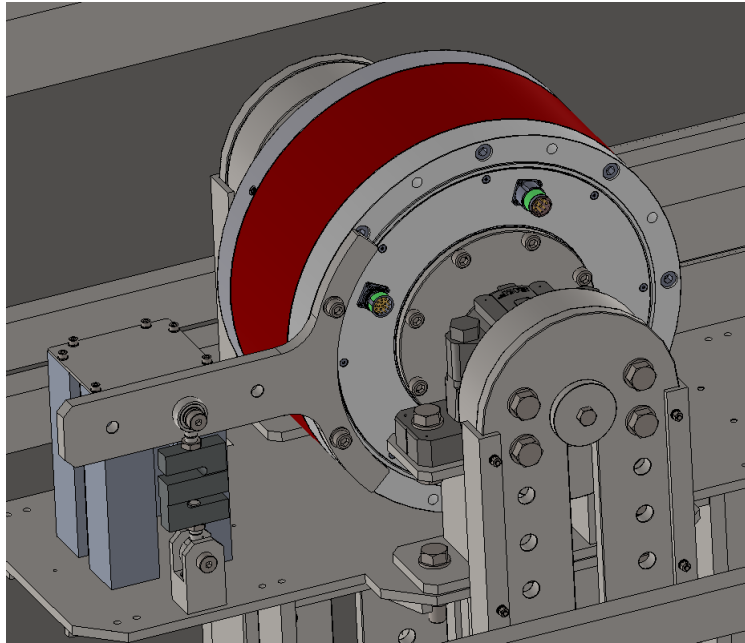
Fig. 5.30 Load cell 3D CAD model detail.

lever has been provided of other two holes, that allow to modify the sensibility of the measurement system. Table 5.8 summarizes the maximum measurable torque as a function of the load cell positing along the lever.

Table 5.8 Load cell positioning and maximum measurable torque.

Load cell position	1	2	3
Load cell distance from PTO axis (*mm*)	240	325	410
Maximum measurable torque (*Nm*)	471	638	804

A couple of spherical joints have been used in order to suspend the load cell and to avoid undesired force components orthogonal to the load cell measurement axis, due to mechanical misalignment.

The arm has been realized with C40 hardened carbon steel and its design has been optimized with a FEM analysis, aiming to limit the lever deformations and to guarantee a sufficient robustness of the component. In Fig. 5.31, the lever stress distribution corresponding to the worst case condition (maximum PTO torque, maximum arm length) is reported, while Fig. 5.32 shows the deformation distribution in the same operating condition. In the worst load condition, the maximum deflection in correspondence of the hole is equal to 0.1 *mm*, that can be acceptable, since it is
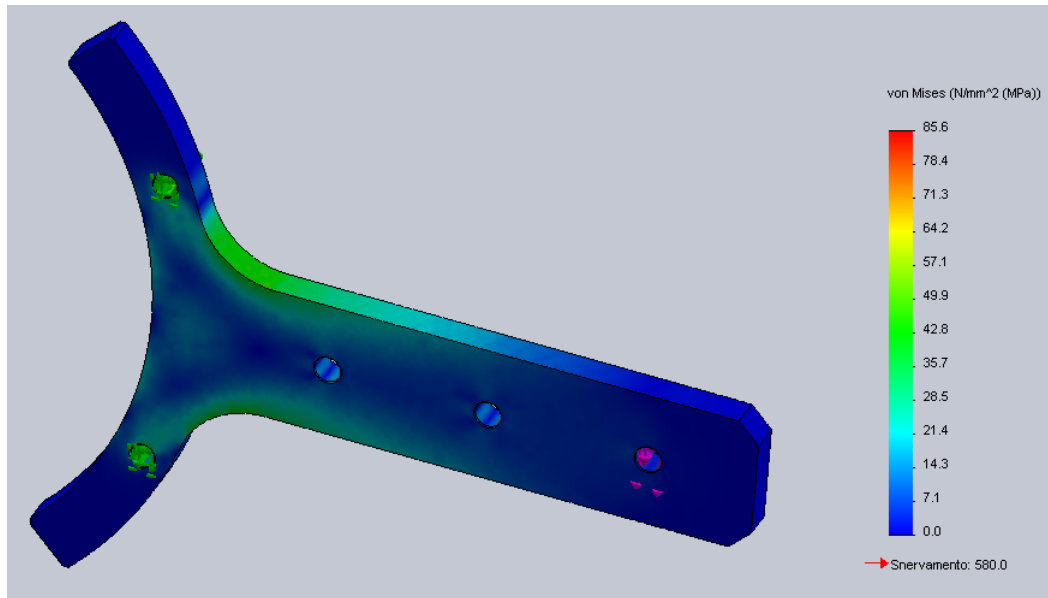
Fig. 5.31 Lever stress distribution in worst load conditions.
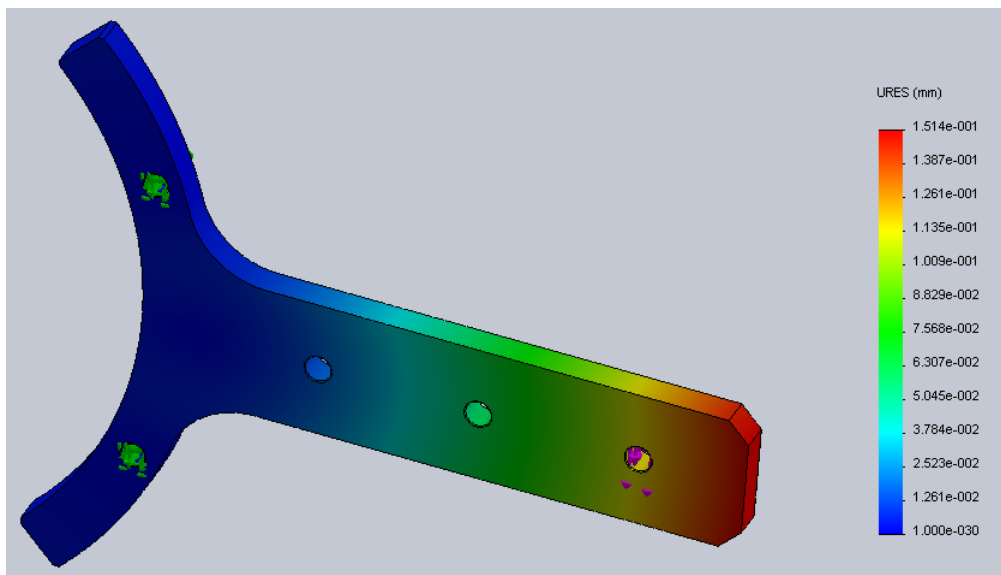
Fig. 5.32 Lever strain distribution in worst load conditions.

four times lower than the load cell deflection at rated capacity (0.4 *mm*). Moreover, if the deformation is known, it is possible to correct the measured data.

5.1.6   Device manufacturing and features summary

The design activity presented in the previous sections has been synthesized in a high fidelity 3D CAD model, including all the mechanical components constituting the device, but also the electric boards in which the control and power supply apparatus (described in section 5.1.8) are placed.
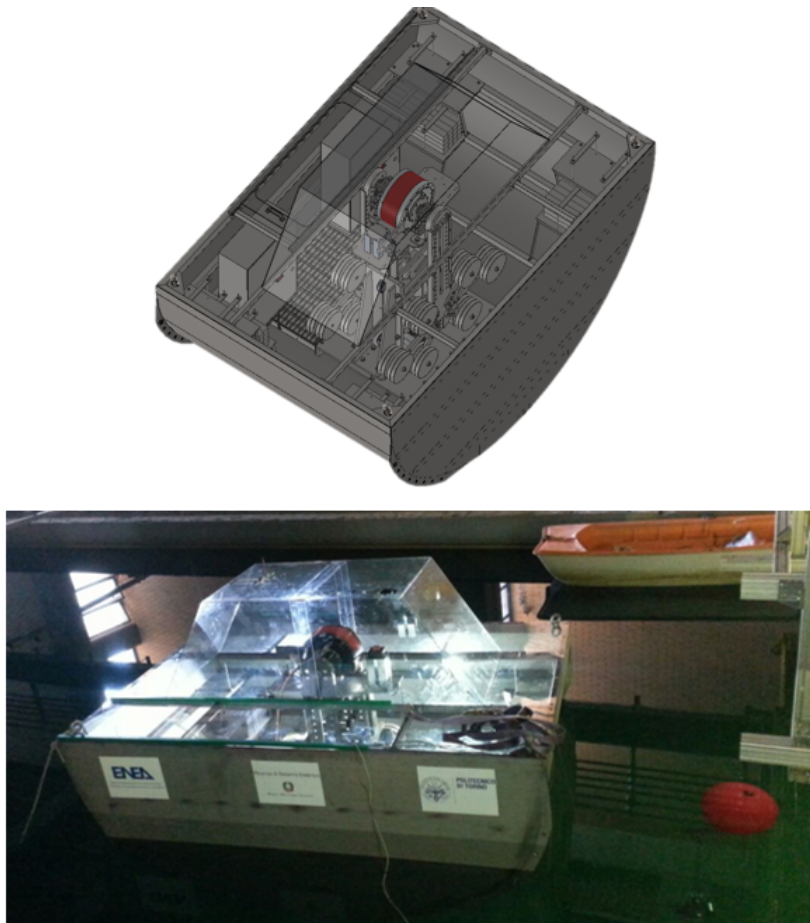
Fig. 5.33 1:12 PeWEC device 3D CAD model (top) and prototype deployed in the INSEAN wave basin (bottom).

From one side the CAD model is very important for the calculation of mass and inertial properties of the device varying the configurations available about ballast positioning, pendulum length and mass and vertical PTO axis positioning. On the

other side, the CAD model is very important for the development of the technical drawings required for the device manufacturing.

In Fig. 5.33, it is possible to compare the 3D CAD model and the real 1:12 scale PeWEC prototype deployed in the wave basin, while in Table 5.10 the main features of the device are summarized. It is noticeable that the latter are determined starting from the device 3D CAD model and taking into account the prototype set up made according to the design specifications indicated in the previous sections.

Table 5.9 1:12 scale device specifications.

Description	Symbol	Values	U.M.
Floater			
Radius	R	1.5	m
Length	L	3	m
Width	W	2	m
Draft	D	0.81	m
Overall mass	m_b	2766	kg
Upper ballast compartment mass	m_{up}	685	kg
Lower ballast compartment mass	m_{down}	204	kg
Center of gravity	COG	[0 0 -0.083]	m
Pendulum hinge - hull COG distance	d	0.909	m
Roll moment of inertia	I_{xx}	1576	kgm^2
Pitch axis moment of inertia	I_{yy}	2253	kgm^2
Yaw axis moment of inertia	I_{zz}	2798	kgm^2
Pendulum			
Semi major axis	a	0.525	m
Ellipse semi-axis ratio	λ	1.85	-
Mass	m_p	410	kg
Inertia	I_y	88.2	kgm^2
Length	l	0.986	m
PTO			
Rated torque	T_{rated}	220	Nm
Rated angular velocity	n_{rated}	90	rpm
Maximum torque	T_{max}	800	Nm
Maximum angular velocity	n_{rated}	90	rpm

In Fig. 5.34 different internal views of the prototype are depicted showing the real implementation of the design described in the previous sections, while a detail of the PTO and of the torque measurement system is proposed in Fig. 5.35.

Fig. 5.34 1:12 PeWEC device internal views.
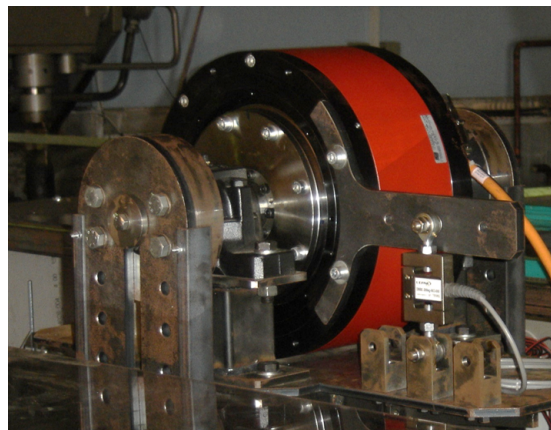
Fig. 5.35 1:12 PeWEC device PTO detail.

5.1.7 Mooring line

The mooring system has been built using the solution described from the theoretical point of view in section 3.4. It is constituted by a submerged jumper and a mass

connected, from one side to the seabed and to the other side to the hull, through three rope segments. The last segment, connecting the hull to the submerged mass, is split in two ropes. Each one is connected to one of the PeWEC sides, forming a *V*. Such configuration helps the self alignment of prototype with respect to the incoming wave. In Fig. 5.36, the mooring line arrangement during the installing operations is depicted.
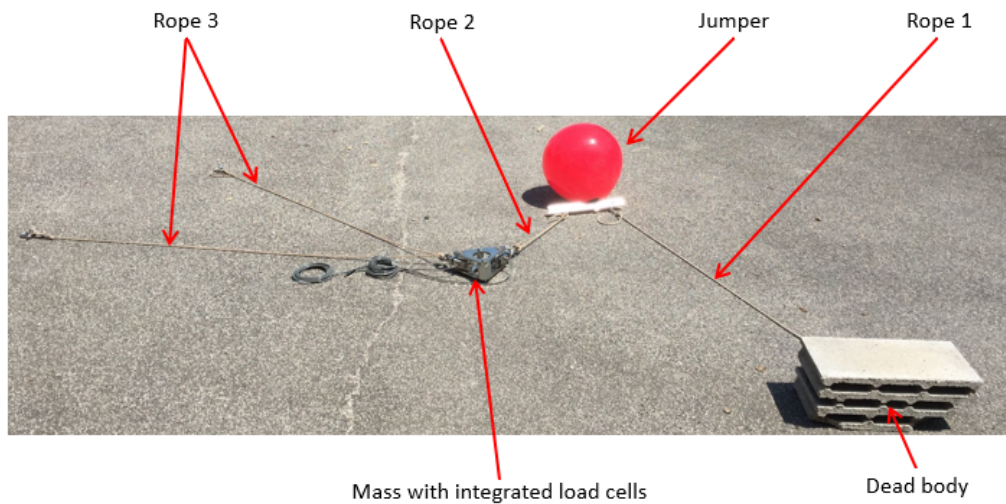
Fig. 5.36 Mooring line arrangement during installing operations.

The jumper has been realized with submerged buoy with 250 *N* of net buoyancy force, while the 98 *N* mass has been made through a structure designed to house two submersible load cells (*Leane DDBW 500*), with 500 *kg* rated capacity [64]. Load cells allow to measure rope 2 and 3 tensions. As stated before, the connection between mooring components and floater has been made with 6 *mm* diameter nylon rope segments. Table 5.10 summarizes the mooring line properties.

Table 5.10 Mooring line specifications.

Description	Symbol	Values	U.M.
Net gravity force	F_g	98	*N*
Net buoyancy force	F_b	250	*N*
Chain mass per unit of length	m_l	0.012	$\frac{kg}{m}$
First line length	l_1	1.8	*m*
Second line length	l_2	0.4	*m*
Third line length	l_3	2	*m*

5.1.8   Electric and control systems

The last part of the device design has been concerned with the development of the electrical and control systems, represented in the scheme reported in Fig. 5.37. It shows the interconnections between the different components: the colored lines allows to distinguish the different voltage levels or the cable typology, while the line width is proportional to the wire section.

The electric system has been organized in two distinct panels: the first contains the power supply systems, while the second contains the low power and control systems.

The device is powered by four 12*V FIAMM 12FLB400* VRLA batteries connected in series, in order to obtain two 24 *V* battery packs. Each battery has a 100 *Ah* capacity. The two battery packs are connected in parallel achieving a 200 *Ah* overall capacity.
Batteries are protected by fuses and are connected to an inverter stored in the first electric board. It converts the direct current provided by the battery in 230 *V* 50 *Hz* alternate current. Circuit breakers protect the power outlets available on the first electric board and the line that delivers the current to the second electric board.
Batteries can be charged connecting the prototype to an external power source (black triangle in Fig. 5.37). When the device is in charging mode, the switch placed between electric board 1 and 2 is open and the power flow is converted in direct current from the inverter and delivered to the batteries.

Considering the second electric board, the 230 *V* a.c. supply two power supplies: one provides the 5 *V* DC voltage, while the second the 24 *V* DC voltage.
The 5 *V* DC voltage is used to power the limits switches (FC1 and FC2), used to interrupt the motor power (M), when the frame reaches the upper or lower position, the frame vertical position transducer (PT) and the inertial platform *UM7*. The latter is very similar to the *MTi* device and it is used as back up. Note that each device is protected by a fuse.

On the other side, the 24 *V* DC voltage supplies the following devices:

- *NI cRio*: as described in section 4.3.7, this device is used for the data logging of the different signals coming from the PeWEC on board sensors and the elaboration of the PTO control reference signal. More in detail, it is equipped with the following modules:
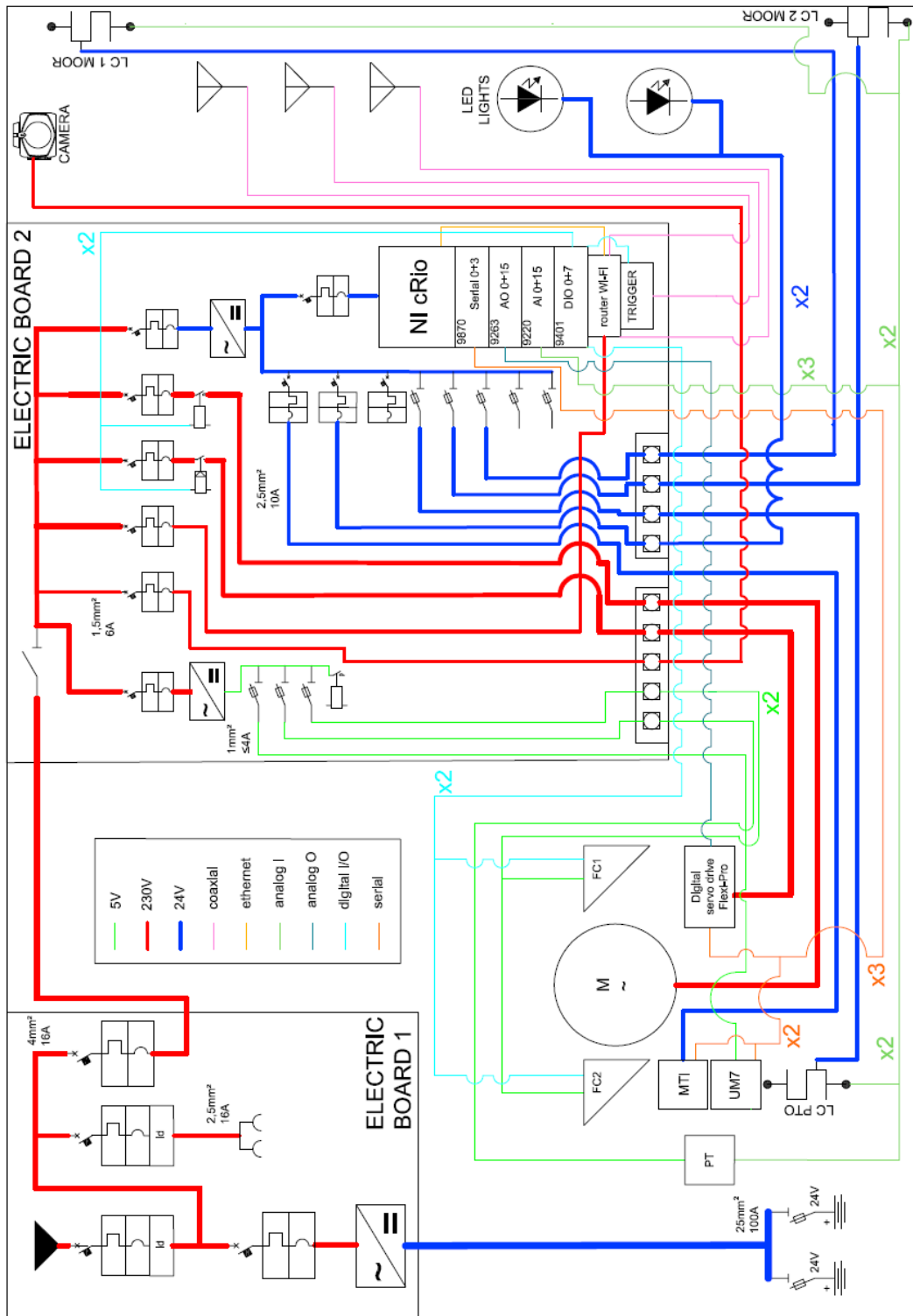
Fig. 5.37 1:12 PeWEC device electrical and control system scheme.

- *Serial module 9870*: configured for the management of the *MTi*, *UM7* and PTO encoder signals. The latter comes from the *FlexiPro* digital servo drive.

- *Analog module 9263*: provides a voltage in the range $\pm$ 10 *V* and proportional to the desired instantaneous PTO torque calculated according to Eq. 4.6. Such voltage is given in input to the PTO digital servo drive.

- *Analog input module 9220*: collects the signals in the range $\pm$ 10 *V* coming from the PTO and mooring line load cells conditioners and the voltage in the range 0 - 10 *V* proportional to the frame vertical position.

- *Digital Input/Output module 9401*: it manages the digital input signal (0 - 5 *V*) related to the limit switched status (open/close). If one of the limit switches is close, the digital output signal that enables the motor switch relay is lowered to 0 *V*, interrupting the motor supply. On the other hand, if the limit switches are not pressed, the corresponding output signals are in the lower logical status (0 *V*), as well as the digital signal that enables the motor switch relay. The motor is activated by the user through the *LabView* interface. The motor rotation direction is managed by a relay card not represented in Fig. 5.37. The latter has not been drawn in order to do not make the scheme to heavy.
Moreover, this module generates a digital signal that enables digital servo drive power. In case of emergency, it is possible to disable the PTO from the *LabView* user interface. Lastly, the digital module manages also the command that enables the TTL trigger device, allowing the synchronization of the PeWEC and INSEAN data logging systems, as described in section 4.4.2. The TTL trigger signal is sent to the INSEAN data logging system via WiFi.

- PTO load cell conditioner.

- Mooring line load cells conditioners.

- Internal LED lights: used to illuminate the device interiors during the experimental testing or set up activities.

Note that all the 5 *V* DC and 24 *V* DC loads are protected through fuses or circuit breakers.

Lastly, the 230 *V* alternate current supply the electrical motor acting the frame screw-nut system, the camera used to monitor and film the pendulum motion and the

WiFi router . The router is connected via coaxial cables to the antennas, that transmit the prototype data to the monitoring station.

5.2 Prototype testing

5.2.1 Testing facility

The 1:12 scale PeWEC device has been tested at the INSEAN towing tank (Rome), the same infrastructure used for the 1:45 scale prototype testing and described in section 4.4.1. In fact, as also described in section 5.1.1, the 1:12 PeWEC floater has been designed specifically taking int account the INSEAN wave basin capabilities.

5.2.2 Experimental set-up

The PeWEC device has been moored on the towing tank sea bed through the mooring line described in section 5.1.7. The dead body was positioned at 60 m from the wave maker, which has been assumed as reference (0 m) (see Fig. 5.38).
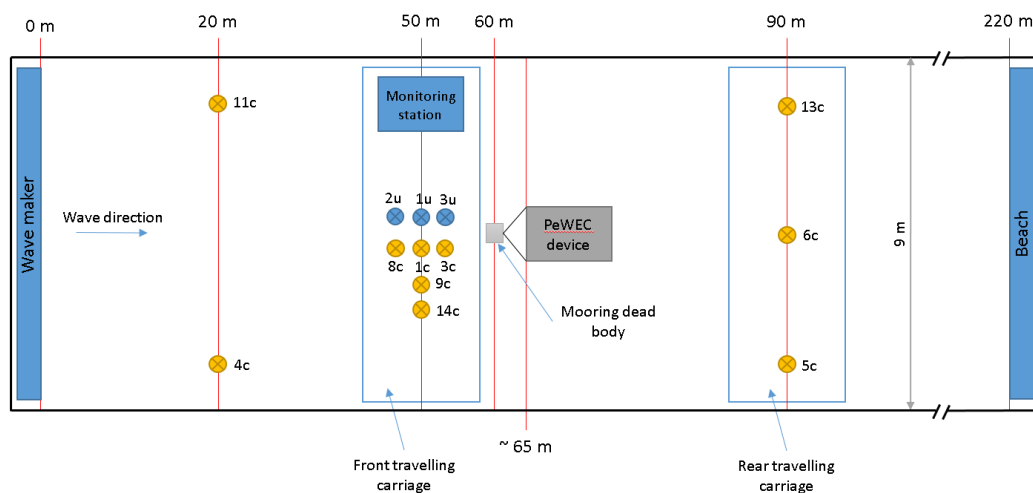
Fig. 5.38 Experimental set-up scheme.

During the operating conditions, the bow of the hull was expected to be in a range between 60 and 70 m from the wave maker, according to the incoming wave characteristics. The dead body distance from the wave maker has been chosen,

considering the case of regular waves, in order to have at least ten cycles of pitch oscillations, without any interference due to the reflected wave. This calculation has been performed using the criteria explained in section 4.4.2. One of the two carriages available has been placed in front of the device under investigation and used as monitoring station: here the laptops used for the system controlling and data logging have been housed, together with the laptop used to control the wave maker. Data from wave probes and cRio are logged with a frequency sampling of 50 *Hz*. Furthermore, on this carriage some probes for wave monitoring have been fasten, with the aim to monitor the wave field in the area in front of the device. In particular, three capacitive (*8c*, *1c*, *3c*) and three ultrasonic probes (*2u*, *1u*, *3u*) have been used. The ultrasonic probes have been fixed around the wave tank center line, while capacitive probes *9c* and *14c* have been placed in parallel to probes *1c* and *1u*. The undisturbed wave profile has been monitored through a couple of capacitive probes positioned on a frame at 20 *m* from the wave maker, while the attenuated wave field on the back of the Wave Energy Converter has been acquired thanks to three capacitive probes (*5c*, *6c*, *13c*) settled on the carriage behind PeWEC, at 90 *m* from the wave maker. The two typologies of probes used are managed by two different data logging systems, synchronized via a TTL trigger signal given, at the begin of each test, by the on board PeWEC control system.

5.2.3   Prototype configurations

The 1:12 scale PeWEC prototype, as previously described, has been designed in order to offer several variation with respect to the design configuration named C1. Starting from this configuration, three different variants have been considered (C2, C3, C4). Each one has been determined by means of the linear numerical model.

In the following bullet a brief description of each configuration and of the related set-up is given, while in Table 5.11 the main features are summarized.

- *Configuration C1*: first configuration investigated corresponding to the design layout carried out through the design and optimization procedure described in section 5.1.

- *Configuration C2*: the second prototype configuration has been developed with the aim to harvest longer wave periods, without changing the pendulum

Table 5.11 Investigated 1:12 prototype configurations properties.

	C1	C2	C3	C4	
		Floater			
m_b	2766	2766	2766	2918	kg
COG	[0 0 -0.083]	[0 0 0.18]	[0 0 -0.005]	[0 0 -0.1]	m
d	0.858	0.842	0.765	0.969	m
I_{xx}	1499	1645	1627	1649	kgm^2
I_{yy}	2168	2608	2589	2238	kgm^2
I_{zz}	2761	3054	3054	2844	kgm^2
		Pendulum			
m_p	410	410	410	258	kg
I_y	88.2	88.2	88.2	58.3	kgm^2
l	0.986	0.986	0.986	0.915	m

set-up and the overall mass of the device. More in detail, the floater resonance period has been increased from 2.2 to 2.5 *s*, as reported in Fig. 5.39, moving the ballasts placed in the upper compartments from the lower to the higher position and increasing the frame vertical position of 0.1 *m*. Observing Fig. 5.40, it is clear to note that the resonance period at 2 *s* does not change, since the pendulum resonance period has not been modified. On the other hand, the second resonance period moved from 2.5 *s* to 2.8 *s*.

- *Configuration C3*: the set up of this configuration, has been obtained starting form configuration *C2* reducing the frame vertical position of 0.1 *m*. The aim is to evaluate the influence of the distance *d* variation, on the prototype dynamics. The overall mass of the device has been maintained constant.

- *Configuration C4*: the last configuration has been prepared in order to evaluate the influence of the pendulum mass on system performances. The latter has been reduced from 410 to 258 *kg*, while the pendulum resonance period has been tuned at 2.2 *s*. Meanwhile, the floater resonance period has been set at 2.2 *s* adjusting the ballast in the lower position available in the upper compartments and adding some steel bars in the lower ballast compartment, in order to compensate the device mass reduction due to the pendulum lightening.
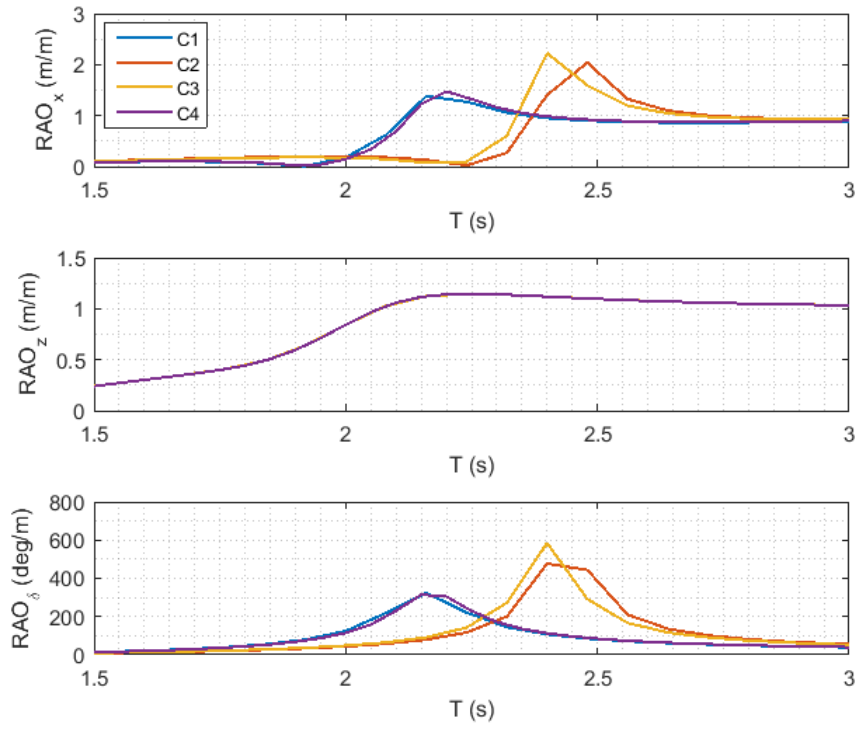
Fig. 5.39 Computed RAOs for the different prototype configurations.
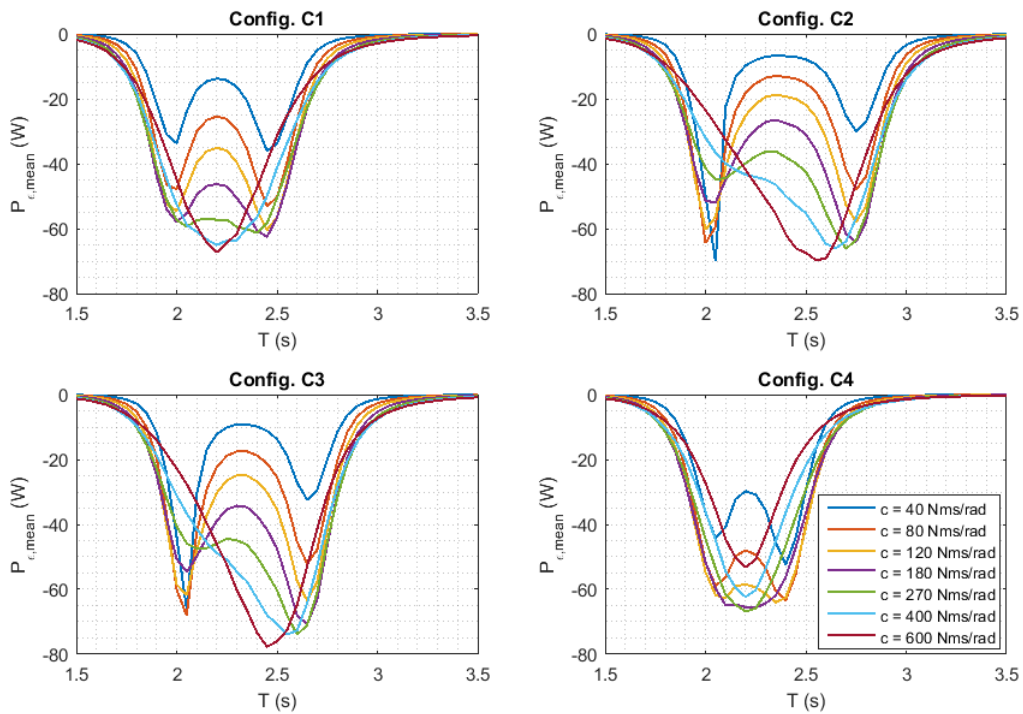
Fig. 5.40 Computed average extracted power for the different prototype configurations.

5.2.4   Regular wave tests

The first part of the prototype testing campaign has been dedicated to the evaluation of its dynamics in regular waves and so the device behavior in frequency domain [39]. According to the wave basin capabilities and to the WEC dynamics estimated through numerical models, a set of regular waves has been defined. Before starting with the device testing procedure, waves calibration process has been performed in order to estimate their quality and eventually adjusting the wave-maker control system. Table 5.12 summarizes the regular wave conditions used for the WEC tank testing, the characteristics of the theoretical wave and the average relative error, calculated comparing theoretical wave properties against the ones generated in the wave basin.

Table 5.12 Regular waves set theoretical parameters and relative error with respect to measured waves.

	Theoretical wave			Relative error		
Code	$H(m)$	$T(s)$	$WPD(\frac{W}{m})$	$H(\%)$	$T(\%)$	$WPD(\%)$
A	0.15	1.90	42.75	0.67	-0.53	0.80
B	0.15	2.00	45.00	-2.00	0.00	-3.96
C	0.15	2.10	47.25	-0.67	-0.48	-1.80
D	0.15	2.20	49.50	0.00	0.00	0.00
E	0.15	2.30	51.75	-0.67	-0.43	-1.76
F	0.15	2.40	54.00	1.33	-0.42	2.26
G	0.15	2.50	56.25	-1.33	0.00	-2.65
H	0.15	2.60	58.50	-2.00	-0.38	-4.33
I	0.15	2.70	60.75	0.67	-0.37	0.96
L	0.15	2.80	63.00	4.00	0.00	8.16

Configuration C1: Moored system Response Amplitude Operator

The modulus of Response Amplitude Operator (RAO) determines the dynamic response of a floating structure with respect to the frequency of the incoming wave. As previously stated, the resonance of the hull must be close to the period of the design wave, in order to achieve the maximum power extraction. The pitch degree of freedom RAO has been experimentally determined tilting the moored floater with

the regular waves from A to F given in Table 5.12, while the internal pendulum has been kept locked.

In Fig. 5.41, the comparison between the experimental results and the numerical data, obtained via Ansys AQWA, is shown: experimental data, represented by the black circles, have been interpolated through the *Piecewise Cubic Hermite Interpolating Polynomial* method [49] over the wave periods used for the numerical simulations. The interpolated data are represented by the red dashed line. A good agreement between the numerical simulations (continuous blue line) and experimental data has been achieved, proving that the hull is very reactive around the design wave period.
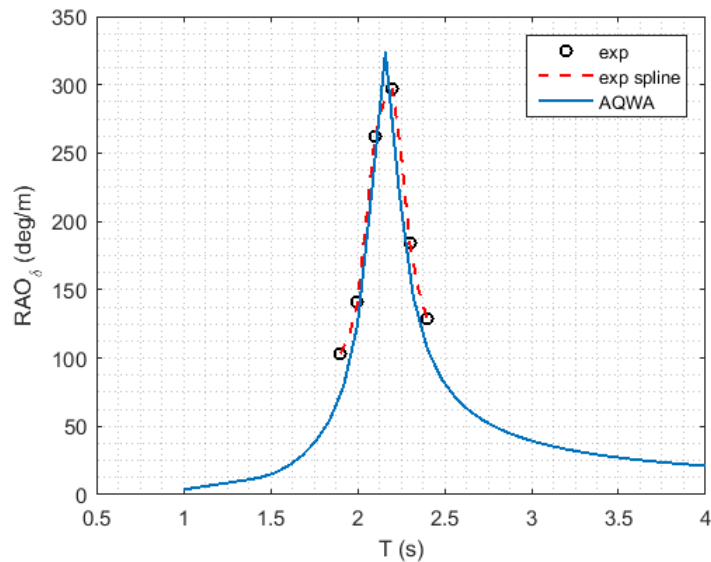
Fig. 5.41 Moored system pitch Response Amplitude Operator: experimental data (black circles), spline over experimental data (red dashed line), numerical data (continuous blue line).

Configuration C1: Frequency sweep

After the hull dynamic response verification, the pendulum has been unlocked and the experimental frequency sweep with constant PTO damping coefficient at 40 $\frac{Nms}{rad}$ has been performed. Wave period has been varied between 1.9 s and 2.8 s, according to the wave set given in Table 5.12.

Fig. 5.42 summarizes the most important results related to the floater and pendulum kinematic, PTO torque and power and Relative Capture Width, highlighting root mean square and maximum values. As foreseen by numerical simulation performed in section 5.1.4, for low PTO control damping values, the device dynamic response is characterized by two distinct resonances: the first at 2 *s*, the second at *2.5* s. In addition, the expected performances in term of extracted power are quite similar in both conditions. Conversely, at 2.2 *s* wave period, the WEC performances are lower.
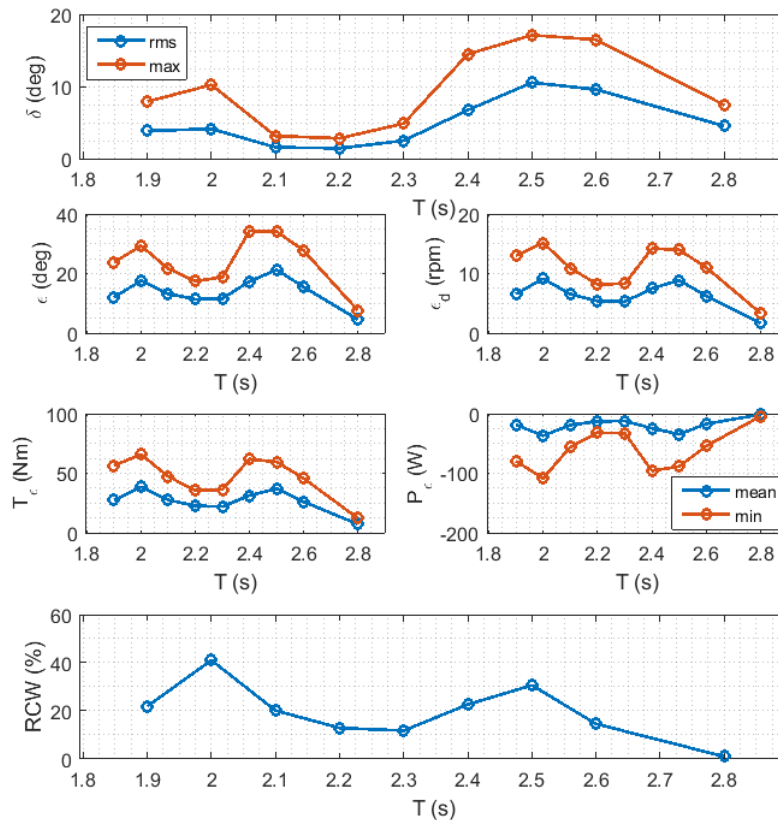
Fig. 5.42 Configuration C1: frequency sweep with constant PTO damping coefficient $\left(40\ \frac{Nms}{rad}\right)$.

Configuration C1: PTO damping coefficient variation

The PTO damping coefficient is the only parameter that can be tuned in order to maximize the device extracted power, taking into account the different sea state conditions that might occur. For this reason, a series of tests have been performed in correspondence of 2, 2.2 and 2.5 *s* wave periods, varying the PTO damping

coefficient, until a maximization of the average extracted power was reached, as reported in Fig. 5.43
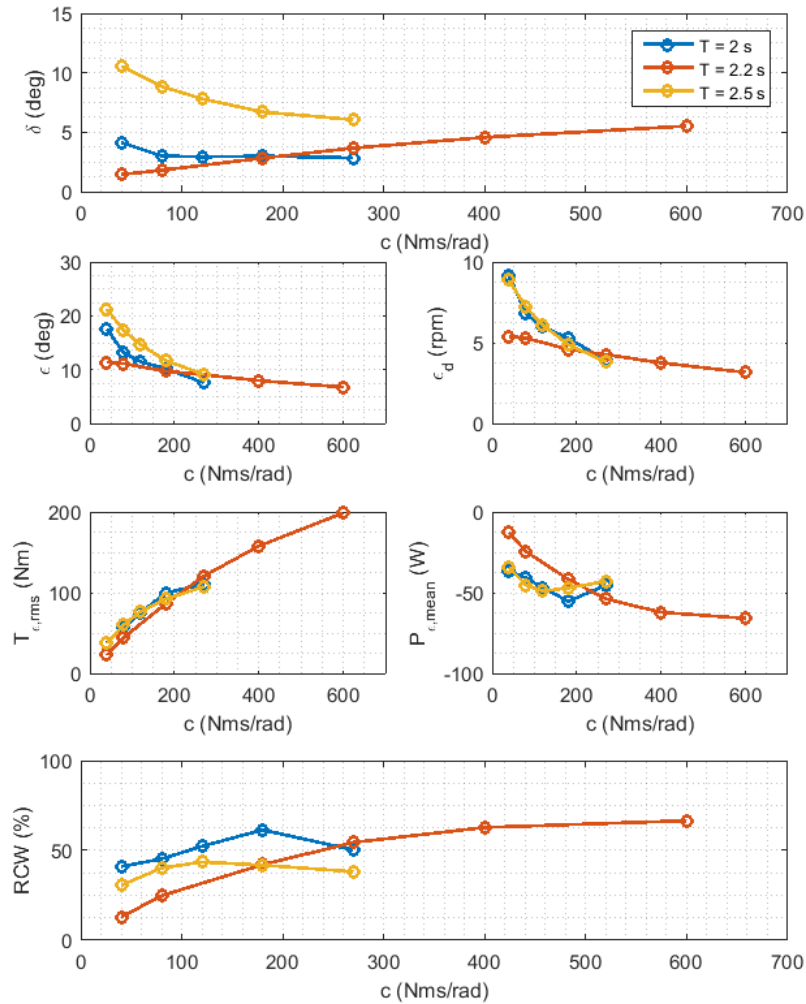
Fig. 5.43 Configuration C1: PTO damping coefficient variation for three different wave periods (2 *s*, 2.2 *s*, 2.5 *s*).

In the case of the tests at 2 *s* wave period the maximum average extracted power is reached when the PTO damping coefficient is equal to 180 $\frac{Nms}{rad}$, while at 2.5 *s* wave period the maximum performances are achieved when the PTO damping coefficient is set at 120 $\frac{Nms}{rad}$. Also the values and the trends of the pendulum angular displacement and speed and PTO torque are very similar for both wave periods. The Relative Capture Width variates between 30% and 50% over the entire damping coefficient span considered (40 $\frac{Nms}{rad}$ - 270 $\frac{Nms}{rad}$). Lastly, it is possible to observe that the pitch motion amplitude is higher when the wave period is set at 2.5 *s*.

A complete different behavior can be observed if the 2.2 *s* wave period is considered: the hull motion amplitude increases when the PTO damping coefficient is raised, in opposition to the trends highlighted previously. Furthermore, in correspondence of this wave period, a positive correlation between the PTO damping coefficient variation and the system performances can be seen. The maximization of the mean power is achieved when this coefficient is equal to 600 $\frac{Nms}{rad}$, both for the average extracted power and for the RCW. The latter is the maximum of the range considered. It is also important to point out that the measured PTO torque root mean square value is below the PTO rated torque (220 *Nm*), while the maximum torque did not exceeded the maximum torque available (800 *Nm*), avoiding the introduction of nonlinearities due to PTO saturations.

More in general, it is possible to find out that varying properly the PTO damping coefficient, it is possible to optimize the system performances for different wave periods.

Configurations C2 and C1 comparison

The configuration C2, as previously described, has been designed in order to harvest longer wave periods, thanks to the increment of the second resonance period from 2.5 to 2.8 *s*. In Fig. 5.44, the dynamic behavior of configuration C1 tested at 2.5 *s* wave period and of configuration C2 tested at 2.8 *s* are compared. Both configurations have been studied varying the PTO damping coefficient.

Floater pitching amplitude and pendulum swinging angle are greater in the case of configuration C2, because of a higher WPD. In fact also the average extracted power is consistently higher. Moreover, the maximum efficiency achieved by configuration C2 is equal to 60%, when the PTO damping coefficient is set at 270 $\frac{Nms}{rad}$, 20% higher than the efficiency achieved by configuration C1 in correspondence of the second resonance period.

As explained above, another system resonance is available at 2 *s* wave period. A series of tests have been performed in correspondence of this condition, with the aim to determine the variation of the system performances with respect to the initial configuration (C1), as represented in Fig. 5.45

The increasing of the floater pitching inertia allows to produce a substantial modification of the second system resonance period, but also a significant reduction
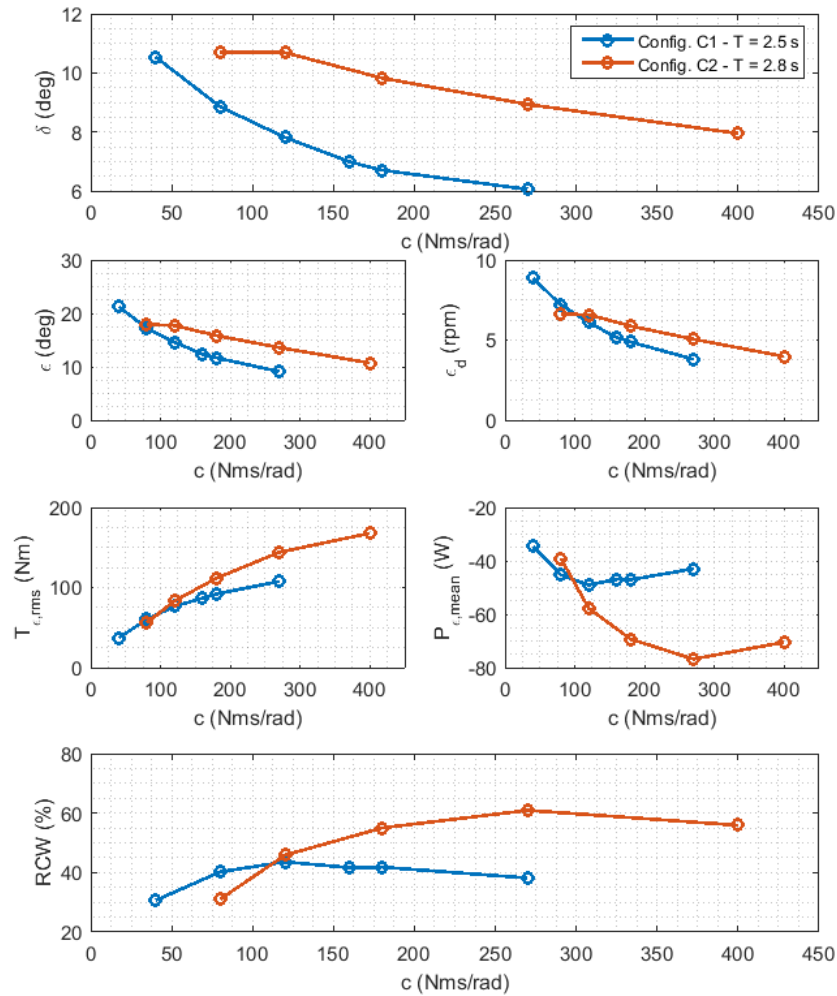
Fig. 5.44 Configuration C2 testing results performed at 2.8 *s* wave period compared to the configuration C1 testing results obtained at 2.5 *s* wave period.

of performances in correspondence of the first resonance period. In particular, when the PTO damping coefficient is set at 40 and 80 $\frac{Nms}{rad}$ the pendulum motion and the extracted power are almost similar, even if the the pitch amplitude is 25% lower (on average). Meanwhile, a divergence of the configurations performances can be highlighted when the control parameter is further increased. In fact, extracted power and RCW are maximized, in the case of configuration C2, when c is equal to 80 $\frac{Nms}{rad}$, that results be a 30% less than the performances of the initial configuration.
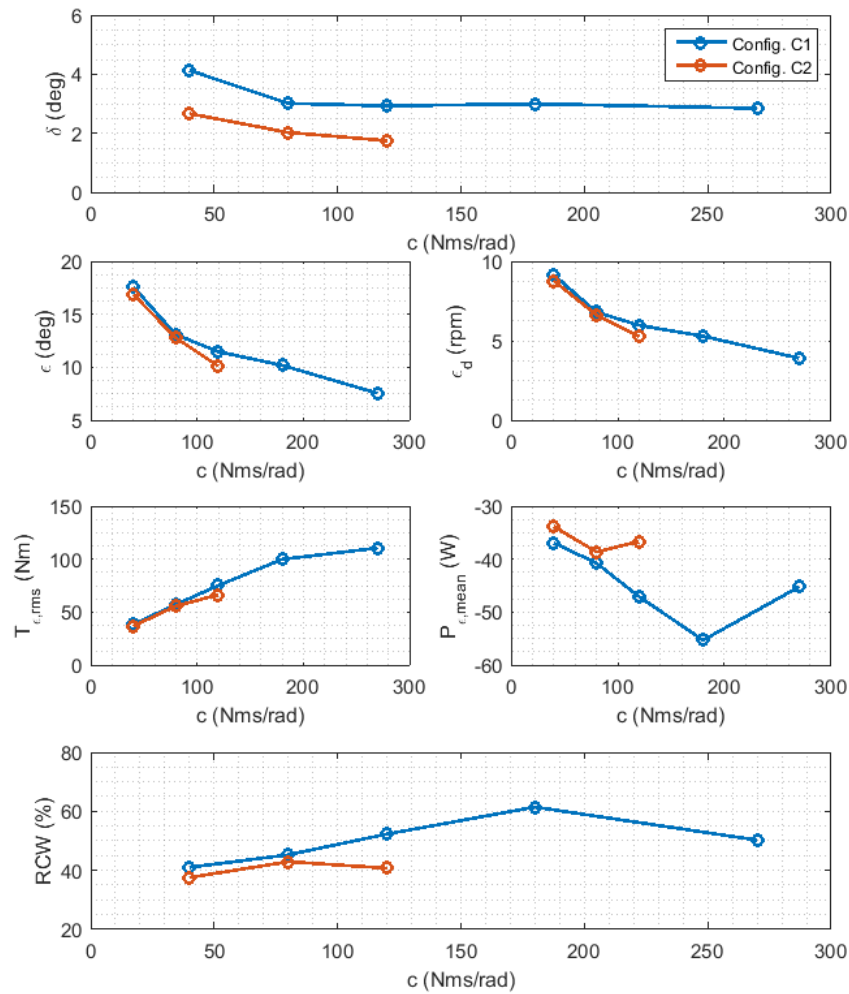
Fig. 5.45 Configuration C2 and C1 comparison at 2 *s* wave period, varying the PTO control damping.

Configurations C3 and C1 comparison

Configuration C3 has been obtained starting form configuration C2 reducing the frame vertical position of 0.1 *m*, equivalent to reduction of the distance *d* of 77 *mm*, aiming to evaluate the influence of such distance variation, on the prototype dynamics.

According to the indications given by simulations results reported in Fig. 5.40, the prototype has been tested at 2.7 *s* wave period, where the second resonance period due to pendulum-floater coupling is expected and proved by the experimental results reported in Fig. 5.46. Moreover, the prototype has been tested at 2.5 *s* wave

period where, according to the numerical simulation, the device extracted power should be higher that the one measured at 2.7 s, when the PTO damping coefficient is raised up to 900 $\frac{Nms}{rad}$. This fact has been proved by the experimental tests reported in Fig. 5.46. It also important to highlight that the behavior detected at 2.5 s wave period is very similar to the one denoted in the case of configuration C1 at 2.2 s wave period. Lastly, the results obtained at 2 s wave period with configuration C3 are comparable with the one described in the previous paragraph.
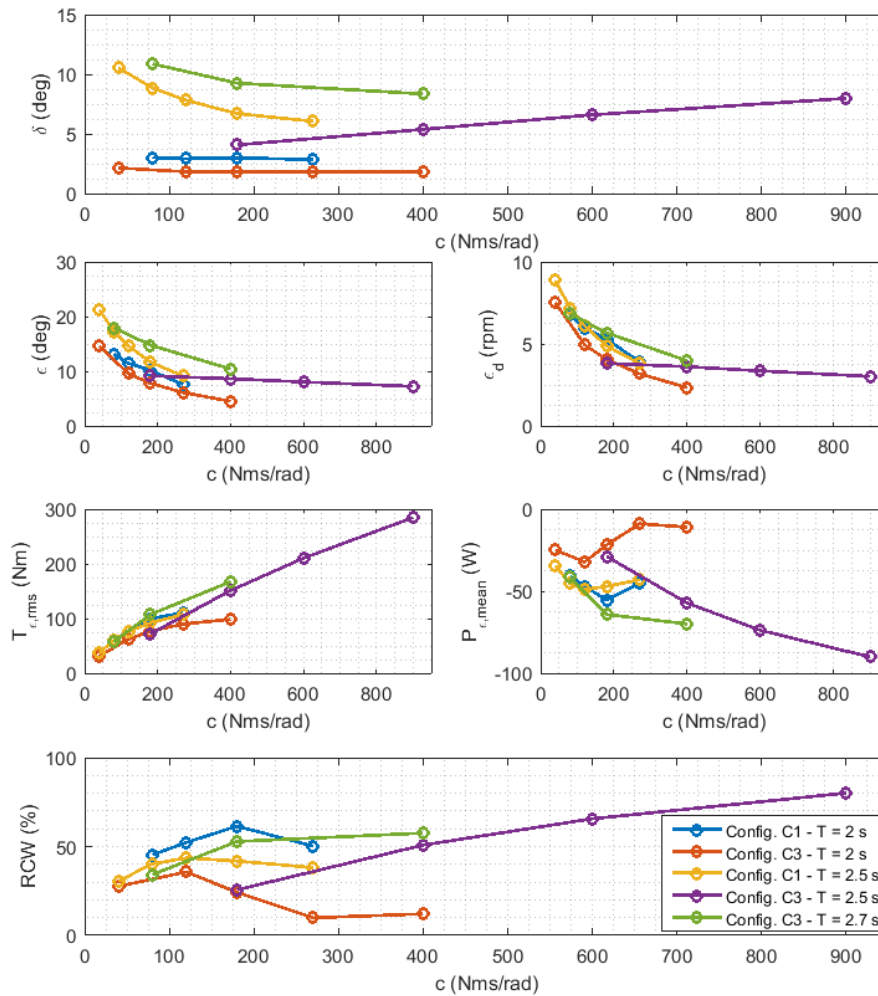
Fig. 5.46 Configuration C3 and C1 comparison at different wave periods and different PTO control damping values.

Configurations C4 and C1 comparison

The last part of the regular wave tests has been dedicated to the evaluation of the pendulum mass influence on the device performances. The configuration C4, as described in section 5.2.3, has been set up in order to obtain a behavior similar with respect to the design configuration C1. It has been tested in correspondence of the design wave period, where the PTO is more stressed in terms of torque. In this condition, the device performances can be maximized raising up the PTO control damping.
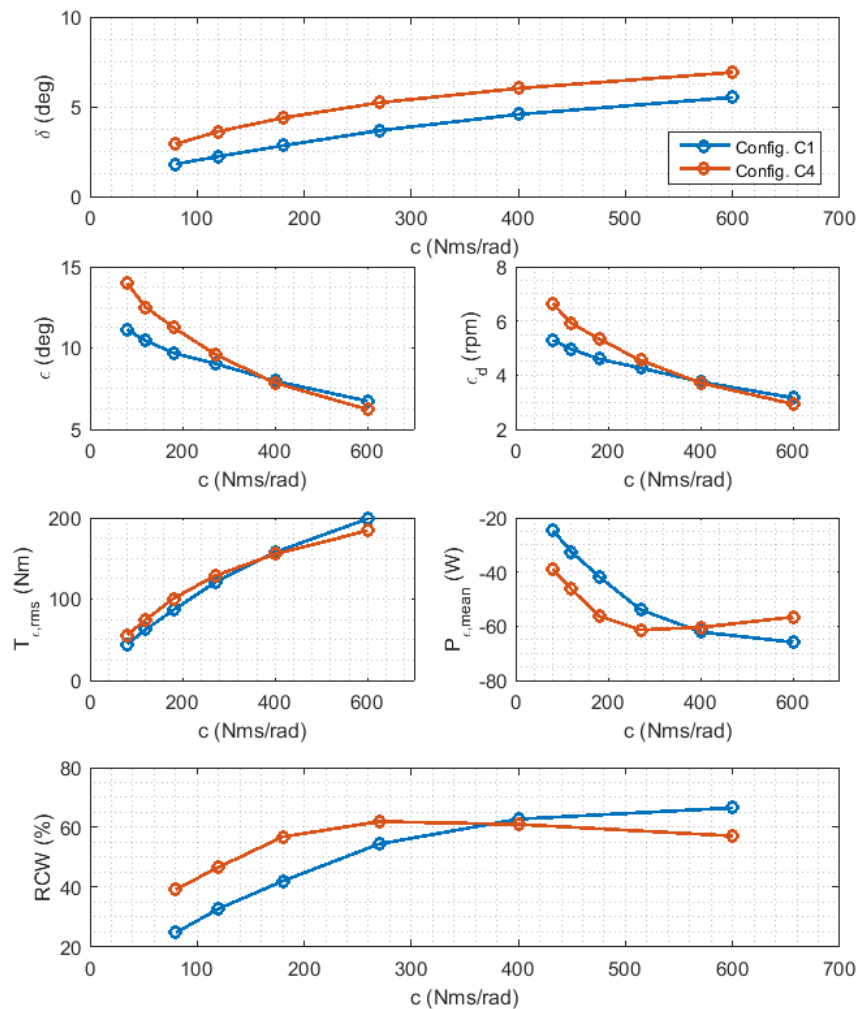
Fig. 5.47 Configuration C4 and C1 comparison at 2.2 *s* wave period and with different PTO control damping values.

Fig. 5.47 reports the comparison between configurations C4 and C1. The configuration C4 pitch motion is slightly wider than the one measured for configuration C1, even if trends have the same shape. The difference is constant for all the PTO control damping values investigated. This means that such difference is due to a not perfect match of the pitch RAOs for configurations C1 and C4. However, the difference can be assumed acceptable for the comparison.

Observing the pendulum swinging angle and its angular velocity measured for the two configurations considered, it is possible to see that the lighter pendulum is characterized by higher velocities and amplitudes of motion, when the PTO damping coefficient is below 400 $\frac{Nms}{rad}$. In fact, in correspondence of this value, a trade off can be observed. The measured PTO torque is very similar for both configurations and on the entire span chosen for the PTO control parameter. However, it is important to underline that configuration C4 reaches the optimal average extracted power and RCW in correspondence of a lower PTO damping coefficient, if compared with configuration C1 results. This also means that it is possible to achieve almost the same efficiency and extracted power in correspondence of the design wave period with a lighter pendulum and a smaller electrical generator.

These results are of remarkable importance, since they allows to validate somehow the considerations developed during the pendulum design phase, reported in section 5.1.4.

5.2.5   Irregular wave tests

The second part of prototype testing campaign has been dedicated to evaluation of its dynamics in irregular waves. As described in in section 4.4.3 and section 5.2.4, monochromatic tests allow to understand how the WEC works, while irregular sea test are useful reveal how the WEC will perform under the action of the real sea state [39].

When specifying a test program in irregular waves, it is important to take into account different factors such as spectrum type (e.g. Bretschneider, JONSWAP), according to the sea state characteristics of the installation site, length of the wave time series, sea state summary statistics, directionality and spreading. On the other hand, if real sea state records are available, it is possible scaled down the wave profile according to the model scaling factor.
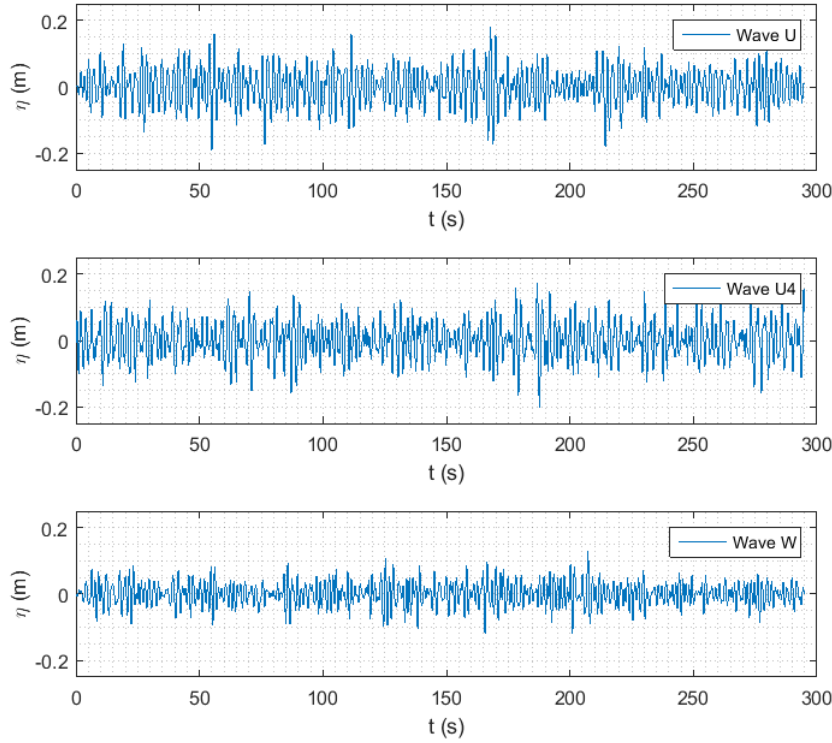
Fig. 5.48 Irregular wave profiles used for the 1:12 PeWEC device testing.

In the case of this work, both methodologies have been considered. Wave U and W correspond to real sea state data acquired in the Pantelleria Island site (as specified in section 4.1) and scaled according to the prototype scaling factor and the Froude scaling law. In particular, wave U represent the design irregular sea state. The design wave has been reproduced also using the JONSWAP spectrum and random phase algorithm for the definition of the phase between the different harmonics. The U4 wave profile generation has been performed by using the WAFO toolbox [126].

Table 5.13 Irregular waves set theoretical parameters and relative error with respect to measured waves.

	Theoretical wave			Relative error			Spectrum
Code	$H_s(m)$	$T_e(s)$	$WPD\left(\frac{W}{m}\right)$	$H_s(\%)$	$T_e(\%)$	$WPD(\%)$	
U	0.221	2.23	54.46	2.26	-4.93	-0.29	-
$U4$	0.221	2.23	54.46	-1.5	0.6	-2.4	JONSWAP
W	0.139	1.94	18.74	2.16	-1.19	2.99	-

Table 5.13 summarizes the irregular waves parameters used for the WEC tank testing and the percentage error with respect to the theoretical wave parameters. In Fig. 5.48 the time series of the three irregular wave profiles used are depicted.

Configuration C1: PTO damping coefficient variation

As stated before, the PTO damping coefficient allows to govern the power extraction of the device and similarly to the test performed in regular sea state, this parameter was varied in order to achieve the maximum power extraction, given a certain wave [95].
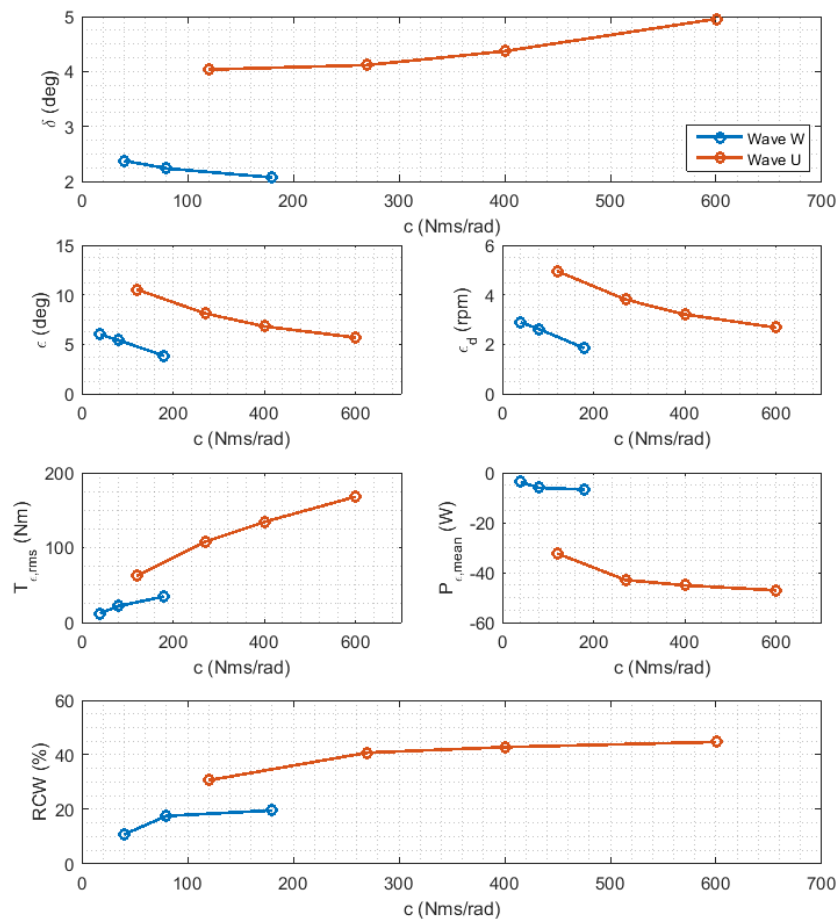
Fig. 5.49 Configuration C1: irregular wave U and W test results, varying the PTO damping coefficient.

Fig. 5.49 summarizes the experimental behavior of the system, when it was excited with the irregular waves U and W and the PTO damping coefficient was

varied from 120 $\frac{Nms}{rad}$ to 600 $\frac{Nms}{rad}$ in the first case and from 40 $\frac{Nms}{rad}$ to 180 $\frac{Nms}{rad}$ in the second one.

Considering the design testing condition defined by the wave U, it is possible to see that the behavior of the system is almost similar to the one denoted with the 2.2 s monochromatic wave. In fact, the hull pitch amplitude increases when the PTO damping coefficient is increased, while the extracted power reaches its maximum when the control parameter is set at 600 $\frac{Nms}{rad}$, which is the maximum value considered during the tests. Consequently, in this condition, the RCW reaches the maximum value of 47%. Globally, the efficiency obtained in the case of irregular sea state is lower than the one obtained in the case of the corresponding regular sea tests. Taking into account the results achieved with the wave W, it is possible to see a diminution of the hull pitch amplitude with the increasing of the PTO damping coefficient, similarly to the monochromatic tests performed at 2 s. Furthermore, the maximum power extraction has been achieved with a lower value of the PTO damping coefficient $\left(180 \frac{Nms}{rad}\right)$.

Configuration C1: device performances comparison under real and synthetic design scale waves

Another relevant aspect regards the irregular sea wave elevation modeling. As reported in section 3.3.4, wave elevation can through can be determined through the superimposition of a finite number of regular waves characterized by different heights and periods, on the base of a standardized spectrum. According to this methodology, the irregular design wave has been generated through the JONSWAP spectrum, built imposing the desired significant wave height and energy period. Then, the device configuration C1 has been tested for different PTO damping coefficients values and using both the real Pantelleria scaled wave and the synthetic wave. Fig. 5.50 reports the experimental results obtained: pitch motion is characterized by a minimum valued, which can be pointed out for different PTO damping values. Pendulum motion and angular speed, PTO torque and extracted power are approximately similar in term of shape, however the performances determined with the synthetic wave are lower than performances achieved with the Pantelleria scale wave profile. In the light of these considerations, it appears of relevant importance a proper modeling of resource, in order to achieve a proper estimation of the WEC performances. For instance, other parameters such as the groupiness factor and the shape of the spectrum
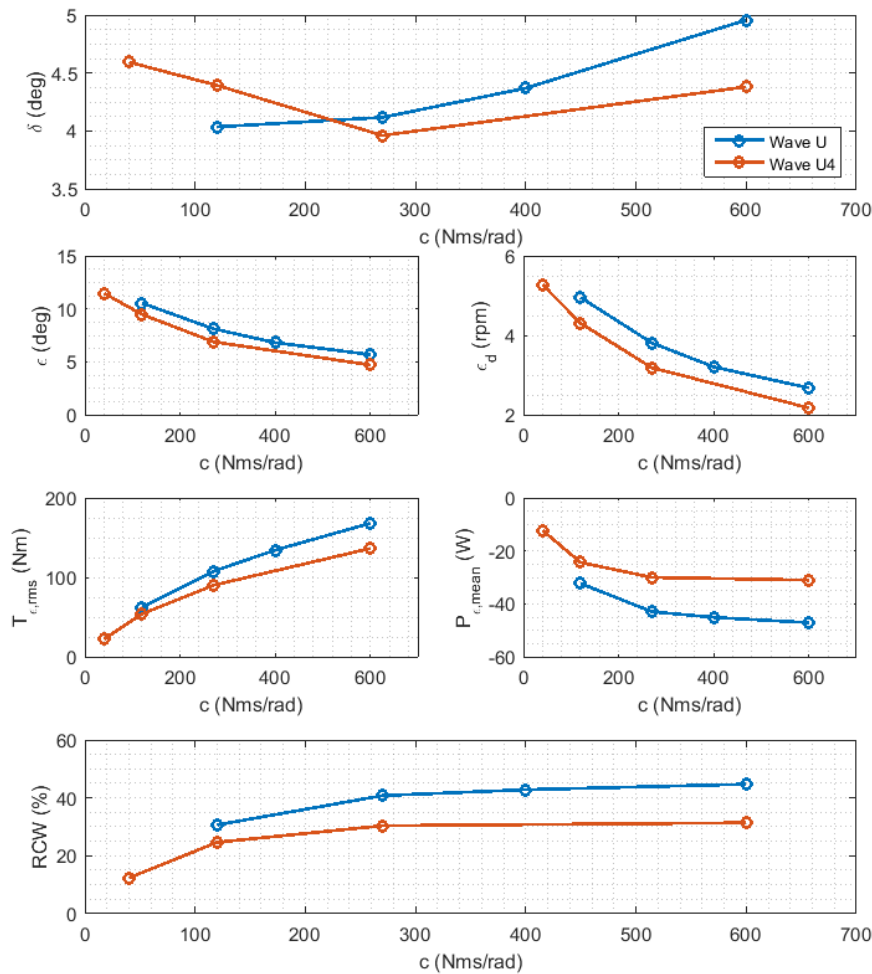
Fig. 5.50 Configuration C1 tests results under different irregular sea state and considering different PTO control damping values.

should be adjusted in order to improve the sea state mathematical representation. Obviously, the wave model tuning should be performed taking into account the wider set of waves, which is representative of the entire site scatter diagram, but this topic is not the core of this work.

Configurations C3, C2 and C1 comparison

The configuration C2 has been tested by using the irregular design sea state and its performances has been benchmarked against the results achieved with configuration C1. Similarly to the experiments run in regular waves, the modification of the device

overall inertia, produces a shift of the second resonance period towards higher values, leading to a worsening of the device performances in correspondence of the design wave period (2.2 *s*), as reported in Fig. 5.51.
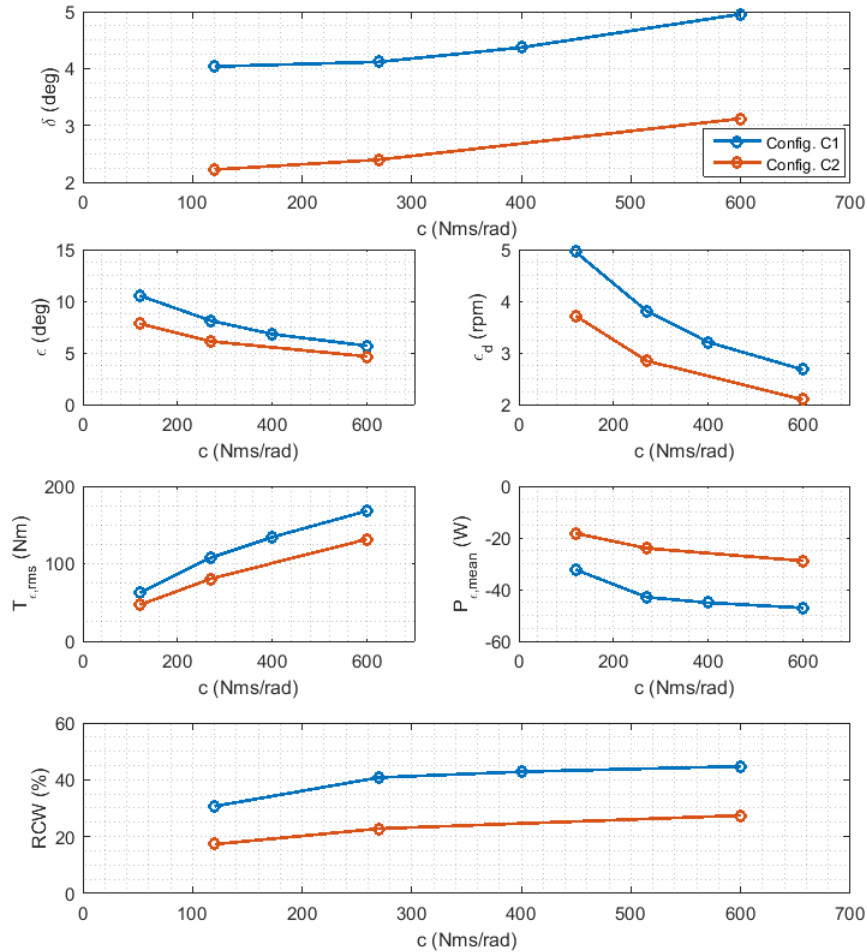
Fig. 5.51 Configuration C2 and C1 experimental results, undergoing to the design irregular wave U and varying the PTO control damping.

On the other hand, comparing configuration C3 and C1 (see Fig. 5.52), it is possible to highlight a smaller difference of the performances, if compared with the results shown in Fig. 5.51 (configuration C2 and C1 benchmarking). In fact, it is worth noting that in the case of configuration C3 a reduction of the distance between pendulum hinge and floater COG allows to shift the second resonance period from 2.8 to 2.7 *s*, diminishing the performances drop around the design wave period. However, in the case of configuration C3, extracted power is maximized at
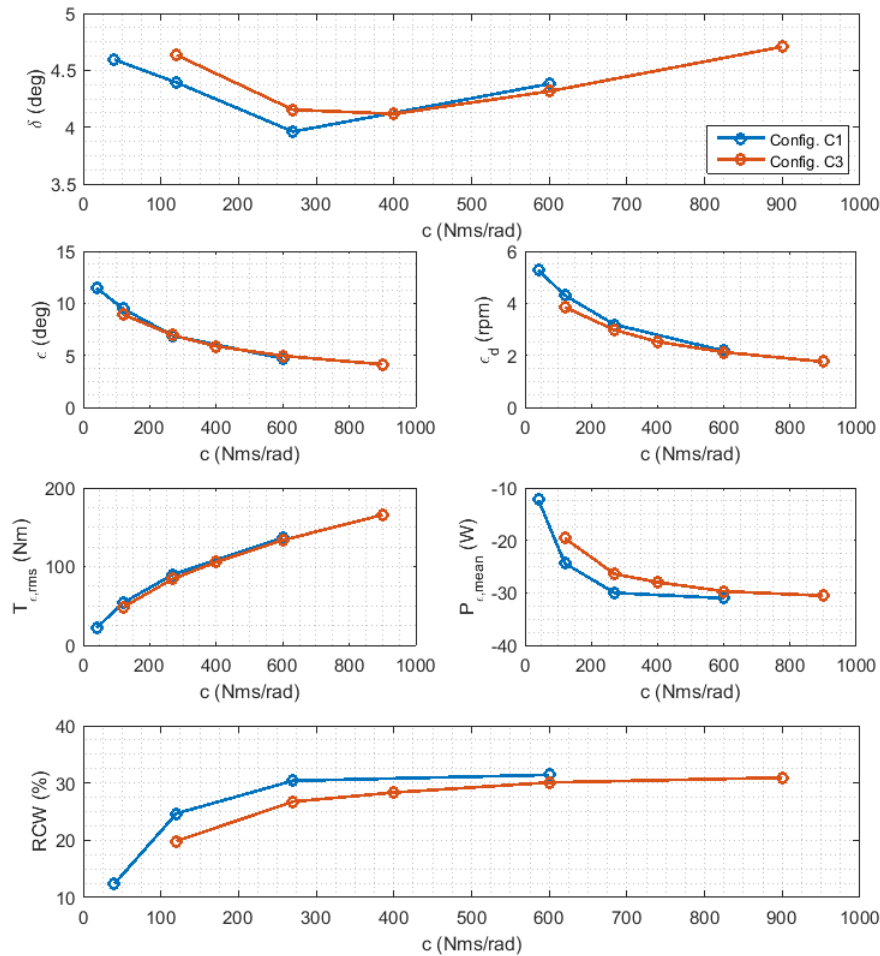
Fig. 5.52 Configuration C3 and C1 experimental results, undergoing the design irregular wave U4 and varying the PTO control damping.

levels similar the one determined wit configuration C1, increasing the PTO damping coefficient up to 900 $\frac{Nms}{rad}$.

Configurations C4 and C1 comparison

The last part of the irregular tests deals with the evaluation of the configuration C4 performances, varying the PTO damping coefficient and considering the design wave U. The prototype behavior is almost similar to the one denoted in the case of regular waves, where the extracted power is maximized increasing the PTO damping coefficient.
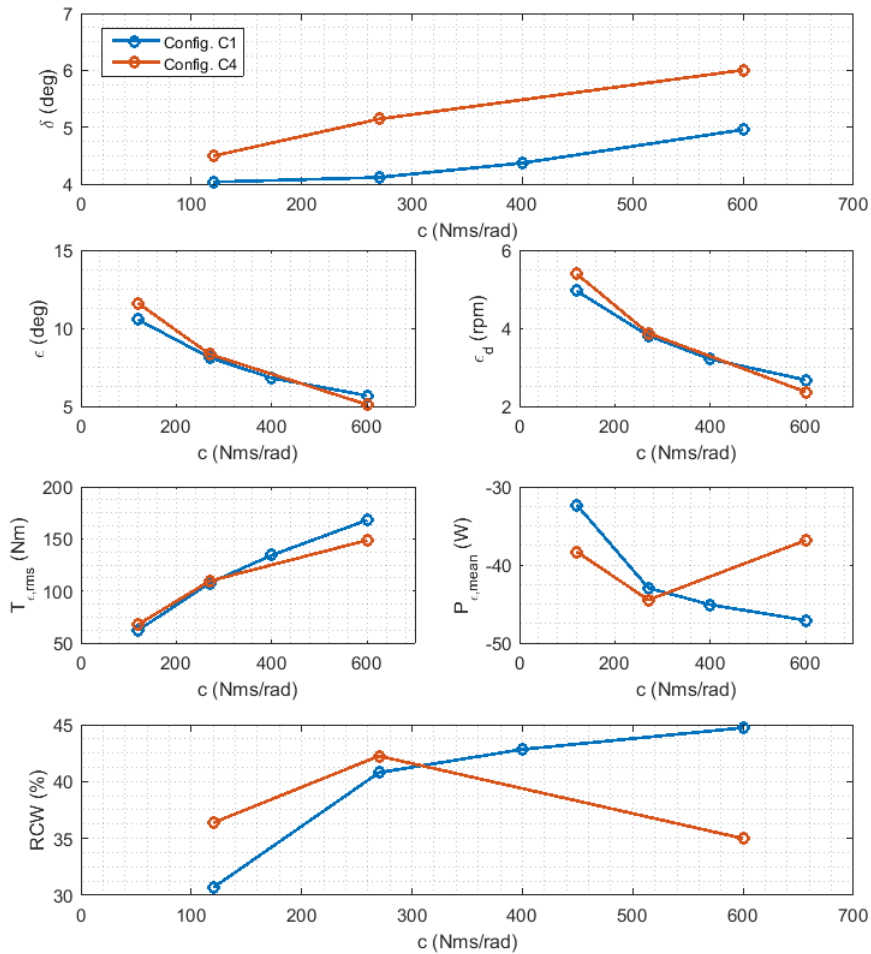
Fig. 5.53 Configuration C3 and C1 experimental results, undergoing the design irregular wave U and varying the PTO control damping.

More in detail, observing Fig. 5.53, the average extracted power is maximized when the control coefficient is set at 270 $\frac{Nms}{rad}$, achieving a level of performance comparable to configuration C1 (44 *W* instead of 47 *W*). Similar consideration are valid also for the device efficiency (42% against 45%), proving that also under irregular waves, a reduction of the mass of 1.6 times from the initial value of 410 *kg*, do not influences considerably the performances in correspondence of the design period. Furthermore, these results allows to prove the reliability of the design method proposed in this chapter, that is mainly based on monochromatic waves and thus on the analysis of the device frequency response. Lastly, it is important to underline that the differences in term of pitch motion amplitude, as discussed in the case of the configuration C4 regular wave tests, are mainly due to a not proper correspondence

between the pitch RAOs of the initial configuration and of the one obtained reducing the pendulum mass from 410 to 258 *kg*.

5.2.6   Chapter remarks

The testing campaign performed on the 1:12 PeWEC device allowed to demonstrate, from the experimental point of view, the PeWEC dynamics determined during the design stage through numerical simulations. In particular, tuning the pendulum and floater resonance periods in correspondence of the design wave period, the following resonance periods can be determined: one below, one above and one in correspondence the design period. The first and the second resonance period arise from the coupling between pendulum and floater, while the third is centered on the floater resonance period (see Fig. 5.40).

Adjusting the PTO control damping, the average extracted power can be maximized over the entire the working range. The latter is identified by the two resonance periods that arise from the couplings between pendulum and floater. More in detail, in the case of both resonance periods due to floater and pendulum coupling, an optimal PTO damping coefficient can be identified, while in the case of the design wave period, the average extracted power is maximized increasing the PTO control parameter.

Increasing the floater pitch moment of inertia, it is possible to shift the second resonance period toward longer wave periods. On the other hand, the first resonance period is less sensible to the floater pitch moment of inertia variation. Then, it results that the first peak of the device dynamic response is mainly determined by the pendulum resonance period, while the second is more correlated to the floater resonance period. Moreover, as previously described, the resonance period between the others moves in correspondence of the floater resonance frequency and in general it tends to approach to the second resonance period, as shown in Fig. 5.40. This fact leads to a less regular envelope of the average extracted power computed in frequency domain.

Reducing the pendulum mass and maintaining the pendulum and floater dynamic responses tuned on the design wave period, a decrease of the WEC performances and efficiency is determined, proving that the mass needs to be properly selected in order to maximize the desired output power and thus the device productivity.

Chapter 6

PeWEC design and optimization methodology

The experimental activity presented in Chapter 3 and Chapter 4, proved that the PeWEC technology can be developed in order to exploit Mediterranean Sea waves energy potential.

Despite the methodology adopted for the design of the 1:12 PeWEC prototype allowed to determine a particularly efficient configuration, it might not be suitable in the perspective of an integrated and optimal design of a full scale device.

For this reason, a design methodology able to determine an optimal device configuration has been implemented. It is based on three different tools characterized by growing level of fidelity. The idea of subdividing the design process in different steps starts from the consideration that higher fidelity means, in general, higher computational costs.

The first tool, called *PeWEC Linear Optimization Tool*, is based on the linear frequency domain model and it has been thought to extrapolate a preliminary optimized device configuration (pendulum mass, moment of inertia, length, pendulum hinge position, etc.), taking into account the installation site scatter diagram characteristics and some geometrical constraints. This tool has very low computational costs and allow to investigate hundred thousands of combinations in the time horizon of one hour.

The second tool has been derived staring from the *ISWEC Design Tool* [109][111], which was designed to optimize the ISWEC control parameters over the entire

scatter diagram, taking into account the linearized system dynamic equations. In this work, this tool has been rearranged, expanding the hydrodynamic model from one DOF to three DOFs, introducing the linear hydrodynamic viscous damping, the linearized mooring characteristic and substituting the ISWEC gyroscope linear dynamic equations with pendulum linearized mechanical equations. The *PeWEC Design Tool* is characterized by very low computational costs and it allows to determine a preliminary evaluation of the device productivity, as well as a panoramic of the device behavior on the entire scatter diagram.

The *PeWEC Parametric Tool* is similar to the *PeWEC Design Tool*, but it is based on the nonlinear PeWEC numerical model, where PTO saturations, hydrodynamics, pendulum and mooring nonlinearities are taken into account. Since, the higher fidelity involves higher computational costs, the *PeWEC Parametric Tool* is used to compute accurately the device performances and the life of its components, such as bearings. Furthermore, this tool is very important since it is useful to determine the most suitable PTO and the influence of its size with respect to the device productivity. This aspect is of particular relevance, especially when the device performances are correlated to the Levelized Cost of Energy (LCOE), that will be discussed in Chapter 7.

However, before starting with the presentation and development of the design and optimization methodology, an overview of the numerical models validation against the experimental results carried out at the INSEAN wave basin on the 1:12 PeWEC device is presented.

6.1   Numerical model validation

In this section the nonlinear model validation is reported. In the first part, the comparison with respect to experimental results carried out in regular waves is performed. More in detail, starting form the frequency sweep, the inaccuracies of the model in resonance condition are highlighted. The identification of the nonlinear hydrodynamic viscous damping and of pendulum bearings friction allowed to improve the overall numerical model reliability. In the second part irregular waves are considered and the accuracy of the numerical model is evaluated, taking into account the different experimental conditions described in Chapter 5. In both cases, numerical model proved to be in good agreement with experiments.

The validation proposed in this section is mainly focused on nonlinear model, that can be considered the most important and accurate tool available, in the context of Wave-to-Wire numerical models, for the prediction of the device dynamics and performances. A validation of the linear model, widely used in Chapter 5 for the design of the 1:12 scale prototype, was proposed at the end of Chapter 4, proving to be in good agreement with experimental data. In order to avoid making the discussion cumbersome, the linear model validation on 1:12 scale prototype experimental results is not reported. A further proof of the linear model reliability can be found in Chapter 7, comparing *PeWEC Design Tool* and *PeWEC Parametric Tool* results. In fact, the first model is based on linear equation, while the second on nonlinear one.

6.1.1   Regular wave tests

The first experimental set considered for the nonlinear numerical model validation is frequency sweep, performed maintaining the PTO damping coefficient constant at $40 \frac{Nms}{rad}$. The design prototype configuration (C1) was here used (see section 5.2.4).

Fig. 6.1 shows the comparison between the experimental and root-mean-square values of pitch angle, pendulum angular position and velocity, PTO torque computed with the nonlinear numerical model. Regarding the extracted power the average value has been considered and the related value of Relative Capture Width. Only in the case of the extracted power the mean value is taken into account. Considering the pitch motion, a good degree of accuracy is reached for all wave periods considered, despite an overestimation can be observed in correspondence of the resonance occurring at 2.5 *s*. Since the hull motions influence the motion of the inner pendulum, the discrepancies observed around 2.5 *s* for the hull pitch motion have a strong impact on pendulum angular displacement and velocity, PTO torque and average extracted power. The latter is the variable mainly affected by the hydrodynamic model inaccuracy, since it depends on both PTO torque and pendulum angular velocity.

Nonlinear model tuning

This difference can be justified taking into account the linear nature of the hydro-dynamic model, which does not contemplate the nonlinear dissipation phenomena, proportional to the square of the velocity, described in section 3.3.5. Hydrodynamic
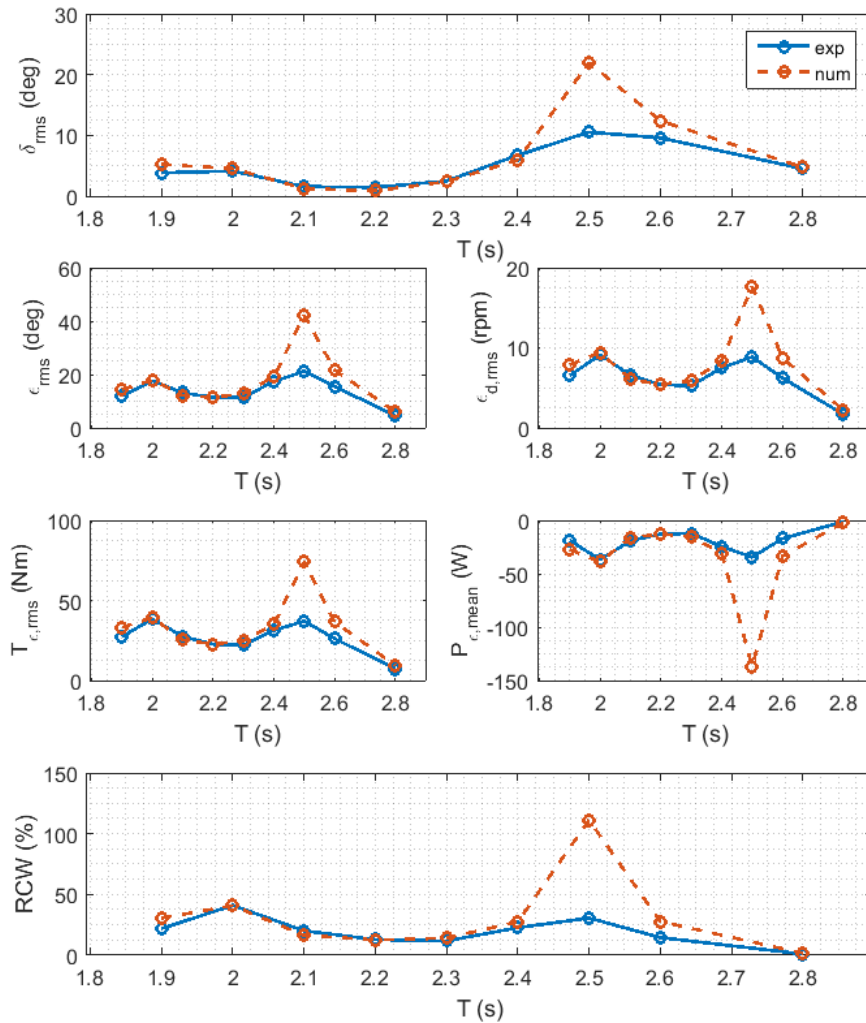
Fig. 6.1 Frequency sweep: experimental data and nonlinear model comparison.

nonlinear viscous damping has been estimated for the pitch DOF minimizing the error between numerical and experimental data around the resonance period. In Fig. 6.2 and in Fig. 6.3, the comparison between the experimental and numerical pitch time series, with and without nonlinear viscous damping, are reported.

The introduction of the nonlinear viscous effects for the pitch degree of freedom, estimated to be equal to $600 \frac{Nms^2}{rad^2}$, allowed to improve the prediction of the floater motion. Beside hydrodynamic viscous effects, bearing friction has been introduced in order to improve pendulum motion prediction, especially around resonance condition.
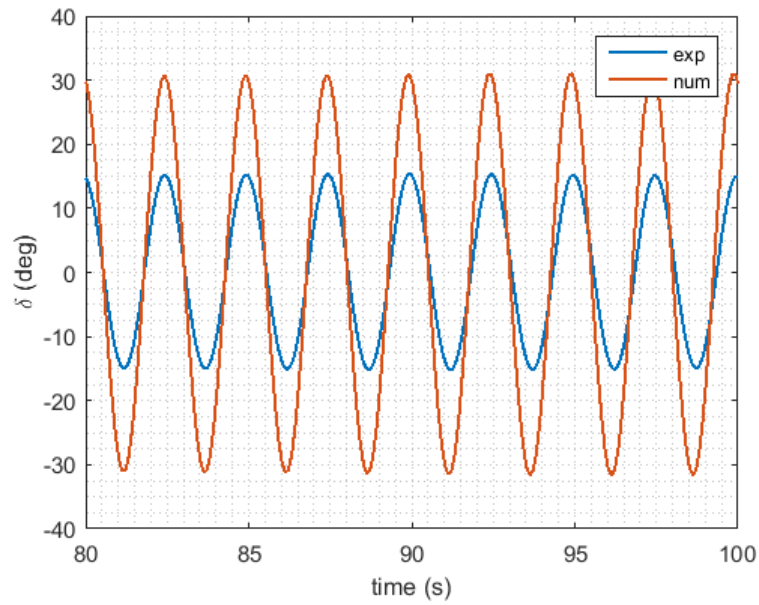
Fig. 6.2 Experimental and numerical pitch time series at 2.5 s wave period and constant PTO damping coefficient (40 $\frac{Nms}{rad}$), without pitch nonlinear viscosity.
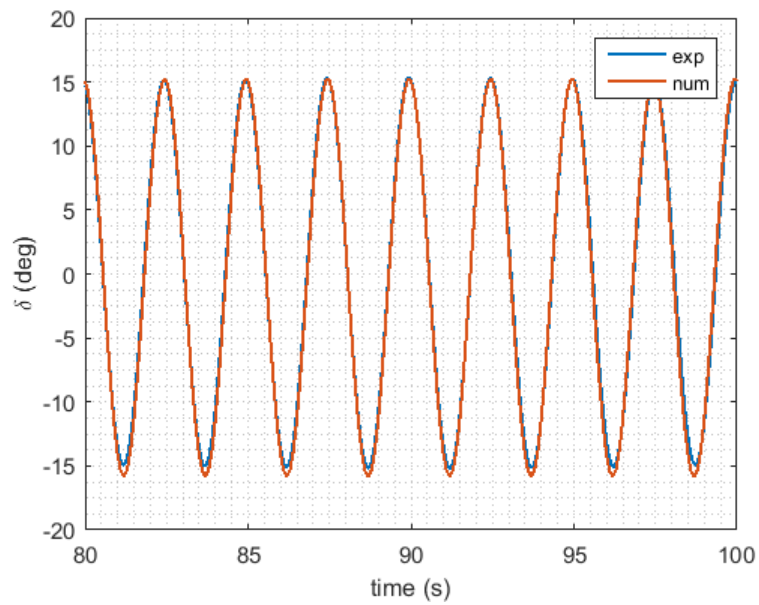
Fig. 6.3 Experimental and numerical pitch time series at 2.5 s wave period and constant PTO damping coefficient (40 $\frac{Nms}{rad}$), with pitch nonlinear viscosity.

Bearings friction has been modeled as the composition of a Coulomb, linear viscous term, as reported by Eq. 6.1.

$$T_{frict} = \mu_c sgn(\dot{\varepsilon}) + \mu_v \dot{\varepsilon} \qquad (6.1)$$

Where μ_c and μ_v are respectively the Coulomb and linear viscous friction coefficients. Each component has been identified through a fitting procedure over the experimental record, based on the Nelder-Mead method [62][72]. In Fig. 6.4, an example of the identification results is depicted, while in Table 6.1 the numerical results are summarized.
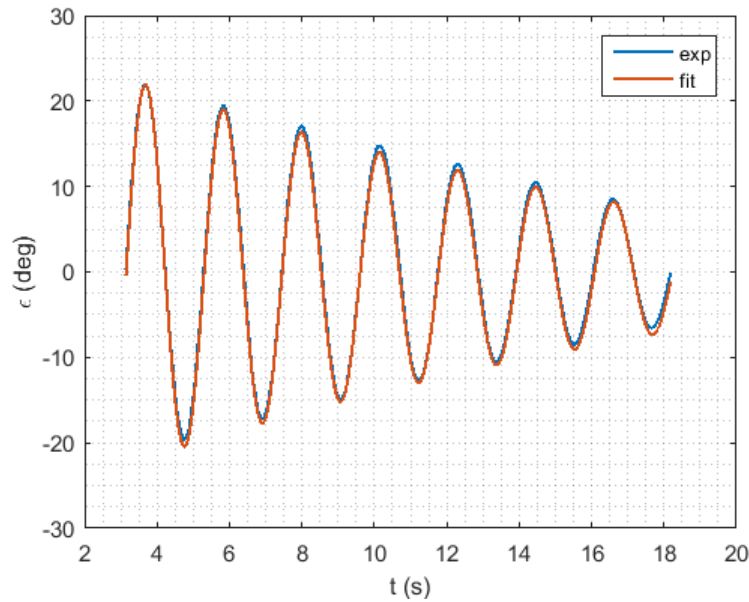
Fig. 6.4 Bearings friction identification results.

Table 6.1 Bearings friction coefficients.

Description	Symbol	Values	U.M.
Coulomb friction coeff.	μ_c	0.0141	*Nm*
Viscous friction coeff.	μ_v	32.4	$\frac{Nms}{rad}$

In Fig. 6.5, a comparison between experimental and numerical pendulum motion, without and with bearing friction is reported. The 2.5 *s* wave period test is used for the comparison. Observing Fig. 6.5, it is possible to note that the introduction

of bearings friction allows to improve the pendulum motion prediction, even if the influence of bearing friction is quite small.
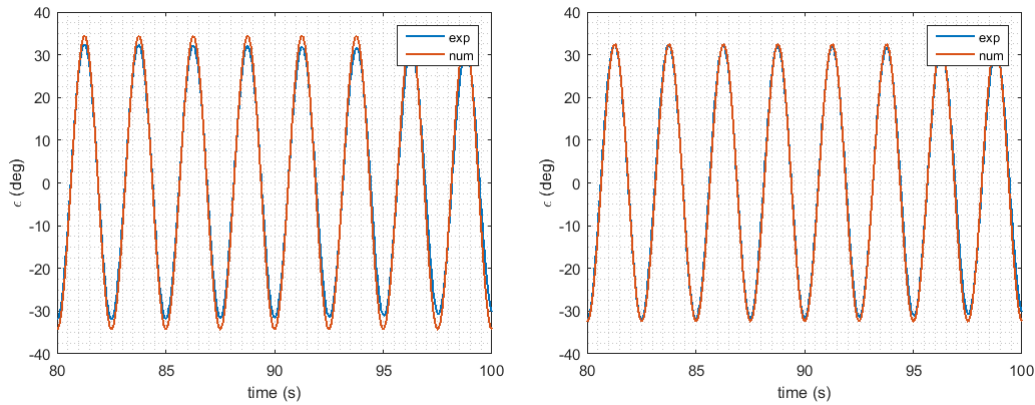
Fig. 6.5 Comparison between experimental and numerical pendulum angular displacement, without bearing friction (left) and with bearing friction (right).

This fact has been proven benchmarking the PTO torque imposed by control against the one measured through the load cell, as depicted in Fig. 6.6.
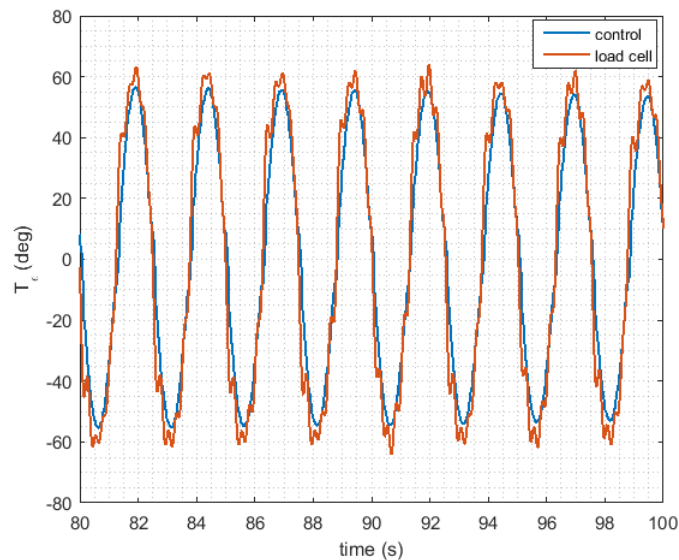
Fig. 6.6 Comparison between reference PTO torque (control) and estimated torque (load cell), at 2.5 *s* wave period.

A second verification of the numerical model prediction of the overall frequency sweep test is reported in Fig. 6.7.
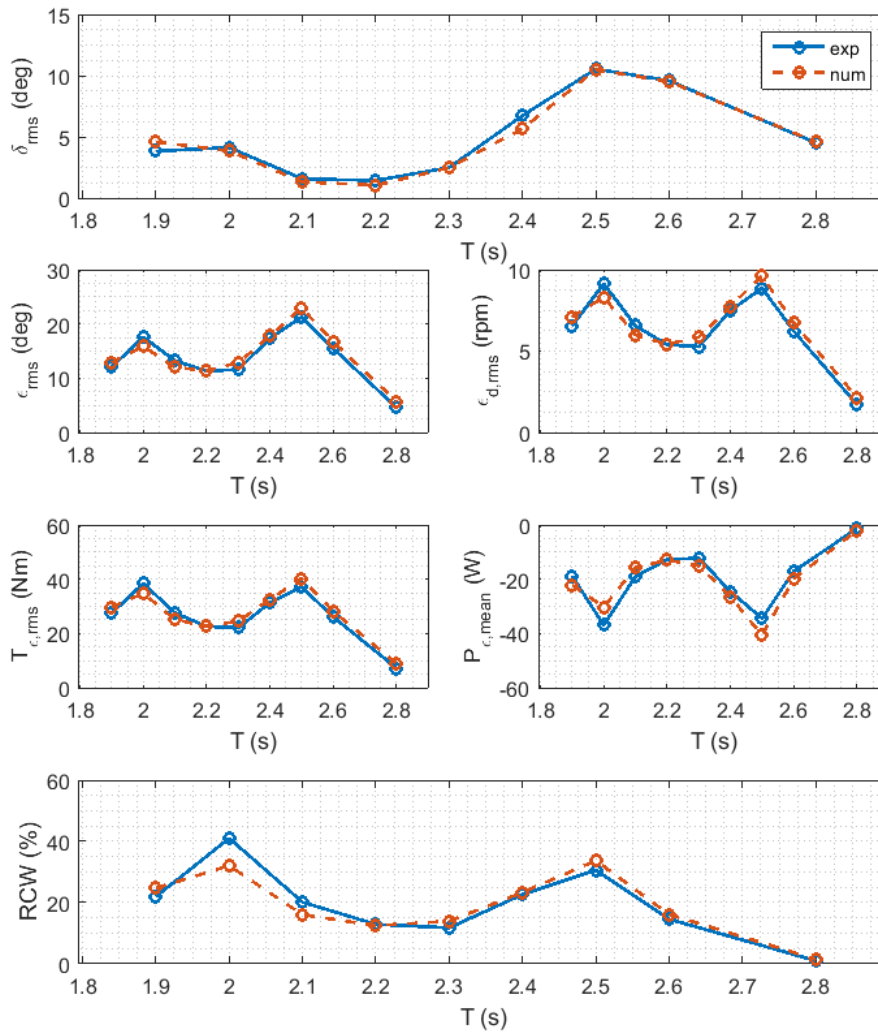
Fig. 6.7 Frequency sweep: experimental data and nonlinear model comparison, including nonlinear hydrodynamic viscous damping and bearings friction.

Overall nonlinear model reliability in regular wave

Once the nonlinear numerical model has been tuned introducing bearings friction and nonlinear hydrodynamic damping, the various regular wave tests presented in Chapter 5 have been used as reference for the validation of the nonlinear numerical model, involving different prototypes configurations, wave period and PTO control damping values.

Considering each test, the percentage error of numerical results with respect to experimental data has been calculated, for all the physical quantities taken into

account (pitch motion, pendulum angular displacement and velocity, PTO torque, etc.), as reported in Eq. 6.2.

$$err = \left(\frac{X_{num}}{X_{exp}} - 1 \right) 100 \tag{6.2}$$

Where X is the generic experimental or numerical physical quantity considered. As example, in Fig. 6.8, the results related to the tests performed on the prototype configuration C1 and varying the PTO control damping are reported. It is possible to highlight the good correspondence between numerical and experimental data.
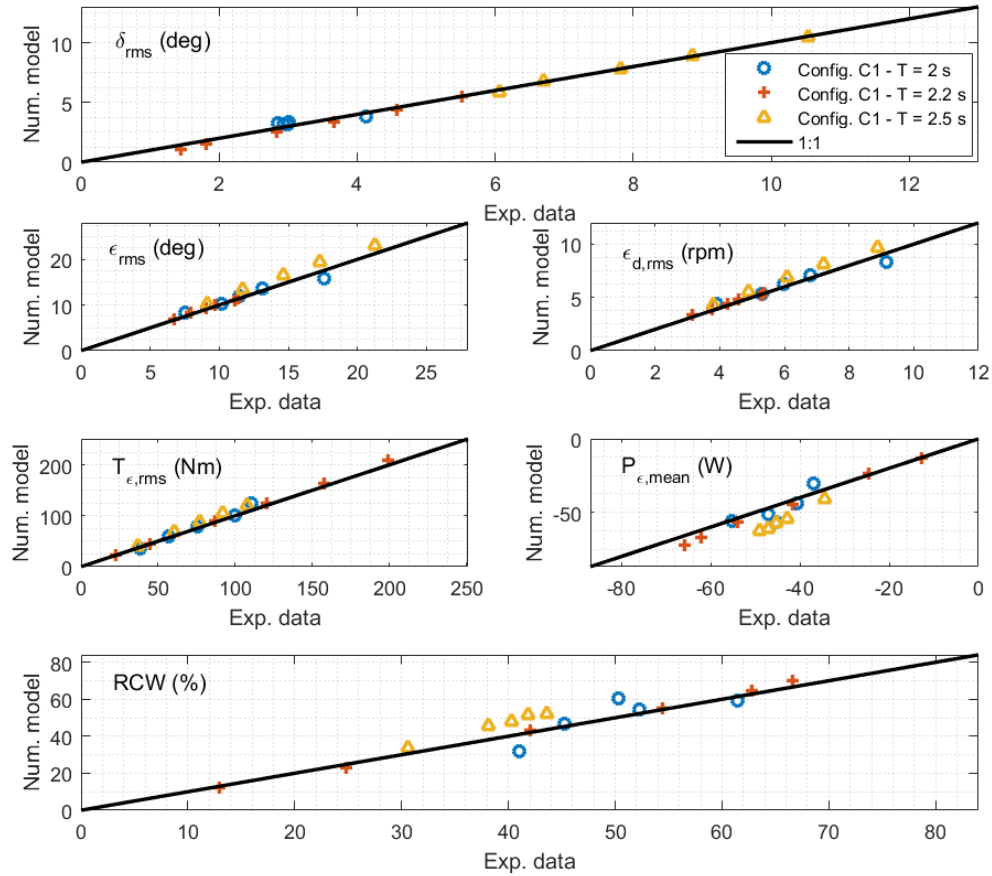
Fig. 6.8 Numerical model comparison against experimental data carried out considering prototype configuration C1, varying the PTO damping coefficient and regular wave height.

In order to give a general idea of the numerical model reliability in the case of regular waves, without burdening the discussion, in Table 6.2 the average error for the different prototype configurations investigated is reported.

Table 6.2 Average error between numerical model and experimental data, for the different 1:12 scale prototype configurations investigated, in regular waves.

Test	Average error (%)					
	δ_{rms}	ε_{rms}	$\dot{\varepsilon}_{rms}$	$T_{\varepsilon,rms}$	$\overline{P}_\varepsilon$	RCW
C1 - freq. sweep	-5.07	4.75	5.36	5.18	11.63	6.65
C1 - PTO damping tuning @ 2 s	7.12	1.63	2.47	2.27	5.08	0.44
C1 - PTO damping tuning @ 2.2 s	-11.4	1.74	2.56	2.38	4.87	0.43
C1 - PTO damping tuning @ 2.5 s	-0.26	9.76	10.13	10.14	11.55	10.19
C2 - PTO damping tuning @ 2 s	8.65	7.82	4.04	5.98	12.90	11.05
C2 - PTO damping tuning @ 2.8 s	-1.48	0.55	1.32	0.70	2.26	-3.68
C3 - PTO damping tuning @ 2 s	-1.27	7.04	9.40	10.89	11.20	10.30
C3 - PTO damping tuning @ 2.5 s	-2.60	3.00	3.28	3.28	7.44	2.99
C3 - PTO damping tuning @ 2.7 s	-2.28	0.94	1.83	1.52	3.49	-0.54
C4 - PTO damping tuning @ 2.4 s	-6.96	1.91	2.71	2.56	5.21	0.72

Numerical model proved to be sufficiently accurate in the prediction of the PeWEC device dynamics in regular waves, with a maximum average error within 13% and a maximum error lower than 25%. The latter occurred in the case of the average extracted power of configuration C2, tested at 2 *s* wave period and varying the PTO damping coefficient.

6.1.2   Irregular wave tests

In the second part of the validation process deals with the verification of the nonlinear model prediction reliability in the case of irregular waves. Similarly to the validation in regular waves, the different tests presented in Chapter 5 are used for the assessment of the overall reliability of numerical model. In this case, any additional model correction has been introduced apart from the nonlinear hydrodynamic viscous damping and bearings friction torque identified through regular wave tests.

As widely described in section 5.2.5, both real waves recorded in Pantelleria Island (and properly scaled down) and synthetic waves were taken into account for the device tank testing. As example, in Fig. 6.9, the comparison between numerical and experimental data, carried out considering the design prototype configuration (C1) tested with the design wave U (real scaled wave), is reported. The model under-estimates the floater rms pitch angle and the difference with respect to experimental
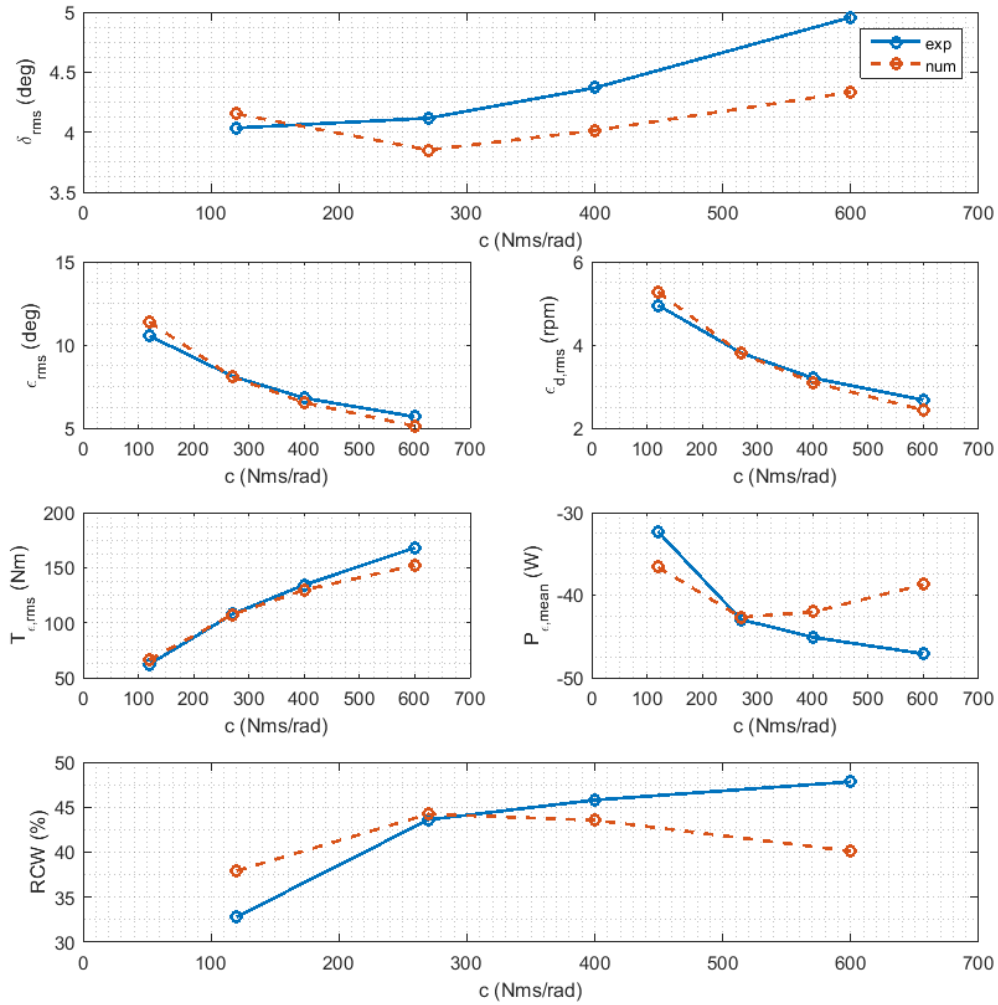
Fig. 6.9 Numerical model comparison against experimental data carried out considering prototype configuration C1, undergoing wave U and varying PTO damping coefficient.

data increases with the PTO damping values, despite the trend is almost correct. The maximum error amount to 15%. The hydrodynamic model discrepancies, in this case, do not affect significantly the pendulum dynamics. However, a slight underestimation of pendulum angular velocity and PTO torque for PTO damping coefficients greater than 270 $\frac{Nms}{rad}$ leads to a significant error between experimental and computed average extracted power.

A better agreement is achieved considering the tests performed on the same configuration, but using the synthetic wave U4, as shown in Fig. 6.10. Also in this case the most important mismatch between experimental and numerical data

regards the floater pitch motion, even if the maximum error is lower than 10% and a more accurate trend prediction is shown. On the other hand, computed pendulum dynamics, PTO torque and average extracted power are in good agreement with experiments, in both trend and numerical values.
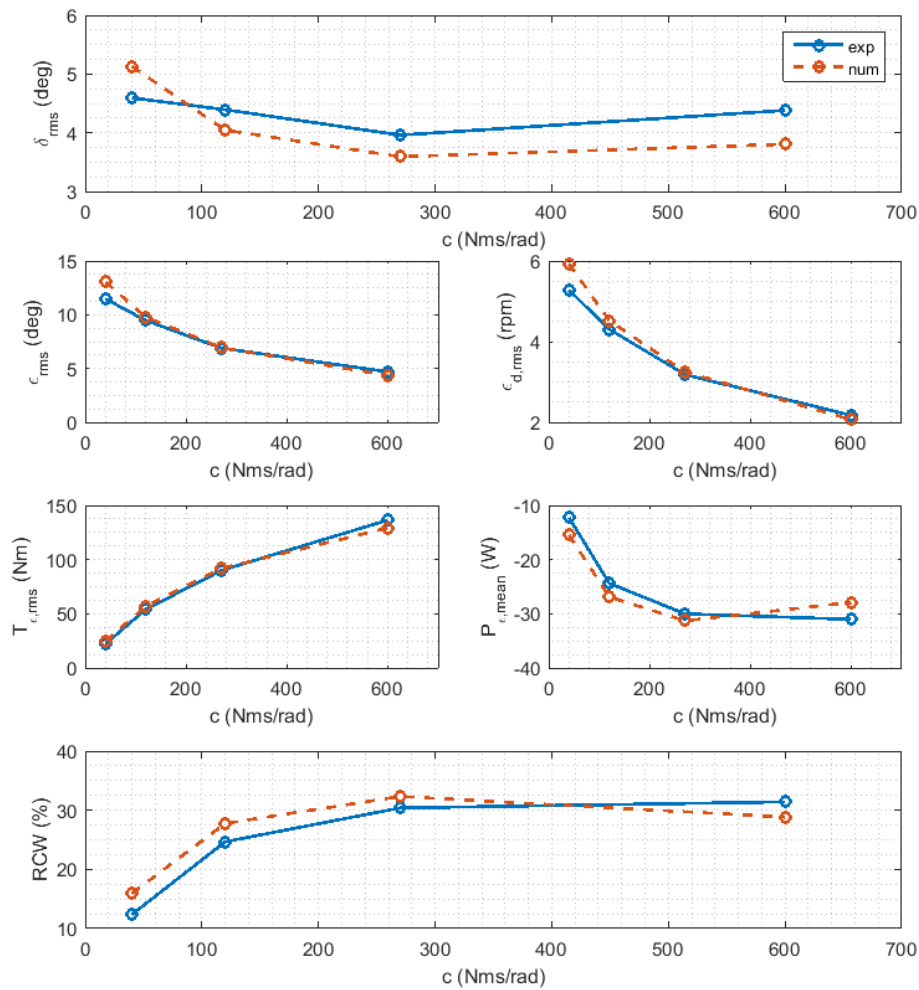
Fig. 6.10 Numerical model comparison against experimental data carried out considering prototype configuration C1, undergoing wave U4 and varying PTO damping coefficient.

Also configurations C2 and C4 were tested with design wave U by varying the PTO damping coefficient. In Fig. 6.11, a summary of the comparison between numerical model and experimental data has been reported. A good prediction of the overall PeWEC dynamic behavior can be highlighted. Again, the most important discrepancies concern the pitch motion. In fact, as described in Chapter 3, the most difficult part to be modeled is the interaction between waves and floater, where
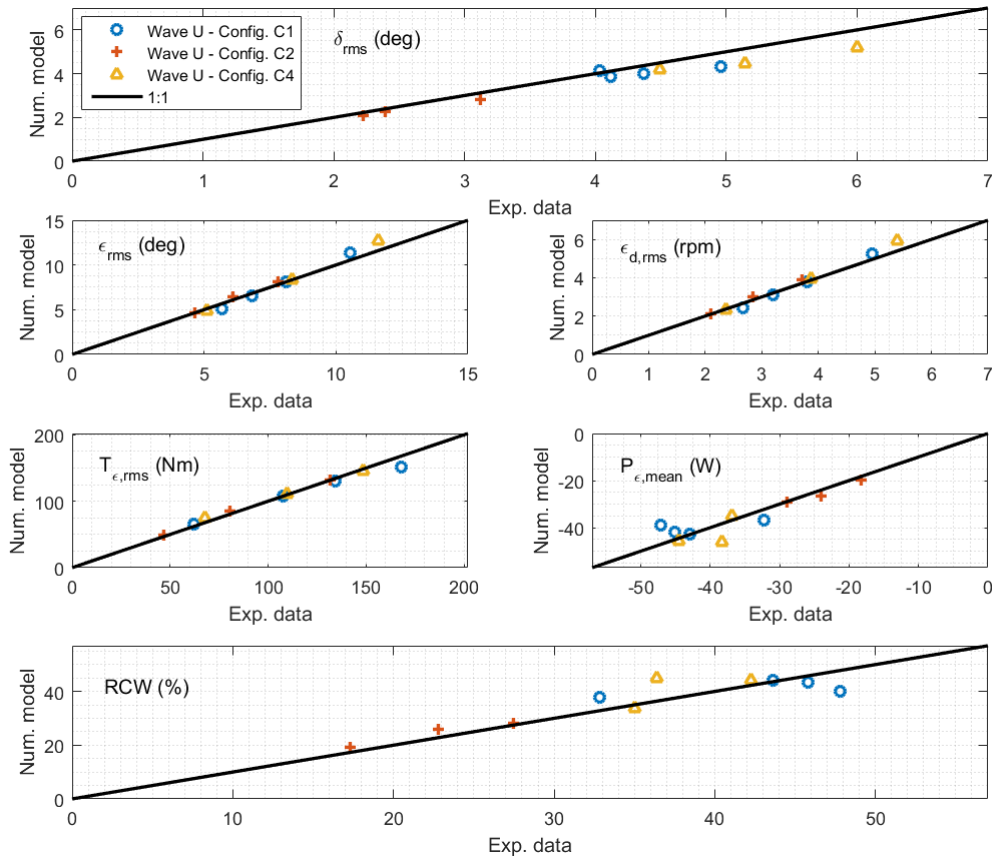
Fig. 6.11 Configuration C1, C2 and C4 tested with irregular wave U and varying PTO damping coefficient: numerical and experimental data comparison.

highly nonlinear phenomena are involved. On the other hand, the error on the floater dynamics prediction seems to do not affect significantly the pendulum dynamics and thus the prediction of the average extracted power.

Lastly, in Table 6.3 a synthesis of the average error of the different test groups performed in irregular waves and reported in section 5.2.5 is depicted. Numerical model proved to in good agreement with experimental data, highlighting a correct prediction of the device performances trends as function of the PTO control damping. Regarding hydrodynamics, an underestimation of the pitch motion around 5% can be highlighted, while the error related to the pendulum dynamics and PTO torque do not exceed 7%. At the same time, a good accuracy of the average extracted power can be pointed out with a maximum average error of 10% in the case of configuration C1 tested with wave U4. A 13% error about average extracted power prediction has been calculated in the case of the test performed on configuration C1 undergoing

Table 6.3 Average error between numerical model and experimental data, for the different 1:12 scale prototype configurations investigated, in irregular waves.

	Average error (%)					
Test	δ_{rms}	ε_{rms}	$\dot{\varepsilon}_{rms}$	$T_{\varepsilon,rms}$	$\overline{P}_\varepsilon$	RCW
C1 - Wave U	-6.06	-1.68	-1.61	-1.71	-2.98	-1.01
C1 - Wave W	4.43	7.98	6.37	6.14	12.79	12.52
C1 - Wave U4	-4.66	2.63	3.61	3.54	7.67	9.87
C2 - Wave U	-5.26	2.01	2.67	2.57	5.27	6.92
C3 - Wave U4	-5.77	-6.31	-3.53	-3.89	-7.11	-5.22
C4 - Wave U	-8.49	1.18	2.14	2.09	4.46	6.08

to wave W. This value is comparable to the one estimated previously during the validation of nonlinear model in regular waves.

6.1.3   Conclusions

The nonlinear model proved to be in good agreement with experiments, in both regular and irregular waves, despite some discrepancies concerning the floater pitch motion modeling can be pointed out. Such discrepancies occurs even if the numerical model has been properly tuned introducing the nonlinear hydrodynamic viscous damping, widely discussed in section 3.3.5. This means that further investigation are required to improve the numerical model. For instance, the computation of the instantaneous wetted surface should be introduced, in order to distinguish geometrical nonlinarities from viscous nonlinearities. Another important aspect, that here has been omitted for reasons of force majeure, is the validation of surge motion and its interaction with pendulum. The main cause of this lack is due to an irreparable failure of the motion tracking system that occurred during experimental activities. In order to cover this lack, it is worth to mention that the 3 DOF hydrodynamic model described in this work was validated against the experimental results carried out on a scaled ISWEC floater at the HMRC wave basin in 2015 [91].

6.2 PeWEC design and optimization methodology

The methodology adopted for the design of the 1:12 PeWEC prototype, has been useful for the determination of a particularly efficient configuration, that has been widely studied and tested in order to achieve a sufficiently robust knowledge of the WEC behavior and a sufficiently wide set of data for the numerical model validation. However, this methodology might not be suitable in the perspective of an integrated and optimal design of a full scale PeWEC device.

In this section, the design and optimization methodology is presented, highlighting the most important features of the three different tools developed:

- *PeWEC Linear Optimization Tool*

- *PeWEC Design Tool*

- *PeWEC Parametric Tool*

It is important to remember that the main objective of this methodology is to subdivide the design process in different steps with increasing level of fidelity and to foster low computational costs in the initial design phase.

6.2.1 PeWEC Linear Optimization Tool

The *PeWEC Linear Optimization Tool* is based on the linear frequency domain model, described by Eq. 3.77 and it has been designed to extrapolate a preliminary optimized device configuration, in term of pendulum mass, inertia, length and hinge position, once the floater geometry and device overall mass are defined.

It is worth noting that generally, the floater geometry design process is the most delicate part, where specific consideration needs to be taken into account. For instance the criteria explained in section 5.1.2 would be a reasonable staring point. Then, the geometry needs to be analyzed through a potential flow code (Ansys AQWA, WAMIT, Nemoh, etc.), in order to compute the corresponding hydrodynamic database.
Another important input is constituted by the installation site scatter diagram, fundamental the identification of a suitable device dynamic response.

The *PeWEC Linear Optimization Tool* is basically organized in three modules, arranged in cascade:

- *Parametric Analysis Module*

- *Optimization Module*

- *Optimal Configuration Representation Module*

In the following paragraphs, a brief description of each module is given.

Parametric Analysis Module

The *Parametric Analysis Module* computes the system dynamic response according to the frequency domain equation Eq. 3.77, combining a the following inputs:

- *Floater properties*: a *stl* file of the floater geometry is used determine a planar representation of its shape (according to the 3 DOFs model hypothesis). Floater representative structural thickness and material density are also given together with the geometry.

- *Ballasts properties*: according to the floater shape, the ballast compartments position, number and ballast material density are selected.

- *Pendulum properties*: the tool has been programmed taking into account the circular pendulum shape discussed in section 5.1.4. Moreover, also the pendulum material density needs to be defined.

- *Parametric simulation parameters*: simulations are performed combining recursively a series of parameters such as wave period, pendulum mass, length, hinge position and PTO control damping. The span for each parameter can be defined by the user.

Once the inputs are defined, the first part of the program combines the information related to the floater determining the mass and the pitch moment of inertia of the external steel parts. Then, per each combination of the simulation parameters, the *Parametric Analysis Module* creates the pendulum geometry and calculates

its moment of inertia and thickness, according to the material properties chosen. Furthermore, it locates the pendulum hinge according to the instantaneous value selected for such parameter. Once the pendulum is positioned, the ballast quantity required is calculated as difference between overall device mass and the sum of the floater and pendulum mass. Then, ballasts are located into the spaces defined for compartments. Lastly, the overall position of the device COG is computed. In the meantime, a series of checks are performed in order to avoid the computation of unrealistic configuration, where the pendulum cannot be located inside the hull or the ballast quantity exceed the space available. If the configuration is considered valid, then the hydrodynamic database is updated according to the structure COG position and moment of inertia previously calculated. It is noteworthy that this operation do not require a new simulation through the potential flow code, in fact they can be updated according to the transformation operation suggested by Korotkin in [61]. Lastly, the configuration obtained is simulated in frequency domain for the different PTO damping coefficients and wave periods declared in the input section, while the corresponding results are saved in a database.

Optimization Module

The *Optimization Module* is the core of the *PeWEC Linear Optimization Tool*, since it allows to extract the optimal configuration among the ones available in the database generated through the *Parametric Analysis Module*. The research of the optimal configuration can be performed through different methodologies, each one characterized by different levels of complexity and working principles. Global search algorithms [119] and heuristic algorithms [107] are a relevant example of advanced methods used for the optimization of a given problem.
In the case of this work, a simpler methodology has been used to determine the optimal configuration, since it is not the goal of this thesis to investigate the application of such techniques.

The optimization algorithm here proposed is based on the maximization of the device harvested energy that, from the results discussed in Chapter 5, depends strongly from its dynamics performances. However, the latter needs to be correlated somehow with the installation site wave climate characteristics. From the experience gained by the author during the research activity emerged that the WEC dynamics should be designed taking into account both the occurrences and wave energy density

distributions.

Therefore, the idea is to create a *weight function* that allows to extract the most suitable layout among the ones available, taking into account both the WEC performances and the site wave climate characteristics. The weight function can be obtained starting from the iso-energetic approach assumptions reported in section 4.2. This criterion allows to convert the occurrences and wave energy density scatter diagrams based on statistical sea state parameters, into an equivalent scatter function of the regular sea state parameters (wave height and period). Then, remembering that the linear frequency domain model results are proportional to the wave height, one can think to collapse the occurrences and wave energy density scatter diagrams into two mono-dimensional normalized distribution functions, depending only on the wave period. Therefore, simulations can be performed considering a unitary wave height. In symbols:

$$D_{Occ}(T_e) = D_{Occ}(T) = \frac{\sum_{m=1}^{M} o_{m,n}}{max\left[\sum_{m=1}^{M} o_{m,n}\right]} \qquad \forall n, \ \ n = 1, 2, ..., N \qquad (6.3)$$

$$D_{WED}(T_e) = D_{WED}(T) = \frac{\sum_{m=1}^{M} e_{m,n}}{max\left[\sum_{m=1}^{M} e_{m,n}\right]} \qquad \forall n, \ \ n = 1, 2, ..., N \qquad (6.4)$$

Where $o_{m,n}$ and $e_{m,n}$ are, respectively, a generic element of the occurrences and wave energy density matrices (**Occ** and **WED**, both *MxN* matrices). In Fig. 6.12, the normalized occurrences and wave energy density distribution functions, determined starting from the Pantelleria site data, are depicted. The two distinct distribution functions can be combined together, obtaining a unique distribution function (*weight function*).

As previously stated, the identification of the optimal device configuration, among the ones available, is individuated searching the one that maximize the weighted harvested energy. The latter is calculated through the integral of the frequency domain optimal average extracted power, multiplied by the weight function. The optimal average extracted power is determined individuating, per each frequency, the PTO control damping that maximizes the output power. In symbols:
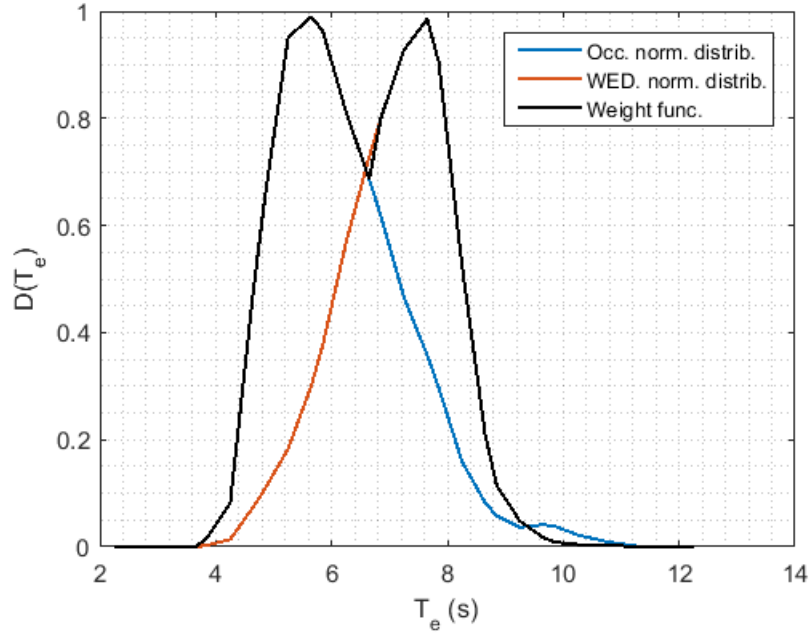
Fig. 6.12 Normalized occurrences, wave energy density and equivalent distribution functions.

$$E_j(T) = \int_{T_{min}}^{T_{max}} \overline{P}_{\varepsilon}(T) D(T) dT \tag{6.5}$$

Where E_j is the harvested energy by the *j-th* configuration, $P_{\varepsilon}(T)$ the frequency domain average extracted power and $D(T)$ the weight function.

Lastly, the harvested energy can be represented as a function of the pendulum radius and length, as depicted in Fig. 6.13. In the same figure, the corresponding resonance period map of the pendulum is reported. Observing Fig. 6.13, it is possible to individuate the pendulum parameters that optimize the device performances.

Optimal Configuration Representation Module

The last module, called *Optimal Configuration Representation Module*, allows to represent a sketch of the optimal configuration, as reported in Fig. 6.14. In addition, this module display also the frequency domain response of the floater and pendulum, together with the device performances, as depicted in Fig. 6.15 and Fig. 6.16.
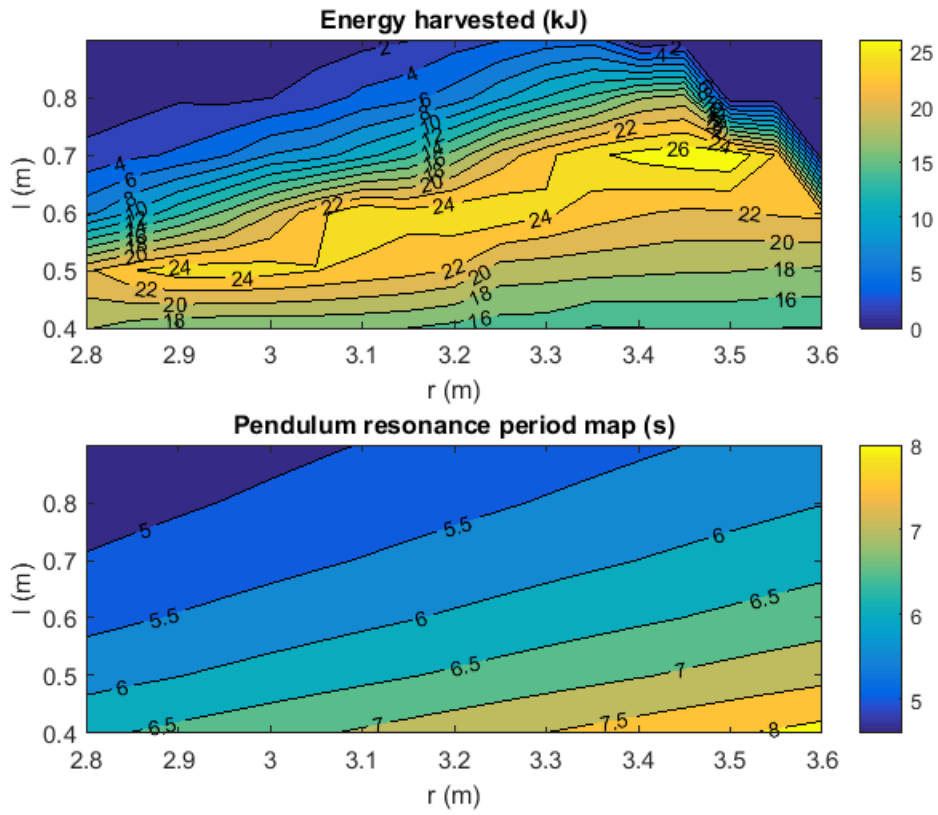
Fig. 6.13 Harvested energy map (top) and pendulum resonance period map (bottom), as a function of the pendulum radius and length.
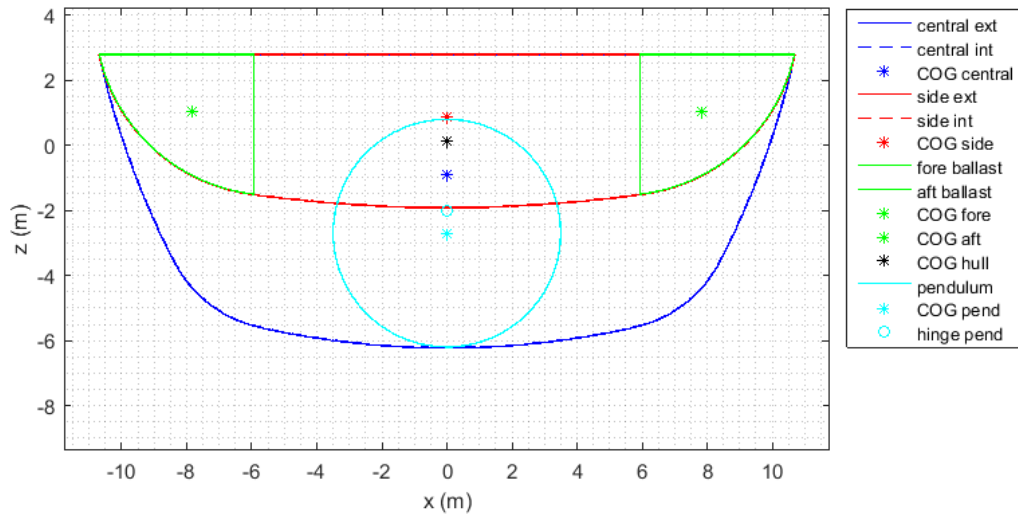
Fig. 6.14 Optimal configuration sketch.
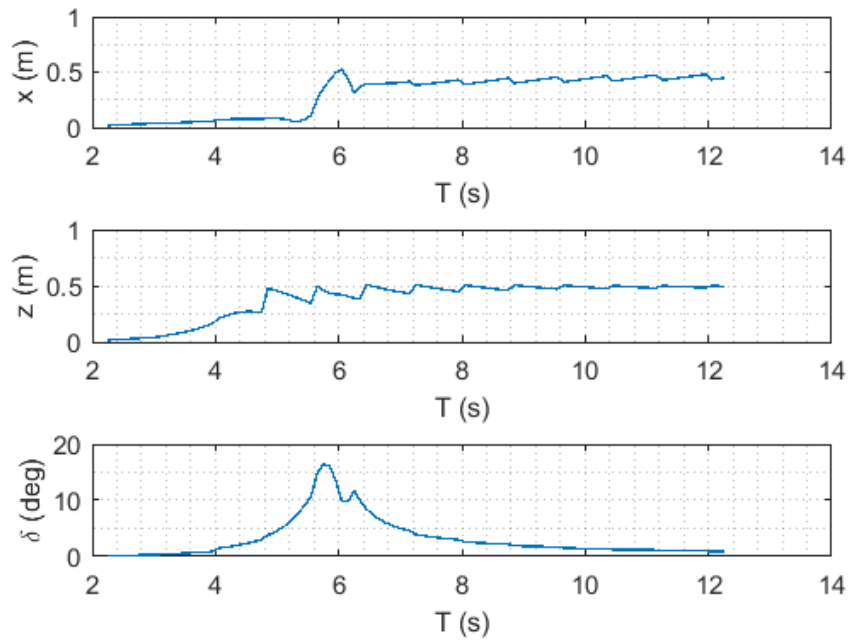
Fig. 6.15 Optimal configuration floater dynamics.
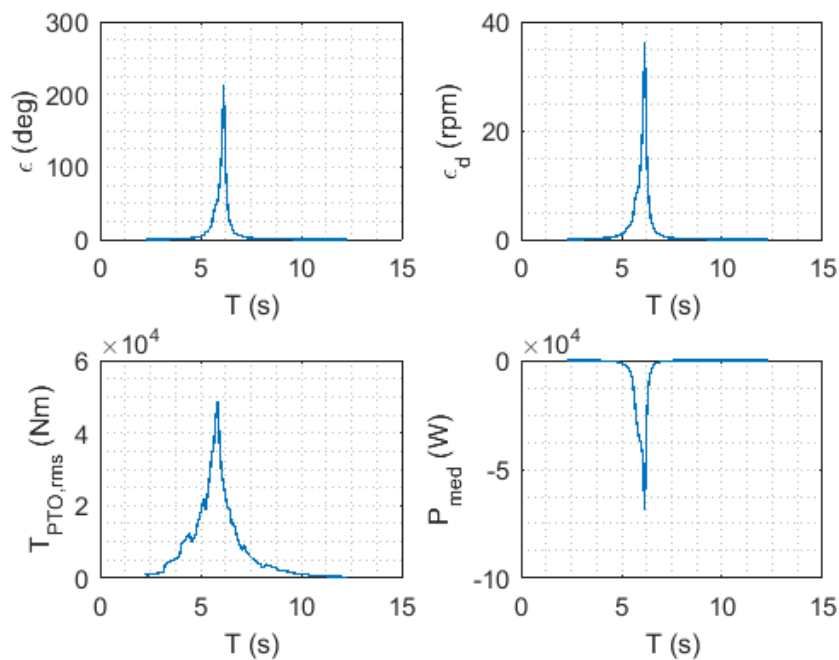
Fig. 6.16 Optimal configuration pendulum dynamics and average extracted power.

6.2.2   PeWEC Design Tool

The *PeWEC Design Tool* is based on the linearized dynamic equations of the system, expressed through the time domain formulation, given by Eq. 3.78. This tool has been developed starting from the *ISWEC Design Tool*, implemented at the Politecnico di Torino by Sirigu and Vissio [109][111]. The idea of this program was to obtain a sufficiently reliable and fast program able to optimize the the ISWEC control parameters and thus its performances over the entire scatter diagram, together with the possibility to carry out quickly and easily some preliminary information about the WEC dynamics.

In this work, *ISWEC Design Tool* has been improved expanding the hydrodynamic model from one DOF to three DOFs, introducing the linear hydrodynamic viscous damping, the linearized mooring characteristic and substituting the ISWEC gyroscope linear dynamic equations with pendulum linearized mechanical equations. Even if the model has been improved introducing new features, *PeWEC Design Tool* is still characterized by very low computational costs.

The algorithm of the *PeWEC Design Tool* is subdivided in three different modules, each one is dedicated to a specific set of operations:

- *Input Data Module*

- *Linear Simulation and Optimization Module*

- *Post Processing Module*

Input Data Module

The *Input Data Module* receives in input the optimal configuration parameters calculated with the *PeWEC Linear Optimization Tool*: the updated hydrodynamic database and the pendulum physical properties (mass, inertia, hinge position, etc.).

Moreover, in this module it is possible to define the installation site scatter diagram and different constraints regarding the PTO maximum and root mean square torque and velocity. Other inputs are related to the pendulum bearings properties and the PTO control damping range.

Linear Simulation and Optimization Module

The *Linear Simulation and Optimization Module*, given the inputs collected by the *Input Data Module*, optimize the PTO net power for each wave sea state described by the scatter diagram, by choosing the most appropriate control parameters. The optimization algorithm is based on the cost function concept, with the aim to do not overcome the system limits determined, for instance, by the PTO torque-velocity characteristic [111].

The simulation is based on the solution of the time domain linearized dynamics equations, reported in Eq. 3.78. Such equations are rearranged according the state-space notation: this step is required for the replacement of the convolution integral with its approximation (see section 3.3.3). Here below, a summary of the PeWEC dynamic equations state space representation is given.

Recalling Eq. 3.78 and Eq. 3.47, it is possible to rewrite Eq. 3.78 as follows:

$$
\begin{aligned}
\left[\mathbf{M}_{\mathbf{s}}^{\text{lin}} + \mathbf{A}\left(\infty\right)\right]\ddot{\boldsymbol{X}}_{sys} + \mathbf{F}_{\mathbf{r}} + \left[\mathbf{B}_{\mathbf{v}}^{\text{lin}} + \mathbf{D}_{\mathbf{PTO}}\right]\dot{\boldsymbol{X}}_{sys} + \left[\mathbf{K} + \mathbf{K}_{\mathbf{p}} + \mathbf{K}_{\mathbf{m}}\right]\boldsymbol{X}_{sys} \\
= \boldsymbol{F}_{\boldsymbol{d}}\left(t\right) + \boldsymbol{F}_{\boldsymbol{w}}\left(t\right)
\end{aligned}
\tag{6.6}
$$

Let be Eq. 6.7 the general expression of the state space representation:

$$
\begin{cases}
\dot{\boldsymbol{X}}_{\boldsymbol{ss}} = \mathbf{A}_{\mathbf{ss}}\boldsymbol{X}_{\boldsymbol{ss}} + \mathbf{B}_{\mathbf{ss}}\boldsymbol{u} \\
\boldsymbol{y} = \mathbf{C}_{\mathbf{ss}}\boldsymbol{X}_{\boldsymbol{ss}} + \mathbf{D}_{\mathbf{ss}}\boldsymbol{u}
\end{cases}
\tag{6.7}
$$

On the base of Eq. 6.7 and taking into account the problem under analysis, the state vector $\boldsymbol{X}_{\boldsymbol{ss}}$ can defined as follows:

$$
\boldsymbol{X}_{\boldsymbol{ss}} = \begin{Bmatrix} \dot{\boldsymbol{X}}_{sys} \\ \boldsymbol{X}_{sys} \\ \zeta \end{Bmatrix}
\tag{6.8}
$$

Expressing Eq. 6.6 with respect to $\ddot{\boldsymbol{X}}_{sys}$ and after some simple algebra, it is possible to outline the state matrix $\mathbf{A}_{\mathbf{ss}}$, output vector $\boldsymbol{u}$ and input matrix $\mathbf{B}_{\mathbf{ss}}$ composition.

$$\mathbf{A_{ss}} = \begin{bmatrix} -\dfrac{\left[\mathbf{B_v^{lin}}+\mathbf{D_{PTO}}\right]}{\left[\mathbf{M_s^{lin}}+\mathbf{A}\left(\infty\right)\right]} & -\dfrac{\left[\mathbf{K}+\mathbf{K_p}+\mathbf{K_m}\right]}{\left[\mathbf{M_s^{lin}}+\mathbf{A}\left(\infty\right)\right]} & -\dfrac{\mathbf{C_r}}{\left[\mathbf{M_s^{lin}}+\mathbf{A}\left(\infty\right)\right]} \\ \mathbf{I} & \mathbf{0} & \mathbf{0} \\ \mathbf{B_r} & \mathbf{0} & \mathbf{A_r} \end{bmatrix} \tag{6.9}$$

$$\boldsymbol{u} = \left\{ \begin{array}{c} \dfrac{\boldsymbol{F_d}\left(t\right)+\boldsymbol{F_w}\left(t\right)}{\left[\mathbf{M_s^{lin}}+\mathbf{A}\left(\infty\right)\right]} \\ \mathbf{0} \\ \mathbf{0} \end{array} \right\} \tag{6.10}$$

$$\mathbf{B_{ss}} = \begin{bmatrix} \mathbf{I} & \mathbf{0} & \mathbf{0} \end{bmatrix} \tag{6.11}$$

Clearly, $\boldsymbol{F_d}\left(t\right)$ and $\boldsymbol{F_w}\left(t\right)$ can be both regular or irregular wave forces, according to the results that needs to be carried out.

On the other hand, the output matrix $\mathbf{C_{ss}}$ and the disturbance matrix $\mathbf{D_{ss}}$ results be:

$$\mathbf{C_{ss}} = \begin{bmatrix} \mathbf{I} & \mathbf{0} & \mathbf{0} \\ \mathbf{0} & \mathbf{I} & \mathbf{0} \end{bmatrix} \tag{6.12}$$

$$\mathbf{D_{ss}} = \mathbf{0} \tag{6.13}$$

As stated before, the optimization algorithm try to maximize the net productivity, thus it takes into account the mechanical dissipation occurring inside bearings (friction forces due to the contact between rolling elements and raceways). Bearings friction torque can be modeled, as suggested by SKF, with the simplified formula [113]:

$$M_{b,f} = \frac{1}{2}\mu_b P d_b \tag{6.14}$$

Where $M_{b,f}$ is the bearing friction moment, μ_b the friction coefficient depending on the bearing typology and reported in the SKF catalogue, P the equivalent dynamic bearing load and d_b the internal bearing diameter.
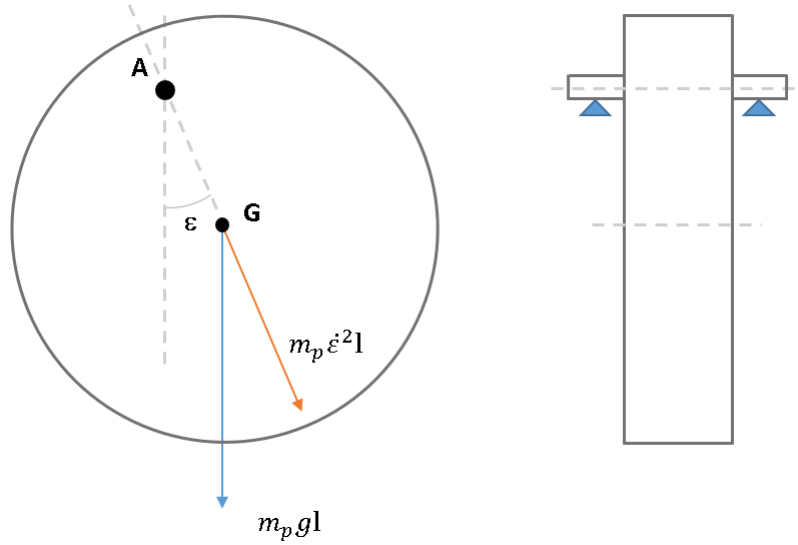
Fig. 6.17 Pendulum and bearings disposition scheme.

The load acting on bearings, assuming that the pendulum is centered with respect to bearings (as shown in Fig. 6.17), results be proportional to the sum of the pendulum gravity and centrifugal force and inversely proportional to the number of bearings n_b used.

$$P = \frac{m_p\left(g\cos\varepsilon + \omega^2 l\right)}{n_b} \tag{6.15}$$

Therefore, the friction moment can be calculated as reported in Eq. 6.16, while the power dissipated by the bearing is governed by Eq. 6.17:

$$M_{b,f} = \frac{1}{2}\mu_b m_p\left(g\cos\varepsilon + \dot{\varepsilon}^2 l\right)\frac{d_b}{n_b} \tag{6.16}$$

$$P_{b,f} = M_{b,f}\dot{\varepsilon} = \frac{1}{2}\mu_b m_p\left(g\dot{\varepsilon}\cos\varepsilon + \dot{\varepsilon}^3 l\right)\frac{d_b}{n_b} \tag{6.17}$$

Considering the optimization algorithm, it is based on the Nelder-Mead method [62][72], where a constrained optimization is defined by the minimization or maximization of an objective function (also called *cost function*) J, under a certain number of constraints g_i. In this work, the cost function is constituted by two distinct parts: the mean net power term and the system constraint terms. The first term is a negative
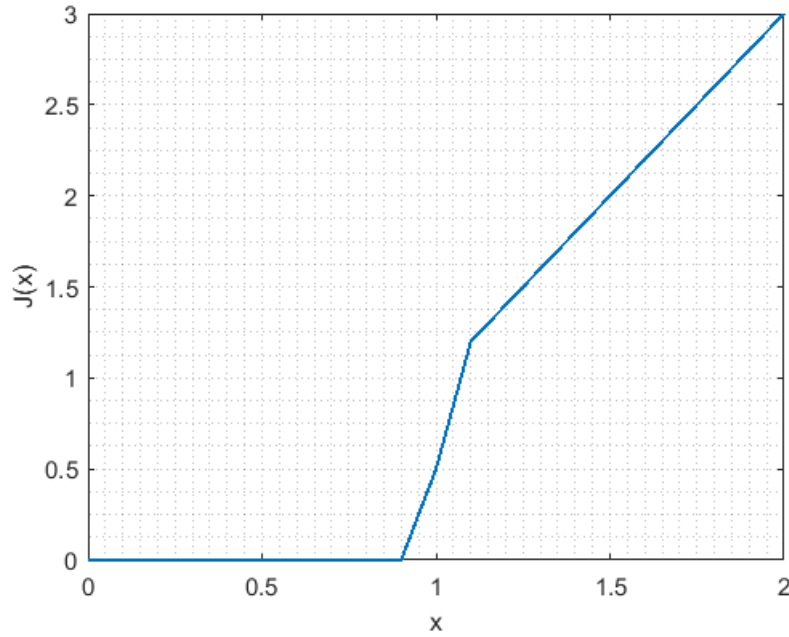
Fig. 6.18 Cost function example.

real value, while cost associated to each constraint is a positive real value. Therefore the sum of the costs is again a positive real number.

$$J = \tilde{\bar{P}}_{\varepsilon,net} + \sum_{i=1}^{N} J_i \tag{6.18}$$

Where $\tilde{\bar{P}}_{\varepsilon,net}$ corresponds to the average extracted net power, normalized with respect to the constraint given by the rated PTO power:

$$\tilde{\bar{P}}_{\varepsilon,net} = \frac{\bar{P}_{\varepsilon,net}}{P_{PTO,rated}} \tag{6.19}$$

On the other hand, the cost J_i due to other constraints related to physical system outputs (velocity, torque, etc.), is calculated through the following function, represented in Fig. 6.18:

$$J(\tilde{x}_i) = \frac{1 + \tanh\left[100(\tilde{x}_i - 1)\right]}{2} + 2H(\tilde{x}_i)(\tilde{x}_i - 1)^2 \tag{6.20}$$

In Eq. 6.20, $\tilde{x}_i$ corresponds to the normalization of the root mean square or maximum value of a generic system physical quantity (velocity, torque, etc.), with respect to the corresponding constraint g_i. In symbols:

$$\tilde{x}_i = \frac{rms\left\{x_i\right\}}{g_i} \tag{6.21}$$

$$\tilde{x}_i = \frac{max\left\{x_i\right\}}{g_i} \tag{6.22}$$

More in detail, in the case of the *PeWEC Design Tool*, the physical quantities subjected to a constraint are pitch motion, PTO angular speed and PTO torque.

$H\left(\tilde{x}_i\right)$, instead, is the *Heaviside function* defined as follows:

$$H\left(\tilde{x}_i\right) = \begin{cases} 0, & \tilde{x}_i < 0 \\ 1, & \tilde{x}_i \geq 0 \end{cases} \tag{6.23}$$

In the end, the optimization algorithm simulates recursively the PeWEC dynamic behavior per each cell of the scatter diagram, determining the optimal PTO control damping that maximizes the net average extracted power, respecting the requested boundaries.

Post Processing Module

The last module, called *Post Processing Module*, operates the numerical results representation in term of floater and pendulum motions, PTO torque and velocity, mooring forces, bearing loads and dissipation. Moreover, this module computes the device power matrix which, together with the occurrences scatter diagram, allows to calculate its productivity. The latter is calculated as follow:

$$Productivity = \sum_{m=1}^{M} \sum_{n=1}^{N} \overline{p}_{m,n} o_{m,n} \tag{6.24}$$

Where $\overline{p}_{m,n}$ and $o_{m,n}$ are, respectively, a generic element of the device power matrix (net or gross) and occurrences scatter diagram.
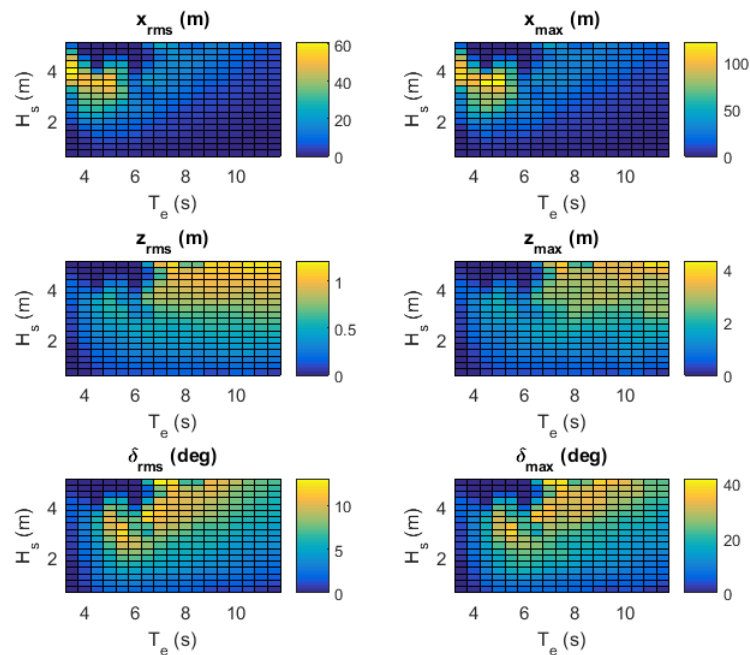
Fig. 6.19 PeWEC floater dynamics along surge, heave and pitch DOFs.

In the following figures, an example of the results that can be obtained from the *PeWEC Design Tool* are reported.

6.2.3   PeWEC Parametric Tool

The *PeWEC Parametric Tool* is a nonlinear simulation tool, programmed in MAT-LAB/Simulink ® environment, on the base of the nonlinear PeWEC dynamic equations expressed by Eq. 3.79. In addition to the nonlinearities described in Chapter 3, the model takes into account also the PTO saturations in term of torque and angular velocity. In Fig. 6.24, the Simulink block diagram is reported.

The inputs are constituted by the irregular wave forces generated according to the scatter diagram properties, the floater hydrodynamic database, pendulum mass and inertia, mooring nonlinear force-displacement characteristic and PTO torque-velocity map. Once the inputs are defined, the tool simulates recursively the system dynamic equation, varying PTO control damping and input wave, until all the sea states described by the scatter diagram are simulated. The simulations results are
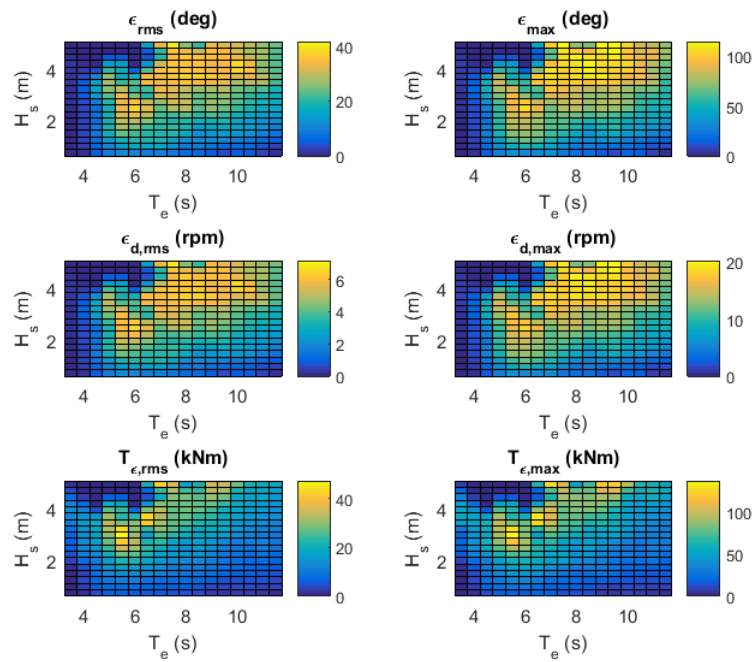
Fig. 6.20 Swinging mass motion, angular velocity and mechanical torque.
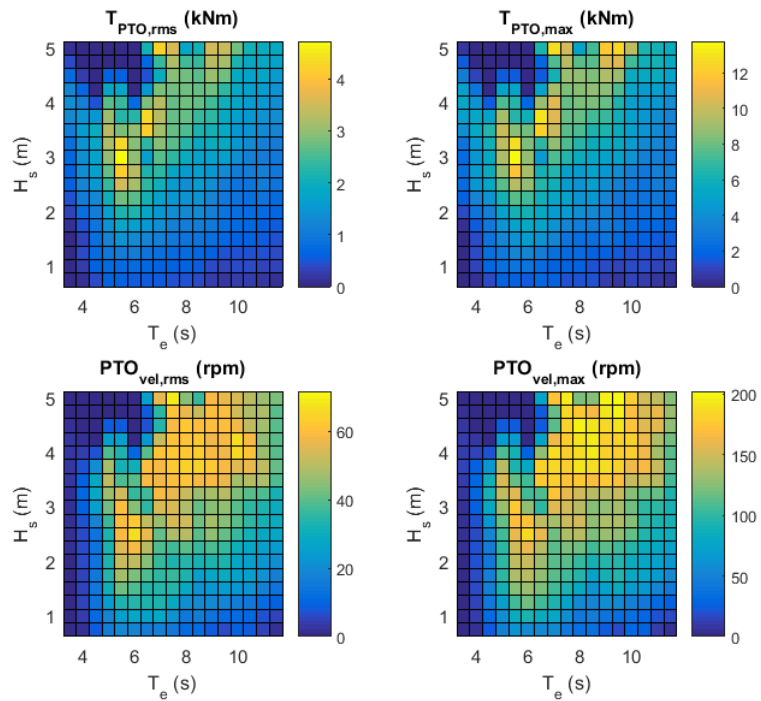
Fig. 6.21 PTO torque and angular velocity.
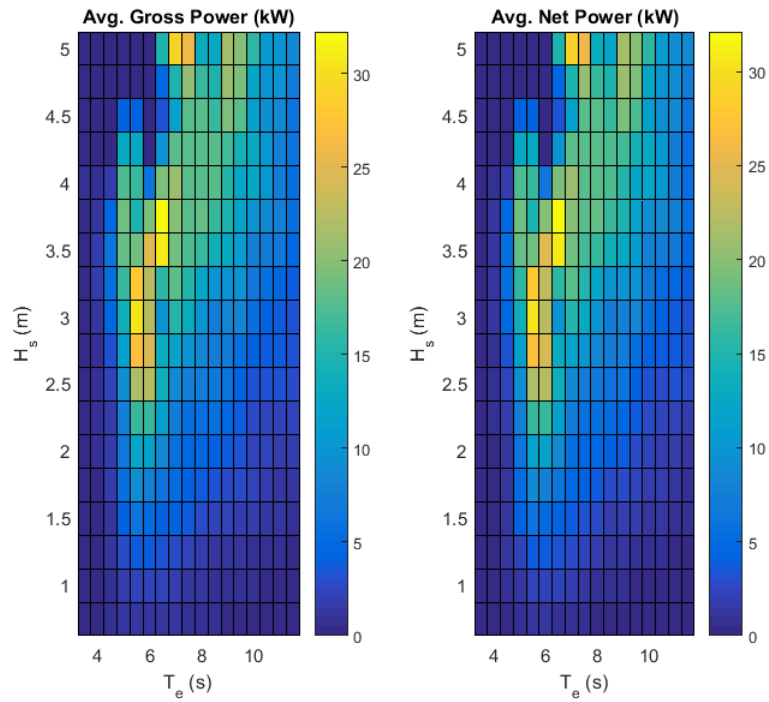
Fig. 6.22 Gross and net average extracted power matrix.
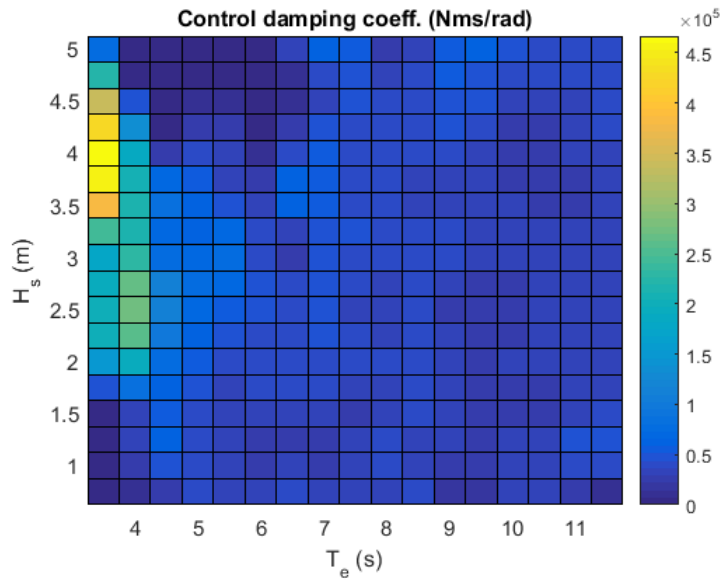
Fig. 6.23 Optimal PTO damping coefficient map.
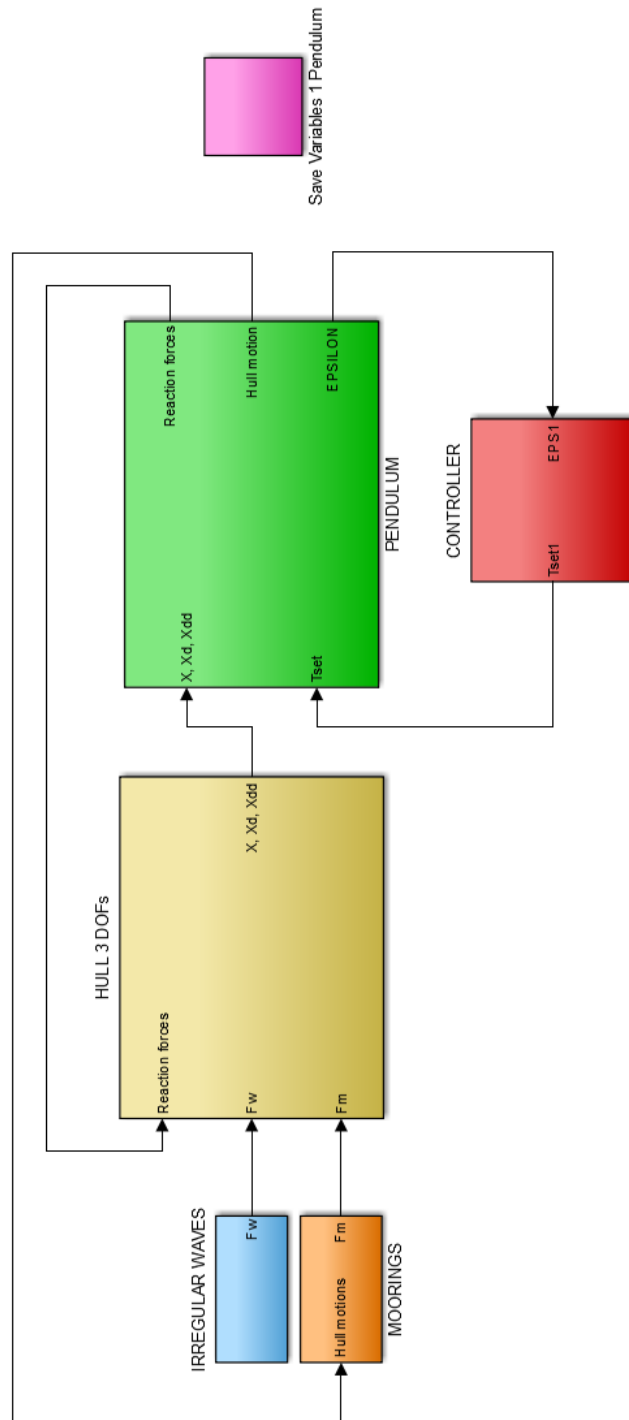
Fig. 6.24 *PeWEC Parametric Tool* MATLAB/Simulink block diagram.

stored in a database, which include all the information about system dynamics, PTO and moorings loads.

The database is read an elaborated through a post-processing and optimization algorithm: it is programmed to maximize the net productivity taking into account a series of constraints regarding the limitation of bearings loads, with the aim to minimize mechanical losses and guarantee an acceptable lifetime of the device. This goal can be achieved selecting, per each wave, a proper value of the PTO control damping. The identification of the optimal control parameter is actuated through a ranking function, reported in Eq. 6.25:

$$r = \overline{P}_{\varepsilon,net}\frac{G_p}{\Delta P} + C\frac{G_c}{\Delta C} + \dot{\varepsilon}_{max}\frac{G_{\dot{\varepsilon}}}{\Delta \dot{\varepsilon}} + T_{\delta,max}\frac{G_{T_\delta}}{\Delta T_\delta} \tag{6.25}$$

In which:

- $\overline{P}_{\varepsilon,net}$: average net extracted power;

- C: bearing basic dynamic load rating;

- $\dot{\varepsilon}_{max}$: maximum PTO angular speed;

- $T_{\delta,max}$: maximum floater pitch torque;

- $\frac{G_p}{\Delta P}$, $\frac{G_c}{\Delta C}$, $\frac{G_{\dot{\varepsilon}}}{\Delta \dot{\varepsilon}}$, $\frac{G_{T_\delta}}{\Delta T_\delta}$: weights of the different parameters included in the ranking functions. Weights are defined on the continuous interval $\begin{bmatrix} 0 & 1 \end{bmatrix}$;

Bearings life is estimated according to the Miner's rule [70][76][104][113], one of the most popular cumulative damage model for fatigue life prediction. The total life is calculated weighting each damage contribution with respect to the occurrences given by scatter diagram.

$$L_{10h} = \frac{1}{\sum_{m=1}^{M}\sum_{n=1}^{N}\frac{o_{m,n}}{L_{10h_{m,n}}}} \tag{6.26}$$

The life assessment per each scatter diagram cell is performed on the base of the SKF formula [113], considering the specific conversion factor for oscillating motions:

$$L_{10h_{m,n}} = \frac{2\varepsilon 10^6}{180 \cdot 60\dot{\varepsilon}} \left(\frac{C}{P}\right)^p \tag{6.27}$$

Where p is the exponent of the life equation. Since bearing loads change in time, an equivalent life load (ELL) needs to be defined: it corresponds to the constant load that produces the same effects of the original random load.

$$P_{ELL} = \left(\frac{1}{\Delta T} \int_0^T [P(t)]^p\right)^{\frac{1}{p}} \tag{6.28}$$

A similar consideration is valid also for ε and $\dot{\varepsilon}$, where the root mean square value should be considered.

Lastly, the optimized results are plotted accordingly to the methodology presented in section 6.2.2 for the *PeWEC Design Tool*.

Chapter 7

PeWEC full scale: a preliminary design for the Mediterranean Sea

Chapter 7 deals with the development of a preliminary design of the PeWEC full scale device for the Pantelleria installation site. The model based methodology presented in Chapter 6 is used to optimize the device performances, starting from a set of floater geometries. In particular, the *Linear Optimization Tool* and the *PeWEC Design Tool* are used to estimate the optimal floater-pendulum match and to assess the system preliminary productivity. This study is performed varying the pendulum mass, in order to determine the optimal value. The results obtained are benchmarked against the *PeWEC Parameteric Tool*, with the intention to prove the *PeWEC Design Tool* reliability.

Then, in the perspective of a real implementation of the technology, a preliminary structural design of the pendulum and of its bearings is performed, pursuing the objective of the identification of a plausible configuration in terms of mechanical manufacturing and costs.

The optimal configurations (pendulum mass and pendulum-floater match) obtained from the previous study are processed with the *PeWEC Parameteric Tool* for the identification of the most suitable electric PTO, among a set of commercial solutions. Moreover, each configuration is analyses with the aim to point out technical criticalities, device lifetime and performances.

A this stage of the design process, it is not possible to determine the optimal configuration that satisfies the best compromise between performances and costs.

Thereafter, an economic assessment of the possible alternatives generated at the end of the previous analysis is calculated, in order to extrapolate the best PeWEC full scale configuration among the ones tested and to asses how the preliminary design is far from a competitive LCOE target.

For this purpose, the *Levelized Cost of Energy* (LCOE) is considered, since it is commonly used for a first-order evaluation of the cost competitiveness of an electricity-generating system.

Lastly, the PeWEC configuration determined is compared with the full-scale ISWEC device operating in the Pantelleria Island site, highlighting the advantages and the drawbacks of each technology.

7.1 Full scale device design

7.1.1 Floater shape identification

Family A

The 1:45 and 1:12 scale PeWEC prototypes hull have been built considering a cylindrical section. This kind of geometry (see Fig. 7.1), as described in Chapter 4 and Chapter 5, is interesting because of the simplicity in terms of design and mechanical manufacturing.
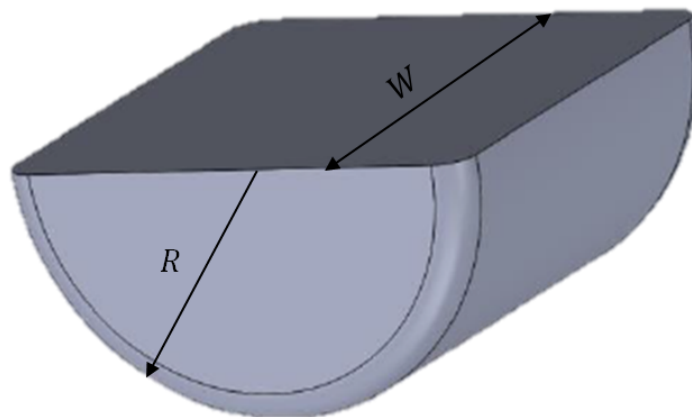
Fig. 7.1 *Family A*: sketch of the geometry.

Moreover, such geometry is particularly unstable with respect to pitch axis. However, this shape is characterized by a very large volume that requires a really considerable ballast quantity to obtain the required draft, that satisfies the stability criteria highlighted in section 5.1.2. Moreover, the space available for ballasts compartments is not enough, especially when a lighter and cheaper material with respect to steel is used. Sand is typical example of material considered for WECs ballasting.

Family B

This geometry is an evolution of the *Family A*, where the cylindrical shape is lightened on the sides, allowing a reduction of the submerged volume and thus of the ballast required to achieve the desired draft. The idea is to maximize the hull height in its central part, where the pendulum needs to be allocated (see Fig. 7.2). In Table 7.1, a comparison of the submerged volume and overall mass of a *Family A* and *Family B* floater is proposed, on the assumption of the same draft and external dimensions.

Table 7.1 *Family A* and *Family B* floater comparison.

Family	R (m)	R_1 (m)	W (m)	W_1 (m)	W_2 (m)	Draft (m)	m (ton)	V_{sub} (m^3)
A	8	-	10	-	-	4.8	510	498
B	8	5	10	2	4	4.8	175	171
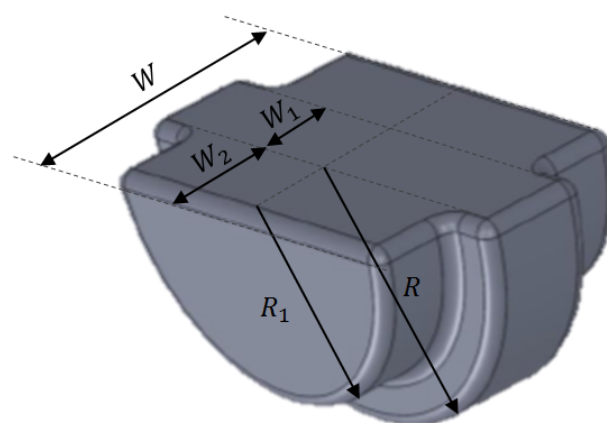
Fig. 7.2 *Family B*: sketch of the geometry.

The drawback of this geometry is represented by the limitation of the pitch resonance period that can be achieved. It is due to the limitation on the distance between ballast compartments and pitch axis. In fact, ballast compartments can be located only in the lateral parts of the floater, where the hull length is smaller.

Family C

In order to overcome the drawbacks of the *family B* floaters, a new hull family has been designed, replacing the cylindrical shape with an elliptical one. In this way, the ballast compartment distance with respect to pitch axis can be increased, leading to an increasing the floater pitch moment of inertia and thus of the resonance period. However, as shown by Fig. 7.3, the hull sides lightening proposed in the case of *family B* is maintained.
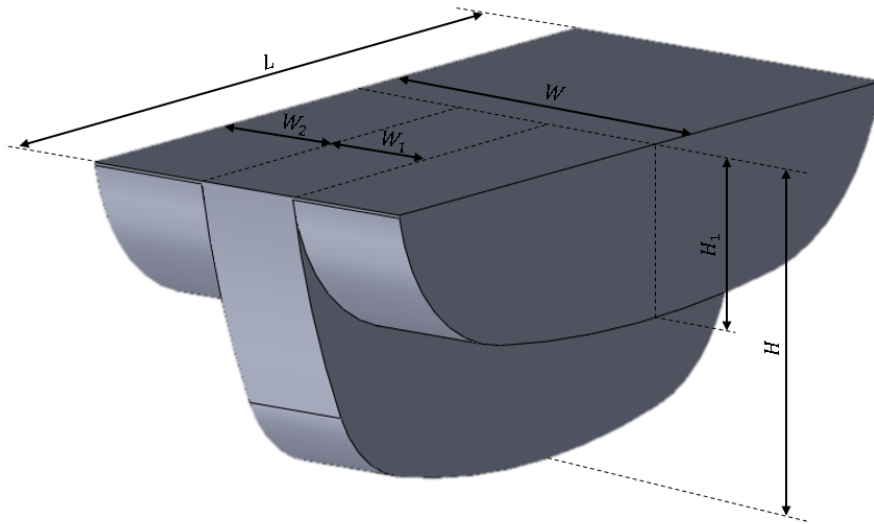
Fig. 7.3 *Family C*: sketch of the geometry.

Overall floater dimensions have been determined taking into account different considerations. First of all, the desired output power and RCW are selected in order to determine the floater width, according to the Eq. 7.1. A target average extracted power of 30 *kW* and a RCW of 15 % is assumed.

$$W = \frac{\overline{P}_\varepsilon}{RCW \cdot WPD} \qquad (7.1)$$

Concerning the hull length, the latter is chosen according to the criteria described in section 5.1.2, where a value between $\frac{\lambda}{4}$ and $\frac{\lambda}{2}$ is suggested to exploit the wave steepness. The limits for an acceptable floater length are calculated taking into account three different sea states selected on the base of the Pantelleria scatter diagram and of the equivalent distribution function described in section 6.2.1. More in detail, the most recurrent, most energetic sea states have been chosen, together with the one determined by the intersection between occurrences and energy normalized distribution functions, reported in Fig. 6.12. In Table 7.2, the sea states properties assumed as reference are summarized.

Table 7.2 Pantelleria scatter diagram sea state conditions assumed for the floater design.

Irregular sea state				
Case	$H_s(m)$	$T_e(s)$	$WPD\left(\frac{kW}{m}\right)$	$\lambda(m)$
Max. occurrence	0.55	6.25	0.94	-
Max. energy	2.65	7.75	26.7	-
Middle wave	1.6	6.7	8.57	-
Iso-energetic regular sea state				
Case	$H(m)$	$T(s)$	$WPD\left(\frac{kW}{m}\right)$	$\lambda(m)$
Max. occurrence	0.39	6.25	0.94	61
Max. energy	1.86	7.75	26.7	94
Middle wave	1.12	6.7	8.57	70

Lastly, the central part width has been designed as the best compromise between floater weight reduction, roll stability and space available for the installation of the swinging mass.

Table 7.3 *Family C* optimal floaters set properties.

Code	$L(m)$	$W(m)$	$W_1(m)$	$W_2(m)$	$H(m)$	$H_1(m)$	$Draft(m)$	$\Delta(tons)$
C19A	21	10	3	3.5	9	4.7	6.2	518
C19B	19	10	3	3.5	8	4.8	4.9	402
C19C	16	10	3	3.5	8	4.8	5.4	323
C19D	16	8	2.5	2.75	8	4.8	5.4	302

Several configurations have been simulated with the aim to find a set of solutions compliant with the criteria described above. For the sake of simplicity, only the

parameters of the optimal set of floaters are here reported (see Table 7.3), while further details of simulation campaign can be found in [20][47].

7.1.2   Preliminary device optimization

The floater configurations carried out from the analysis described in the previous section have been simulated with the *PeWEC Linear Optimization Tool*, optimizing pendulum dimensions, vertical position of its hinge and the quantity of ballast required in order to achieve the desired draft. Moreover, the optimal pendulum mass has been investigated taking into account the following values: 60000, 90000, 135000 and 203000 *kg*.

The optimized device parameters have been given in input to the *PeWEC Design Tool* for the preliminary calculation of the device productivity and its dynamic behavior over the entire scatter diagram. The latter has been described with 228 irregular waves. The 1200 *s* wave profile for each wave has been generated through the WAFO toolbox [126] and selecting the JONSWAP spectrum.

A preliminary estimation of the bearing size has been obtained through a static design of such components, according to the suggestion given by SKF manual [113]. More in detail, spherical roller bearings have been selected as suitable choice, while static load has been calculated including only the pendulum weight. This assumption can be assumed sufficiently realistic for a preliminary design, since pendulum angular velocity is particularly low and thus centrifugal forces can be neglected. Once bearings size is known, the it is possible to evaluate the device net productivity and thus its efficiency.

A verification of the *PeWEC Linear Optimization Tool* algorithm has been tested comparing the performances of the optimal configuration with the ones of a sub-optimal layout. As a case study, the results obtained in the case of the C19A version equipped with the 135 *tons* are considered. This case is particularly interesting since, from the map reported in Fig. 7.4, it is possible to highlight two energy peaks very similar in terms of value.

The optimal and sub-optimal configurations power computed in frequency domain are compared in Fig. 7.5. Even if sub-optimal configuration is characterized by a slightly wider bandwidth, the average extracted power in correspondence of the most recurrent waves is lower, leading thus to worst performances.
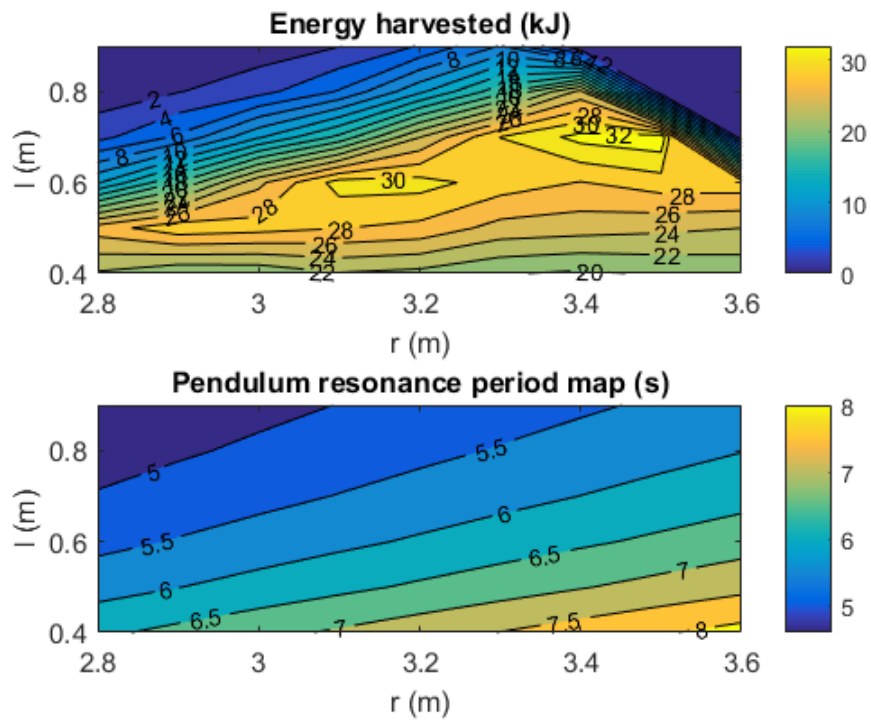
Fig. 7.4 Energy harvested map for configuration C19A, 135 *tons* pendulum mass.
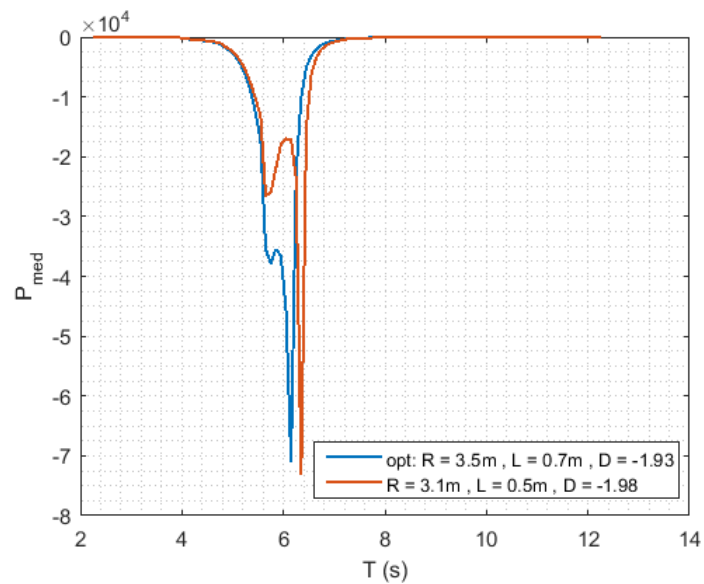
Fig. 7.5 Optimal and sub-optimal configuration frequency domain average extracted power comparison.
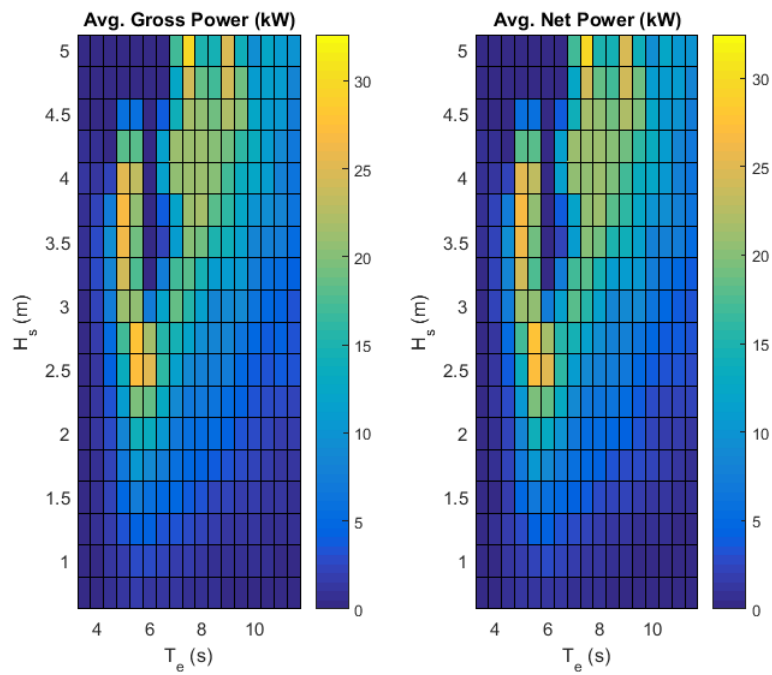
Fig. 7.6 Optimal layout (C19A, 135 *tons* pendulum mass) net and gross power matrices.
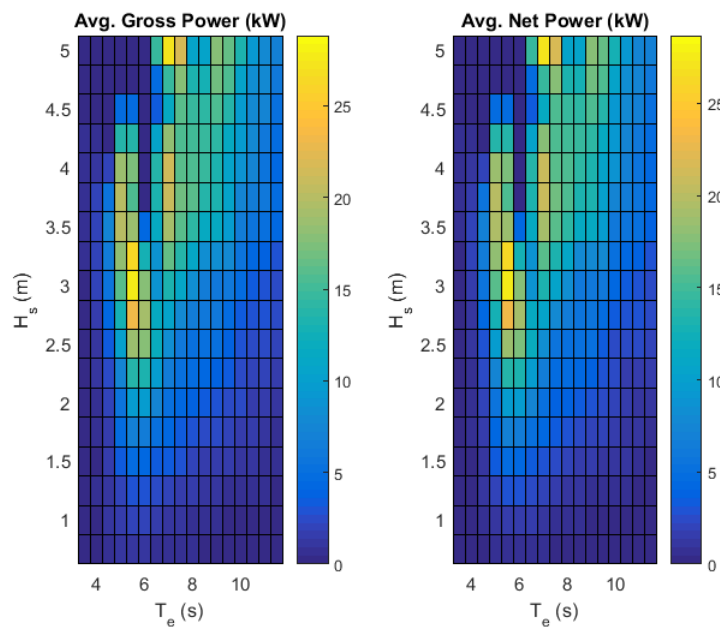
Fig. 7.7 Sub-optimal layout (C19A, 135 *tons* pendulum mass) net and gross power matrices.

Meanwhile, a verification of the *PeWEC Linear Optimization Tool* has been performed simulating the two configuration under investigation with the *PeWEC Design Tool*. The calculation of the productivity, performed on the base of the net power matrices reported in Fig. 7.6 and Fig. 7.7, showed that the sub-optimal layout considered is characterized by a net productivity 30% lower than optimal layout.

Returning back to the objective of the preliminary device optimization, in Fig. 7.8 gross and net productivity for each device layout have been plotted against the pendulum mass, proving that the performances depend on pendulum mass. This relation has been demonstrated by Pozzi in [90], taking into account the unconstrained PeWEC linear dynamic equations and proving that the optimal power absorption is directly proportional to the pendulum mass. Clearly, in the case of a constrained optimization problem, an optimal value of the pendulum mass is achieved and the latter depends on the boundaries assigned.
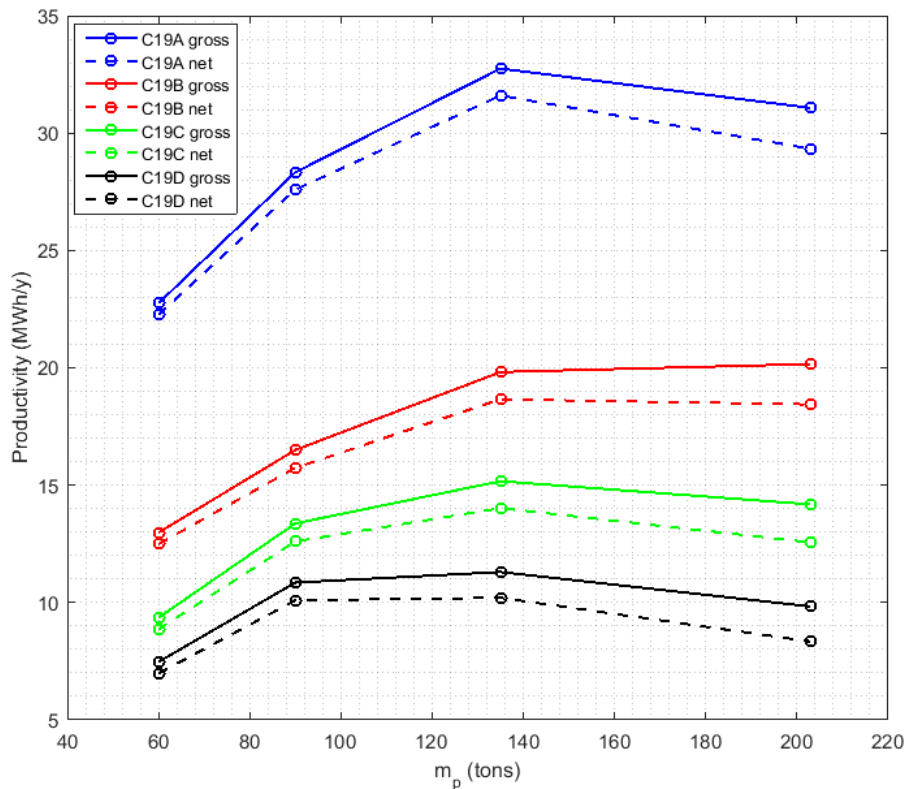
Fig. 7.8 Gross and net layouts productivity, as a function of the pendulum mass.

Observing Fig. 7.8, it is possible to highlight that, on the base of the net productivity, the 135 *tons* pendulum mass is the one that allows to maximize the performances

for all the configuration investigated. In Table 7.4, the optimal layout features are summarized.

Table 7.4 Optimal full-scale layouts properties.

	C19A	C19B	C19C	C19D	
	Floater				
m_{steel}	94050	79464	68990	60150	kg
$m_{ballast}$	283340	187206	119300	106500	kg
m_b	512390	401670	323290	301650	kg
COG	[0 0 -0.074]	[0 0 0.019]	[0 0 -0.29]	[0 0 -0.41]	m
d	-1.93	-1.48	-1.21	-1.09	m
I_{xx}	$6.74 \cdot 10^6$	$5.15 \cdot 10^6$	$3.99 \cdot 10^6$	$2.83 \cdot 10^6$	kgm^2
I_{yy}	$2.83 \cdot 10^7$	$1.65 \cdot 10^7$	$9.13 \cdot 10^6$	$8.14 \cdot 10^6$	kgm^2
I_{zz}	$2.96 \cdot 10^7$	$1.88 \cdot 10^7$	$1.08 \cdot 10^7$	$8.7 \cdot 10^6$	kgm^2
	Pendulum				
m_{steel}	16003	13260	13717	15089	kg
m_{concr}	118997	121740	121283	119911	kg
m_p	135000	135000	135000	135000	kg
I_y	824610	566120	646900	733060	kgm^2
r	3.5	2.9	3.1	3.3	m
l	0.7	0.5	0.6	0.6	m

7.1.3   Pendulum and PTO group detailed design

A detailed pendulum and PTO group design has been carried out in order to investigate the feasibility of the layout determined on the base of the numerical models and to find out a technological solution that allows to achieve the mass calculated using cheap materials.

The idea is to built a concrete filled steel pendulum: its external part, as represented in Fig. 7.9, is made by thin steel sheets formed in order to obtain the desired geometry and welded together. Moreover, the structure is reinforced internally with a series of bars, terminating in the pendulum hubs. Each hub is provided with a steel ring with a calibrated hole, whose function is to host the pendulum shaft. On the rings, the threaded hole required to keep the shaft in place and to transfer the torque are located. The pendulum is supported by a couple of spherical roller
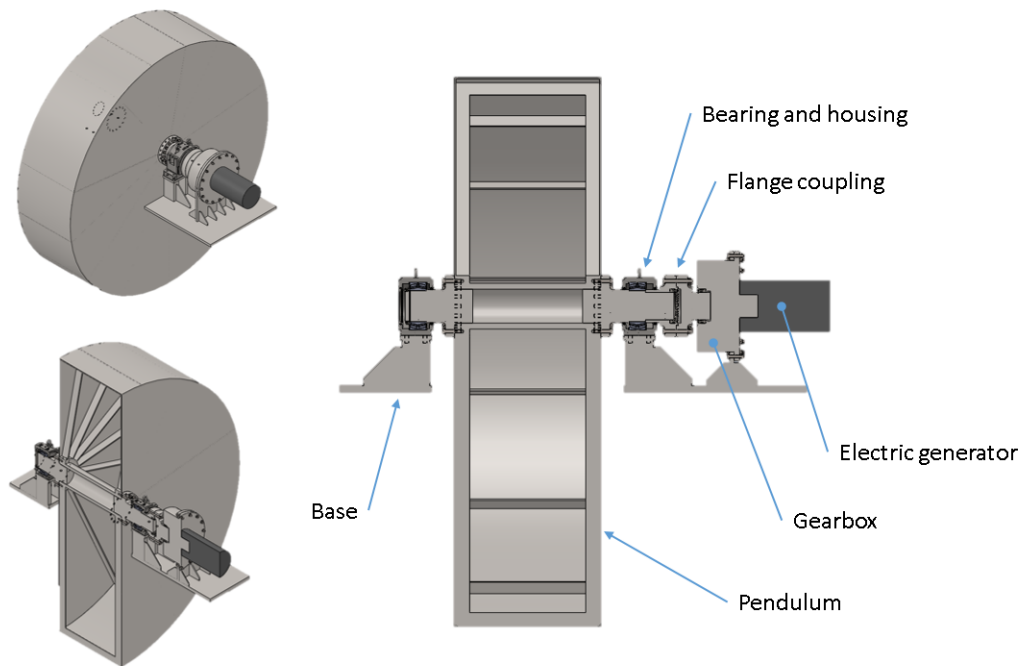
Fig. 7.9 Pendulum and PTO group CAD detail (concrete filling not represented).

bearings seated in the respective split plummer block housing [113]. A couple of flanges connects the pendulum shaft with respect to gearbox, on which the electrical generator is mounted. Note that for the sake of clarity, in Fig. 7.9 the concrete filling has not been represented.

A series of Finite Element Method simulations have been performed in order to asses the stresses of pendulum structure and shafts (see Fig 7.10). A more accurate calculation of the bearings has been carried out, aiming to a more realistic identification of the power losses. A couple of SKF 24068 CC/W33 spherical roller bearings have been selected. The main dimensions are reported in Table 7.5.

Table 7.5 SKF 24068 CC/W33 spherical roller bearings details.

Description	Symbol	Value	U.M.
Internal diameter	d_b	340	*mm*
External diameter	D_b	520	*mm*
Breadth	B	180	*mm*
Basic dynamic load rating	C	3621	*kN*
Basic static load rating	C_0	6200	*kN*
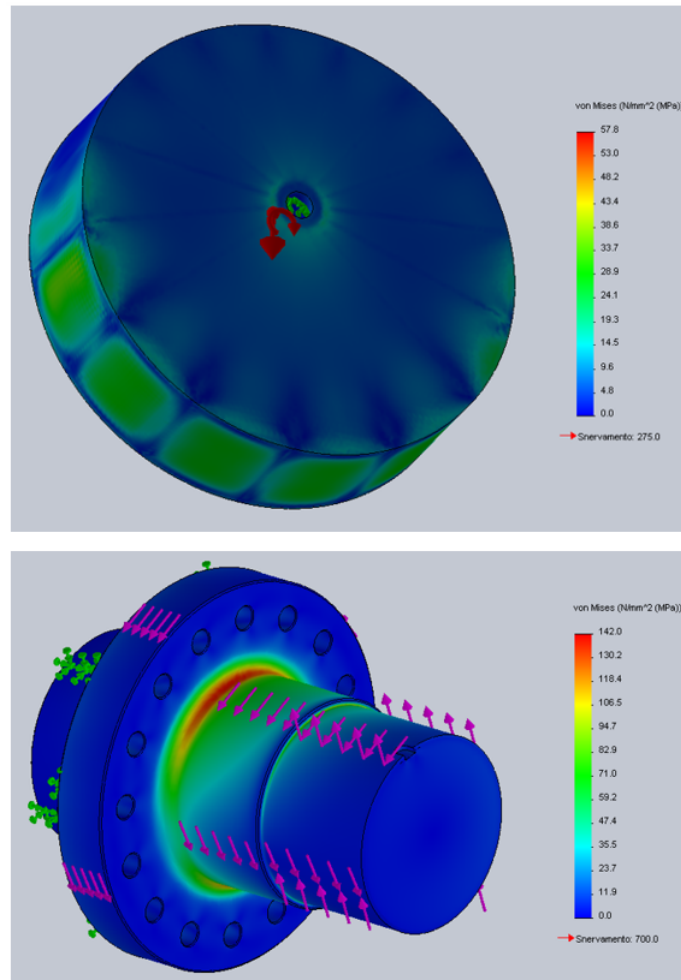
Fig. 7.10 Pendulum and shafts FEM analysis results.

7.1.4 Nonlinear simulations and PTO size identification

Nonlinear simulations are based on *PeWEC Parameteric Tool*, which solves the PeWEC nonlinear dynamic equations. The input of the simulations is constituted by the irregular waves chosen for the representation of the installation scatter diagram. Clearly, the wave profiles used in this analysis are the same used for the preliminary optimization performed through the *PeWEC Design Tool*. Other inputs are the floater hydrodynamic database and the pendulum properties corresponding to the optimal layouts identified in the previous design stage. As described in section 6.2.3, the optimization is related to the maximization of net productivity, according to a certain value of bearings lifetime.

Another important aspect of the design is the identification of the PTO size. A preliminary choice can be performed on the base of the *PeWEC Design Tool* results, individuating the maximum root mean square and maximum PTO angular velocity and torque. As example, in Fig. 7.11 the PTO estimated working conditions for the C19A layout equipped with the 135 *tons* pendulum are reported, while in Table 7.6, the maximum PTO working conditions for each one of the optimal layouts are reported.
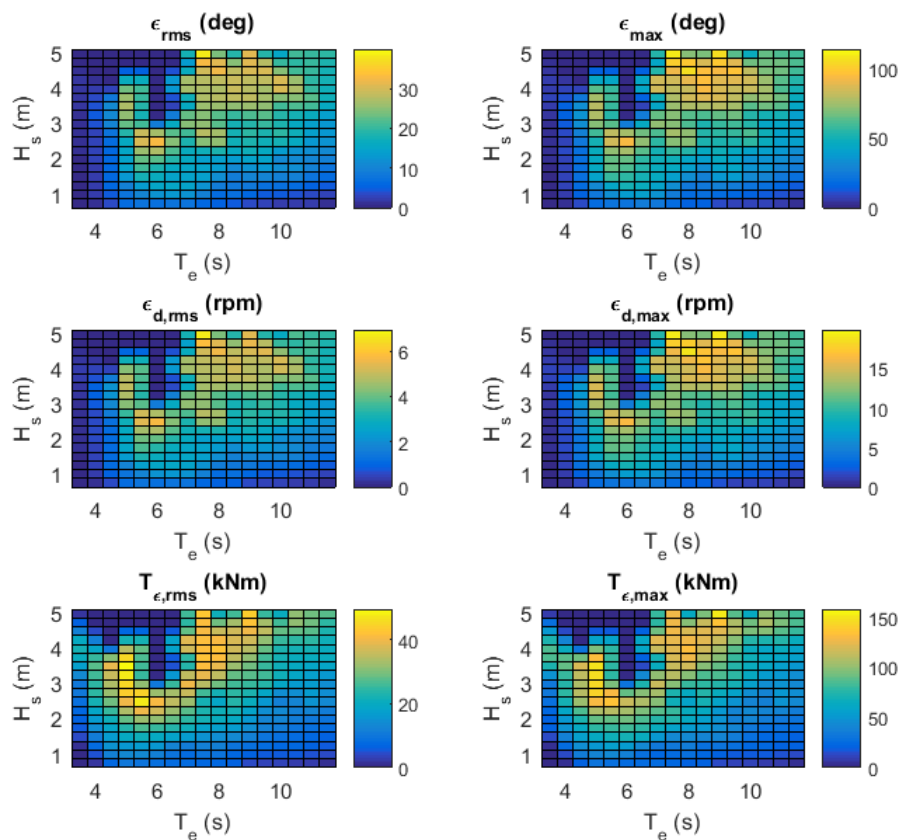
Fig. 7.11 Pendulum working conditions for the C19A layout equipped with the 135 *tons* pendulum.

A gear unit between the pendulum shaft the electric generator is required. The function of this component is to increase the angular speed and decreases the torque of the pendulum shaft. In this way it is possible to find a Power Take Off size available on the market. In this case a 1:10 gear ratio is chosen.

The values reported in Table 7.6 multiplied by the gear ratio chosen are compared with the technological solutions available on the Siemens catalogue, which has been

Table 7.6 Maximum pendulum working conditions for the optimal PeWEC layouts.

Description	C19A	C19B	C19C	C19D	U.M.
$max(T_{\varepsilon,rms})$	49560	51000	52020	50410	Nm
$max(T_{\varepsilon,max})$	150000	156700	145400	151600	Nm
$max(\dot{\varepsilon}_{rms})$	6.94	6.87	6.76	7.42	rpm
$max(\dot{\varepsilon}_{max})$	19.86	21.2	20.89	19.53	rpm

assumed as reference [108]. More in detail, three solutions have been considered, starting from a PTO solution very close to the torque and speed specifications determined. The second solution has the same rated velocity of the first option, but a higher rated and maximum torque. On the other hand, the last option has a lower rated and maximum torque. In Table 7.7, the main features of the electric generator chosen are summarized, while in Fig. 7.12 the Siemens 1FW-3285 torque-speed map is depicted.

Table 7.7 Siemens electric generators main features.

Description	Symbol	PTO 1	PTO 2	PTO 3	U.M.
Rated torque	T_{rated}	4950	6900	3450	Nm
Max. torque	T_{max}	8150	11400	5700	Nm
Rated speed	n_{rms}	250	250	250	rpm
Max. speed	n_{max}	440	460	460	rpm
Rated power	P_{rated}	130	181	90	kW
Max. power	P_{max}	137	209	105	kW
Siemens code	-	1FW-3285	1FW-3287	1FW-3283	-

The PTOs chosen are compliant in term of rated torque, rated speed and maximum speed, while no one of them can support the maximum torque computed by linear simulations. However, it is important to remark that the peak value computed by the linear model might be affected by some uncertainties, due to the intrinsic simplification of the model, even if proper constraints have been included.

In Fig. 7.13, the productivity computed through nonlinear simulations is reported, as a function of the PTO version and of the device layout. It is important to point out that nonlinear model results are in agreement with the estimations performed through the *PeWEC Design Tool*, proving its reliability. Observing again Fig. 7.13, layout C19A is the most interesting in term of performances with a peak of 39.7 $\frac{MWh}{y}$ net productivity, when equipped with PTO 2. PTO 1, corresponding to the
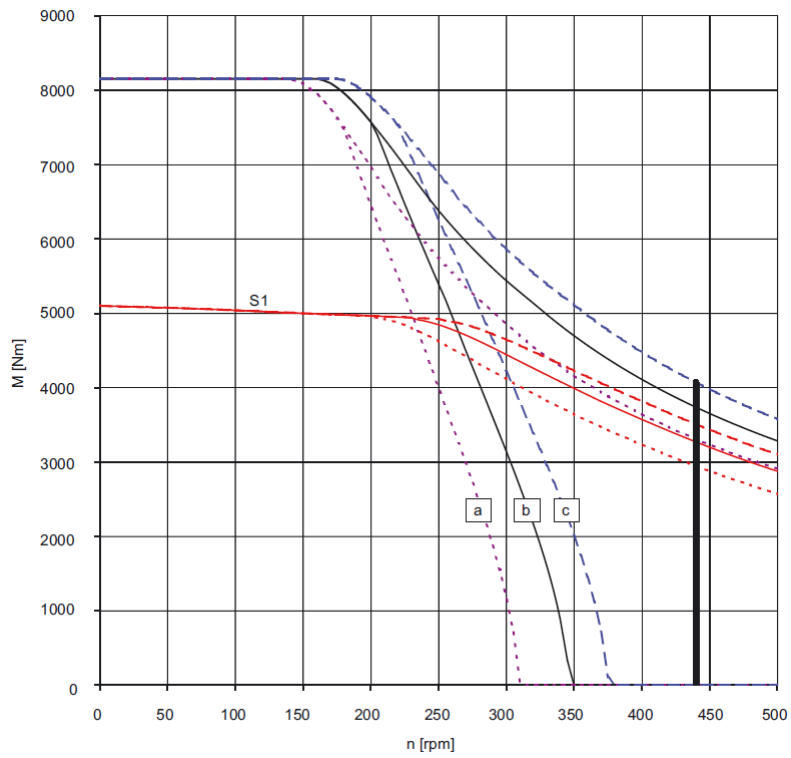
Fig. 7.12 Siemens 1FW-3285 torque-speed map.
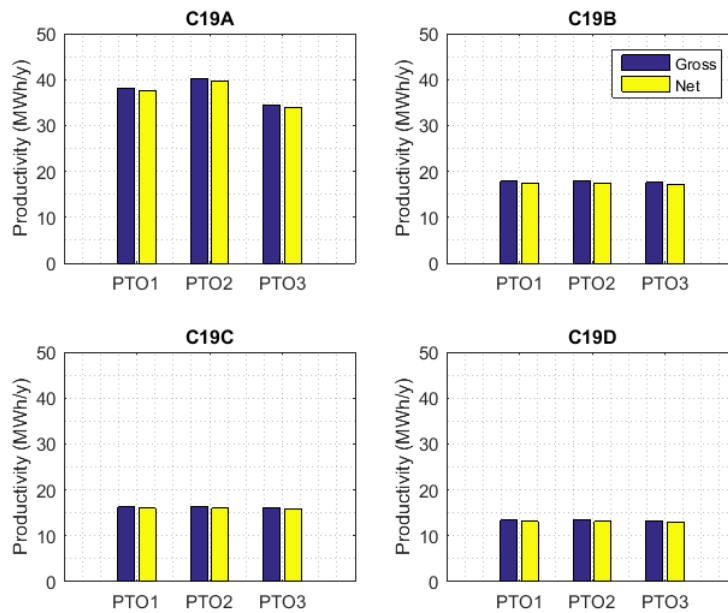
Fig. 7.13 Gross and net productivity of the investigated configurations, varying the PTO size.

initial choice, allows to achieve slightly lower net productivity, around 37.6 $\frac{MWh}{y}$, while PTO 3 leads to a remarkable reduction of device performances. Therefore, it is clear that the PTO solution determined starting from the *PeWEC Design Tool* results was almost correct.

On the other hand, the expected performances decrease moving from layout C19B to C19D, as already observed from the *PeWEC Design Tool* analysis. Moreover, the productivity variation with respect to the PTO size becomes less relevant.

A common point of all the configurations investigated is represented by the very low entity of the bearings losses, which are less than 1 $\frac{MWh}{y}$. Regarding dissipation, PTO and auxiliary systems losses are neglected at this stage, since they strongly depends on the design solutions adopted for the final device layout.

On the base of the performances, arise that the layout C19A equipped with PTO 2 should be the best option, however this assumption is not correct if the economic assessment of the technology is ignored. For this reason, in the next section the techno-economic analysis of the different configurations considered is performed, aiming to the identification of the best layout through the Levelized Cost of Energy (LCOE).

7.2 Techno-economic analysis

7.2.1 Levelized Cost of Energy

The last part of the full scale PeWEC preliminary design deals with the economic assessment of the technology. The Levelized Cost of Energy (LCOE) is the most important factor in determining whether an energy production technology is ready for commercialization and it is widely reported in the energy policy literature [12]. Basically, it is defined as the average total cost to build and operate a power generating asset over its lifetime divided by the total energy output of the asset over that lifetime and it allows to compare different technologies (e.g. wind, solar, natural gas, etc.) of unequal life spans, project size, different capital cost, risk, return and capacities on a consistent basis.

Accordingly to Fig. 7.14, the LCOE is composed by three main terms:
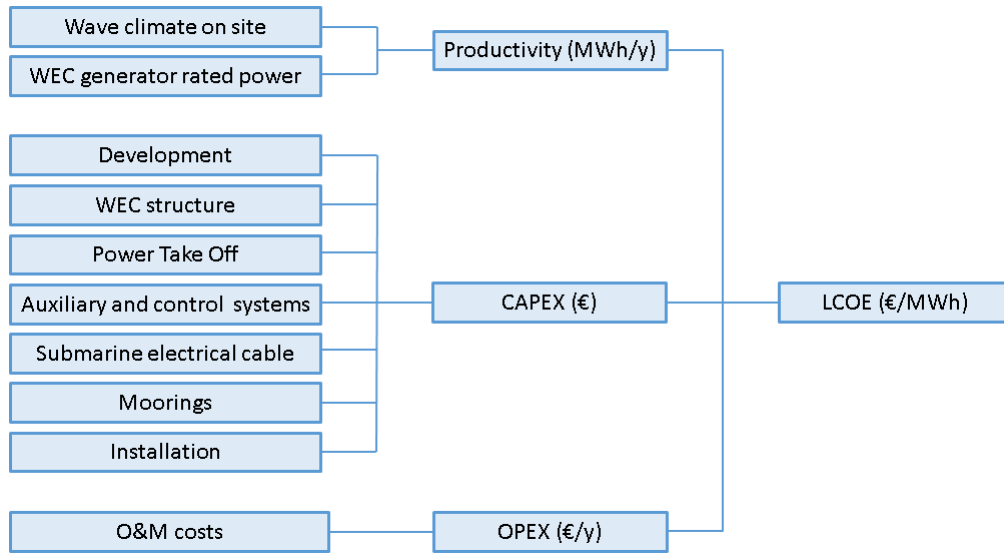
Fig. 7.14 Levelized Cost of Energy scheme.

- *Annual productivity*: estimated through the combination of the installation site wave climate and the WEC power matrix;

- *Capital Expenditure* (CAPEX): takes into account the initial investment for the development and construction of the device and installation, including moorings and submarine cables.

- *Operating Expenditure* (OPEX): includes the costs incurred annually to maintain the plant in terms of ordinary and extraordinary maintenance.

Typically the LCOE is calculated over the design lifetime of a plant, which is usually 20 to 40 years and given in the units of currency per *kWh* or *MWh*, for example $\frac{€}{kWh}$. In symbols:

$$LCOE = \frac{CAPEX + \sum_{t=1}^{n} \frac{OPEX}{(1+r)^t}}{\sum_{t=1}^{n} \frac{E_t}{(1+r)^t}} \tag{7.2}$$

Where, E_t is the device productivity at the *t-th* year, while *n* in plant lifetime and *i* the discount rate.

Despite the LCOE is commonly used, care should be taken in comparing different LCOE studies, since it is highly dependent on the assumptions, financing terms and

technological deployment analyzed. Thus, a key requirement for the analysis is a clear statement of the applicability of the analysis based on justified assumptions [29]. Besides assumptions, uncertainties about wave climate data [96], device response and efficiency under real conditions, extraordinary maintenance expenses and socio-economic issues have a relevant impact on the LCOE estimation [51]. Such uncertainties, in the case of the Wave Energy, arise because most technologies have rarely been tested under real conditions. One of the most remarkable consequence of uncertainties is a reduction of the profitability competitiveness of an investment project. Therefore, a careful analysis of the multiple factors involved in the metric for economic assessment is suggested, including a deep evaluation of the stakeholders' requirements for a commercially successful plant [13].

7.2.2   PeWEC project LCOE evaluation

The PeWEC project LCOE has been evaluated taking into account, as reference, the experience gained during the development of the ISWEC full scale plant, deployed in 2015 in Pantelleria Island, Italy (see Chapter 1). This choice, from one side is particularly helpful in the estimations of the costs, which can be based on a real application; on the other side, it is possible to compare, under the same assumptions, the economic of the ISWEC and PeWEC technologies. In this section, the assumptions, together with the LCOE calculation results are reported.

CAPEX assumptions

Capital expenditure has been calculated splitting the PeWEC device in its main subsystems and calculating the corresponding cost.

- *Floater*: its cost has been calculated using a coefficient of 3.5 $\frac{\text{€}}{kg}$, that takes into account the material and manufacturing costs. The coefficient assumed is a little bit higher than the ISWEC one, because of the more complex geometry of the hull. The complexity will affect mainly the manufacturing cost. Moreover, this factor has been increased to 4 $\frac{\text{€}}{kg}$ in the case of hulls C19C and C19D, because despite they are smaller, the overall cost will not change much. Therefore, the price per unit of mass will rise. It is important to highlight that the specific price has been calculated including the external coating.

- *Ballast*: it is made of dry sand, a very common and cheap material. The cost per unit of mass has been determined also from the literature and it is equal to $0.05 \frac{€}{kg}$.

- *Pendulum*: it is composed by an external steel structure filled with concrete. A specific price of $3 \frac{€}{kg}$ and $0.5 \frac{€}{kg}$ has been assumed for the steel and concrete part, respectively. The steel specific price is determined on the base of both the experience gained on the ISWEC project and manufacturing considerations. The steel structure, as described in 7.1.3, is constituted by formed steel sheets welded together and properly reinforced in the internal part with a series of stiffeners. The overall precision and complexity of such structure is medium-low. Only in correspondence of pendulum hub tolerance are tighter, in order to guarantee a proper coupling and coaxiality of the shafts on pendulum structure. Therefore, most of the costs are related to welds, which need to be executed by specialized workers in order to be compliant with respect to the certifying agencies requirements. Another aspect of relevant importance is coating, in order to prevent corrosion due to inevitable infiltration of brackish air.

- *Shafts*: according to the design prescriptions, an alloyed steel is used. After a process of rough machining, shafts are nitrided, quenched and tempered, improving fatigue strength, hardness and corrosion resistance. Then, shafts are finished by grinding, with aim to obtain the desired precision of bearings seats and a proper alignment of the shafts in the pendulum hub. In the light of these considerations, a cost of $7 \frac{€}{kg}$ has been chosen.

- *Gearbox*: the gearbox cost has been estimated through a series of quotations of commercial solutions suitable with respect to the specification required.

- *Bearings and housings*: similarly to gearbox, the price of bearings and housing has been assessed through a quotation from a SKF dealer.

- *Moorings*: the ISWEC device mooring configuration and costs have been chosen as reference. On the base of these data, the mooring line cost has been calculated. A higher cost has been considered for the heavier configurations (C19A and C19B).

- *Auxiliary systems*: include all the electronic and electrical equipment required for the device functioning and monitoring. Costs have been assessed starting from the ISWEC equipment layout.

- *Other CAPEX*: this item includes project implementation cost, comprising installation, electrical connection to the platform and project set-up cost.

In Fig. 7.15, a table summarizing the CAPEX of the configurations investigated is proposed, together with the percentage incidence of each CAPEX component on the overall cost. The average CAPEX composition for the configurations investigated is reported in the pie chart of Fig. 7.16.

Observing Fig. 7.16, arise that the floater cost constitutes the most important component and together with pendulum cost covers the 50% of the overall CAPEX. Moorings and other CAPEX are also relevant (12% and 13% respectively), contributing for a 25% of the entire device cost. Obviously, the cost analysis presented in this work is preliminary, but allows to highlight the most important sources of cost. As suggested in [13], CAPEX should be minimized through an accurate design of each subsystem, avoiding waste of material, reducing as much as possible the use of specialized tools and equipment and avoiding highly qualified workers. Another important aspect is represented by an accurate planning of the device installing procedures, that should be in minimum quantity and as much simple as possible. Lastly, the cost of the most expensive subsystems can be reduced in the perspective of the implementation of a farm of WECs, where the multiple devices needs to be built. In this case, discounts on material, commercial components and manufacturing process can be achieved.

OPEX assumptions

Operating expenditures are mainly driven by unplanned maintenance (reliability) and planned maintenance (durability). WEC reliability is achieved with high-quality components, by minimizing the number of parts subject to well-known failure modes (fatigue, wear, abrasion, etc.) and by avoiding impulsive loads. On the other hand, durability is determined by the design and choice of high durability components.

At this stage of the PeWEC full scale device development, few considerations can be made about maintenance intervals and costs. For instance, bearings have been designed to withstand to the expected external loads up to 50 years, a time interval higher than the imposed plant lifetime (30 years). This means that, the particularly expensive operation related to bearings replacement, could be avoided. Other maintenance operations could be the revamping of the floater external coat-

	C19A PTO1	C19A PTO2	C19A PTO3	C19B PTO1	C19B PTO2	C19B PTO3	C19C PTO1	C19C PTO2	C19C PTO3	C19D PTO1	C19D PTO2	C19D PTO3
hull [€]	329175	329175	329175	278124	278124	278124	275960	275960	275960	240600	240600	240600
ballast [€]	14167	14167	14167	9360	9360,3	9360,3	5965	5965	5965	5325	5325	5325
pendulum [€]	107508	107508	107508	100650	100650	100650	101793	101793	101793	105223	105223	105223
shafts [€]	12530	12530	12530	12530	12530	12530	12530	12530	12530	12530	12530	12530
bearing + housing [€]	32844	32844	32844	32844	32844	32844	32844	32844	32844	32844	32844	32844
gearbox [€]	28000	39000	20000	28000	39000	20000	28000	39000	20000	28000	39000	20000
PTO & drive [€]	39376	52832	32375	39376	52832	32375	39376	52832	32375	39376	52832	32375
mooring [€]	100000	100000	100000	100000	100000	100000	80000	80000	80000	80000	80000	80000
auxiliary systems [€]	60000	60000	60000	60000	60000	60000	60000	60000	60000	60000	60000	60000
other CAPEX [€]	100000	100000	100000	100000	100000	100000	100000	100000	100000	100000	100000	100000
CAPEX [€]	823600	848056	808599	760884	785340	745883	736468	760924	721467	703898	728354	688897

	C19A PTO1	C19A PTO2	C19A PTO3	C19B PTO1	C19B PTO2	C19B PTO3	C19C PTO1	C19C PTO2	C19C PTO3	C19D PTO1	C19D PTO2	C19D PTO3	Average
hull [%]	39,97	38,82	40,71	36,55	35,41	37,29	37,47	36,27	38,25	34,18	33,03	34,93	36,91
ballast [%]	1,72	1,67	1,75	1,23	1,19	1,25	0,81	0,78	0,83	0,76	0,73	0,77	1,13
pendulum [%]	13,05	12,68	13,30	13,23	12,82	13,49	13,82	13,38	14,11	14,95	14,45	15,27	13,71
shafts [%]	1,52	1,48	1,55	1,65	1,60	1,68	1,70	1,65	1,74	1,78	1,72	1,82	1,66
bearings + housings [%]	3,99	3,87	4,06	4,32	4,18	4,40	4,46	4,32	4,55	4,67	4,51	4,77	4,34
gearbox [%]	3,40	4,60	2,47	3,68	4,97	2,68	3,80	5,13	2,77	3,98	5,35	2,90	3,81
PTO & drive [%]	4,78	6,23	4,00	5,18	6,73	4,34	5,35	6,94	4,49	5,59	7,25	4,70	5,47
mooring [%]	12,14	11,79	12,37	13,14	12,73	13,41	10,86	10,51	11,09	11,37	10,98	11,61	11,83
auxiliary systems [%]	7,29	7,08	7,42	7,89	7,64	8,04	8,15	7,89	8,32	8,52	8,24	8,71	7,93
other CAPEX [%]	12,14	11,79	12,37	13,14	12,73	13,41	13,58	13,14	13,86	14,21	13,73	14,52	13,22
CAPEX [%]	100	100	100	100	100	100	100	100	100	100	100	100	100

Fig. 7.15 CAPEX composition and percentage weight of its components on the overall cost, for the different configurations investigated.
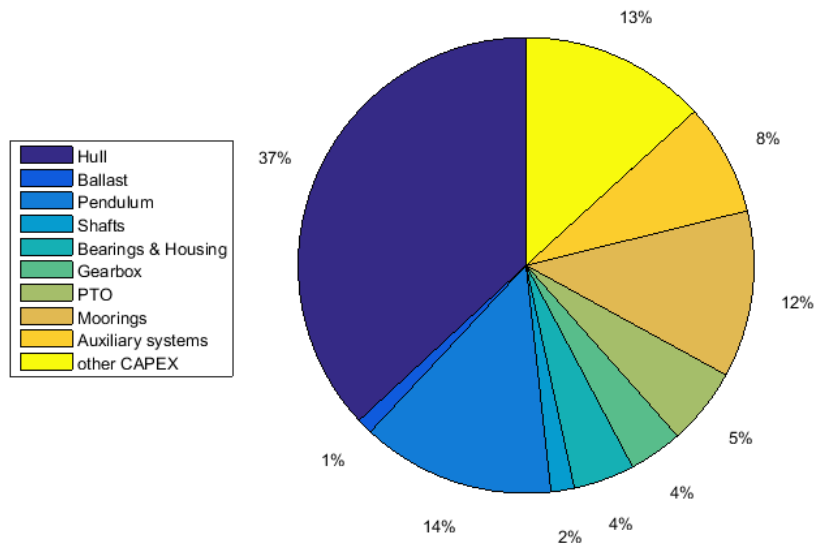
Fig. 7.16 PeWEC device average CAPEX composition.

ing, the inspection or replacement of the gearbox lubricant, inspection of bearings status and lubrication, inspection of the PTO coolant. Among these operations, the revamping of the floater coating is the most critical, since it is performed each 3 - 5 years, according to the material used and to the inspection rules determined by the certification agency (RINA, DNV, etc.).

In short, because of the lack of information, the OPEX has been calculated the 2.5% of the CAPEX.

Financial assumptions

Beside technical assumptions, some financial terms needs to be considered in order to complete the LCOE calculation. In the perspective of a comparison between ISWEC and PeWEC technologies, financial assumptions are the same for both projects. In particular:

- Electricity price has been imposed equal to 100 $\frac{€}{MWh}$, including incentives.

- Banks and debts operations are neglected (full equity). This means also that money comes from the investors involved in the project.

- The discount rate is assumed to be 2.5%.

Results

Bringing together all the assumptions, it is possible to calculate the Levelized Cost of Energy (LCOE) per each one of the configurations investigated. Table 7.8 and Fig. 7.17 summarizes the results achieved.

Table 7.8 PeWEC LCOE results.

Version	CAPEX $(\text{\euro})$	OPEX $\left(\frac{\text{\euro}}{y}\right)$	LCOE $\left(\frac{\text{\euro}}{MWh}\right)$
C19A - PTO 1	723600	18090	1528
C19A - PTO 2	748600	18701	1491
C19A - PTO 3	708599	17715	1657
C19B - PTO 1	660884	16522	3031
C19B - PTO 2	685340	17134	3122
C19B - PTO 3	645883	16147	2905
C19C - PTO 1	636468	15912	3202
C19C - PTO 2	660924	16523	3305
C19C - PTO 3	621467	15537	3161
C19D - PTO 1	603898	15097	3723
C19D - PTO 2	628354	15709	3848
C19D - PTO 3	588897	14722	3668
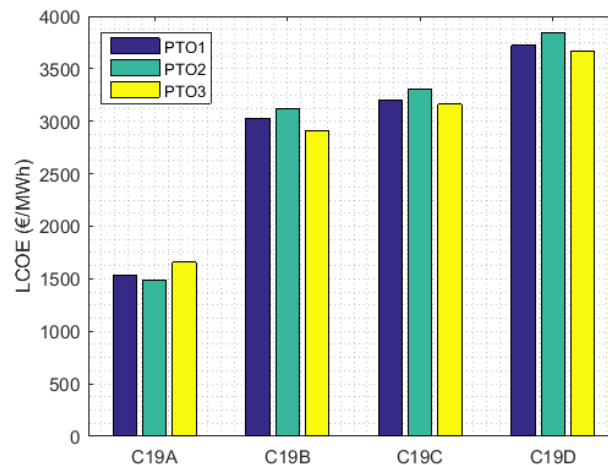
Fig. 7.17 LCOE results for the different configurations investigated, varying the PTO size.

The configuration C19A equipped with PTO 2, among the other layouts considered, is the one that minimizes the Levelized Cost of Energy. The corresponding

value is equal to 1491 $\frac{€}{MWh}$. In this case, the biggest PTO solution is the most convenient, even if more installed power means more expensive components (PTO, drives, gearbox). This means also that the productivity increment with respect to the initial PTO version (PTO1, carried out from preliminary design) justify the CAPEX increment. On the other hand, a smaller solution with respect to the initial PTO size (PTO 3) leads to a productivity drop and thus it is not suitable.

On the other hand, in the case of the less performing layouts, the smaller PTO size is preferred, since it allows to reduce device costs and then to optimize the LCOE. However, such configurations are very far from a competitive perspective, and thus they can be discarded from the analysis.

In the light of these considerations, arise that configuration C19A is the most competitive and it can be considered a good starting point for further analysis and the development of a more detailed design of the different subsystems and internal equipment, with the aim to better evaluate CAPEX and hence, to reduce the device costs. In Fig. 7.18, a 3D CAD model of the PeWEC C19A layout is depicted, showing the pendulum installed on the support frame described in section 7.1.3 and the ballasts positioned in the floater corners.
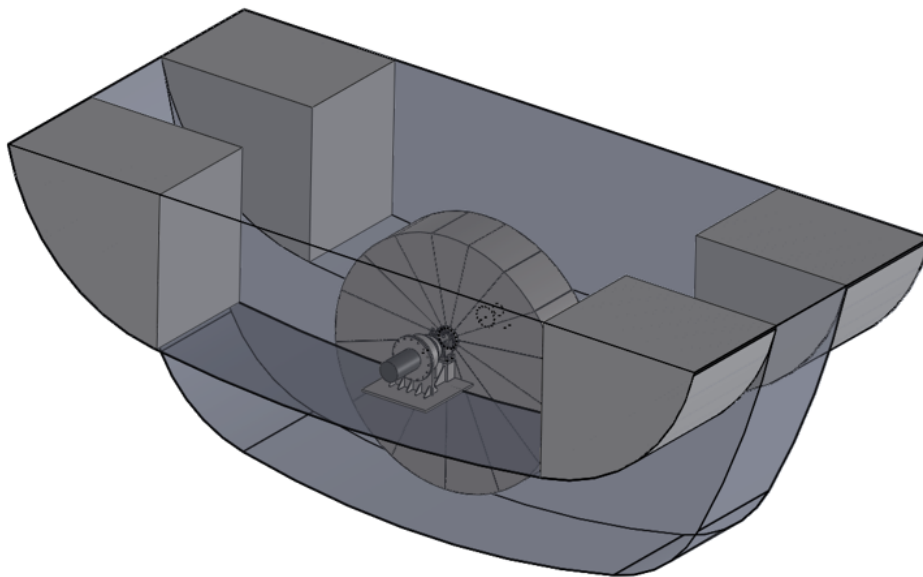
Fig. 7.18 3D CAD model of the PeWEC C19A layout.

7.3 PeWEC vs. ISWEC

The last part of this chapter is concerned about the comparison between PeWEC and ISWEC technologies, with the aim to identify the corresponding advantages and drawbacks. The comparison can be performed from several points of view however, for the sake of clarity and brevity, the following aspects have been taken into account:

- Performances and Efficiency

- Technological considerations

- Levelized Cost of Energy

Here below a brief discussion of each point of view is reported.

Performances and efficiency

Performances and efficiency are the most important parameters in the evaluation of a WEC technology: higher is the extracted power and higher the attractiveness of a WEC will be. This means also that the device must be sufficiently tunable with respect to the incoming sea state, that clearly varies during the day. On the other hand, performances means also stresses on mechanical and electrical components of the device. Hence, arise that forcing the system over a certain limits, device reliability and durability can drop down drastically, reducing its competitiveness.

In the case of the ISWEC device, flywheel bearings are the most critical component: increasing flywheel speed it is possible to increase the average extracted power; in contrast loads on bearings rise together with dissipation due to bearings friction, resulting in a worst durability and efficiency of the system. As consequence, a greater portion of the produced electricity needs to be recirculated in order to keep the flywheel spinning.

Therefore, in order to properly compare PeWEC and ISWEC devices, the same bearings lifetime (50 years) has been considered for both technologies.

Observing Fig. 7.19, it is possible to see that the net PeWEC average extracted power is lower that the ISWEC one over the entire scatter diagram. Moreover, it is possible to highlight that the PeWEC device is less tunable that the ISWEC device:
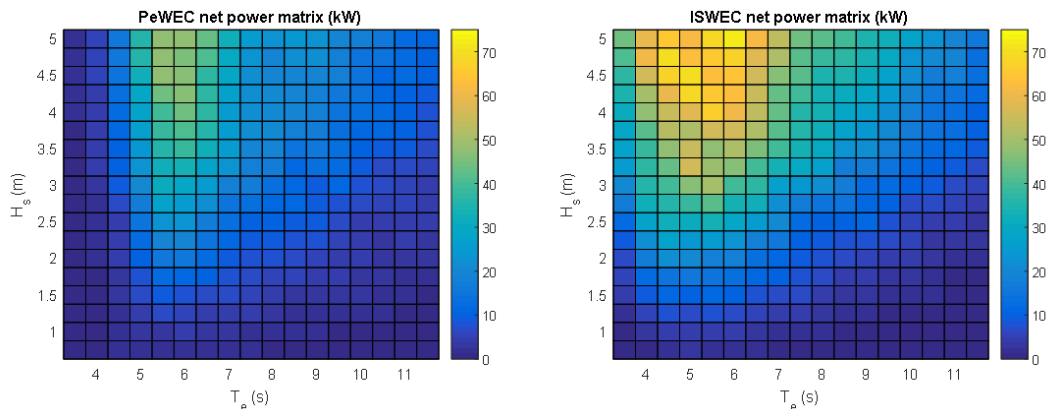
Fig. 7.19 PeWEC C19A (left) and ISWEC (right) net power matrices, calculated for the same bearings lifetime (50 years).

in the case of waves with energy period lower than 4 s, device performances are approximately null, while ISWEC device is able to harvest energy. Regarding the area of maximum average extracted power, it is possible to note that, in the case of the passive device, it is concentrated between 5.5 s and 6.5 s energy period, while the ISWEC device allows to harvest energy on a wider energy period spectrum. In term of net productivity, calculated with respect to the Pantelleria Island scatter diagram, the ISWEC device has a capacity 21% higher than the PeWEC converter. Such differences can be explained considering that the ISWEC device can be tuned acting on flywheel speed, PTO control damping and PTO control stiffness. On the contrary, the PeWEC dynamics can be adjusted tuning only PTO control damping.

Despite the limited tuning capability of the PeWEC device with respect to the incoming sea state, it is of remarkable importance the low incidence of bearings losses on the overall productivity, as reported in Fig. 7.20. It is also interesting to highlight that, imposing a bearings lifetime of 15 years and thus pushing flywheel speed, the net productivity will rise of 12%, while losses incidence on net productivity will rise around 24%, as shown in Fig. 7.21. In this case a revamping of bearings is supposed at half of the plant lifetime (30 years). In this case, the ISWEC productivity is 31% higher than the PeWEC one.

Technological considerations

The PeWEC and ISWEC technologies can be also compared from the technological and manufacturing point of view. In this case, both devices have the same layout
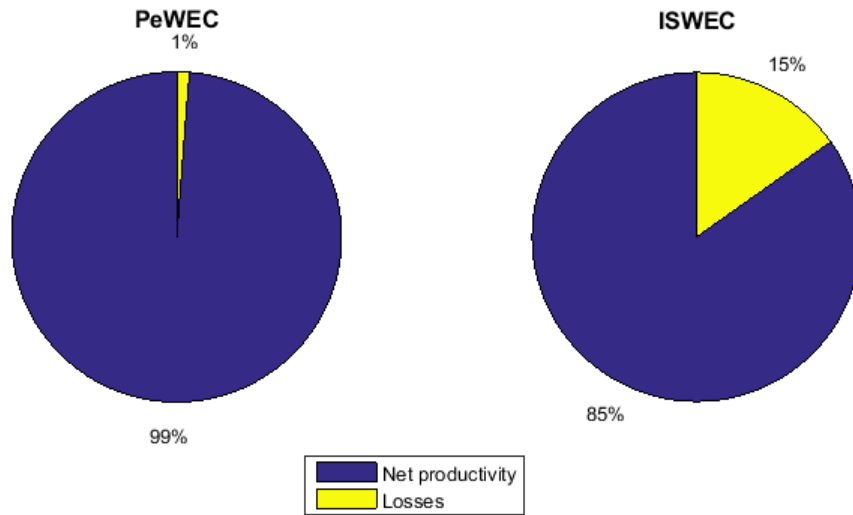
Fig. 7.20 Bearing losses incidence for the two technologies considered, 50 years bearings lifetime.
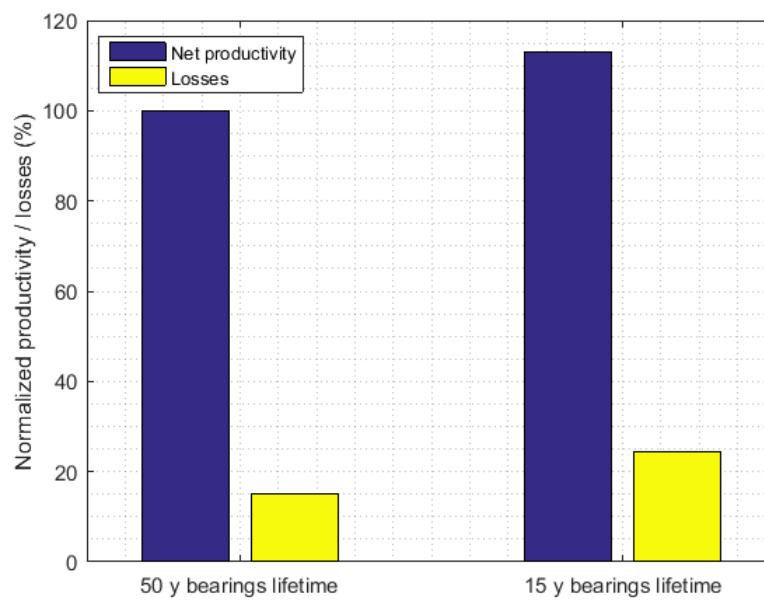
Fig. 7.21 ISWEC productivity and bearings losses dependency with respect to bearings expected lifetime.
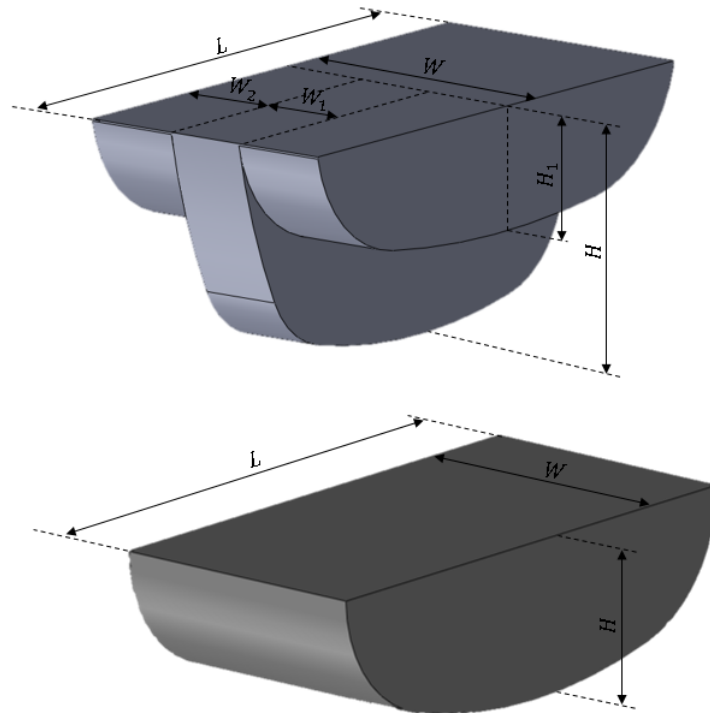
Fig. 7.22 PeWEC C19A (top) and ISWEC (bottom) floater geometry.

and can be compared easily. The following bullet describes the comparison of the different subsystems of the devices under investigation.

- *Floater*: the PeWEC floater is bigger and more complex in terms of geometry than ISWEC one, as shown in Fig. 7.22. In fact, the PeWEC C19A layout is 21 *m* long, 10 *m* wide and 9 *m* high, while the ISWEC device is 15 *m* long, 8 *m* wide and 4.5 *m* high. Moreover, the PeWEC floater mass, considering only the steel structure, amount to 94 *tons*, instead of the 56 *tons* of the ISWEC floater. Therefore, it is clear that the PeWEC floater is more expensive than the ISWEC one.

- *Mechanical conversion subsystem*: the ISWEC device is equipped with two 65 *tons* gyroscopes, a value quite close to the pendulum mass. However, pendulum materials and manufacturing costs are lower than gyroscope, as well as the complexity of the mechanical conversion system. Moreover, pendulum is a passive device, thus no energy is required to maintain in movement parts, as in the case of the gyroscope. Another interesting aspect is the lower

complexity of the system and the absence of the criticality due to flywheel
bearings in term of losses, durability strongly dependent on productivity and
forced lubrication. In fact, in the case of the pendulum, because of the low
angular speed and of the constant load acting on bearings, the latter can be
lubricated with grease. The absence of a forced lubrication system allows also
to avoid energy consumption due to auxiliary systems (oil pump).

- *PTO and gearbox*: these components are the same for both devices. The
  necessity to integrate a water cooling system for the PTO is required also in
  the case of the PEWEC device.

- *Auxiliary systems*: control and monitoring systems can be assumed almost the
  same for both devices, while regarding the electrical equipment there are some
  differences. First of all, in the case of the PeWEC device, the drive required
  for the controlling of the flywheel motor is not present, as well as the electrical
  equipment and sensors required for the management of the lubrication system.
  The cooling system needs to be installed also in the case of the PeWEC device
  for the limitation of the PTO temperature. However, the installed capacity for
  the thermal exchange is lower, since only one PTO is installed and there is no
  necessity to cool the flywheel motor and to reduce the bearings oil temperature.
  This leads to a lower complexity of the system and thus to lower costs and
  failure probability.

- *Mooring*: it is the same for both devices, in terms of layout. The unique
  difference is represented by a greater dimension of the chains sections, due
  to the higher mass of the PeWEC floater and thus of the forces exchanged
  between floater and mooring lines.

Levelized Cost of Energy

The ISWEC Levelized Cost of Energy has been calculated according to the same
hypothesis and methodology described in section 7.2.2. More in detail, it has
been calculated taking into account the possibility to guarantee a bearings lifetime
equal to 50 years (same lifetime of PeWEC bearings) or 15 years. The lifetime
assumption mainly affects the device productivity and thus the LCOE. For the sake
of confidentiality with respect to Wave For Energy s.r.l., CAPEX and OPEX values

cannot be declared completely. In the following, only the percentage difference with respect to the PeWEC Levelized Cost of Energy is reported (see Fig. 7.23).
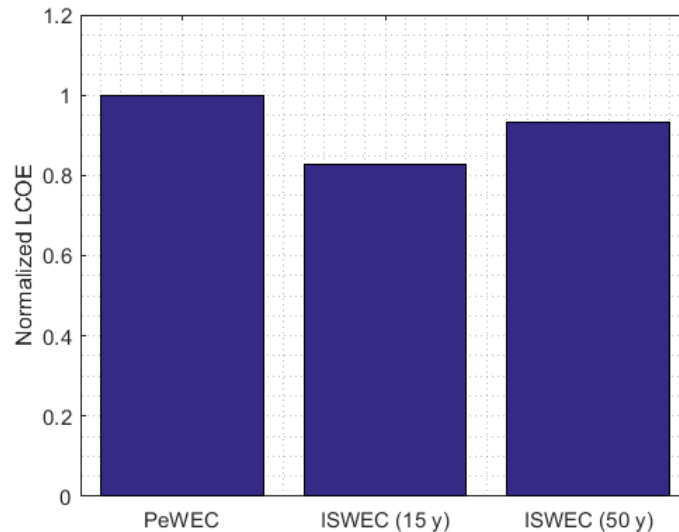
Fig. 7.23 Normalized LCOE with respect to the PEWEC device.

ISWEC LCOE is between 7% and 17% lower that PeWEC LCOE, depending on the lifetime assumed for bearings. The similarity of the techno-economic parameter calculated for the two different technologies allows to state that the PeWEC device, even if less tunable and performant with respect to the active technology, it can be competitive thanks to its simplicity and the consequently lower cost. Clearly, the PeWEC LCOE can be reduced after a more detailed design of the subsystems and a more detailed evaluation of the CAPEX cost components. Furthermore, other advantages of the PeWEC device that could promote its competitiveness are the lower bearings losses and lower auto-consumption. The simplicity of the PeWEC device equipment have also a positive effect on the OPEX: a lighter maintenance is required and a lower risk of failure is guaranteed.

Chapter 8

Conclusions

This thesis deals with the development of a pendulum Wave Energy Converter (PeWEC), specifically developed for the exploitation of the Mediterranean Sea potential. In particular, the Pantelleria Island site wave climate has been assumed as reference for the device performances analysis.

The candidate was involved in various activities of different nature: numerical modeling of the device dynamic behavior, development and experimental testing of the 1:45 and 1:12 scale prototypes, numerical model validation, development of a model based methodology for the the full scale device design and its application for the identification of a preliminary configuration. A techno-economic assessment of this configuration was also performed in the last part of this work, together with a comparison against the ISWEC device, deployed in 2015 in Pantelleria. Both technical and economic points of view were considered. The benchmarking activity is one of the main objectives of this work, highlighting the differences between a *active* power conversion system (ISWEC) and a *passive* technology (PeWEC).

The experimental activity performed on the 1:45 scale device allowed to assess the working principle validity and device performances, its applicability into the Mediterranean Sea context and to preliminary validate numerical models.

Once numerical models were validated, the design of an intermediate scale prototype was carried out, according to the general recommendations given for wave power technologies development (EquiMar). As already mentioned, the prototype was designed taking into account the Pantelleria Island site wave climate.

During the design activities of the 1:12 scale device a particular attention was given

to the dynamic interaction between pendulum and floater, in order to identify the optimal pendulum, in term of mass and geometry, for the selected floater. In particular, the optimal pendulum identification was obtained through a methodology based on the correlation between pendulum and floater resonance periods. Moreover, all the hypothesis and consideration adopted for the design of the different device subsystems (PTO, control, mooring, etc.) have been also shown. Beside functional design, the technical drawing and a structural design required for the device manufacturing were carried out. During this phase, a flexible layout of the prototype was developed, with the aim to investigate configurations different from the optimal one.

More than 120 tests were performed at the INSEAN wave tank, in both regular and irregular waves and varying the prototype settings in term of pendulum mass, floater moment of inertia, COG and pendulum hinge vertical position. More in detail, starting from the design configuration, three other solutions were tested. The main outcomes of this testing campaign can be summarized as follows:

- Tuning the pendulum and floater resonance periods in correspondence of the design wave period, it is possible to identify a resonance period below and one above the design period. These resonances arise from the coupling between pendulum and floater.

- Increasing the PTO control damping and thus braking the pendulum, a single resonance can be identified in correspondence of the design period. Therefore, adjusting properly the PTO control damping, the average extracted power can be maximized over the entire the working range, delimited by the two resonance periods.

- Increasing the floater pitch moment of inertia, it is possible to shift the second resonance period toward longer wave periods, while the first resonance period is slightly influenced by such variation. This means that the first resonance strongly depends on the pendulum dynamic response. Clearly, also the resonance period of the floater increases and in general it tends to approach to the second resonance period. This fact leads to a less regular envelope of the average extracted power computed in frequency domain.

- Reducing the pendulum mass and maintaining the pendulum and floater dynamic responses tuned on the design wave period, a decrease of the WEC performances and efficiency is determined, proving that the mass needs to be

properly selected in order to maximize the desired output power and thus the device productivity.

The linear and nonlinear formulations of the planar model developed for the representation of the PeWEC device were validated against 1:45 and 1:12 scale devices experimental results.
More in detail, the linearized frequency-domain dynamic model initially validated considering the 1:45 scale device experimental results, proving a sufficient degree of fidelity and reliability in performances, dynamics and PTO load prediction. The sufficient reliability combined with the low computational cost characterizing the linear frequency-domain model was used to design and optimize the intermediate scale device layout (pendulum mass, length, pendulum hinge position, floater pitch moment of inertia, etc.). A qualitative validation was carried out during the 1:12 scale device experimental testing, where tests were chosen according to the expected optimal performances predicted by the numerical model varying the wave period and the PTO control damping.
Then, the wide range of experimental data obtained during the intermediate scale device testing were used to validate the nonlinear dynamic model, considering both regular and irregular waves. The influence of nonlinear hydrodynamic effects and of pendulum bearings friction were investigated and introduced, leading to a remarkable improvement of the floater and pendulum dynamics prediction. Considering the most unfavorable conditions (device resonance), the error related to the average extracted prediction was estimated to be lower than 13% in both regular and irregular waves.

Starting from validated numerical models, a model-based a design methodology able to optimize the device performances has been implemented. It is based on three different tools characterized by growing level of fidelity. The idea of subdividing the design process in different steps is based on the consideration that higher fidelity means, in general, higher computational costs.
More in detail, the first tool, called *PeWEC Linear Optimization Tool*, is based on the linear frequency domain model and it has been thought to extrapolate a preliminary optimized device configuration (pendulum mass, moment of inertia, length, pendulum hinge position, etc.), on the base of some constraints given by the installation site scatter diagram characteristics. Then, the preliminary optimization results are given to the *PeWEC Design Tool* that optimizes the PTO control damping over the entire scatter diagram. This tool offers an estimation of the device productivity,

including also different boundaries (PTO size, loads, etc.) that allows to improve linearized model reliability. Lastly, an accurate simulation of the device productivity and life of the most critical components, such as bearings, is performed through the nonlinear *PeWEC Parametric Tool*.

The tools previously described where used to design a preliminary configuration of a full scale PeWEC device, optimized for the Pantelleria site wave climate. First of all a suitable floater shape was identified, taking into account the following requirements: minimize the ballast required to get the hydrostatic stability and maximize the space available for the installation of the swinging mass. Then, several simulation were performed, with the aim to calculate the optimal pendulum mass value and to find a feasible solution in term of costs and structural strength. The 135 *tons* concrete filled steel pendulum was identified as a suitable solution. Further investigation were performed in order to chose properly pendulum bearings and PTO size, taking into account components available on the market. A preliminary CAD layout of the power conversion system has been proposed too.

The economic viability of the technology, as widely discussed in this work, is one of the most important topics in the renewable energy field. For this reason the different PeWEC configurations obtained from the design activities were compared each other on the base of the Levelized Cost of Energy (LCOE). This methodology leaded to the configuration optimal from both performances and costs.

The latter was compared against ISWEC full scale device deployed in 2015 in Pantelleria, on the base of the following parameters:

- Performances and Efficiency

- Technological considerations

- Levelized Cost of Energy

From this analysis emerged that the PeWEC device is less tunable with respect to the current wave climate with respect to ISWEC device: it happens since the PeWEC device has not any *active* system that allow to adjust its dynamic response. In fact, it is mainly related to pendulum and floater mass and inertia. More specifically, the optimal PeWEC configuration net productivity is 21% lower than the ISWEC device. However, it is important to underline that the PeWEC device is affected by

lower bearings losses, since there are not any rotating parts at significant speed (the flywheel in the case of the ISWEC device).

Other important advantages of the PeWEC device are the low speed and almost constant loads acting on pendulum bearings. These working condition are less problematic than the case of the flywheel bearings, where loads are alternate and combined with flywheel velocity. In this case, a careful design is crucial to guarantee a suitable durability and reliability of the device. In the end, it is possible to state that the PeWEC device is characterized by a higher simplicity and probably by a higher reliability, than the ISWEC device. Despite these advantages, the Levelized Cost of Energy calculated for the optimal PeWEC device configuration is very far form the grid parity and to the wave energy competitiveness target, actually fixed at 500 $\frac{€}{MWh}$. However, the value of 1500 $\frac{€}{MWh}$ is affected by several uncertainties, regarding capital expenditure (CAPEX) and operating and maintenance costs (OPEX). Even if a detailed design of the pendulum has been performed, it is worth noting that in the case of the floater only a representative structural thickness has been considered. The latter was calculated on the base of the experience gained on the ISWEC device. This assumption may overestimate the floater mass and thus its costs. Therefore, a more detailed design of such component should be carried out, together with the detail design of the other device subsystems (control, electrical panels, safety equipment, etc.).

Concluding, the research activities reported in this thesis constitute a robust starting point for the comprehension of the dynamic behavior of a pendulum based Wave Energy Converter and of its capabilities in context of the Mediterranean Sea. Given the variety of the topics treated in this thesis, possible work on both the theoretical and experimental aspect of this thesis, can be undertaken in the future. Regarding numerical models the following improvements should be made:

- Validation of surge motion, DOF that is strongly coupled with pitch motion and thus fundamental for a proper prediction of the pendulum motion. A new experimental campaign needs to be carried out, since during the 1:12 scale prototype testing the motion tracking system failed. It is important to remark that for surge motion validation the absolute position of the device with respect to the mooring anchoring point on the seabed is required. This information of primary importance for the evaluation of the mooring line distension and thus of the forces discharged on the floater;

- A better representation of the mooring line behavior should be introduced, substituting for instance the rigid body representation of the chains with a catenary model;

- Expansion of the planar device dynamics representation to a more general representation along the 6 DOFs, with the aim to include the effect of roll, yaw and sway motion on device performance, when muti-directional sea states are considered.

The design methodology proposed for the design and optimization of the full scale device proved to be effective. However, some aspects can be further improved:

- The floater geometry has been optimized on the base of some of basic criteria that are not enough in the perspective of the development of commercial plant. An optimization through sophisticated codes based on genetic algorithms would be a possible solution: Examples of genetic algorithms applied to the optimization of a WEC floater can be found in [75][105][106];

- The *PeWEC Linear Optimization Tool* should be integrated with the Nemoh BEM code for the calculation of the floater hydrodynamic database. The main advantage is represented by the possibility to test different geometries without the necessity to use any external program (Ansys AQWA as example) for the calculation of the hydrodynamic coefficients. In fact, the Nemoh code is programmed in MATLAB and thus fully compatible with the *PeWEC Linear Optimization Tool* routines. The reliability of this code has been widely tested by many authors. A benchmarking of the Nemoh code against Ansys AQWA was performed by the author in [91];

- The optimization algorithm implemented in the *PeWEC Linear Optimization Tool* for the identification of the optimal layout should be tested considering other floater and pendulum geometries or considering another device, for example the ISWEC. Moreover, the it should be compared against more sophisticated optimization algorithms, such as global search algorithms [119] or heuristic algorithms [107].

Lastly, regarding the full scale plant, the following activities should be undertaken:

- Improvement of the floater geometry, efficiency and dynamic response;

- Evaluation of the C19A floater geometry feasibility from the structural point of view. This analysis should be helpful for the determination of a more detailed layout of the internal stiffeners distribution and external panels thickness. This aspect is of relevant importance for a proper estimation of the floater costs;

- Evaluation of the performances improvement by introducing more sophisticated PTO control techniques. For instance, considering the SEAREV project, latching-declucthing control techniques can be the right way to improve significantly the device productivity. More details can be found in [15]. Other examples of latching-declutching control techniques applied to WECs are reported in [48][130][131].
  Beside latching-declutching control techniques, many other control strategies can be considered to improve the PeWEC performances (LQR, MPC, etc.). The state of the art about the various control strategies applied to the WECs can be found in [100]. Another valuable reference is represented by [124], where the effect of different control strategies on the ISWEC performances are discussed. Lastly, recent studies were oriented to the application of a novel maximum power tracking algorithm (MPPT), specifically developed for WECs [5][65]

- Detailed evaluation of the auxiliary systems required for the device management and operation. This analysis is very important to determine the device auto-consumption and thus a more realistic productivity. Moreover, the design of auxiliaries is important for the implementation of the Failure Modes and Effects Analysis (FMEA).

References

[1] 40South Energy [2017], '40South Energy R115'. [Online; Accessed Jan-2017].
URL: *https://www.40southenergy.com*

[2] Agati, G., Alikhani, A., Borello, D., Bracco, G., Mattiazzo, G., Pozzi, N., Sannino, G., Rispoli, F. and Vissio, G. [2016], Assessment of Loads and Performance of a Wave Energy Converter for the Mediterranean Sea, *in* 'Offshore Energy and Storage 2016', Malta.

[3] Airy, G. [1849], *Tides and Waves*, J.J. Griffin.

[4] Akin, J. E. [2010], *Finite Element Analysis Concepts*, WORLD SCIENTIFIC.
URL: *https://dx.doi.org/10.1142/7785*

[5] Amon, E. A., Brekken, T. K. A. and Schacher, A. A. [2012], 'Maximum Power Point Tracking for Ocean Wave Energy Conversion', *IEEE Transactions on Industry Applications* **48**(3), 1079–1086.
URL: *https://dx.doi.org/10.1109/tia.2012.2190255*

[6] Ansys [2013], *AQWA Theory Manual*. Release 15.0, USA.

[7] Arena, F., Fiamma, V., Laface, V., Malara, G., Romolo, A. and Strati, F. M. [2015], Monitoring of the U-OWC under construction in Civitavecchia (Rome, Italy), *in* '11th European Wave and Tidal Energy Conference (EWTEC)', Nantes, France.

[8] Arena, F. and Filianoti, P. [2007], 'Small-Scale Field Experiment on a Submerged Breakwater for Absorbing Wave Energy', *Journal of Waterway, Port, Coastal and Ocean Engineering* **133**(2), 161–167.
URL: *https://dx.doi.org/10.1061/(asce)0733-950x(2007)133:2(161)*

[9] Arena, F., Laface, V., Malara, G., Romolo, A., Viviano, A., Fiamma, V., Sannino, G. and Carillo, A. [2015], 'Wave climate analysis for the design of wave energy harvesters in the Mediterranean Sea', *Renewable Energy* **77**, 125–141.
URL: *https://dx.doi.org/10.1016/j.renene.2014.12.002*

[10] Arinaga, R. A. and Cheung, K. F. [2012], 'Atlas of global wave energy from 10 years of reanalysis and hindcast data', *Renewable Energy* **39**(1), 49–64.
URL: *https://dx.doi.org/10.1016/j.renene.2011.06.039*

[11] Asmuth, H., Schmitt, P., Elsaesser, B. and Henry, A. [2015], Determination of non-linear damping coefficients of bottom-hinged oscillating wave surge converters using numerical free decay tests, *in* 'Renewable Energies Offshore', CRC Press, pp. 507–513.
URL: *https://dx.doi.org/10.1201/b18973-71*

[12] Astariz, S. and Iglesias, G. [2015], 'The economics of wave energy: A review', *Renewable and Sustainable Energy Reviews* **45**, 397–408.
URL: *https://dx.doi.org/10.1016/j.rser.2015.01.061*

[13] Babarit, A., Bull, D., Dykes, K., Malins, R., Nielsen, K., Costello, R., Roberts, J., Ferreira, C. B., Kennedy, B. and Weber, J. [2017], 'Stakeholder requirements for commercially successful wave energy converter farms', *Renewable Energy* **113**, 742–755.
URL: *https://10.1016/j.renene.2017.06.040*

[14] Babarit, A., Clément, A., Ruer, J. and Tartivel, C. [2006], SEAREV: A fully integrated wave energy converter, Technical report, École Centrale de Nantes.

[15] Babarit, A., Guglielmi, M. and Clément, A. H. [2009], 'Declutching control of a wave energy converter', *Ocean Engineering* **36**(12-13), 1015–1024.
URL: *https://dx.doi.org/10.1016/j.oceaneng.2009.05.006*

[16] Bailey, H., Robertson, B. and Buckham, B. [2018], 'Variability and stochastic simulation of power from wave energy converter arrays', *Renewable Energy* **115**, 721–733. ISSN 0960-1481.
URL: *https://dx.doi.org/10.1016/j.renene.2017.08.052*

[17] Besio, G., Mentaschi, L. and Mazzino, A. [2016], 'Wave energy resource assessment in the Mediterranean Sea on the basis of a 35-year hindcast', *Energy* **94**, 50–63.
URL: *https://dx.doi.org/10.1016/j.energy.2015.10.044*

[18] Bhinder, M. A., Babarit, A., Gentaz, L. and Ferrant, P. [2011], Assessment of Viscous Damping via 3D-CFD Modelling of a Floating Wave Energy Device, *in* '9th European Wave and Tidal Energy Conference (EWTEC)', Southampton, UK.

[19] Boccotti, P. [2003], 'On a new wave energy absorber', *Ocean Engineering* **30**(9), 1191–1200.
URL: *https://dx.doi.org/10.1016/s0029-8018(02)00102-6*

[20] Bonetto, A. [2017], PeWEC: full-scale design, Master's thesis, Department of Mechanical and Aerospace Engineering, Politecnico di Torino.

[21] Bonfanti, M., Sirigu, S. A., Bracco, G., Passione, B., Vissio, G., Pozzi, N. and Mattiazzo, G. [2017], Application of a Passive Control Technique to the ISWEC, *in* '12th European Wave Energy and Tidal Energy Conference (EWTEC)', Cork, Ireland.

[22] Borthwick, A. G. L. [2016], 'Marine Renewable Energy Seascape', *Engineering* **2**, 67–78.
URL: *https://dx.doi.org/10.1016/J.ENG.2016.01.011*

[23] Bracco, G. [2010], ISWEC: a gyroscopic wave energy converter, PhD thesis, Politecnico di Torino, Italy.

[24] Bracco, G., Bonanti, M., Scaiola, F., Passione, B., Pozzi, N., Sirigu, S. A. and Mattiazzo, G. [2017], Integration of renewable energy to power public transport at the Island of Pantelleria, *in* 'Offshore Energy and Storage 2017'.

[25] Bracco, G., Giorcelli, E., Giorgi, G., Mattiazzo, G., Passione, B., Raffero, M. and Vissio, G. [2015], Performance assessment of the full scale ISWEC system, *in* '2015 IEEE International Conference on Industrial Technology (ICIT)', Institute of Electrical and Electronics Engineers (IEEE).
URL: *https://dx.doi.org/10.1109/icit.2015.7125466*

[26] Bracco, G., Giorcelli, E. and Mattiazzo, G. [2008], One Degree of Freedom Gyroscopic Mechanism for Wave Energy Converters, *in* 'Volume 2: 32nd Mechanisms and Robotics Conference, Parts A and B', ASME.
URL: *https://dx.doi.org/10.1115/detc2008-49847*

[27] Bracco, G., Giorcelli, E. and Mattiazzo, G. [2011], 'ISWEC: A gyroscopic mechanism for wave power exploitation', *Mechanism and Machine Theory* **46**(10), 1411–1424.
URL: *https://10.1016/j.mechmachtheory.2011.05.012*

[28] Bracco, G., Giorcelli, E., Mattiazzo, G., Orlando, V. and Raffero, M. [2015], 'Hardware-In-the-Loop test rig for the ISWEC wave energy system', *Mechatronics* **25**, 11–17.
URL: *https://dx.doi.org/10.1016/j.mechatronics.2014.10.007*

[29] Branker, K., Pathak, M. and Pearce, J. [2011], 'A review of solar photovoltaic levelized cost of electricity', *Renewable and Sustainable Energy Reviews* **15**(9), 4470–4482.
URL: *https://dx.doi.org/10.1016/j.rser.2011.07.104*

[30] Budar, K. and Falnes, J. [1975], 'A resonant point absorber of ocean-wave power', *Nature* **256**(5517), 478–479.
URL: *https://dx.doi.org/10.1038/256478a0*

[31] Clément, A., Babarit, A., Gilloteaux, J.-C., Josset, C. and Duclos, G. [2005], The SEAREV Wave Energy Converter, *in* '6th European Wave and Tidal Energy Conference (EWTEC)', Glasgow, UK.

[32] Cordonnier, J., Gorintin, F., Cagny, A. D., Clément, A. and Babarit, A. [2015], 'SEAREV: Case study of the development of a wave energy converter', *Renewable Energy* **80**, 40–52.
URL: *https://dx.doi.org/10.1016/j.renene.2015.01.061*

[33] Cummins, W. E. [1962], The impulse response function and ship motions, Technical Report 1661, Department of the Navy, David Taylor model basin, Washington DC.

[34] DNV [2010], *Environmental conditions and environmental loads*. Recommended practice DNV-RP-C205.

[35] Drew, B., Plummer, A. R. and Sahinkaya, M. N. [2009], 'A review of wave energy converter technology', *Proceedings of the Institution of Mechanical Engineers, Part A: Journal of Power and Energy* **223**(8), 887–902.
URL: *https://dx.doi.org/10.1243/09576509jpe782*

[36] Drocco, S. [2013], Analisi dinamica di un sistema per la produzione di energia da moto ondoso con architettura a pendolo, Master's thesis, Politecnico di Torino.

[37] Duarte, T., Gueydon, S., Jonkman, J. and Sarmento, A. [2014], Computation of Wave Loads Under Multidirectional Sea States for Floating Offshore Wind Turbines, *in* 'International Conference on Offshore Mechanics and Arctic Engineering', Vol. 9B: Ocean Renewable Energy, ASME.
URL: *https://dx.doi.org/10.1115/OMAE2014-24148*

[38] EERE [2017], 'Wave energy prize'. [Online; Accessed Dec-2017].
URL: *https://waveenergyprize.org/*

[39] EMEC [2009], *Tank Testing of Wave Energy Conversion System*, Marine Energy Guides, BSI.

[40] EMEC [2017], 'European Wave Energy Center'. [Online; Accessed Dec-2017].
URL: *https://www.emec.org.uk/marine-energy/wave-devices/*

[41] EquiMar [2017], 'Equimar protocols'. [Online; Accessed Jan-2017].
URL: *https://www.equimar.org/*

[42] ExxonMobil [2017], '2017 Outlook for Energy: A view to 2040'. [Online; Accessed Jan-2017].
URL: *https://www.corporate.exxonmobil.com/en/energy/energy-outlook*

[43] Falcão, A. [2010], 'Wave energy utilization: A review of the technologies', *Renewable and Sustainable Energy Reviews* **14**(3), 899–918.
URL: *https://dx.doi.org/10.1016/j.rser.2009.11.003*

[44] Falnes, J. [2012], *Ocean Waves and Oscillating Systems: Linear Interactions Including Wave-Energy Extraction*, Cambridge Univ Press. ISBN 0521782112.

[45] Falnes, J. and Hals, J. [2011], 'Heaving buoys, point absorbers and arrays', *Philosophical Transactions of the Royal Society A: Mathematical, Physical and Engineering Sciences* **370**(1959), 246–277.
URL: *https://dx.doi.org/10.1098/rsta.2011.0249*

[46] Faltinsen, O. M. [1993], *Sea Loads on Ship and Offshore Structures*, Cambridge University Press. ISBN 987-0521458702.

[47] Faraggiana, E. [2016], Techno-Economic Analysis of the Pendulum Wave Energy Converter, Master's thesis, Department of Mechanical and Aerospace Engineering, Politecnico di Torino.

[48] Feng, Z. and Kerrigan, E. C. [2015], 'LatchingDeclutching Control of Wave Energy Converters Using Derivative-Free Optimization', *IEEE Transactions on Sustainable Energy* **6**(3), 773–780.
URL: *https://dx.doi.org/10.1109/tste.2015.2410784*

[49] Fritsch, F. N. and Carlson, R. E. [1980], 'Monotone Piecewise Cubic Interpolation', *SIAM Journal on Numerical Analysis* **17**(2), 238–246.
URL: *https://dx.doi.org/10.1137/0717021*

[50] Goda, Y. [2008], Overview on the applications of random wave concept in coastal engineering, *in* 'Japan Academy, Series B Physical and Biological Sciences', Vol. 84, pp. 374–385.
URL: *https://dx.doi.org/10.2183/pjab/84.374*

[51] Guanche, R., de Andrés, A., Simal, P., Vidal, C. and Losada, I. [2014], 'Uncertainty analysis of wave energy farms financial indicators', *Renewable Energy* **68**, 570–580.
URL: *https://dx.doi.org/10.1016/j.renene.2014.02.046*

[52] Gunn, K. and Stock-Williams, C. [2012], 'Quantifying the global wave power resource', *Renewable Energy* **44**, 296–304.
URL: *https://dx.doi.org/10.1016/j.renene.2012.01.101*

[53] Himeno, Y. [1981], Prediction Of Ship Roll Damping - State Of The Art, Technical Report 239, The University of Michigan College Of Engineering.

[54] Holmes, B. [2011], *EquiMar: Sea Trial Manual*, The University of Edinburgh, School of Engineering. ISBN 9780950892047.

[55] Huijsmans, R. [1996], Mathematical modeling of the mean drift force in current: A numerical and experimental study, PhD thesis, Delft University of Technology.

[56] INSEAN [2012], *International Towing Tank Conference Catalogue of Facilities Towing Tanks, Seakeeping and Manoeuvering Basins*. Towing Tank NO. 2.

[57] IRENA [2017], 'REthinking Energy 2017: Accelerating the global energy transformation'. International Renewable Energy Agency, Abu Dhabi, ISBN 987-92-95111-06-6.

[58] Ji, X., Liu, S., Bingham, H. B. and Li, J. [2015], 'Multi-directional random wave interaction with an array of cylinders', *Ocean Engineering* **110**, 62–77. ISSN 0029-8018.
URL: *https://dx.doi.org/10.1016/j.oceaneng.2015.09.039*

[59] Journèe, J. M. J. and Massie, W. W. [2001], *Offshore Hydromechanics*, first edn, Delft University of Technology.

[60] Kim, Y. and Park, M.-J. [2015], 'Identification of the nonlinear roll damping and restoring moment of a FPSO using Hilbert transform', *Ocean Engineering* **109**, 381–388.
URL: *https://dx.doi.org/10.1016/j.oceaneng.2015.09.019*

[61] Korotkin, A. I. [2008], *Added Masses of Ship Structures*, Springer-Verlag GmbH. ISBN 1402094310.

[62] Lagarias, J. C., Reeds, J. A., Wright, M. H. and Wright, P. E. [1998], 'Convergence Properties of the Nelder–Mead Simplex Method in Low Dimensions', *SIAM Journal on Optimization* **9**(1), 112–147.
URL: *https://dx.doi.org/10.1137/s1052623496303470*

[63] Leane [2014], *Miniature Tension Load Cells*, Leane International srl. Model UMM, UMMA catalogue.

[64] Leane [2015], *Tension and Compression Sealed 'S' Beam Load Cell*, Leane International srl. DBB Series catalogue.

[65] Lettenmaier, T., von Jouanne, A. and Brekken, T. [2017], 'A new maximum power point tracking algorithm for ocean wave energy converters', *International Journal of Marine Energy* **17**, 40–55.
URL: *https://dx.doi.org/10.1016/j.ijome.2017.01.006*

[66] Liberti, L., Carillo, A. and Sannino, G. [2013], 'Wave energy resource assessment in the Mediterranean, the Italian perspective', *Renewable Energy* **50**, 938–949.
URL: *https://10.1016/j.renene.2012.08.023*

[67] Lim, C., Park, J., Choi, J., Cheon, H. and Shin, S. [2015], 'The study on design of the floating pendulum wave energy converter (fpwec) operation system', *International Society of Offshore and Polar Engineers (ISOPE)* **2015**, 951–956.

[68] López, I., Andreu, J., Ceballos, S., de Alegría, I. M. and Kortabarria, I. [2013], 'Review of wave energy technologies and the necessary power-equipment', *Renewable and Sustainable Energy Reviews* **27**, 413–434.
URL: *https://dx.doi.org/10.1016/j.rser.2013.07.009*

[69] Luczko, E., Robertson, B., Bailey, H., Hiles, C. and Buckham, B. [2018], 'Representing non-linear wave energy converters in coastal wave models', *Renewable Energy* **118**, 376–385. ISSN 0960-1481.
URL: *https://10.1016/j.renene.2017.11.040*

[70] Lund, T. B. [2012], Rolling Contact Fatigue Testing, Bearing Life Prediction and Steel Properties, *in* 'Bearing Steel Technologies: 9th Volume, Advances in Rolling Contact Fatigue Strength Testing and Related Substitute Technologies', ASTM International, pp. 1–20.

[71] Masuda, Y. [31 Aug 1965], 'Ocean wave electric generator'. Patent US3204110A.

[72] MATLAB [2017], *Optimization Toolbox User's Guide*, MathWorks.

[73] Mattiazzo, G. and Giorcelli, E. [2007], Mathematical model of a energy converter from sea waves, *in* 'World Energy Congress'.

[74] McAllister, M. L., Venugopal, V. and Bothwick, A. G. L. [2017], Wave directional spreading from point field measurements, *in* 'Mathematical, Physical, and Engineering Sciences', Vol. 473.
URL: *https://10.1098/rspa.2016.0781*

[75] McCabe, A., Aggidis, G. and Widden, M. [2010], 'Optimizing the shape of a surge-and-pitch wave energy collector using a genetic algorithm', *Renewable Energy* **35**(12), 2767–2775.
URL: *https://10.1016/j.renene.2010.04.029*

[76] Morales-Espejel, G. E., Gabelli, A. and de Vries, A. J. C. [2015], 'A Model for Rolling Bearing Life with Surface and Subsurface Survival–Tribological Effects', *Tribology Transactions* **58**(5), 894–906.
URL: *https://10.1080/10402004.2015.1025932*

[77] Mørk, G., Barstow, S., Kabuth, A. and Pontes, M. T. [2010], Assessing the Global Wave Energy Potential, *in* '29th International Conference on Ocean, Offshore and Arctic Engineering: Volume 3', ASME.
URL: *https://dx.doi.org/10.1115/omae2010-20473*

[78] Motor Power Company [2014], *SKA DDR Direct Drive Servomotors*. Motor Catalogue.

[79] Motor Power Company [2015], *SKA RT Direct Drive Servomotors*. Motor Catalogue.

[80] Newman, J. N. [1974], Second order, slowly-varying forces on vessel in irregular waves, *in* 'International Symposium on the Dynamics of Marine Vehicles and Structures in Waves', London IME, pp. 182–186.

[81] Ogilvie, T. F. [1964], Recent progress toward the understnding and the prediction of ship motions, *in* 'Proceedings of the 5th Symposium on Naval Hydrodynamics', Bergen, Norway.

[82] Passione, B., Pozzi, N., Sirigu, S. A., Bracco, G., Brizzolara, S. and Mattiazzo, G. [2017], Numerical and Experimental Analysis of Oscillating Fluid Tanks, *in* 'The Twenty-seventh International Ocean and Polar Engineering Conference (ISOPE)', San Francisco, USA, pp. 1013–1020.

[83] Payne, G. [2008], 'Guidance for the experimental tank testing of wave energy converters', *SuperGen Marine* .

[84] Pecher, A. [2016], Experimental Testing and Evaluation of WECs, *in* 'Handbook of Ocean Wave Energy', Springer International Publishing, pp. 221–260.
URL: *https://dx.doi.org/10.1007/978-3-319-39889-1_9*

[85] Penãlba, M., Giorgi, G. and Ringwood, J. V. [2015], A review of non-linear approaches for wave energy converter modelling, *in* '11th European Wave and Tidal Energy Conference (EWTEC)', Nantes, France.

[86] Penãlba, M., Giorgi, G. and Ringwood, J. V. [2017], 'Mathematical modelling of wave energy converters: A review of nonlinear approaches', *Renewable and Sustainable Energy Reviews* **78**, 1188–1207.
URL: *https://dx.doi.org/10.1016/j.rser.2016.11.137*

[87] Pérez, T. and Fossen, T. I. [2008], 'Time- vs. Frequency-domain Identification of Parametric Radiation Force Models for Marine Structures at Zero Speed', *Modeling, Identification and Control: A Norwegian Research Bulletin* **29**(1), 1–19.
URL: *https://dx.doi.org/10.4173/mic.2008.1.1*

[88] Pérez, T. and Fossen, T. I. [2009], 'A Matlab Toolbox for Parametric Identification of Radiation-Force Models of Ships and Offshore Structures', *Modeling, Identification and Control: A Norwegian Research Bulletin* **30**(1), 1–15.
URL: *https://dx.doi.org/10.4173/mic.2009.1.1*

[89] Pozzi, N. [2014], Modeling and testing of a wave energy converter, Master's thesis, Department of Mechanical and Aerospace Engineering, Politecnico di Torino.

[90] Pozzi, N., Bracco, G., Passione, B., Sirigu, S. A., Vissio, G., Mattiazzo, G. and Sannino, G. [2017], 'Wave Tank Testing of a Pendulum Wave Energy Converter 1:12 Scale Model', *International Journal of Applied Mechanics* **09**(02).
URL: *https:dx.doi.org/10.1142/s1758825117500247*

[91] Pozzi, N., Castino, A., Vissio, G., Passione, B., Sirigu, S. A., Bracco, G. and Mattiazzo, G. [2017], Experimental evaluation of different hydrodynamic modelling techniques applied to the ISWEC, *in* '12th European Wave and Tidal Energy Conference (EWTEC)', Cork, Ireland.

[92] Prins, H. [1995], Time-domain calculation of drift forces and moments, PhD thesis, Delft University of Technology.

[93] Quéré, C. L., Andrew, R. M., Canadell, J. G., Sitch, S., Korsbakken, J. I., Peters, G. P., Manning, A. C., Boden, T. A., Tans, P. P., Houghton, R. A., Keeling, R. F., Alin, S., Andrews, O. D., Anthoni, P., Barbero, L., Bopp, L., Chevallier, F., Chini, L. P., Ciais, P., Currie, K., Delire, C., Doney, S. C., Friedlingstein, P., Gkritzalis, T., Harris, I., Hauck, J., Haverd, V., Hoppema, M., Goldewijk, K. K., Jain, A. K., Kato, E., Körtzinger, A., Landschützer, P., Lefèvre, N., Lenton, A., Lienert, S., Lombardozzi, D., Melton, J. R., Metzl, N., Millero, F., Monteiro, P. M. S., Munro, D. R., Nabel, J. E. M. S., ichiro Nakaoka, S., O'Brien, K., Olsen,

A., Omar, A. M., Ono, T., Pierrot, D., Poulter, B., Rödenbeck, C., Salisbury, J., Schuster, U., Schwinger, J., Séférian, R., Skjelvan, I., Stocker, B. D., Sutton, A. J., Takahashi, T., Tian, H., Tilbrook, B., van der Laan-Luijkx, I. T., van der Werf, G. R., Viovy, N., Walker, A. P., Wiltshire, A. J. and Zaehle, S. [2016], 'Global carbon budget 2016', *Earth System Science Data* **8**(2), 605–649.
URL: *https://dx.doi.org/10.5194/essd-8-605-2016*

[94] Raffero, M. [2014], Design of a Wave Energy Converter - a case of application: ISWEC, PhD thesis, Politecnico di Torino, Italy.

[95] Raffero, M., Martini, M., Passione, B., Mattiazzo, G., Giorcelli, E. and Bracco, G. [2015], 'Stochastic Control of Inertial Sea Wave Energy Converter', *The Scientific World Journal* **2015**, 1–14.
URL: *https://dx.doi.org/10.1155/2015/980613*

[96] Reguero, B., Méndez, F. and Losada, I. [2013], 'Variability of multivariate wave climate in Latin America and the Caribbean', *Global and Planetary Change* **100**, 70–84.
URL: *https://dx.doi.org/10.1016/j.gloplacha.2012.09.005*

[97] Reikard, G. [2017], 7 - Wave energy forecasting, *in* 'Renewable Energy Forecasting', Woodhead Publishing Series in Energy, Woodhead Publishing. ISBN 978-0-08-100504-0.

[98] REN21 [2017], 'Renewables 2017 Global Status Report'. (Paris: REN21 Secretariat), ISBN 978-3-9818107-6-9.

[99] Rinaldi, G., Fontanella, A., Sannino, G., Bracco, G., Giorcelli, E., Mattiazzo, G. and Bludszuweit, H. [2016], 'Development of a simplified analytical model for a passive inertial system solicited by wave motion', *International Journal of Marine Energy* **13**, 45–61.
URL: *https://dx.doi.org/10.1016/j.ijome.2015.10.003*

[100] Ringwood, J. V., Bacelli, G. and Fusco, F. [2014], 'Energy-Maximizing Control of Wave-Energy Converters: The Development of Control System Technology to Optimize Their Operation', *IEEE Control Systems* **34**(5), 30–55.
URL: *https://dx.doi.org/10.1109/mcs.2014.2333253*

[101] Rodriguez, G. R., Soares, C. G. and Ferrer, L. [2000], 'Wave Group Statistics of Numerically Simulated Mixed Sea States', *Journal of Offshore Mechanics and Arctic Engineering* **122**(4), 282.
URL: *https://dx.doi.org/10.1115/1.1313532*

[102] Ruellan, M., Ahmed, H. B., Multon, B., Josset, C., Babarit, A. and Clement, A. H. [2007], Design Methodology for a SEAREV Wave Energy Converter, *in* '2007 IEEE International Electric Machines and Drives Conference', IEEE.
URL: *https://dx.doi.org/10.1109/iemdc.2007.383631*

[103] Salter, S. H. [1974], 'Wave power', *Nature* **249**(5459), 720–724.
URL: *https://dx.doi.org/10.1038/249720a0*

[104] Santecchia, E., Hamouda, A. M. S., Musharavati, F., Zalnezhad, E., Cabibbo, M., Mehtedi, M. E. and Spigarelli, S. [2016], 'A Review on Fatigue Life Prediction Methods for Metals', *Advances in Materials Science and Engineering* **2016**, 1–26.
URL: *https://dx.doi.org/10.1155/2016/9573524*

[105] Shadman, M., Estefen, S. F., Rodriguez, C. A. and Nogueira, I. C. [2018], 'A geometrical optimization method applied to a heaving point absorber wave energy converter', *Renewable Energy* **115**, 533–546.
URL: *https://dx.doi.org/10.1016/j.renene.2017.08.055*

[106] Sharp, C. and DuPont, B. [2016], A Multi-Objective Real-Coded Genetic Algorithm Method for Wave Energy Converter Array Optimization, *in* 'Volume 6: Ocean Space Utilization, Ocean Renewable Energy', ASME.
URL: *https://dx.doi.org/10.1115/omae2016-54996*

[107] Sharp, C., Miller, A., Ferrero, V., Bentivoglio, M., Ebrahimi, M. and DuPont, B. L. [2018], Characterizing the Use of Heuristic Optimization Methods for Renewable Energy Systems Design, *in* '2018 AIAA Information Systems-AIAA Infotech @ Aerospace', American Institute of Aeronautics and Astronautics.
URL: *https://dx.doi.org/10.2514/6.2018-1369*

[108] Siemens [2015], *SINAMICS S120, Motori Torque completi 1FW3, Manuale di progettazione*, Siemens. Italian version manual.

[109] Sirigu, S. A. [July 2015], ISWEC: a design tool, Master's thesis, Department of Mechanical and Aerospace Engineering, Politecnico di Torino.

[110] Sirigu, S. A., Vissio, G., Bracco, G., Dafnakis, P., Passione, B., Pozzi, N. and Mattiazzo, G. [2017], A performance assessment methodology for floating pitching WEC arrays, *in* '12th European Wave and Tidal Energy Conference (EWTEC)', Cork, Ireland.

[111] Sirigu, S. A., Vissio, G., Bracco, G., Giorcelli, E., Passione, B., Raffero, M. and Mattiazzo, G. [2016], 'ISWEC design tool', *International Journal of Marine Energy* **15**, 201–213.
URL: *https://dx.doi.org/10.1016/j.ijome.2016.04.011*

[112] SIT [2015], *Calettatori per attrito*, SIT S.p.a. Italian version catalogue.

[113] SKF [2015], *I cuscinetti volventi*. Italian version catalogue.

[114] Soares, C. G., ed. [2016], *Progress in Renewable Energies Offshore: Proceedings of the 2nd International Conference on Renewable Energies Offshore (RENEW2016), Lisbon, Portugal, 24-26 October 2016*, CRC Press. ISBN 978-1-138-62627-0.

[115] Stansberg, C. T., Contento, G., Hong, S. W., Irani, M., Ishida, S., Mercier, R., Wang, Y. and Wolfram, J. [2002], Final Report and Recommendations to the 23rd ITTC, *in* '23rd International Towing Tank Conference', Vol. 2, The Specialist Committee on Waves, pp. 505–736.

[116] Titah-Benbouzid, H. and Benbouzid, M. [2014], Ocean wave energy extraction: Up-to-date technologies review and evaluation, *in* '2014 International Power Electronics and Application Conference and Exposition', IEEE.
URL: *https://dx.doi.org/10.1109/peac.2014.7037878*

[117] Todalshaug, J. H. [2013], 'Practical limits to the power that can be captured from ocean waves by oscillating bodies', *International Journal of Marine Energy* **3-4**, e70–e81.
URL: *https://dx.doi.org/10.1016/j.ijome.2013.11.012*

[118] Tollefson, J. [2014], 'Power from the oceans: Blue energy', *Nature* **508**(7496), 302–304.
URL: *https://dx.doi.org/10.1038/508302a*

[119] Ugray, Z., Lasdon, L., Plummer, J., Glover, F., Kelly, J. and Martí, R. [2007], 'Scatter Search and Local NLP Solvers: A Multistart Framework for Global Optimization', *INFORMS Journal on Computing* **19**(3), 328–340.
URL: *https://dx.doi.org/10.1287/ijoc.1060.0175*

[120] UNEP [2017], Global trends in renewable energy investment 2017, Technical report, Frankfurt School.

[121] United Nations [1992], *United Nations Framework Convention on Climate Change*. 1771 UNTS 107; S. Treaty Doc No. 102-38; U.N. Doc. A/AC.237/18 (Part II)/ Add.1; 31 ILM 849.
URL: *https://unfcc.int/resource/docs/convkp/conveng.pdf*

[122] United Nations [1998], *Kyoto protocol to the United Nations framework convention on climate change*. UN Doc FCCC/CP1997/7/Add.1.
URL: *https://unfcc.int/resource/docs/convkp/kpeng.pdf*

[123] Vertechy, R., Fontana, M., Papini, G. P. R. and Forehand, D. [2014], In-tank tests of a dielectric elastomer generator for wave energy harvesting, *in* Y. Bar-Cohen, ed., 'Electroactive Polymer Actuators and Devices (EAPAD) 2014', SPIE.
URL: *https://dx.doi.org/10.1117/12.2045046*

[124] Vissio, G. [2017], ISWEC toward the sea: Development, Optimization and Testing of the Device Control Architecture, PhD thesis, Politecnico di Torino, Italy.

[125] Vissio, G., Valério, D., Bracco, G., Beirão, P., Pozzi, N. and Mattiazzo, G. [2017], 'ISWEC linear quadratic regulator oscillating control', *Renewable Energy* **103**, 372–382.
URL: *https://10.1016/j.renene.2016.11.046*

[126] WAFO [2011], *A Matlab Toolbox for Analysis of Random Waves and Loads*, Lund University. version 2.5.

[127] WAMIT [2015], *WAMIT User Manual*. USA.

[128] WES [2017], 'Wave Energy Scotand'. [Online; Accessed Dec-2017].
URL: *http://www.waveenergyscotland.co.uk/*

[129] WMO [1998], *Guide to wave analysis and forecasting (WMO)*, number 702, Secretariat of the World Meteorological Organization. ISBN 92-63-12702-6.

[130] Xie, J. and Zuo, L. [2013], 'Dynamics and control of ocean wave energy converters', *International Journal of Dynamics and Control* **1**(3), 262–276.
URL: *https://dx.doi.org/10.1007/s40435-013-0025-x*

[131] Zou, S., Abdelkhalik, O., Robinett, R., Bacelli, G. and Wilson, D. [2017], 'Optimal control of wave energy converters', *Renewable Energy* **103**, 217–225.
URL: *https://dx.doi.org/10.1016/j.renene.2016.11.036*